Hybrid Synthetic Biological-Polaritonic Light Harvesting Systems

By:

Brice Darroch

A thesis submitted in partial fulfilment of the requirements for the degree of
Doctor of Philosophy

Molecular Scale Engineering Centre for Doctoral Training

The University of Sheffield
Faculty of Science
Department of Chemistry

Submission Date:

28th September 2018

Acknowledgements

Contents

Abstract

It has been observed that when plasmon modes are coupled to light-harvesting complexes from plants and bacteria, they are split to yield hybrid light-matter states called plexcitons. Modelling of the spectra suggests that the protein complex serves as a scaffold on which the transition dipole moments are organised within the plasmon mode volume. The objective of this thesis is to determine whether these effects can be replicated using synthetic scaffolds for this organisation. The simplest such system consists of a monolayer of bacteriochlorins adsorbed at a gold surface, a system which is structurally close to the arrangement found in chlorosomes, the antenna complexes of green sulfur bacteria. A synthetic bacteriochlorin was prepared with thioacetate anchoring groups to form SAMs on gold films and nanostructures. Splitting of the plasmon mode was observed, but the coupling energy obtained was ~ 0.12 eV, short of the threshold for strong coupling (~ 0.24 eV). Analysis of the system by X-ray photoelectron spectroscopy suggests a surface density of ~ 3.7×10^{-17} m^{-2}, which may be below the limit for strong coupling of these molecules. Poly(cysteine methacrylate) brushes were also used as scaffolds. Chlorophyll a, purified from spinach, was derivatised by modification of the phytyl ester to give a succinimidyl active ester, which was then attached to the poly(CysMA) brushes. Strong coupling, leading to a pronounced splitting in the plasmon mode approach a coupling energy of ~ 0.5 eV, was observed as a function of decreasing density of the polymer brush scaffold, allowing more dipoles to derivatise the brush layer. Polymer brush-pigment hybrid materials therefore may be attractive candidates for further development of hybrid biological polaritonic light-harvesting systems.

Chapter 1: Introduction

1. Photosynthesis: From light to energy with a bacterial case study

Photosynthesis is a process where light energy is converted into chemical potential energy and used to drive biochemical reactions. It is perhaps one of the most important biochemical processes found in nature, used by virtually all plant species and photosynthetic forms of bacteria in the production of glucose with oxygen as an important by-product. Today, there are many different photosynthetic systems which exist in nature with varying levels of complexity (1). Universally, these systems mediate four phases of energy storage – 1) light energy absorption and transport by antenna structures, 2) primary electron transfer within reaction centres, 3) energy stabilization to maintain a cyclic electron transfer chain and 4) synthesis of stable products which are transported to elsewhere to provide energy for the organism. Generally, the systems are organised into chromatophore vesicles for bacteria and chloroplasts for plants. These are structures which arrange light-harvesting antenna pigments, reaction centres and synthesising proteins in a membrane over a nanometre-scale surface area, maximising the efficiency of light energy conversion into chemical potential. Many of these structures have been well documented and understood for many photosynthetic systems.

To discuss the transfer of electron excitation energy in this process and the important role that chlorophylls play in this, a bacterial light-harvesting structure will be used as an example with a simple anoxygenic photosynthetic process. Figure 1.1 shows a representation of the light-harvesting vesicle from the purple bacteria *Rhodobacter Sphaeroides* (2).
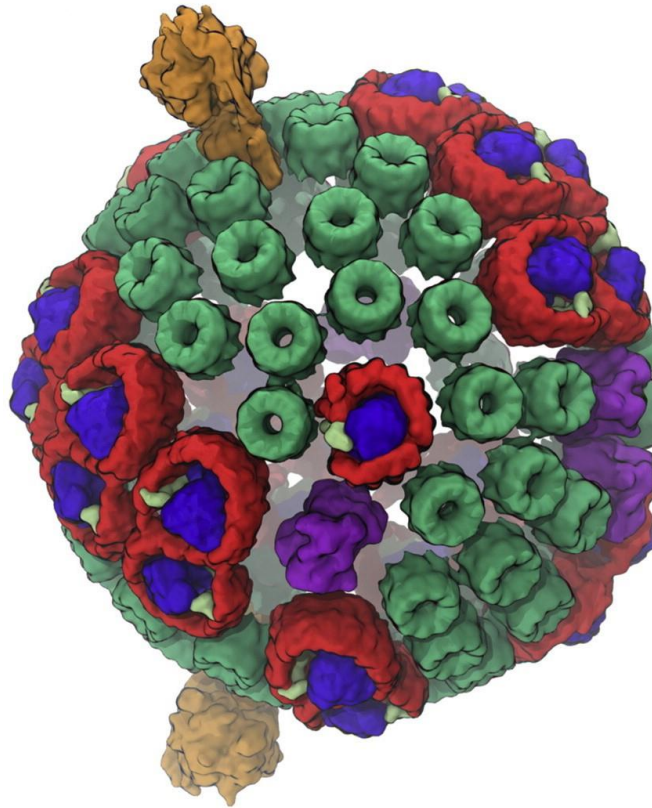
Figure 1.1: *A three-dimensional representation of the light-harvesting vesicle used by Rhodobacter Sphaeroides to photosynthesise, with several light-harvesting proteins assembled across the surface of the lipid membrane in order to supply energy to the ATP synthase structure (2). The individual proteins are identified as LH1 (red), LH2 (green), RC (blue), Cytochromes (purple) and ATP Synthase (yellow).*

Figure 1.2 illustrates the photosynthetic process and begins with the harvesting of energy from photons which come into contact with the vesicle. This is the purpose of the LH2 complexes, and to a lesser extent the LH1 complexes, which act as antenna complexes containing carotenoids and bacteriochlorophylls which can reach excited electronic states upon absorption of photonic energy. The bacteriochlorophylls are able to transfer their excitation between themselves and to adjacent LH2 complexes. After several Förster resonance energy transfer (FRET) steps the excitation is transferred to LH1, which then funnels the excitation to the RC. Here, the energy is used to generate electrons from a "special pair" of bacteriochlorophylls denoted as P870 (3):

$$2\ P870 + 2\ Photons \ \rightarrow 2\ P870^+ + 2\ e^- \tag{1.1}$$
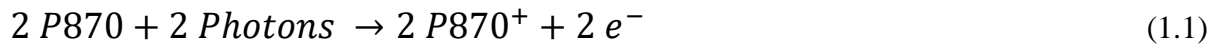
which are then transferred to a membrane-diffusible electron carrier called quinone (Q) by reduction to hydroquinone with cytoplasmic protons:

$$Q + 2\ e^- + 2\ H_{in}^+ \rightarrow QH_2 \tag{1.2}$$

This electron carrier is then transported across the vesicle membrane to the bc_1 complex. Here, a reaction occurs with a Fe^{3+} complex to regenerate protons:

$$2\ QH_2 + 2\ cytc_2(Fe^{3+}) \ \rightarrow 2\ Q + 2\ cytc_2(Fe^{2+}) + 4\ H_{out}^+ + 2\ e^- \tag{1.3}$$

These output protons are then transferred to the ATP synthase structure where they are used as the fuel to drive the formation of ATP from adenosine diphosphate (ADP) with inorganic phosphate (P_i):

$$ADP + P_i + H_{out}^+ \ \rightleftharpoons \ ATP + H_2O + H_{in}^+ \tag{1.4}$$
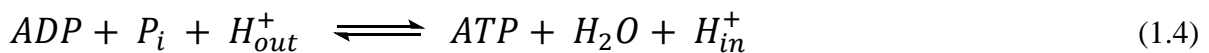
ATP is a stable molecule which is the driver of biochemical processes elsewhere in the bacterium. Finally, to stabilize the electron transfer chain, the reduced cytochrome-iron complex and the oxidised centre complex of the reaction centre engage in a redox reaction:

$$2\ cytc_2(Fe^{2+}) + 2\ P870^+ \ \rightarrow \ 2\ cytc_2(Fe^{3+}) + 2\ P870 \tag{1.5}$$
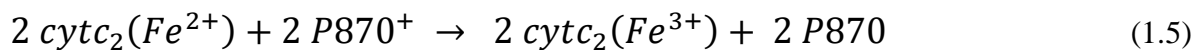
The cycle of reactions for photosynthesis is thus completed and will begin again with the supply of excitation energy transported through the LH2 complexes. This is where the primary role of chlorophyll in the process is played out.
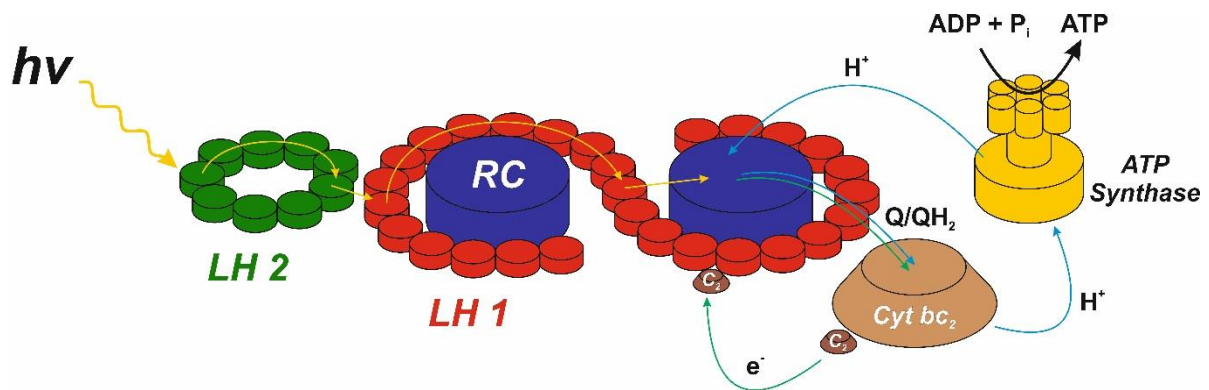
Figure 1.2: The mechanism of energy transfer from incoming light through the components of the bacterial light-harvesting vesicle, whereupon reaching the reaction centre it is used to drive several redox processes to facilitate the production of ATP (1, 3).

2. A brief overview of chlorophylls

Chlorophylls are a class of light-harvesting pigment that is ubiquitous in light-harvesting organisms. They are by far the most numerous pigments to be found – for example, in the *R. Sphaeroides* vesicle up to 4,400 chlorophylls packed into a spherical structure with a 30 nm radius (2). The basic chlorophyll unit is a type of tetrapyrrole structure called a chlorin. A metal cation is co-ordinated to the nitrogen atoms in the centre of the macrocycle, most commonly being a Mg^{2+} ion, although Zn^{2+} has been found in some bacteria which reside in harshly acidic environments. Secondly, an additional 5-membered ring is formed at one corner of the tetrapyrrole system, thus breaking the symmetry found in most porphyrins. A variety of unsymmetrical side groups are also present; usually alkane or alkene substituents but some varieties also include carbonyls such as aldehydes or ketones. The other important feature is that a long hydrocarbon chain, the phytyl tail, is attached to the

chlorophyll by an ester linkage. The purpose of this tail is to anchor the chlorophyll to the protein superstructure of its home light-harvesting complex. A library of different chlorophylls has been identified where these substituent groups can vary greatly (1).

The important difference of the chlorophylls from the porphyrins is the number of π-electrons in the aromatic system. Porphyrins have 26 π-electrons, from 11 planar double bonds as well as two lone pairs from the hydrogen- or metal-substituted nitrogen atoms. Chlorophylls have two less as a double bond from one of the pyrrole rings has been removed, making the central ring structure a chlorin. In the chlorophylls found in anoxygenic bacteria, a further double bond is lacking and thus the electron count is reduced to 22. The new structure is referred to as a bacteriochlorin. Two common variants of chlorophylls and bacteriochlorophylls are illustrated in figure 1.3.
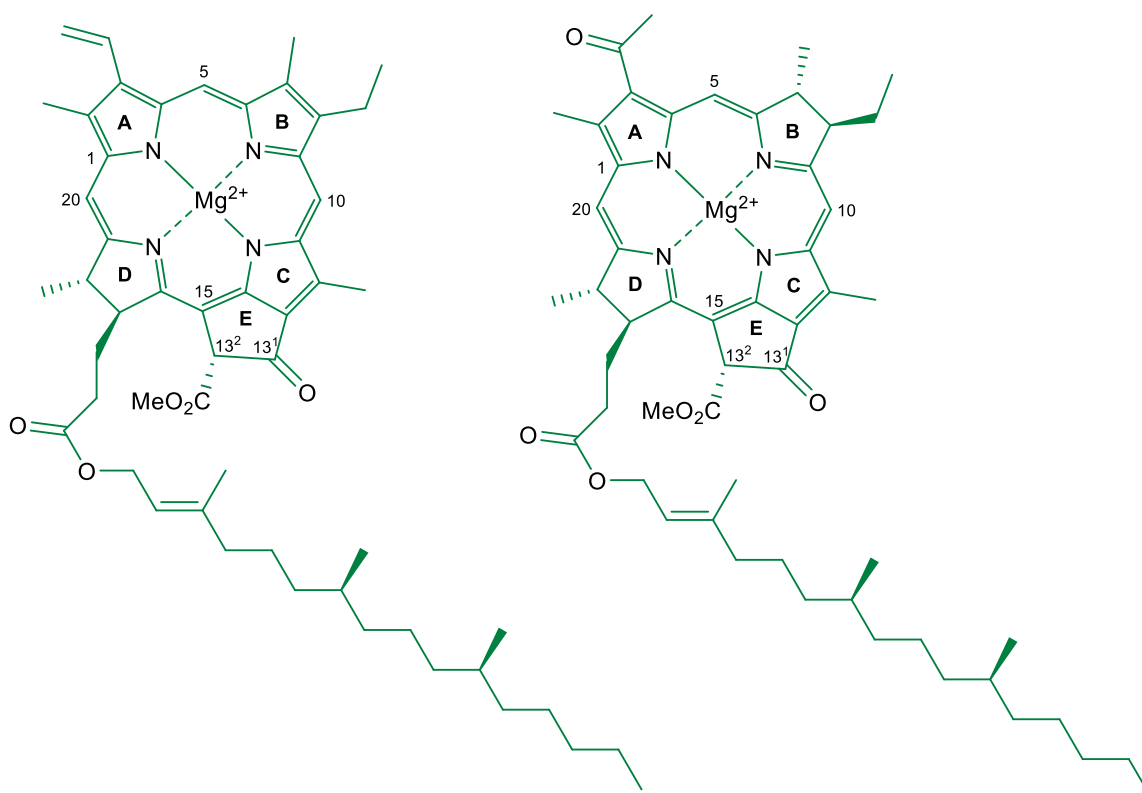
Figure 1.3: (Left) Chlorophyll a, most commonly found in the eukaryotic photosynthetic cells of plant organisms. (Right) Bacteriochlorophyll a, found in purple anoxygenic bacterial light-harvesting complexes.

While these differences are modest for the molecular structure, they are in fact very significant for the spectroscopic properties of this family of molecules. Because of the role they play as pigment molecules in light-harvesting complexes, energy absorbed from sunlight promotes an electron from the highest occupied molecular orbital (HOMO) to the lowest unoccupied molecular orbital (LUMO), generating an excited state. In chlorins and bacteriochlorins these are $\pi - \pi^*$ transitions, and the energy of the HOMO-LUMO transition depends on the electronic structure of the pigment. An oversimplified MO diagram comparing the ring systems (1, 4) is shown in Figure 1.4.
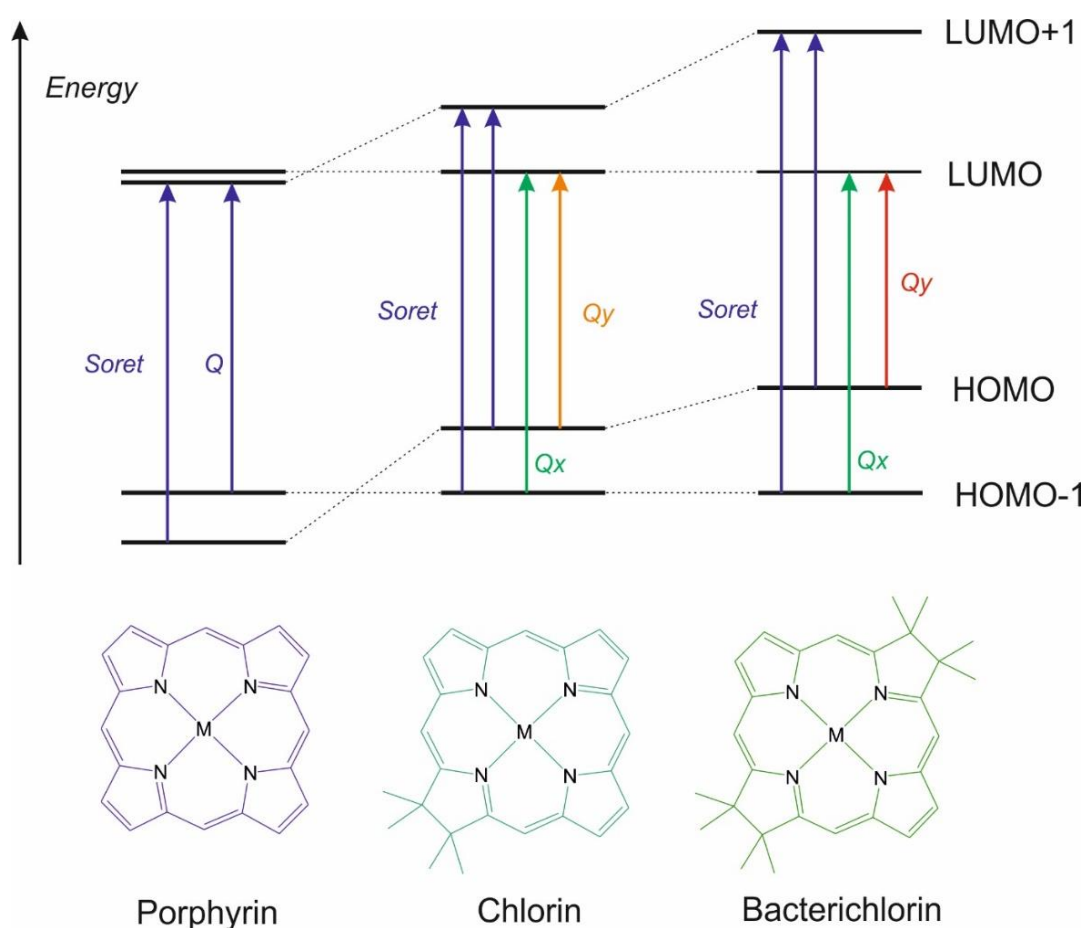
Figure 1.4: A simplified molecular orbital representation of the optical transitions of porphyrins, chlorins and bacteriochlorins.

In porphyrins, there are two transitions: from the HOMO (b_1) and the HOMO-1 (b_2) bands to the LUMO. Unlike cyclic polyenes, the porphyrins were shown to have unequal energies between the b bands due to orbital mixing in the aromatic system (4). This results in the b_1-LUMO transition becoming lower in energy, while the b_2-LUMO transition becomes higher. The latter gives a very strong high-energy absorption band as a result, known as the Soret band, while the former gives a weak series of Q bands. Chlorophylls, because of their missing double bond, have an unsymmetrical aromatic system. This results in an increase of the HOMO energy, as well as a new LUMO+1 emerging. The Soret transitions now occur from the two HOMOs to the new LUMO+1 level, but now there are new transitions to the previous LUMO which have recognisably different energies. These are known as the Q_x and Q_y bands and are polarized along the molecular axes of the chlorophyll as the light energy couples to the π-electrons and shifts the electron density along these axes. These bands have smaller transition energies than the Soret bands, especially Q_y. As a result, new absorbance peaks appear in in the UV/Vis spectrum. The Q_y peak is prominent and appears at low energy, for example chlorophyll a has a Q_y absorbance of 662 nm. The Q_x transition has a larger energy than Q_y but is much weaker spectroscopically and less resolved from the vibronic components of the spectrum. (5, 6).

These bands shift once again when the number of π-electrons becomes 22, and thus the chlorophyll becomes the bacteriochlorophyll. The HOMO and LUMO+1 once again are higher in energy, and thus according to the simplified MO diagram the Q_y transition decreases in energy. This places the absorbance energy further into the infrared region – for example, bacteriochlorophyll a has an absorbance at 773 nm. The Q_x energy does not change much, so there is not a large shift in this absorbance, but it is more intense due to the increased asymmetry of the ring, and thus an increased x-axial polarization. The Soret bands

are now shifted significantly also as the transition energy has increased. This places the Soret absorbances further in to the near UV region – 358 nm for bacteriochlorophyll *a*.

These absorbance shifts result in characteristic absorbance profiles differentiating porphyrins, chlorophylls and bacteriochlorophylls which can be observed by ultraviolet-visible light spectroscopy (fig. 1.5). This has been implied to be an evolutionary adaptation for photosynthetic organisms - for example, certain kinds of bacteria in dark oxygen-deficient environments, having the bacteriochlorophyll variant pigment, can access wavelengths at the extremes of the visible spectrum and into the UV and IR regions, allowing them to continue photosynthesis without direct sunlight.
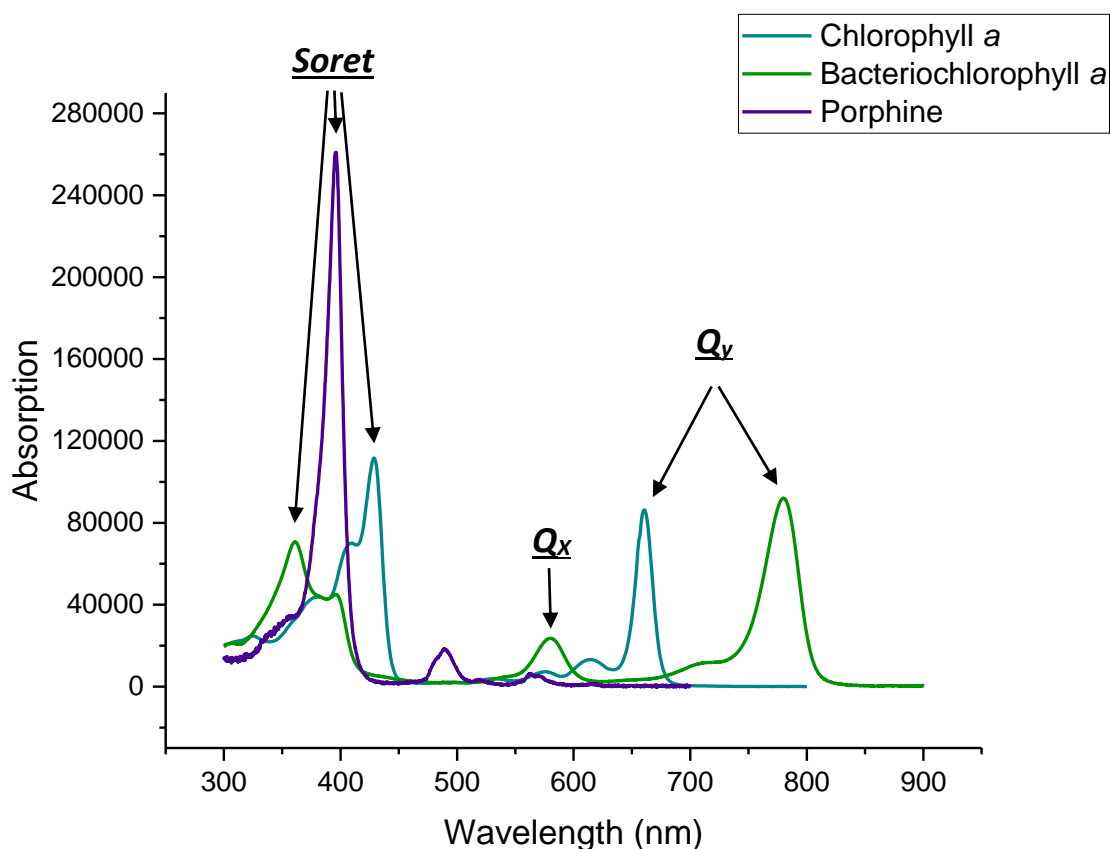
Figure 1.5: The ultraviolet/visible absorption spectra of examples of a porphyrin, chlorophyll and bacteriochlorophyll, with major transition lines indicated. Data supplied from the PhotochemCADTM 3 database, Copyright © 2004-2011 Jonathan S. Lindsey.

3. The organisation and energy transfer of bacteriochlorophylls in the bacterial LH2 complex

For light-harvesting organisms, their absorption properties are determined mostly by the characteristics of the pigments they contain. However, the light-harvesting complexes can control the arrangements of these pigments. This arrangement not only modifies the absorption properties, but also controls their energy transfer characteristics, which is crucial for the efficient transport of light energy.

For example, LH2 is a pigment-protein complex binding bacteriochlorophyll *a* (BChl *a*) and carotenoids (*Car)* in a peptide scaffold, organising them in space (figure 1.6) (7). The structure is approximately toroidal, consisting of 9 α-β apoprotien pairs organised as a ring. Each pair binds three BChl *a* and two *Car* molecules. This results in a total of 18 carotenoids and 27 BChl *a* molecules in the LH2 complex. The bacteriochlorophylls are arranged into two rings – the B800 ring in which 9 BChl *a* are separated by ~ 2 nm and orientated parallel to the plane of the vesicular membrane, and the B850 ring where 18 BChl are arranged cofacially to the plane less than 1 nm apart (8, 9), with an inter-ring separation of ~ 17.7 Å (10). The two different arrangements of BChl *a* give separate resolvable absorption maxima which are red-shifted from the standard Q_y absorption of the individual molecule. The top ring absorbs at 800 nm while the lower one absorbs at 850 nm, and so they are denoted as B800 and B850, respectively.

The energy transfer is a stepwise process between the three pigment systems, flowing in the direction of decreasing pigment absorption energy – an energy "funnel" (1). The carotenoids absorb the initial sunlight, then the excitation is transferred to the lower-energy B800 ring. The last transfer step then occurs from B800 to B850, and from B850 transfer can take place to adjacent LH2 or LH1 complexes for transport to the reaction centres.
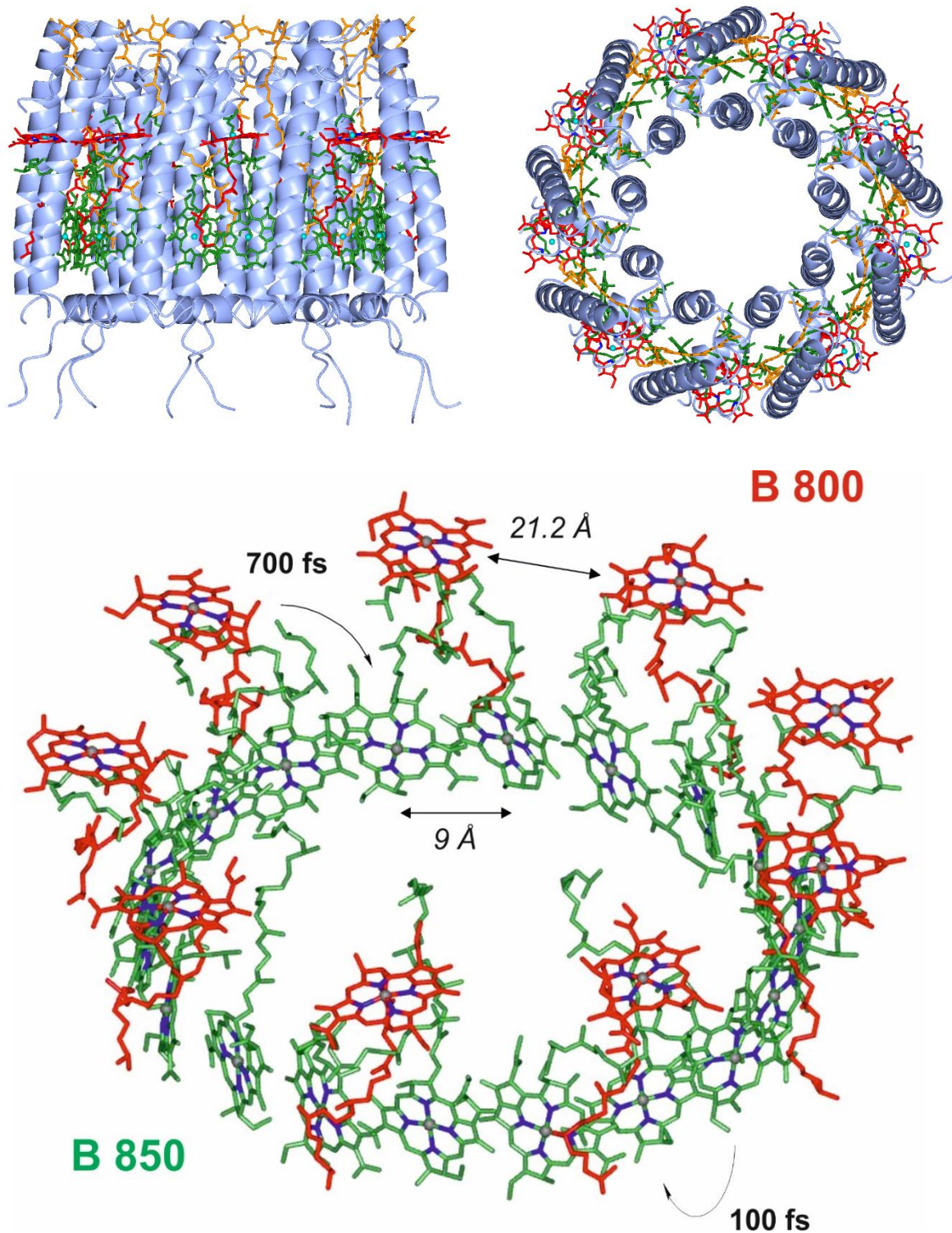
*Figure 1.6: (**Top**) Profile and plane-perpendicular views of the crystal structure of light-harvesting complex II, isolated from* Rps. Acidophilia *at a 2.45 Å resolution. Blue helices represent the protein scaffold with the pigment molecules spheroidenone (**orange**) and the B800 and B850 bacteriochlorophyll a (red and green respectively) embedded in this matrix. (**Bottom**) The orientations of the two types of bacteriochlorophyll a present in LH2, with relevant centre-to-centre differences and energy transfer lifetimes denoted. Crystal structure data for LH2 was obtained from the RCSB Protein Data Bank.*

Spectroscopic analysis of the complex reveals that the kinetics of energy transfer between the rings, as well as the BChl - BChl transfer within B800 and B850, are different. The transfer time for an excited state from B800 to B850 has been measured to between 700 – 800 femtoseconds, but the migration between bacteriochlorophylls internally within the B850 ring takes place in 100 fs. This large difference does suggest that the mechanisms of transfer are different between these environments. It is widely accepted that transfer from B800 – B850 is mediated by a Förster dipole-dipole transfer mechanism (10). Here, the molecules are only weakly coupled so that the absorption spectra of the donor and acceptor are not affected, so the transfer time depends on the square of the dipole coupling between them and emission-absorption wavelength overlap. The method of transfer between the B850 bacteriochlorophylls, however, is mediated by a stronger coupling of molecular orbitals made possible by the shorter distance. For this reason, the mechanism of transfer is believed to be excitonic in nature, and the study of this energetic state has been of considerable interest for many in explaining the high efficiency of energy storage for photosynthetic systems compared to materials-based solar generation systems.

4. Molecular excitons - formation and transport in light-harvesting systems

For many years, the prevailing theory of energy transfer in light-harvesting structures was that it was mediated by the migration of localized excited states in an incoherent process, analogous to random "hopping" until the required energy reached a reaction centre (figure 1.7) (13). Such a transfer would be mediated by a Förster mechanism, which is non-radiative resonance transfer process occurring where the donor and acceptor have aligned and coupled dipoles. (1, 10, 14). This occurs between weakly coupled pigments and is dependent on the spectral overlap of the donor and the acceptor, as a similar energy state between them is

necessary for conservation of energy. The Förster mechanism of transfer is also dependent on the distance between the acceptor and donor, with coupling energy being proportional to $1/r^6$. The energy transfer between the B800 and B850 rings has been theorised to have an R_0 of 66 Å (14) and the measured distance between them, at 17.7 Å (8), is well within the distance required for efficient Förster energy transfer.
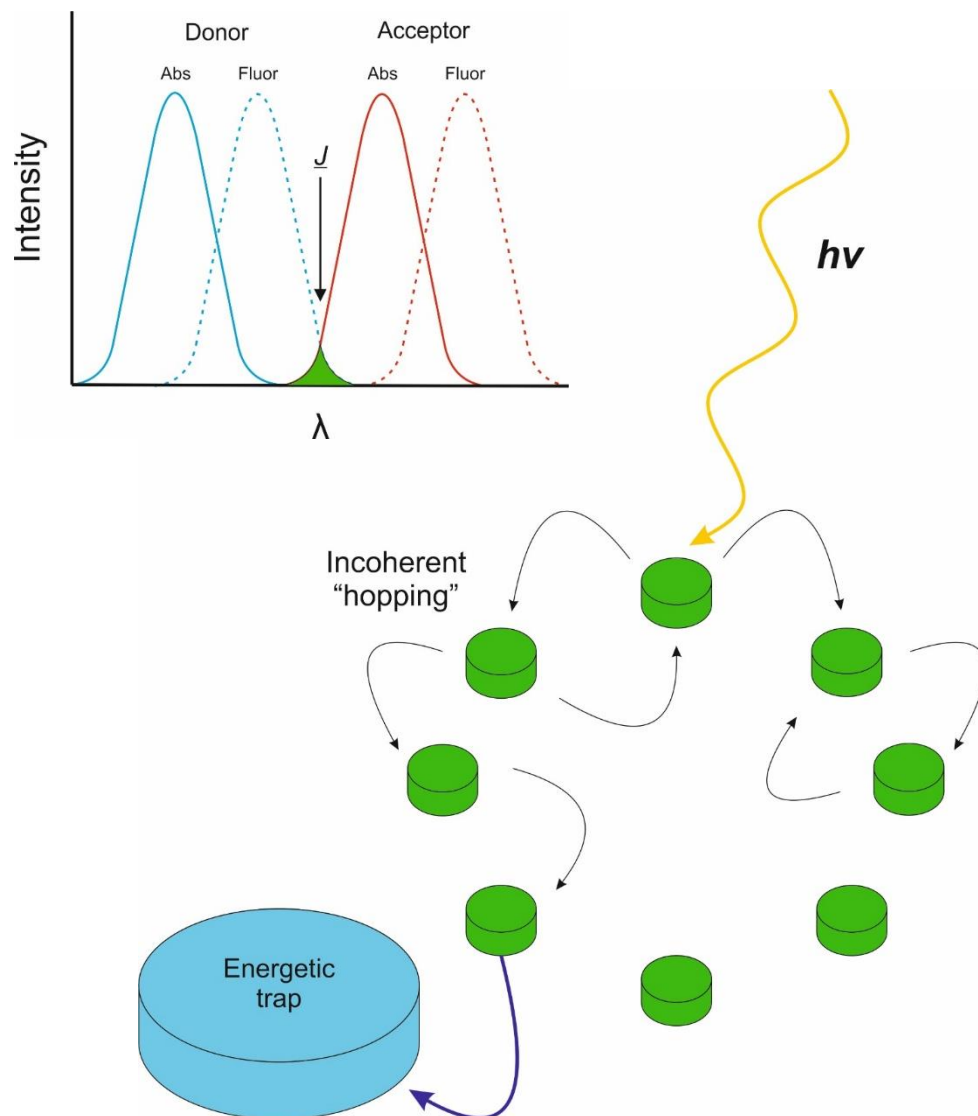
Figure 1.7: A representation of the mechanism of Förster energy transfer. Energy is transferred as a function of the overlap factor J mediating the donor fluorescence and acceptor absorbance. When light excites a chromophore in an array which all have similar absorption properties, excitation energy is transferred by a "hopping" mechanism incoherently. Random hopping forwards and backwards around the array eventually leads the excitation to the point nearest the energy "trap" where the intercomplex energy transfer may take place.

However, experimental data collected by pump-probe spectroscopy has since suggested that an additional model was needed to explain all the transfer dynamics between chlorophylls (15). By exposing a mutant of *rhodobacter sphaeroides* containing only LH1 antenna complexes to femtosecond light pulses, with a pump exposure followed by varying time-delayed probe exposures, the absorption and stimulated emission intensity was found to oscillate in a coherent manner over a series of pump-probe delay time periods, with a maximum lifetime of 300 fs measures at 4.2 K. This data suggested that upon exposure with the pump pulse an exciton population is generated within LH1 complexes, although the measured anisotropy of the polarized emission signals did not show any oscillatory behaviour which would indicate interaction of the light with a coherent excitonic state. However, in subsequent experiments studying the LH2 complex of *sphaeroides* as well as the LH1 for *Rhodopseudomonas viridis* well-resolved anisotropy data showed oscillations that lasted for femtosecond timescales (16, 17). This would appear to show that a coherent exciton state is generated and delocalised within the light harvesting complexes before decaying back a "dark" lower-energy state over a picosecond-scale lifetime, while the use of specific laser wavelengths to specifically probe the higher-absorbing chlorophylls rings suggest these as the source of these excitons.

An exciton is a molecular excited electron-hole pair state generated by electronic transitions (11, 12). When an electron in its ground energetic state absorbs a quantum of energy from light and transitions to a higher energy level, it leaves a positively charged "hole" behind, giving an electron-hole charge pair which is bound together by a mutual Coulomb interaction. Depending on the dielectric environment of the material excitons can take two significantly different forms, found for example in semiconductors and organic molecules (figure 1.8). In the former, electron orbitals are delocalised and form band structures where charge carriers are highly mobile (18). Coupled with the high dielectric
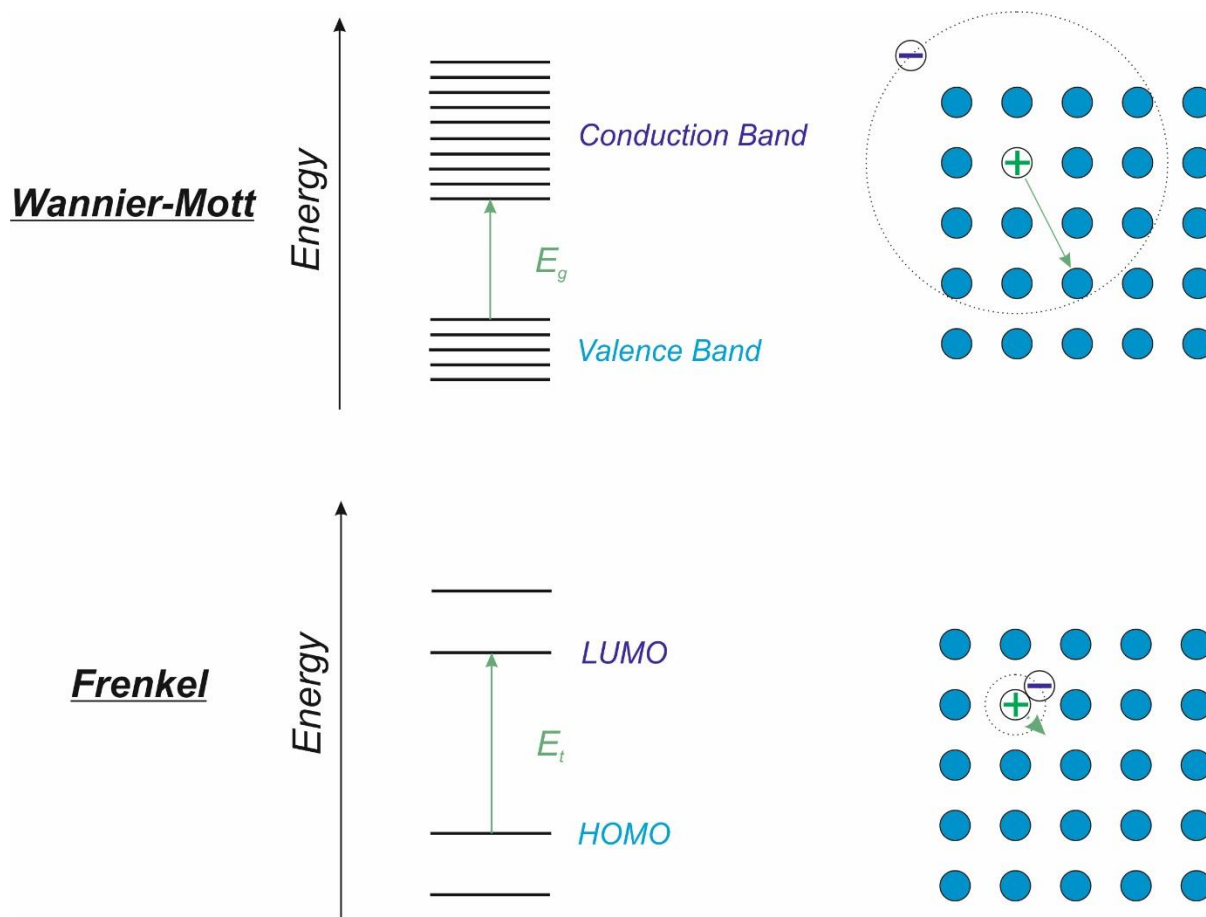
Figure 1.8: Two types of excitons characterised by the dielectric environment they occupy. Wannier-Mott excitons, in high-dielectric semiconductors, experience rapid transfer between energy sites across the material. Frenkel excitons, in low-dielectric organic materials, experience high coulombic attraction in the electron-hole pair and have a low probability of transfer to another energy site.

constant characteristic of inorganic semiconductors (for example ~ 80 for TiO_2), the Coulomb interaction between the electron and the hole in an exciton is thus quite weak. This results in an exciton with a large radius which extends over multiple lattice spacings and is highly mobile through the crystal – a Wannier-Mott exciton. In organic molecules, the dielectric constant is very low in comparison (ranging between 2-4) which results in a high Coulomb interaction in the electron-hole pair. This stronger interaction has the effect of making excitons both less mobile through organic systems and more susceptible to recombination. These are known as Frenkel excitons.

A central problem in the field of photovoltaics has been the transport of excitons generated by light absorption for photocurrent generation. Semiconductors, with weakly bound and highly mobile excitons, have been the material of choice for this purpose, but are both expensive and inefficient compared to the total energy conversion in natural systems. There has therefore been interest in the exploitation of molecular excitons to transport energy from sunlight efficiently across cheaper organic conducting materials, and it has been one of the major driving forces behind the development of organic photovoltaic structures (19 - 21). This entails matching or increasing the efficiency using materials such as π-conjugated polymers, which can generate excitonic states, which act as donors to a fullerene acceptor. Once the exciton is transported by diffusion through the polymer phase and reaches the interface with the fullerene material phase, a charge-transfer state is produced where the exciton exists partially across the interface. It is at this stage that full charge dissociation can occur into the two charge carriers – the electron diffuses into the fullerene phase and the electron hole remains back in the polymer phase. However, the Frenkel excitons in these materials experience very short lifetimes, $\sim$ 1 ns, and have poor diffusion distance through the polymer with an average of 10 nanometres achieved. Efforts have thus been made to increase the dielectric constant of organic photovoltaic materials using dopants (21), by combination with semiconducting nanodots (22) or by trying to exploit π-π stacking between polymer chains (23), but most devices were still struggling to achieve above 7% photon-to-current efficiency.

This makes the observation of possible high-efficiency transport of excitons within light-harvesting complexes very interesting. Chlorophylls and bacteriochlorophylls, like conjugated polymers, generate molecular Frenkel excitons from absorption of light, giving their characteristic transition lines. The difference in the lifetimes of energy transfer between the two arrangements of BChl *a* in LH2 however points to how these excitons could be

transported efficiently. The B850 ring of LH2 contains twice as many bacteriochlorophylls as B800, they are spaced at less than half the distance from each other, and they are orientated vertically with aligned dipole moments. As such the transfer rate of energy between these chlorophylls is much faster than the B800-B850 transition, taking place over 100 fs. This quick transfer implies that there are very strong interactions between neighbouring pigments. Examination of the BChl *a* orientation in B850 shows that their Q_y dipoles are arranged along the same plane, forming a circle. These are therefore likely to couple with each other, resulting in strong dipole coupling between the pigments, and this can link their molecular orbitals in such a way that the molecules cannot be considered individuals in the traditional sense and instead form part of an aggregated "supermolecule". When considering the absorption energy for this system, the energy of an excited state for a monomer, *E*, is split into new eigenstates as the electronic coupling allows excitation energy in the form of excitons to be delocalised along the orbitals of the contributing units.

To examine the formation of excitons in chlorophylls, the electronic structure of each pigment can be simplified as a two-level system with a single transition energy, E_i for example (24). If we imagine a dimer of chlorophylls *i* and *j* with a strong dipole moment interaction of V_{ij}, the exciton states generated by the absorption of energy from ground state ‹i| to excited state |i› with interaction with the neighbouring ground state, ‹j|, has energies and wavefunctions described by a new Hamiltonian operator:

$$H_{el} = \sum_{i=1}^{N} E_i \, |i\rangle\langle i| + \sum_{j \neq 1}^{N} V_{ij} \, |i\rangle\langle j| \qquad (1.10)$$

With N, the number of chromophores in the system, being 2 in this case. In principle, in the dimer this means that the excited eigenstate for a monomer splits into 2 new eigenstates which are now delocalised across the neighbouring chlorophylls. For two chlorophylls which

have identical transition dipole moments, these two exciton bands are split in equal

magnitude but have opposite signs. The new wavefunctions for these states are now:

$$\psi^+ = \frac{1}{\sqrt{2}}(\psi_i + \psi_j) \tag{1.6}$$

$$\psi^- = \frac{1}{\sqrt{2}}(\psi_i - \psi_j) \tag{1.7}$$

And their energies are given as:

$$E^+ = \frac{1}{2}(E_i + E_j) + V_{ij} \tag{1.8}$$

$$E^- = \frac{1}{2}(E_i + E_j) - V_{ij} \tag{1.9}$$

When this system is expanded to include more units, such as the 16 bacteriochlorophylls in

the B850 structure of LH2, a multitude of exciton eigenstates results from the strong coupling

of the monomers to each other. As a result, the electronic structure could be described as an

excitation band in which energy can freely interchange between the composite energy levels

within – thus, molecular exciton states generated from photon absorption by a

bacteriochlorophyll become delocalised throughout the entire ring structure as a coherent

supramolecular superpositional state, a transfer property much different from the localised,

incoherent hopping of energy characteristic of Förster theory (figure 1.9).
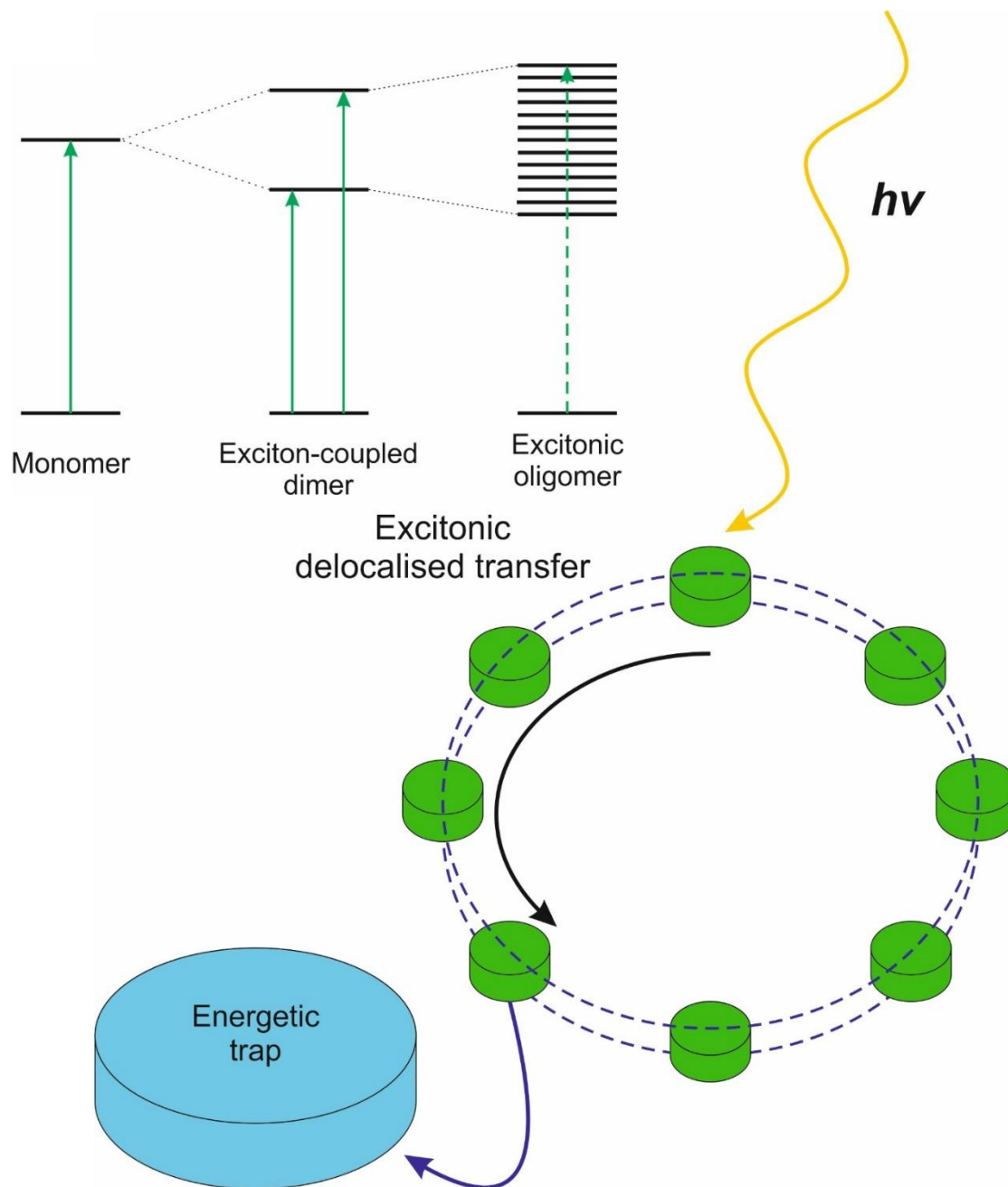
Figure 1.9: A representation of the excitonic energy transfer mechanism. When chromophore monomers are strongly coupled along their transition dipole moments, new eigenstates are produced with a splitting energy. Increasing numbers of involved monomers results in in a "supermolecule" with delocalised excitation transfer – light absorbed by one chromophore is quickly shared around the ring. Energy is thus brought into close contact with the energetic trap almost instantaneously for transfer along the long-range energy gradient.

There is some significance in the generation of excitons when considering the efficiency of the transfer of energy to the reaction centre. In the bacterial light-harvesting

vesicles, captured light energy must be transferred between the separate pigments and antenna complexes toward the reaction centre. However, the kinetics of the entire transfer process are limited by the transfer time between the antenna complexes and the trap, which between bacterial LH1 and the reaction centre can take up to 35 picoseconds, much longer than inter-bacteriochlorophyll transfer times. In this process, delocalised exciton bands may serve an important dual purpose. Firstly, they may have an advantage in maximising the efficiency of their transfer. While the B800 pigments transfer energy by incoherent hops between isolated neighbours, the exciton band across the B850 ring approximately encompasses the planar dimension of LH2, therefore simultaneously adjacent to multiple light-harvesting complexes in the neighbouring space. As such, it is possible that the band can selectively transfer its energy to whichever complex has the lowest energy absorbance. A network of excitons can then transfer the energy to the reaction centre in the shortest time possible. Secondly, they may be critical in ensuring the generated excitation energy survives for the length of time required to overcome the rate-limiting steps of the transfer process. This longevity will be especially important for the LH1-RC transfer step, and LH1 has been shown to have a very strong exciton coupling.

Utilising the methods of arrangement for chromophores as seen in light-harvesting complexes may therefore be advantageous for raising the efficiency of energy transport in artificial devices. If frameworks inspired by, but more durable than, natural proteins could be made to house pigments in selected arrangements or orientations, it is possible that molecular excitons could be transported more easily along farther distances as a form of "Mott-Frenkel" hybrid excitons. The exciton band energy may also be selectively changed depending on the application required. This could be controlled by changing the distance between pigments, as V is very dependent on separation. This was illustrated by using naphthalene dimers to investigate intramolecular dipole coupling (24, 25). By decreasing the bridge length between

two naphthalene aromatic cycles with a strong absorbance transition, the cycles were brought closer together and allowed the molecular orbitals associated with this transition to interact. As a result, this coupling was found to increase with decreasing distance, illustrated by a progressively larger splitting magnitude between the two new exciton peaks, suggesting an increase in V. Exploring this possibility could therefore allow more informed design of exciton-transporting organic materials with optimised performance.

5. Utilising surfaces to organise chlorophylls to study and transport excitons

There are some strategies that could be used to organise chlorophylls in space, either by using a solid matrix (like the light-harvesting complexes) or an assembly in liquid. A matrix would be more desirable, as most chlorophylls adopt their monomeric forms in polar solvents such as tetrahydrofuran (26). However, there are several examples in the literature of modified bacteriochlorophylls that are capable of self-assembly in various non-polar solvents such as hexane or cyclohexane, commonly derived from the c and d varieties (fig 1.10) (26 - 33). These are aggregates that are produced from non-covalent interactions, mainly hydrogen bonds and hydroxyl-metallic bonding with zinc metal centres inserted in the chlorin rings. Larger supramolecular networks of either identical or mixed variants of chlorophylls (27, 29, 31, 33) have also been produced. These have been produced as a means of producing ultrafast energy transfer like that of chlorosomes found in green photosynthetic bacteria. Other unique formations have been produced using more exotic functional groups, such as pyridine rings used by Kelley *et al.* to produce chlorophyllous tetramers (30). However, the range of distance that can be studied between the individual units is somewhat limited as a supramolecular network will not form unless the chlorophylls are only separated by a few angstroms – studying chlorophylls with greater separations would therefore be a challenge.

One could control the separation by using chemical bridges, such as in dyads of chlorophyll-type molecules chemically linked by the phytyl ester tail site (26, 27), as well as π-system linked bridges that have been synthesised to link artificial tetrapyrrole analogues (34). To produce a variety of dyads with increasing separation would require ever increasing bond lengths, however, and is likely to be synthetically demanding.
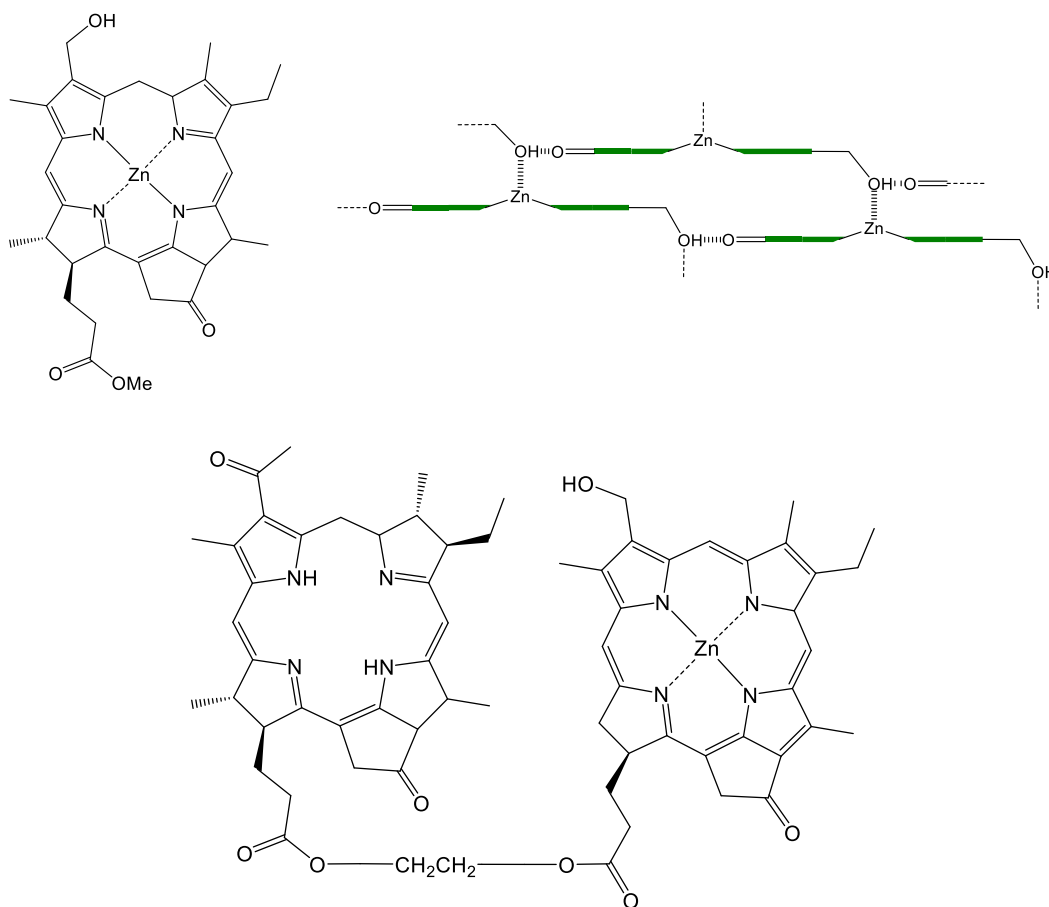
*Figure 1.10: (**Top**) A chlorophyll derivative synthesized for self-assembly into a supramolecular network in solution mediated by intermolecular Zn-O and hydrogen bonding (viewed in planar orientation) (48). (**Bottom**) An example of a two-chromophore dyad comprised of a bacteriochlorin linked to a zinc-metallated chlorophyllide for energy transfer studies (47).*

A more convenient method would be to mount the chlorophyll pigments to a substrate. One method of doing this, if indirectly, is to adsorb the light-harvesting proteins containing the pigments to a surface. Such methods have already been used in conjunction

with photovoltaic devices (35), for example as thin films assembled as crystals on an electrode, or as a layer between bulk heterojunctions (36, 37). However, while these composites showed an increase of device efficiency, it was often a modest increase with ~ 4% efficiency at maximum given for the embedded layers. Besides from this, using light-harvesting complexes themselves still does not allow for control of the separation between chlorophylls specifically. Isolated chlorophylls, however, have been used for this purpose, for example embedded in films of fatty acids (38) and quasi-solid gel electrolytes (39), or by spin-coating to act as dye sensitizers for solid state solar cells (40). However, all these attempts still do not produce efficiency ratings above 5%, let alone anywhere close to what nature has achieved, indicating that more thought must be given to the organisation of chlorophylls in order to achieve higher conversion and transport efficiency.

What may be the most effective methods of organising chlorophylls on a substrate may be to enable their self-assembly on the surface by design. There is already a wide field of study which is devoted to the molecular functionalisation of solid surfaces – that of self-assembled monolayers (SAMs) (41). These are structures consisting of a molecule or surfactant which has a functional "head" group capable of chemical interaction with the substrate, a "tail" group, commonly a long hydrocarbon chain, and a terminal group at the end which can be used to give the substrate system new chemical functionality at the interface with the surrounding environment. A SAM is formed either when the substrate is immersed into a solution containing the surfactant, or where the surfactant is introduced to the substrate in the gaseous phase by chemical vapour deposition (CVD). The main driving force for their formation is the affinity of the head group to react chemically with the substrate accompanied by the maximisation of intermolecular interactions (such as van der Waals' forces) between neighbouring molecules. For a monofunctional system, this results in a layer of molecules on the substrate which is only one molecule thick, hence the term
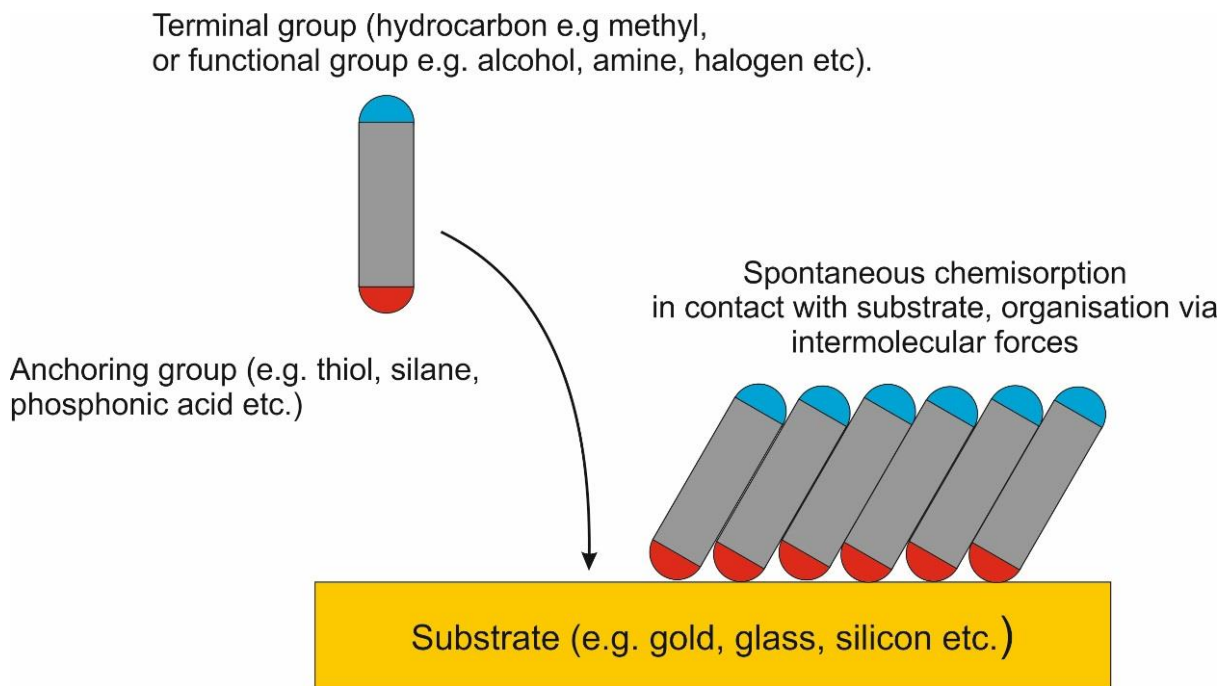
Figure 1.11: *Self-assembly of a simple long chain molecular monolayer on a substrate. An anchoring group chemisorbs to the substrate while organisation and packing occurs to maximise intermolecular interactions (Van der Waal's, hydrogen bonding etc.). A terminal group can provide new chemical properties to the functionalised substrate.*

monolayer, organised into a two-dimensional crystalline structure at the surface (figure 1.11). As a general system, SAMs are very versatile. Changing the head group for example can allow modification of many useful substrates such as metals or semiconductors. Organosulfur molecules, most commonly thiol-terminated hydrocarbons, are a popular and well-understood class of SAMs used to coat metal surfaces such as gold (42). For silicate and silicon structures used widely in many areas such as the semiconductor industry, alkylsilanes can be used to react with both hydrated and bare silicon surfaces to obtain SAMs (43, 44). Other examples include phosphonic acids on a variety of transition metal substrates (45, 46) and even supramolecular arrays of porphyrins (47), In addition, SAMs can provide a convenient way to add new chemical functionality to the surface if they incorporate reactive terminal groups that can graft new molecules, thus providing an anchoring intermediate layer between the surface and a molecule of interest (48), and their substrate selectivity and self-assembling

properties lend themselves well to patterning techniques to introduce new micro- and nanostructured features to a surface (49, 50).

The last alternative strategy which may be tried is to immobilize chlorophylls in a scaffold material, which is either bound, or adsorbed, to a substrate. Rather than using disorganised films and matrices, a scaffold would provide a more intelligently designed method of organising the chlorophylls relative to each other. This approach is inspired by the light-harvesting complexes, where the main purpose of the protein structure is to organise pigments in space to facilitate the energy transfer. One approach would be to utilise proteins engineered for this purpose – in recent years, model chromophores have been conjugated to artificial protein assemblies, primarily as prototype biohybrid light-harvesting devices (51 – 54). However, other materials may prove to be useful. Keeping within the biological domain, lipid vesicles have been used to create self-assembling scaffolds for hydrophobic chromophores, adopting a toroidal shape reminiscent of LH2 (55). However, in these structures, chlorophyll density may be limited by the arrangement afforded by the scaffold structure and the maximum packing densities of these artificial complexes on the substrate. Instead, scaffolds bound to or grown from the surface may provide a great variety of organisational variety. One prominent example could be to use polymer brushes (56). These are polymers which have been polymerized from initiators bound to the substrate. The height of these brushes can range between a few to hundreds of nanometres depending on the polymerization conditions, and a large selection of functional targets for attachment are available. Such assemblies have been used to immobilize both small molecular species and large protein complexes (57), as well as larger nanoparticles (58). Chlorophylls may, therefore, be integrated successfully into these scaffolds, and their flexibility may be ideal for exploring a wide variety of pigment densities.

Once chlorophylls have been organised on a substrate, the question remains of how to measure the exciton dynamics between them. An electron spectroscopy method has been used increasingly in recent years to show evidence of coherent exciton states (59 – 86). However, the results generated from this have been the subject of much debate and scepticism.

6. The limitations of using two-dimensional electron spectroscopy to measure exciton transitions

To try and gain a greater understanding of the role of exciton band energy transfer in natural light-harvesting complexes, pump-probe ultra-fast spectroscopy has been expanded in recent years. The major variant technique used for this purpose is called two-dimensional Fourier-transform electronic spectroscopy (2D-FT-ES) (59, 60). Here a three-pulse experiment with femtosecond interpulse delays produces a stimulated emission signal from the light-harvesting complex being measured. By plotting the signal amplitude with the Fourier-transformed frequency of the emission signal and the frequency of the initial excitation pulse, a two-dimensional amplitude spectrum is produced (figure 1.12). Peaks of amplitude are observed in the spectrum caused by the electronic transitions within and between molecules. Where peaks are present in a straight-line diagonal across the two frequency axes, the linear absorption spectrum of the subjected molecule is mirrored for the frequency range studied. Where there are peaks that are cross-diagonal, known as cross-peaks, these indicate that the electronic transitions arise from the same ground state, and therefore the same molecule. The cross-peaks arise due to reduced absorptions for certain energy levels where the excitation frequency depopulates the energetic ground state of the molecule, indicating a transition through an exciton band over two or more molecules (59).
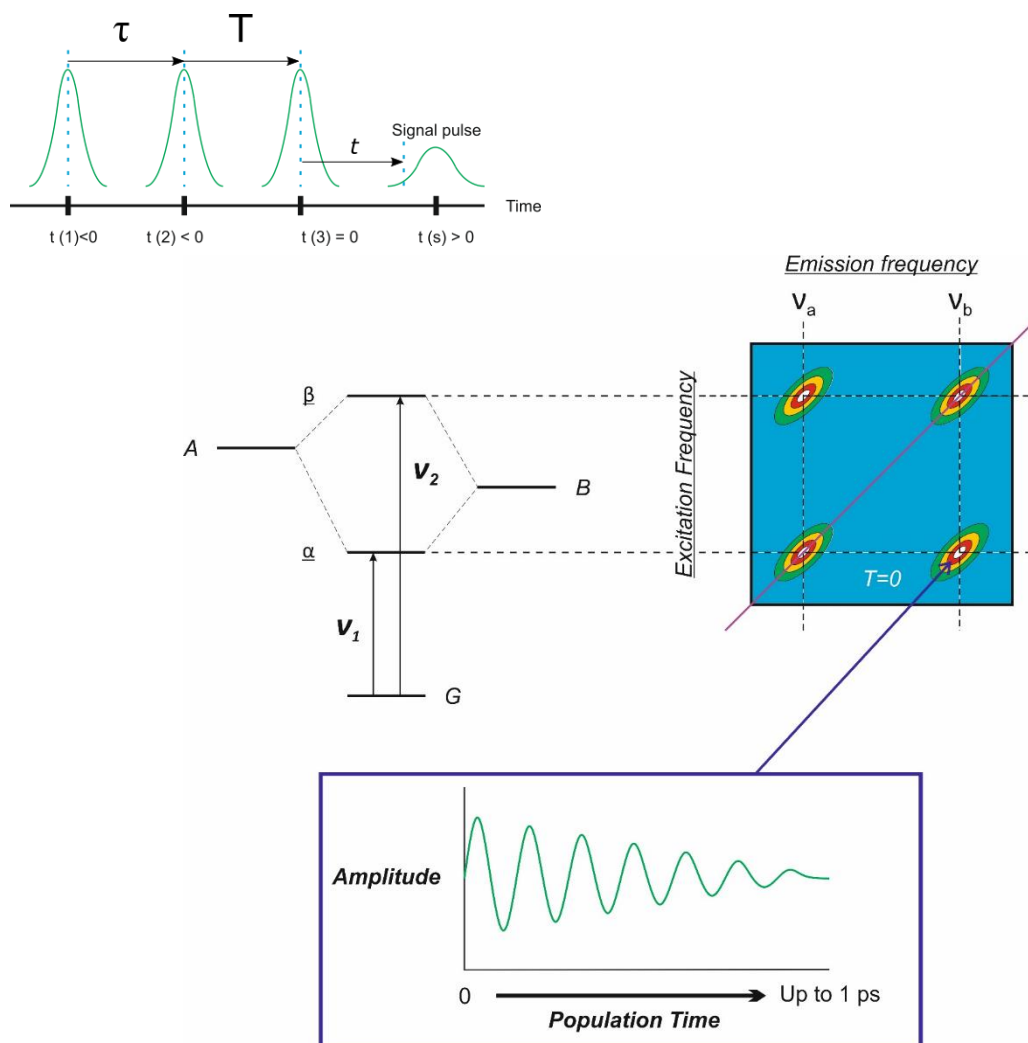
Figure 1.12: The technique of 2D-FT-ES for studying exciton band transitions. Two pulses are used to generate a population of coherent exciton states for time T. Pulse 3 (the "probe" pulse) then triggers rephasing of the coherent states, giving a signal pulse. Typical experiments measure the changes of the emission signal in relation to population time T. Mapping the range of excitation frequencies used with each resulting emission frequency detected results in an amplitude map with diagonal and off-diagonal peaks. Measuring the amplitude of the off-diagonals with T for many light harvesting complexes has displayed purported "quantum beating" spectra used as evidence for quantum coherence in the energy transfer process.

In initial experiments, the Fenna-Matthew-Olson (FMO) complex from photosynthetic bacteria, which contain seven strongly-coupled bacteriochlorophyll complexes, was studied with this technique (61, 62). From the resulting spectra where the excited state population time, *T*, allowed for the complex was 0 fs, several cross-peaks from the interaction of electronic states within the complex suggest that there is strong coupling

between the different pigments which gives rise to delocalised excitonic states. Furthermore, when the population time was increased incrementally from 100 to 1000 fs, the amplitudes of the cross-peak features change, indicating that excitons are correlated in the structure and are relaxing while others are being excited due to transfer of energy between them. Purportedly, with this technique the state-to-state energy transfer pathway can be followed over both time and space. The next step was to examine the amplitude of a cross-peak as a function of time, which would give an estimate of the lifetime of coherent states in these complexes (63). For this, several electronic spectra of the FMO complex were taken at increasing population time in 10-20 fs intervals, up to 660 fs, and measuring the amplitudes of the exciton 1 diagonal peak and the exciton 1-3 correlation cross-peak showed an oscillating relaxation and excitation behaviour. This "quantum beating", therefore, suggested that the coherent transfer of energy between exciton states is possible. The comparatively long timeframe of coherence achieved compared to the first pump-probe experiments is also significant, as longer lifetimes may be observable, giving credence to the role of excitons in enhancing energy transfer between light-harvesting complexes.

Many other light-harvesting complexes have thus been studied using this technique in the intervening years, with timescales up to 5 picoseconds or similar (64 - 67). However, limitations to this technique have emerged which may affect the applicability of the exciton transfer theory to light-harvesting complexes in physiological conditions. Almost all the proteins examined were cryogenically preserved at temperatures around 77 K to preserve their structure over the course of the experiments. The effect on temperature was thus measured on the FMO complex (68). The length of time before the dephasing of this coherence was found to decrease significantly when the measurement temperature was increased from 1.8 ps at 77 K to 600 fs at 277 K. There is some speculation that this may still be long enough to provide the optimal transport efficiency between bacteriochlorophylls, and

that to "sample" the possible transfer pathways the coherence between excitons must complete only one full oscillation cycle. However, this does illustrate the problem of dephasing of the delocalised exciton band in these systems (24). Dephasing can result from an off -resonance of the electronic transitions due to misalignment of the transition dipole moments results in the coupling strength *V* being reduced, thus excitations become more localized on individual chromophores (figure 1.13). In proteins, random conformational changes on longer time-scales compared to those needed for exciton dynamics can change the alignment of the chlorophyll dipoles, introducing disorder. Even in LH2, the symmetry of the aligned bacteriochlorophylls in the B850 ring can be broken by these fluctuations and limit the delocalisation between the bacteriochlorophyll units (69). The temperature-dependent nature of conformational vibronic changes therefore explains longer coherence times observed at cryogenic temperatures.
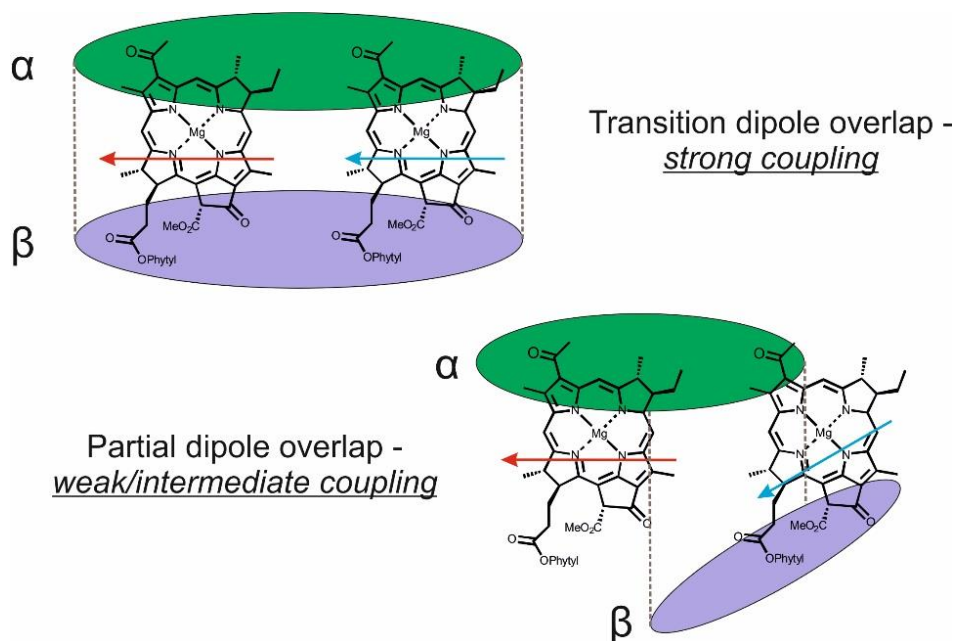
Figure 1.13: *The coupling strength* **V** *between identical chlorophylls is determined by the orientation of interaction of the transition dipole moments – parallel alignment gives resonant strong coupling (high* **V***) while off-vector orientation gives weak coupling (low* **V***).*

Further limitations of 2D-FT-ES have engendered more doubt of the significance of quantum coherence in light-harvesting systems since. First, evidence suggests that vibronic states were observed to couple in two-dimensional spectra, complicating the interpretation of the results. For example, a study of simple pinacyanol chloride (PIN) dimers (70) suggested that the excitation and relaxation transitions for the exciton are almost indistinguishable energetically from the transitions of a single monomer which is coupled to its vibrational mode. A subsequent study comparing the PC645 light-harvesting complex and several laser dyes at ambient temperature suggested that most of the coherence observed was vibronic in nature (71). Further theoretical work concluded that vibrational coherences are much stronger the electronic ones for the scale of electronic couplings expected for photosynthetic pigments, making attributing a peak oscillation specifically to quantum coherence ambiguous (72). Furthermore, the technique itself may give a misleading picture of the energy transfer dynamics that occur in nature in contrast to the experimental conditions. This problem was explored recently (73, 74) that as sunlight is an incoherent thermal excitation source with a wide spectral range compared to coherent laser sources used in 2D-FT-ES experiments, the transfer processes are more likely to be incoherent in nature as transport must occur through a non-equilibrium steady state which prevents the wavelike excitation transfer mechanism. Consequently, the effect of using incoherent light pulses was explored theoretically (75). Calculations showed that coherent light produces a well-defined oscillatory plot, while incoherent light produces highly unstructured wave function plot consisting of smaller wave packets of short oscillation time which decay almost instantly.

Since then, alternative transfer mechanisms that can operate under incoherent illumination have been proposed to justify the coherence hypothesis, such as environmentally-assisted quantum transport (EnAQT) or supertransfer (76 - 83). However, recent experimental evidence is still being produced which questions the significance of

quantum coherence – for example, recent in-depth examinations of the FMO complex showed that observed coherences dephased below 100 fs at physiological temperature, which is highly unlikely to increase transfer efficiency given the observed transfer kinetics for light harvesting complexes (84, 85). From the literature evidence given so far then, the foremost conclusion that can be drawn is that the system may behave much differently in experiments performed under ideal conditions compared to how they behave under incoherent sunlight. There is much doubt on whether "quantum biology" (86) is even applicable in the study of natural photosynthesis owing to the fundamental difference between coherent narrow band light pulses and incoherent constant thermal illumination used to excite the complexes. With a lot of theoretical studies having taken place around this issue, the picture is still ambiguous at best with no definitive realization of the transport mechanism being yet defined.

A different way of studying excitons may therefore be useful which has the advantage of studying only the electronic system, thus avoiding the interference of vibronic effects which makes 2D-FT-ES a flawed technique. In recent years, surface plasmons have emerged as such a useful tool to probe the electronic properties of biological and chemical structures.

7. Surface plasmon resonance as a probing technique to examine single molecule properties

A plasmon is a collective oscillation of surface electrons – a periodic displacement of the electrons about their mean positions. Plasmons can couple to incoming electromagnetic radiation. When the plasma frequency is matched with that of the incident radiation, the system comes into resonance, a state called surface plasmon resonance (SPR). SPR leads to absorption of photons with the same resonance frequency and the formation of a surface plasmon polariton, a wave of oscillating electron polarization (87 - 90). Along a flat metal surface, this wave is propagated along the x and y dimensions of the surface for several tens

of μm, but decays evanescently in the *z* direction to 200 – 300 nm, making it only a surface-localised field. The quantized alternating polarized components are denoted as a new quasiparticle called a surface plasmon polariton. There is also a second type of phenomenon which occurs where the surface dimensions of the metal are smaller than the incident wavelength of the exciting light, a characteristic unique to nanoparticles (NPs). Here, the electron field oscillates locally around the nanoparticle to form a standing wave in resonance with the oscillation of polarisation of the light wave, in a behaviour known as localised surface plasmon resonance (LSPR) (figure 1.14).

One of the most important characteristics of surface plasmons is their strong optical response - with the resonances resulting from the strong interaction with light waves of a certain frequency, they can give intense extinction spectra, especially for NPs capable of LSPR. The other major benefit in this regard is that the plasmon resonance field energy and extinction coefficient for the material is very sensitive to several external factors. First is the dielectric constant of the material itself, which determines the resonance wavelength of the plasmon. This is dependent on the material used and the wavelength of incident light used. The second factor is the dielectric constant of the external environment at the interface. This can be observed experimentally from the extinction spectra of NPs where the extinction maximum, λ_{LSPR}, exhibits a red shift when a medium of higher refractive index is used (91). This shift behaviour is also a core aspect for the application of plasmonics to sensing of molecular systems, as the adsorption of a molecule changes the external dielectric constant and so the energy of the plasmon resonance shifts accordingly. For LSPR, this shift can be related to the effect of the adsorbate by (87):

$$\Delta\lambda_{max} = m\Delta n[1 - e^{\frac{-2d}{l_d}}] \qquad\qquad (1.10)$$

where *m* is the NP bulk refractive index response, *Δn* is the change in refractive index resulting from the adsorption of an analyte to the NP, *d* is the layer thickness of said analyte and l_d is the decay length of the plasmon field.
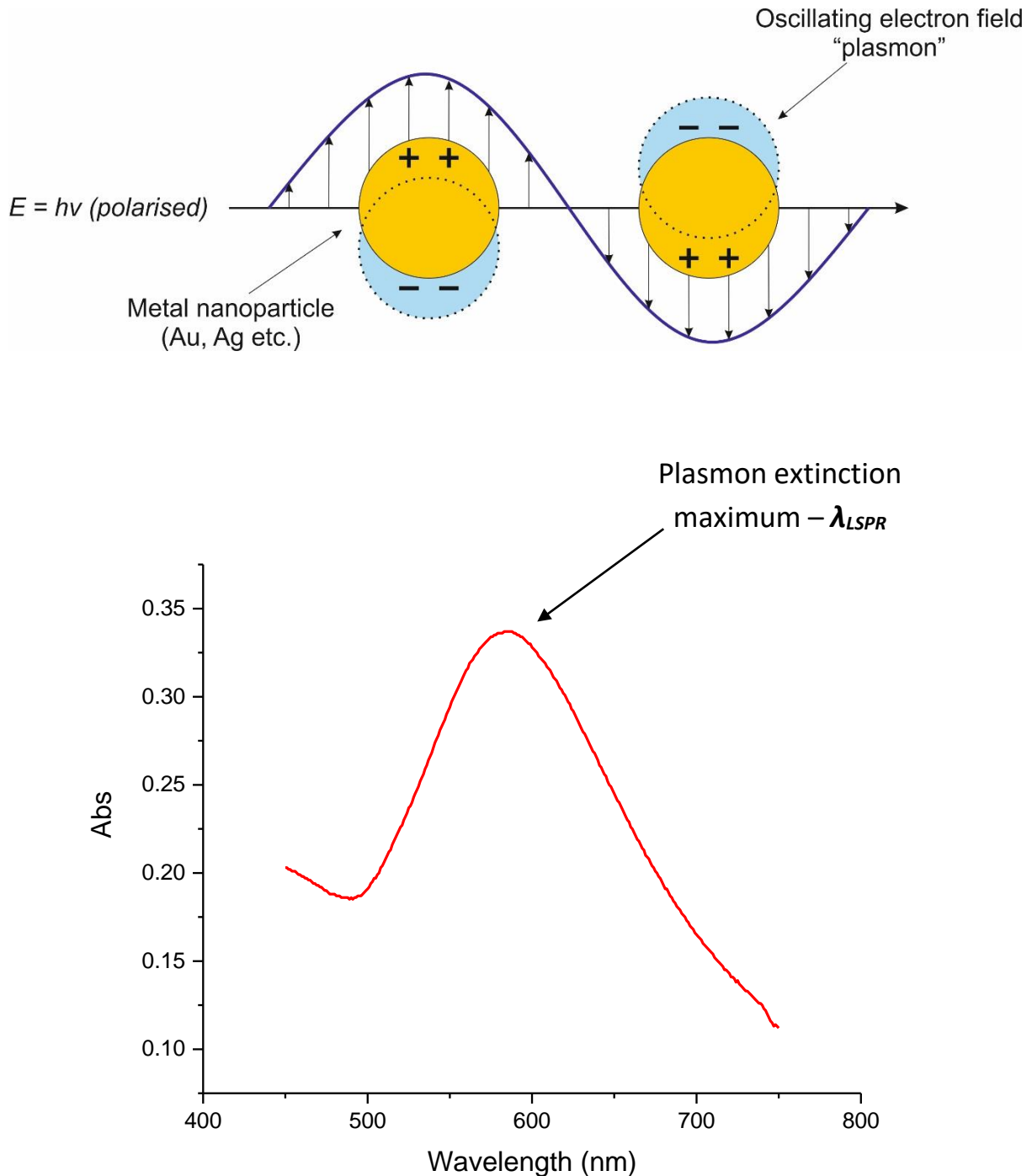
Figure 1.14: **(Top)** *The generation of localised plasmon surface resonance for metal nanoparticles in a polarised light field.* **(Bottom)** *An example of the measured plasmon absorbance spectrum for a surface array of gold nanostructures, as fabricated by interference lithography (117).*

The last major factor in the context of LSPR is the radius of the nanoparticle used. Extinction spectra of gold and silver nanoparticles show extinction maxima in the visible range, but these are shifted by nanometre-scale changes in their dimensions and morphology (figure 1.15) (92, 93). As such, NPs are attractive candidates for sensing applications as their optical properties can be tuned by making small changes to their manufacturing process to produce different sizes. For example, in nanosphere lithography where arrays of gold or silver NPs are produced by evaporation of the metal between the gaps in packed nanosphere layers on a substrate, changing the nanosphere size, and thus gap dimensions which changes the final NP array dimensions, results in a highly controllable λ_{max} range as a function of NP size (94).

One of the first spectroscopy techniques developed to employ plasmon optical effects was surface-enhanced Raman scattering (SERS) (95, 96). In Raman spectroscopy, a monochromatic light source is directed at the analyte, which then absorbs energy to shift to a new vibrational-rotational state. This results in both Rayleigh (elastic) and Raman (inelastic) scattering of the light. The inelastic component is collected which exhibits a shift in energy due to its earlier transfer of energy to the analyte, known as the Stokes shift. The collected spectrum of the observed Stokes shifts then gives information about the vibrational-rotational states of the analyte. However, a major disadvantage to the technique is the high inefficiency of Raman scattering, thus giving spectra of inherently weak intensity (95). To address this, SPR has been used to enhance the sensitivity of Raman measurements for single-molecule adsorption experiments. For example, it was found that Raman spectra for ethene deposited onto silver films was enhanced significantly when a silver nano-islands was used in place of a smooth substrate (96). Similarly, an enormous enhancement effect is achieved when colloidal silver NPs where used to adsorb rhodamine G6 (95). The effect is due to the greater intensity of the plasmonic field in close proximity to an NP, which increases the amount of

energy absorbed. NPs therefore can act as antennas for enhancing Raman transitions, and they can be usefully designed to respond to specific wavelengths used in Raman spectroscopy. There is also recent evidence of long-range enhancement of Raman spectra where nanostructures are coated with silicon oxide films of up to 60 nm thickness, showing potential as robust reusable arrays for SERS (97).

With the growing interest in using NPs to sense adsorbates, however, the field of LSPR spectroscopy has expanded widely in recent years. As discussed previously, adsorbance of an analyte to a NP results in a shift of its characteristic λ_{LSPR} due to the change in the dielectric environment close to the LSPR field (figure 1.15). As a result, NPs have a great sensitivity to a wide range of analytes which can be detected using simple absorbance spectroscopy methods. The sensitivity is such that miniscule concentrations of simple molecules still result in a measurable λ_{LSPR} shift: for example, adsorption of 1-hexadecanethiol with a maximum surface concentration of approximately 1×10^{-22} moles around a single NP can shift λ_{LSPR} by as much as 40.7 nm (98). Further experiments showed that the shift magnitude also increases linear with increasing size of the carbon chain on a series of alkanethiols, behaving as expected from equation (1.10) above (99). The implication is therefore that for very large molecules, which should both increase the layer thickness and the change in dielectric environment around the plasmonic NP, the change is not only larger, but the characteristic shift could be used to identify unknown components in a mixture that can be adsorbed. An area where this has become an attractive technique is the sensing and interrogation of biological molecules (100). The nanoparticles are modified to attach a "probe" biomolecule, designed to bind to a "target" in solution which leads to a shift in λ_{LSPR}. By measuring the extinction spectra before and after immersion in the protein solution, the shift caused by the specific protein binding can be obtained. This was initially obtained by covalently attaching biotin to 11-mercaptoundecanoic acid molecules preassembled with
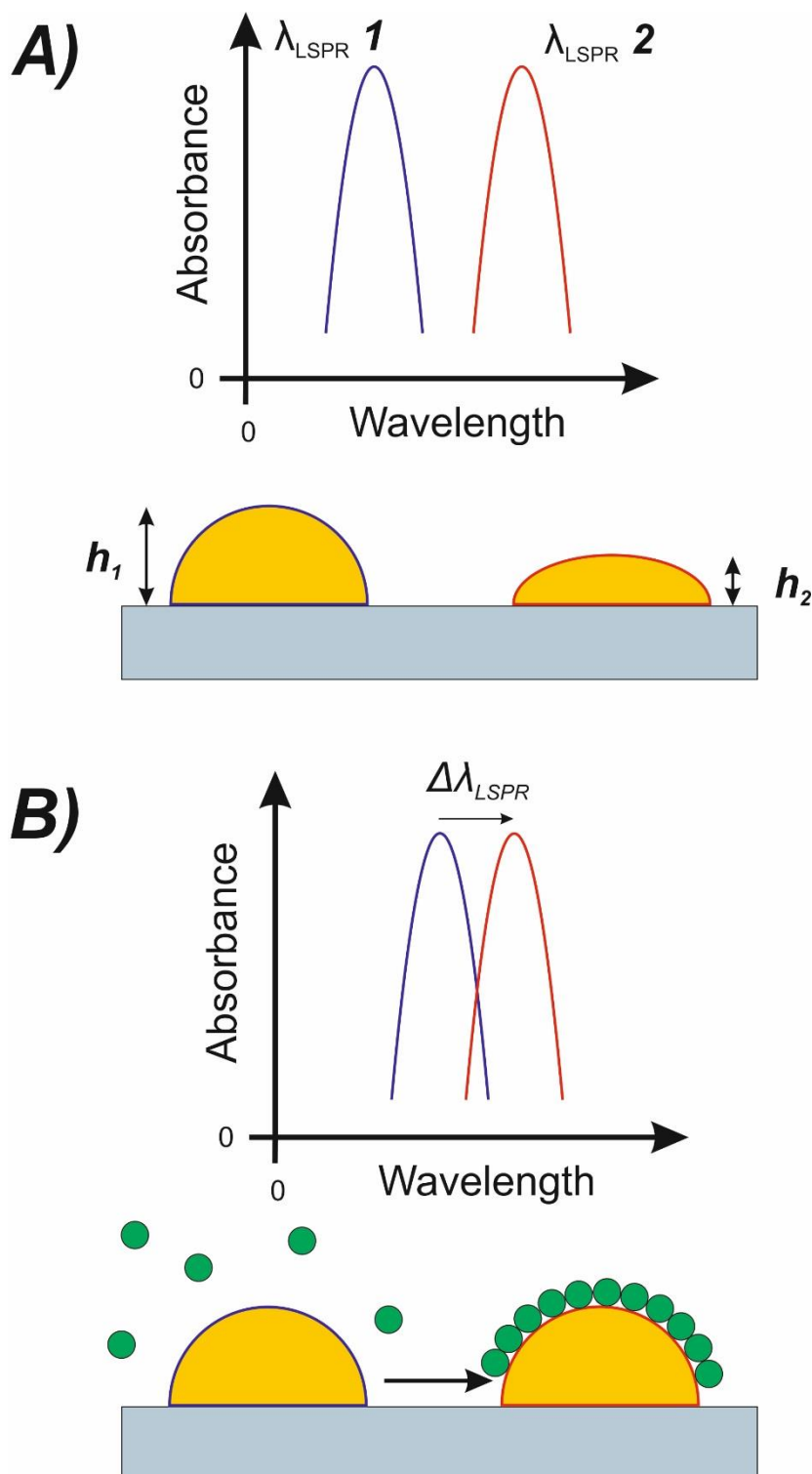
Figure 1.15: The plasmon absorbance maximum (**λ**$_{LSPR}$) of a surface-bound nanostructure can be affected by several factors. In example **A)**, a change in morphology such as a decrease in structure height can result in a shift of plasmon absorbance, as well as changes in structure width and geometry (101, 102). In diagram **B)**, a change of dielectric environment resulting from the adsorbance of an analyte to the particle results in a red-shift, illustrating the sensing capabilities of such structures with high sensitivity (106).

1-octanethiol on the surface of silver nanostructures, followed specific binding of the antibodies streptavidin (102) and anti-biotin (103). In the first study, a shift in λ_{LSPR} of 11 nm was measured after adsorption of the acid and binding of biotin, with a further larger shift of 27 nm being observed after the binding of streptavidin, showing the nanosensor's capability of differentiating between different binding events. In addition, the change in the shift as a function of the concentration of streptavidin was used to find an estimate for the thermodynamic binding constant on the surface, providing some information about surface dynamics. A larger shift of 42.6 nm was observed for anti-biotin, but a smaller binding constant (102). LSPR nanosensors are thus shown to be effective at determining the surface-modified thermodynamics of protein dynamics in addition to molecule-specific sensing.

In recent years however, an additional effect has been observed which suggests that LSPR can experience some additional interaction with molecular adsorbates beyond a simple change in the dielectric environment. In an experiment to determine if electronic transitions can affect the biosensing capability, the porphyrin derivative [2,3,7,8,12,13,17,18-octakis(propyl)porphyrazinato]magnesium(II) (MgPz), with a strong absorbance maximum at 598 nm, was adsorbed to silver NP arrays which were fabricated to give a range of extinction maxima (103). After adsorption, a shift in the position of λ_{LSPR} was observed on each array. However, the magnitude of the shift was found to vary depending on the correlation of the original maxima to the absorbance maximum of the Q-band of the molecule. Where λ_{LSPR} and the Q-band were closest in their respective absorbances, a large shift of 59.6 nm was measured, whereas on an array with an absorbance further away from the Q-band a shift of only 20 nm was observed. Also, the smallest shift was observed where the absorbances were separated by only 2 nm, and the absorption lineshape is modified to be narrower and more intense. This effect suggests that beyond a change in dielectric environment the plasmon field may be affected by an interaction with the electronic transition specific to the adsorbate

bound to the surface and that some kind of resonance is taking place. Not only does this have uses for increased sensitivity of sensing by designing plasmonic devices to achieve an absorption spectrum that "mirrors" that of the target analyte, but it is also suggested that the optical properties can be enhanced by close correlation. When the experiment was repeated with the cationic complex iron(II) tris-2,2'-bipyridine, which has two absorbance maxima at 490 and 520 nm with different directions of polarization, only the close correlation of the former peak produced the enhanced shifting effect. This would further suggest that an interaction takes place only where the plasmon field and the electronic transition are polarized in the same direction, with the associated dipole oriented perpendicular in relation the surface. This behaviour has since been used successfully as a sensitive probe for surface reactions, such as the binding of camphor to the Cytochrome P450 protein (104). Other optical characteristics of molecules can also be affected by coupling in this manner. Fluorescence is one, where the intensity of emission of fluorophores can be enhanced through coupling of the associated transitions with surface plasmon polaritons (105). Once again, dipoles involved in fluorescence that are aligned perpendicularly to the surface are enhanced. Further studies have shown similar effects with single-molecule fluorophores (106), as well as natural complexes like LH2 (107).

The above evidence suggests that utilising surface plasmons would therefore be a useful strategy for studying light-harvesting complexes and molecules, such as chlorophylls, which are assembled on surface substrates. To this end, in recent years strategies have been developed to assemble light harvesting complexes specifically to self-assembled monolayer systems on metal substrates that can be processed to make arrays of plasmonic nanostructures. Alkanethiols are a popular class of molecules to use given their affinity to bind to gold and silver, the most widely used metals for plasmonic applications (108, 109). Many light-harvesting complexes and other proteins have been successfully adsorbed to these

monolayers, but for the purposes of this review we shall focus on select light harvesting complexes as the primary examples. The typical method of attaching these complexes is by chemical interaction with a thiol monolayer terminated with a reactive functional group, sometimes coupled with a protein-resistant domain to prevent non-specific adsorption of the protein (110). This was successfully done with oligo(ethylene glycol) monolayers patterned by photolithography, upon which bacterial LH2 was deposited (111). In this system, the base monolayer was selectively removed by ultraviolet (UV) light to form patterns (112, 113). After this, a new thiol terminated by a carboxylic acid was introduced and was converted to an active ester, which then reacted with the lysine residues of the LH2 protein scaffold to allow chemisorption. Clean specific patterns of LH2 functionalisation on the surface were identified by fluorescence, and the surface plasmon resonance (SPR) response was recorded to show the dynamic binding of the protein over time. The LH1-RC complex has also been deposited onto gold using a thiol monolayer intermediate, albeit without specific chemisorption but rather as a study on the effect of the monolayer terminating group on physisorption and their photocurrent response when coupled in this way to a gold electrode (114). The LHCIIb complex from green plants, however, was chemisorbed like LH2 but with a more complex anchoring structure (115). Here, a hydroxyl-terminated SAM was derivatised to terminated with nitrilo(triacetic acid) (NTA) groups which formed a tridentate ligand around a nickel (II) ion. Then, the LHCIIb complex was introduced with a histidine tag on the C-terminus of the protein – this was bound with the nickel ion as a bidentate ligand thus anchoring the complex. Once again, the SPR response was used to measure the relative adsorption of the complex as a function of NTA coverage on the surface.

Recently the attachment of LH2 to gold nanostructures has been described (116). Arrays of gold nanostructures were produced over large areas using interferometric lithography. This technique produces a pattern of lines from a laser interferogram, regions of

high and low intensity. When photolithography on an alkanethiol SAM is performed with a

rotation of the substrate between two exposures, series of gold nanodisks is produced. The

large patterning area and systematic production allows for repeatable and uniform fabrication,

where periodicity and λ_{LSPR} can be controlled by the rotation angle (117). After high-

temperature annealing of the disks to produce spheres with strong LSPR signatures, the LH2

complexes were then immobilised on the structures by a built-up monolayer structure

terminated with the Ni-NTA complex, binding to the histidine tag of protein. The ring shaped

LH2 was thus assembled on the surface in a planar orientation. In terms of the carotenoids

and the bacteriochlorophylls contained within the complexes, their transition dipoles μ(Crt)

and μ(Q_x) (for the B850 bacteriochlorophylls) were orientated perpendicularly to the surface

plane. The UV-visible absorption spectrum was then measured for the samples, where a new

phenomenon was observed. In these systems, the plasmon band was not shifted as had been

observed previously for plasmonic particles coated with proteins. Instead, the peak was found

to split into two features (figure 1.16). The splitting was found to be dependent on the

pigment complement of the proteins and the new feature was correlated in energy with the

exciton energies of these pigments. This behaviour was therefore attributed to the strong

coupling of excitons in the light-harvesting complexes to the plasmon mode of the

nanoparticles.
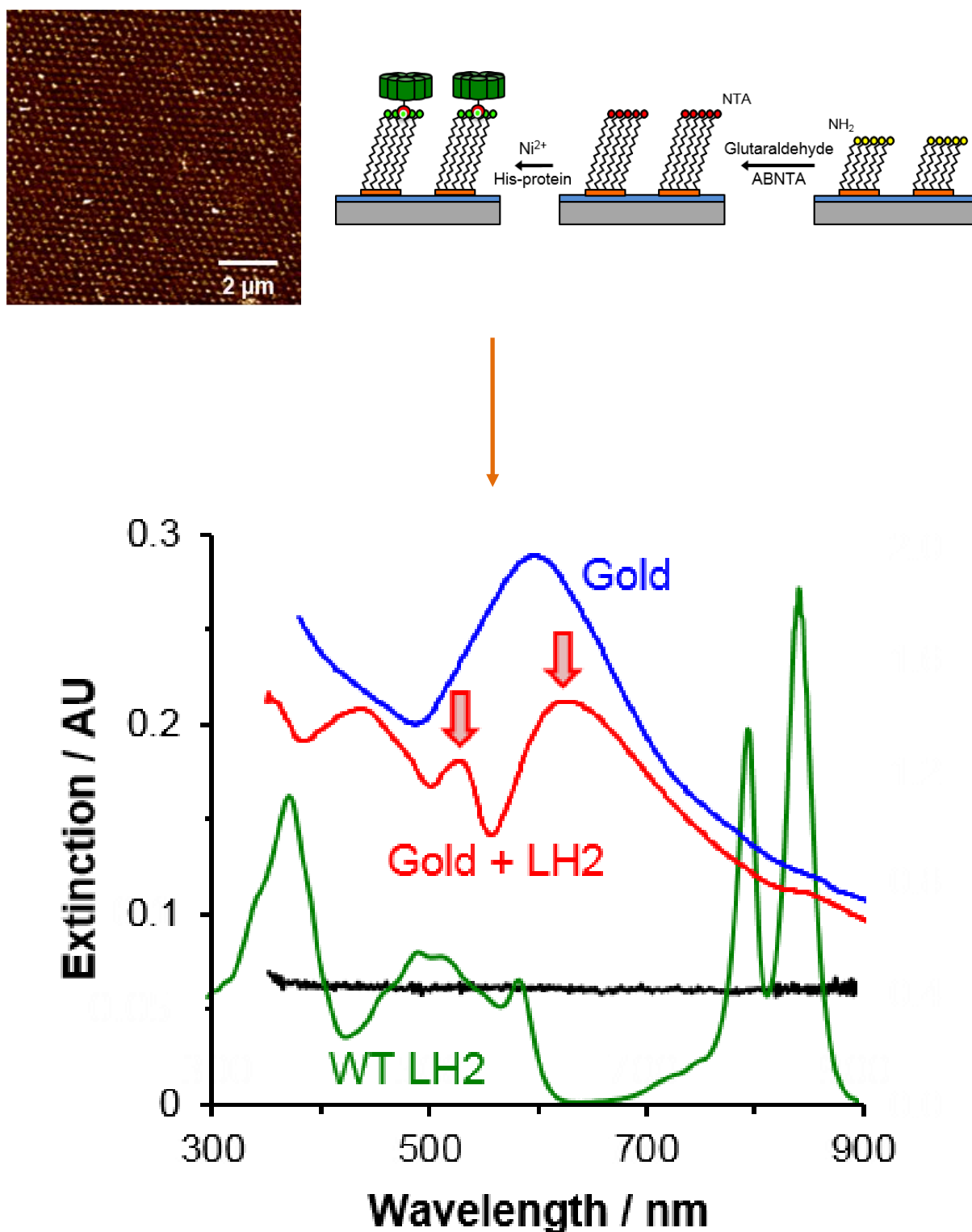
*Figure 1.16: (**Top**) A hexagonal array of gold nanostructures fabricated by interferometric lithography (dimensions may be found in the supporting information of [116]). Functionalised monolayers were them assembled on the nanostructures were used to immobilise LH2 complexes with a Ni^{2+}-NTA group complexed to histidine residues on the protein. (**Bottom**) The extinction spectra of the unfunctionalized array (blue), wild-type LH2 (green) and the array with adsorbed LH2 (red). Once adsorbed, a red-shift is observed in the plasmon peak along with the appearance of a new peak feature, indicating the occurrence of a new energy state in the system.*

8. Plasmon-emitter strong coupling – a new light-matter interaction phenomenon

In strong coupling, plasmon and exciton states are mixed to form new hybrid states that combine the properties of light and matter (118 - 123). In the previous literature of coupling plasmon particles to biomolecules, the plasmon and exciton (or dipole) interaction did not change the energies of either state. This was therefore a weak coupling state. However, in strong coupling the energies of the coupled plasmon and exciton states do change because of the interaction. As a result, they become hybridised to become new states called "plexcitons".

Much of the physics behind strong plasmon-exciton coupling is very complicated, with three conceptual frameworks emerging to model the phenomenon in the classical, semi-classical and quantum descriptions (119). However, a good approximation has been reached by using a model describing the plasmon and exciton modes as coupled harmonic oscillators, where their free oscillations are altered by a coupling interaction g (figure 1.17).

In the context of a gold nanoparticle array which has an LSPR field with a molecule or protein which has an exciton transition, the interaction is a Fano resonance where a broad mode is coupled to a narrow mode. The LSPR field is a broad line width mode which has a resonance frequency, ω_b, accompanied by a high damping magnitude, γ_b. The plasmon field is also coupled to an external field, i.e. incoming light, and thus its oscillation is driven by the harmonic external force imparted by this light which has an amplitude of $fe^{i\omega t}$ (where ω is the frequency of the external force, t is a unit of time and i is an imaginary complex number). The exciton, a narrow line width mode, also has a resonance frequency ω_d and damping γ_d. Experimental spectra for the LH2 complexes adsorbed on clean glass shows no absorbance features (116) so it is inferred that almost all coupling of the light field occurs with the nanoparticle array and so there is no driving force acting on the exciton oscillator.
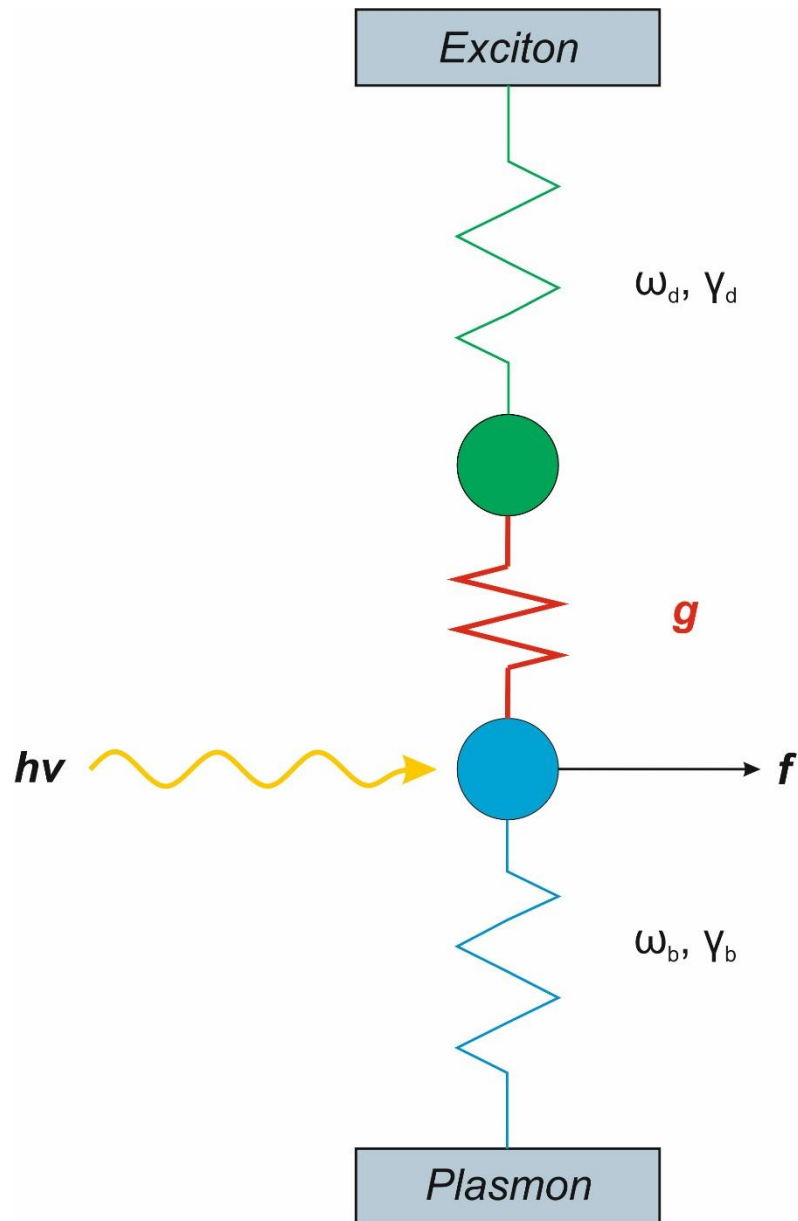
*Figure 1.17: A simple representation of a localised surface plasmon and a molecular exciton as an analogous coupled harmonic oscillator system tethered by a coupling strength **g**, with light imparting an external force on the plasmon oscillator.*

Finally, the coupling interaction between the two is denoted by *g* in the units of frequency squared.

Most of the characteristics of the system therefore can be described by the frequencies of the oscillators and their coupling strength. For the coupling of an LSPR field and an exciton, it is useful to scale the equations to energies via the Planck-Einstein relation using

the reduced Planck constant (as oscillation frequencies are usually described as angular frequencies), and so $E = \hbar\omega$. For the LSPR field ω_b becomes E_{LSPR} and for the exciton ω_d becomes E_{mol}. It is necessary to scale the coupling strength g also as this is expressed as units of frequency squared, thus applying $\hbar^2 g$ gives a new coupling strength G.

When the LSPR field and the exciton interact in a linear combination, if they are close in energy, a similar effect occurs as described before when chromophores closely interact to form excitons. In the oscillator analogy then, when these modes are close in energy, they are in resonance with each other. Thus, the coupling results in two new eigenstates, E_1 and E_2, which appear above and below E_{LSPR}. These are the states which result in the new peaks that can be observed in the extinction spectra of LH2 assembled on the gold nanoarrays (116). From these spectra, the energy difference between the new energies can be measured and is noted as the coupling energy, E_C. This can also be observed when one measures the dispersion relation for the system – how the energy or frequency for each mode changes with the in-plane wavevector κ (figure 1.18) (119). Under weak coupling, the energy of the plasmon mode varies monotonically as a function of the energy of the uncoupled exciton mode. However, in the strongly coupled system there is an avoided crossing. At resonance, where E_{mol} is equal to the energy of the uncoupled plasmon mode, the two plexcitonic states are separated by an energy hΩ, where Ω is the coupling strength. This is called the Rabi splitting. Measuring the energy difference between the curves at this point can give E_c. In the frequency notation the splitting at the resonance point is approximately g/ω, so scaling to the energy notation then gives $E_C = G/E_{LSPR}$.
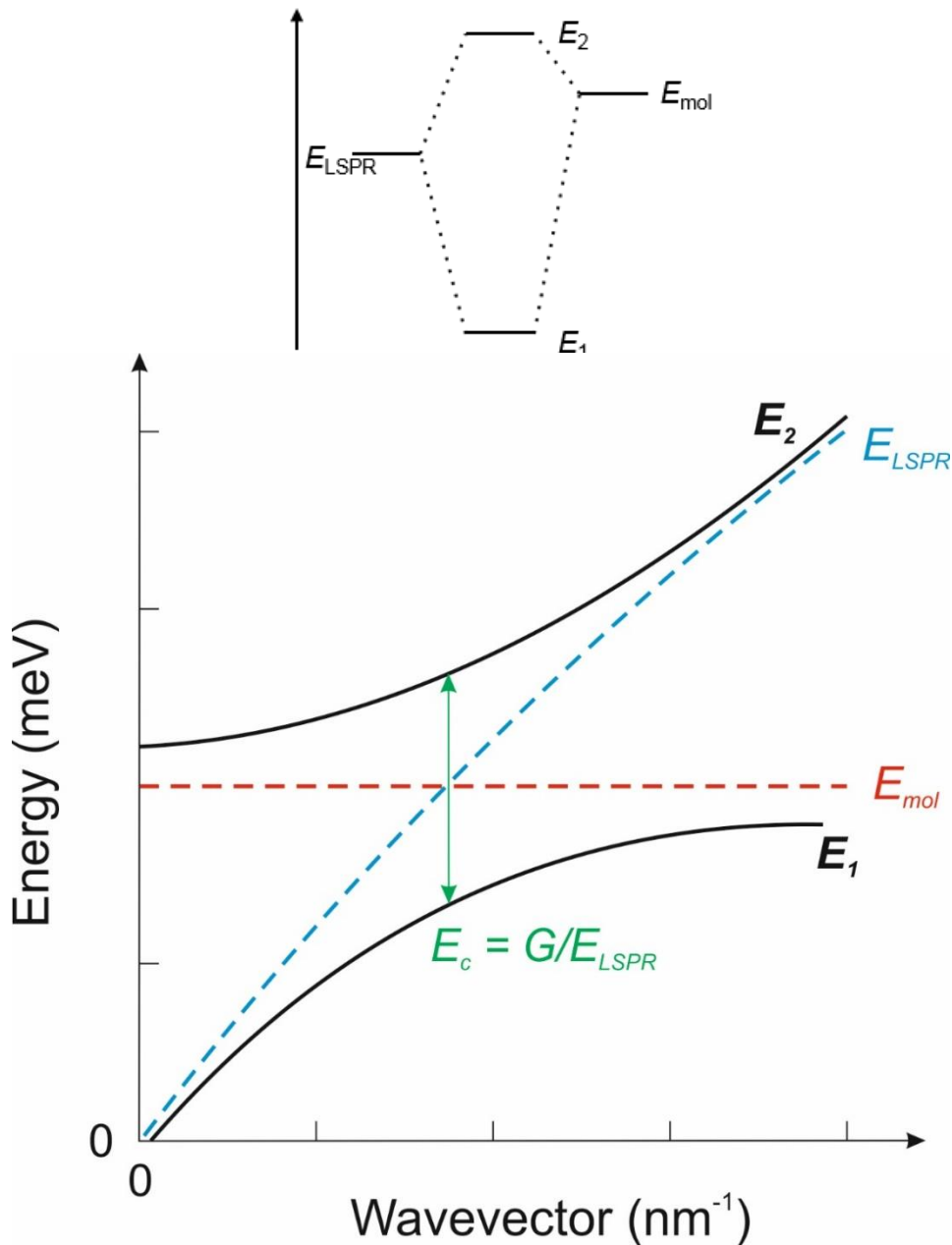
*Figure 1.18: (**Top**) A simple energy state diagram, indicating the interaction of E_{LSPR} and E_{mol} to produce two new eigenstates, E_1 and E_2. (**Bottom**) An ideal representation of Rabi splitting for the energy of the two modes against wavevector in both the non-coupled (dashed lines) and strongly coupled (solid lines) regimes.*

The magnitude of G determines whether the system occupies the strong coupling

regime – the higher it is, the higher the value E_c is. However, another factor to consider is the

linewidth of the new modes, which are determined by the damping on each of the original

oscillators. These can be represented on a dispersion diagram by the thickness of the

dispersion curves for example – the thicker the curve, the greater the linewidth. This then reduces the distance between the two curves at resonance compared to the undamped case, which in turn reduces the magnitude of splitting. If the coupling is weak the two linewidths can meet and thus the separation cannot be measured certainly. The Rabi splitting therefore becomes observable when the linewidths of each mode are far from contact; hence strong coupling can be defined as the region beyond where the coupling strength exceeds the linewidths of the two modes. This is the usual case where the linewidths are narrow and of approximately the same size, and can be described as (119):

$$\frac{\gamma_b}{2} + \frac{\gamma_d}{2} \tag{1.11}$$

In the LSPR-exciton coupled system, the LSPR oscillator is more heavily damped than the exciton. Here, the fundamental criterion of strong coupling can be used and is given by:

$$E_C \geq \frac{1}{2}\left(\gamma_p - \gamma_{mol}\right) \tag{1.12}$$

Where γ_p and γ_{mol} are the linewidths of the plasmon and exciton modes respectively. This can be viewed experimentally by returning to the LH2 assemblies assembled on the large-area patterned gold NP arrays (116). When the LSPR absorption band was split by the coupling, the result was a broad near-resonance band and a narrower band further from the original LSPR band. This was the result of the new energy states expressing hybridisation of the asymmetric linewidths of the original modes. The linewidths for each state could then be measured and compared to E_c, given by the energy gap between the peaks of the new bands.

For most samples the criterion was found to be satisfied and so the system was observed to be producing strong coupling.

Another important feature in this context that affects the coupling energy is the number of dipoles present to couple to the plasmon mode. In strong coupling, the plasmon mode couples collectively to an array of excitons, and the coupling energy depends on the density of excitons in the plasmon mode volume. For example, for wild-type LH2 deposited on the arrays E_C was observed to decrease as a function of the square root of the fractional coverage, θ (figure 1.19). In the UV-vis extinction spectra, this progression was shown as two well defined peaks at a high coverage coming closer together until at a lower coverage (0.56) the higher energy peak becomes a shoulder feature of the broad peak. This is due to the decreasing number of dipoles, the molecules in the LH2 complex which have a transition dipole moment, that are coupling to the LSPR field as the fractional coverage decreases. For an electron of charge e and mass $m,$ the coupling strength Ω is found to scale in proportion to the square root of dipole number per unit volume (119):

$$\Omega = \sqrt{\frac{N}{V}} \frac{e}{\sqrt{\varepsilon_0 m}} \tag{1.13}$$

where N is the number of dipoles, V is the volume occupied by the plasmon field and ε_o is the permittivity of free space. The magnitude of coupling is therefore dependent on the concentration of dipoles inside the three-dimensional plasmon field. In the case of LH2 the coupling picture is more complex, where the plasmon is coupled to the excitons that are polarized along the dipole moments of the molecules which are in line with the LSPR field polarization. The excitons themselves are also quantized systems which can't necessarily be described as having classical dynamics. However, for each possible description of plasmon

strong coupling systems (classical, semiclassical and quantum) the same dipole concentration

relationship to splitting was found to be adhered to.
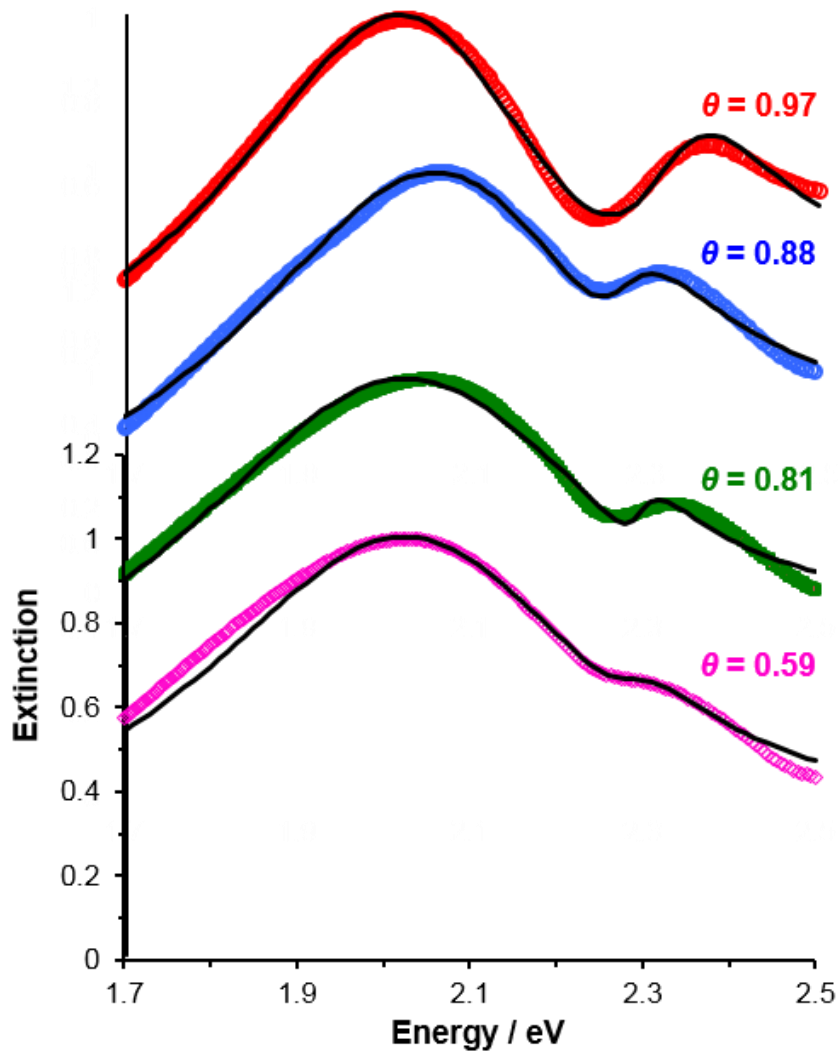
Figure 1.19: Extinction spectra comparing the observed peak energies with decreasing fractional coverage of wild-type LH2 complexes on a plasmonic nanostructure array. This represents a progressive decrease in the number of dipoles assembled across the array surface.

The model used for LH2 complexes coupled to plasmonic nanoarrays was that of a

classical electromagnetic field describing the LSPR mode with a quantum two-level system

being the excitons in the complexes – a semiclassical picture. To relate the coupling energy

E_C with the transition dipole moment μ and the exciton and LSPR energies, E_{mol} and E_{LSPR},

the microscopic expression of the coupling energy was utilised (124, 125). For example, for

cyanine dye J-aggregates deposited onto microcavities with surface plasmon polaritons (124)

the square of the coupling strength was given by:

$$\Omega^2 = \frac{\pi p_{0f}^2 E_0^2}{\varepsilon_b E_{cav}} \frac{N}{V} \tag{1.14}$$

with ε_b being the relative permittivity of the background medium. This was adapted for the

LH2-LSPR system to now give an approximation for the coupling energy:

$$E_C \cong \sqrt{\frac{\mu^2 E_{mol}^2}{\varepsilon_0 \varepsilon_b E_{LSPR}} \frac{N}{V}} \tag{1.15}$$

This equation becomes useful in estimating how the change in dipole density affects

the coupling as the fractional coverage of LH2 is varied, and for finding the surface density

of dipoles for monolayer assemblies of LH2. First, the experimental absorption spectrum can

be fitted to a theoretical model for the coupled harmonic oscillator system, which derives E_{mol}

from the known experimental values of E_C and E_{LSPR}. Then, by coupling these parameters

with the transition dipole moments given in the literature for carotenoids and B850

bacteriochlorophylls (126), an estimated value for N/V was found 1.57 x 10^{25} m^{-3} for wild-

type LH2. However, knowing additional information about the dimensions, structure and

pigment arrangement in LH2 (127, 128) can used to give the extension of the plasmon field

from the surface. Using the derived surface area densities of the pigments from the literature,

the height L of the plasmon field can be estimated by $N/V \div N/A = 1/L$. For the plasmonic

gold nanoarrays studied, a height range of 1-35 nanometres was obtained.

The microscopic theory resulting in equation (1.15) also relates the coupling energy to the transition dipole moments, μ, for the excitons involved. The dependence of coupling energy on this and the exciton energy was demonstrated when mutant variants of light-harvesting complexes were assembled on the nanostructure arrays (116). When a complex was used which incorporated a different carotenoid pigment, splitting was observed but red-shifted from the spectra for the wild-type. This may reflect a change in E_{mol} of the carotenoid transition which has a dipole moment aligned with the plasmon field polarization. Significant changes were also found when mutant LH1 complexes were adsorbed. A mutant, containing lower-energy absorbing carotenoids, showed a much lower intensity in the minor peak. Finally, when a mutant containing no carotenoids was adsorbed the splitting was almost completely gone, with only a shoulder absorption visible joined to the main red-shifted LSPR peak. This indicated that the coupling that it was no longer in the strong regime.

Together, this indicates the importance of dipole magnitude for strong coupling. In the LH2 subunit for *Rs. Molischianum* for example (126), the lycopene carotenoid has the transition $1^1 B_u^+$ which has a dipole moment of 15.101 Debye, but for the Q_x transition of the B850 bacteriochlorophylls is almost five times smaller at approximately 3.4 Debye for each one. As a result, the collective carotenoid dipoles have a much stronger contribution to the coupling than the bacteriochlorophylls. It makes sense therefore that the coupling interaction is significantly reduced in strength once the carotenoids are removed from a complex. This raises an important question on whether strong coupling to bacteriochlorophylls is possible if the dipole density could be increased.

This treatment of strong coupling could prove to be a powerful tool for studying the excitons between chlorophylls which have been immobilised on surfaces with plasmonic resonances. By measuring the change in the UV-vis absorption spectrum of an LSPR array once chlorophyll or a chlorophyll-containing layer has been adsorbed to it, an observable split

in the peaks may indicate strong coupling if the conditions are satisfied. The magnitude will be dependent of the density of chlorophylls, the magnitude of their dipole moments and the orientation of said dipoles. Artificial analogues of chlorophylls have been used recently to study strong coupling in artificial "maquette" protein structures to illustrate that this is possible (129). By incorporating the chlorins into these new protein scaffolds, the orientation could be controlled to ensure a perpendicular orientation of the chlorin to the surface plane and the number of chlorins incorporated (either 1 or 2) could be manipulated to study the effect of chlorin dipole-dipole interactions on the magnitude of coupling (figure 1.20). The two-chlorin maquettes displayed visible strong coupling when adsorbed, but the one-chlorin maquettes showed a split of a much lower magnitude, indicating coupling below the strong regime. This difference was hypothesised to be due to the formation of *J-* or *H*-dimers with aligned dipole moments in the plasmonic field. When this dimer is strongly coupled to the plasmonic field, the chlorins could then exchange energy through the plasmon field. The inference here is that not only do chlorophyll-type molecules have the capability of displaying strong-coupling when isolated from the light-harvesting complex, but that controlling the dipole density, orientation and organization could be used to modulate energy transfer between them, carried by the plasmonic field. As such, the scaffold material used may be integral in producing strong coupling for chlorophylls. These structures may not necessarily be proteins – the evidence gathered so far indicates that the proteins themselves do not contribute to the coupling except as a framework for the orientation of dipoles. This allows for the flexibility to explore a variety of surface-based materials as candidates for scaffolds to contain strong-coupled chlorophyll energy-transfer networks, potentially for much lower cost and complexity than protein design as well as higher durability and potentially ease of integration into devices and other technologies.
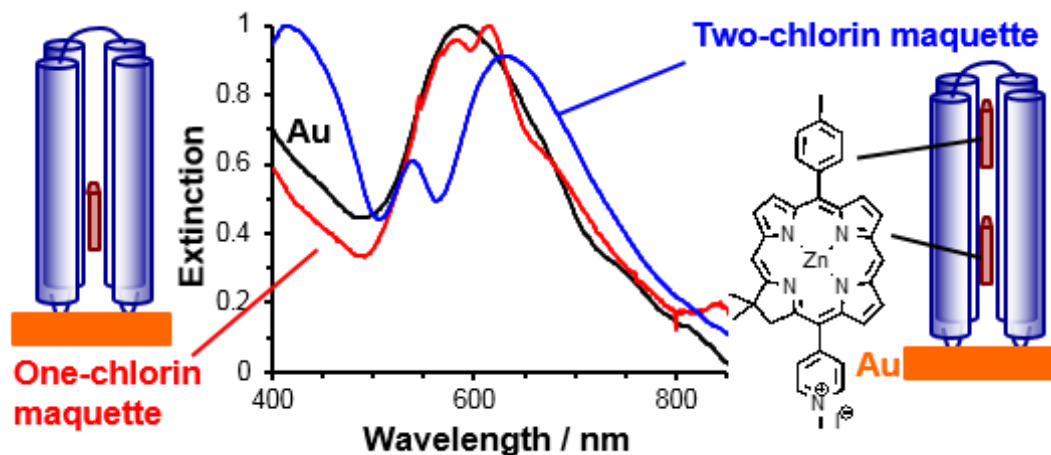
Figure 1.20: Chlorin-containing maquettes were adsorbed to gold nanostructure arrays using the same surface chemistry for the LH2 and LH1 complexes previously. The change in extinction spectra is noticeable between 1 and 2 chlorin maquettes, pointing to strong dipole-dipole interactions in the latter which boosts the plasmon-exciton coupling strength (129).

9. Aims, approaches and predictions for this project

In light-harvesting complexes, energy is captured from sunlight and transferred highly efficiently to drive biochemical processes. As a consequence of the protein scaffold structure, chlorophyllous pigments are arranged to allow transport of energy in the form of excitons. This transport is done via orbital delocalisation in the form of exciton bands and inter-complex FRET-transfer. Here, we would like to design materials which are inspired by this biological mechanism to transport energy much more efficiently than current exciton transport materials. By using the strong coupling of a plasmonic field to excitons organised within the field boundary, polaritonic mechanisms (whereby transfer between pigments can be mediated coherently via new plasmon-exciton hybrid states) could be used to match, or even improve on, nature's achievements. By controlling the density and arrangement of dipoles in these new systems, we therefore hope to use this different kind of coherence to control the exciton dynamics within. The primary goal of this project is therefore to explore

designs for synthetic structures that organise chlorophyllous pigment molecules within plasmon modes which will allow control of exciton transport using polaritonic mechanisms.

Two approaches will be explored to achieve these aims. First, a bacteriochlorin will be self-assembled on the surface to make a complete monolayer, isolated from any scaffold structure. To achieve the maximum surface coverage possible on gold, the chlorin must have a thiol moiety or similar derivative which can bind effectively to the surface. This necessitates the synthesis of the chlorin with reactive groups to attach long-chain anchoring groups. Once synthesised, the assembly may proceed by a model which is dominated by the organisation of the central chlorins into aggregated stacks, like those found in the chlorosomes of green sulfur bacteria (146), while the anchoring groups should allow the dipoles to be aligned perpendicular to the surface plane where the packing is maximised. The monolayers will be fully characterised with surface analysis techniques such as ellipsometry, x-ray photoelectron spectroscopy and secondary ion mass spectrometry, which will give the layer thickness, surface elemental analysis and mass fragmentation analysis respectively. This analysis should give information on the chemical binding of the molecules to the surface and potentially the planar orientation of the chlorins. These monolayers will then be assessed with manufactured plasmonic nanoarrays and UV-vis spectroscopy to determine if they display strong coupling behaviour. In this case there two possibilities. If the number of molecules and the dipole moment strength and orientation allow for strong coupling at full coverage, then the monolayer coverage may be reduced as a function of chlorin concentration to determine the effect on the coupling and identify the coverage limit for strong coupling. In turn, modelling the spectra using the coupled harmonic oscillator model can give an estimate of the exciton energy between the chlorins on the surface. However, if a complete monolayer does not produce a strong coupling interaction, then the density of dipoles in the plasmon mode volume may need to be increased vertically by the formation of simple multilayers. If the

molecule is synthesised with two anchoring groups, and the binding occurs with only one of these groups bound the surface, this may lead to a free reactive group at the monolayer terminus which may be derivitised to form bridges to new chlorins assembled above the initial layer. If there is the possibility of forming *J*- or *H*-dimers in these vertical domains, it is possible that strong coupling could then be achieved, indicating fast coherent transport.

Secondly, naturally derived chlorophyll derivatives will be attached to assembled polymer brush structures with available reactive functional groups. Mathematical modelling of strong plasmon-exciton coupled systems in light-harvesting complexes shows that the protein scaffolds serve only as an organisational framework for dipoles and does not contribute to the coupling dynamics. In principle, non-proteinaceous structures, such as polymer brushes, should serve the same function. In this manner, large vertical brush structures with an amorphous, flexible arrangement can be grown from the surface using established surface-initiated polymerization methods (211). These flexible brushes can then be functionalized with chlorophylls incorporating compatible functional groups, potentially forming dense layers of chlorins organised three-dimensionally within a plasmonic field. Here, the aim is to use poly(cysteine methacrylate) brushes as such a scaffold, bearing accessible amine side groups which may be derivatised with wide-used cross-linking chemistry. By controlling the organisation and density of chlorophylls in these brushes within the plasmon mode volume, it is hoped a wide range of structures may be designed to explore plasmon-exciton coupling in synthetic biologically-inspired systems.

Chapter 2: Materials and Methods

1. Materials and substances

The following materials were utilised for the experiments described herein:

a) *General solvents and substances*

- Acetic acid, $\geq$ 99.7% (Sigma-Aldrich, 695092)

- Acetone, HPLC grade, $\geq$ 99.8% (Honeywell, 34850)

- Acetone-d_6, $\geq$ 99% (Sigma-Aldrich, 444863)

- Acetonitrile, $\geq$ 99.8% (Fisher Scientific, A/0626/PB17)

- Ammonia solution, 35% (Fisher Scientific, A/3240/PB17)

- Argon gas (BOC, ISO 14175-I1-Ar, Pureshield)

- Chloroform, HPLC grade, $\geq$ 99.98% (Fisher Scientific, C/4966/17)

- Chloroform-D, 99.8% (VWR, 87153.0100)

- Dichloromethane, $\geq$ 99.8% (Fisher Scientific, D/1856/17)

- Diethyl ether, $\geq$ 99.8% (Honeywell, 32203)

- Dimethylformamide, > 99% (Fisher Scientific, D/3840/17)

- Ethanol, Absolute, $\geq$ 99.8% (Honeywell, 32221)

- Ethyl acetate, HPLC grade, $\geq$ 99.5% (Fisher Scientific, E/0906/17)

- n-Hexane, HPLC grade, $\geq$ 97% (Honeywell, 34859)

- Hydrochloric acid, 35% (VWR, 20246.323)

- Hydrogen peroxide, 30% (VWR, 23622.298)

- Lithium hydroxide monohydrate, $\geq$ 98% (Sigma, 402974)

- Magnesium sulfate, anhydrous, $\geq$ 62, 70% (Fisher Scientific, M/1100/53)

- Methanol, HPLC grade, 99.99% (Fisher Scientific, M/4056/17)

- Paraffin oil, puriss (Sigma-Aldrich, 18512)

- Petroleum ether 60-80 ℃, puriss (Sigma-Aldrich, 32248)

- Potassium hydroxide, 86.6% (VWR, 26668.268)

- 2-Propanol, HPLC grade, ≥ 99.9% (Honeywell, 34863)

- Sand, acid-washed (VWR, 27461.298)

- Silica gel, 40-63 μm particle size (VWR, 15445P)

- Sodium chloride, ≥ 99.5% (Fisher Scientific, S/3120/60)

- Sodium dodecyl sulphate, micropellets (Fisher Scientific, 1281-1680)

- Sodium hydrogen carbonate, ≥ 99% (Fisher Scientific, S/4200/60)

- Sodium hydroxide, ≥ 97% (Fisher Scientific, S/4880/53)

- Sulfuric acid, ≥ 95% (Fisher Scientific, S/9160/PB17)

- Tetrahydrofuran, 99.7% (VWR, 28559.320)

- Water was deionised and filtered for use with an Elga Purelab Option DV35 water filtration system, measured to a conductivity rating of 15 mΩ.cm.

b) *Substrate preparation*

- Coverslips, borosilicate glass, 22 x 60 mm (Menzel-Gläser, # 1,5)

- Silicon wafers (PI-KEM Ltd., Test Grade, (100), P14723)

- Chromium chips, 99.99% (Agar, E435)

- Gold (Goodfellow Advanced Materials, Cambridge)

- Titanium (Goodfellow Advanced Materials, Cambridge)

c) *Gold plasmonic nanostructure array fabrication*

- Octadecanethiol, 98% (Sigma-Aldrich, O1858)

- Cysteamine hydrochloride, ≥ 98% (Sigma-Aldrich, M6500)

d) Chapter 3 experiments

- Ammonium acetate, ≥ 98% (Sigma-Aldrich, A7330)

- Ammonium chloride, 99.99% (Sigma-Aldrich, 326372)

- Ammonium persulfate, ≥ 98% (Sigma-Aldrich, 248614)

- 1,8-Diazabicyclo[5.4.0]undec-7-ene, 98% (Sigma-Aldrich, 139009)

- 1,12-Dibromododecane, 98% (Sigma-Aldrich, 174866)

- Dimethyl sulfoxide, ≥ 99.9% (Sigma-Aldrich, 34943)

- Diphenyl diselenide, 98% (Sigma-Aldrich, 180629)

- 2,6-Di-tert-butylpyridine, ≥ 97% (Sigma-Aldrich, 219584)

- Ethyl trans-2-butenoate, ≥ 96% (Sigma-Aldrich, W348600)

- Lithium borohydride, ≥ 95% (Sigma-Aldrich, 62460)

- Methylamine hydrochloride, ≥ 98% (Sigma-Aldrich, M0505)

- 4-Methyl-3-penten-2-one, 90% (Sigma-Aldrich, W336807)

- Nitromethane, 98+% (Alfa Aesar, A11806)

- Oxalyl chloride, 98% (Acros Organics, 129611000)

- Phosphorous (V) oxychloride, 99% (Sigma-Aldrich, 201170)

- Potassium acetate, 99% (Alfa Aesar, A16321)

- Potassium thioacetate, 98% (Sigma-Aldrich, 241776)

- Sodium acetate, ≥ 99% (Sigma-Aldrich, S8750)

- Sodium hydride, 60% dispersion in mineral oil (Sigma-Aldrich, 452912)

- Sodium methoxide, 25 weight % in methanol (Sigma-Aldrich, 156256)

- Titanium (III) chloride, 27-33% in 10% aqueous hydrochloric acid (Merck, B1309908 617)

- P-Toluenesulfonylmethyl isocyanide, 97% (Alfa Aesar, A14312)

- Trimethylsilyl trifluoromethanesulfonate, 99% (Sigma-Aldrich, 225649)

e) **Chapter 4 experiments**

- 3-(Acryloyloxy)-2-hydroxypropyl methacrylate, ≥ 70% (Sigma-Aldrich, 454982)

- L-Ascorbic acid, reagent grade, ≥ 98% (Sigma-Aldrich, A7506)

- 2,2'-Bipyridyl, ≥ 99% (Sigma-Aldrich, D216305)

- Bis[2-(2-bromoisobutyryloxy)undecyl]disulphide, 97% (Sigma-Aldrich, 733350)

- Copper (II) chloride, 99% (Sigma-Aldrich, 751944)

- L-Cysteine, ≥ 97% (Sigma-Aldrich, W326305)

- N-(3-Dimethylaminopropyl)-N'-ethylcarbodiimide hydrochloride, crystalline (Sigma-Aldrich, E6383)

- 4-Dimethylaminopyridine, 99% (Alfa Aesar, A13016)

- Dimethylphenylphosphine, 99% (Sigma-Aldrich, 265020)

- n-Hydroxysuccinimde, 98% (Sigma-Aldrich, 130672)

- Spinach leaves, pre-washed (Sainsbury's)

- p-Toluenesulfonic acid monohydrate, ≥ 98% (Sigma-Aldrich, T35920)

- 2,4,6-Trimethylpyridine, 99% (Sigma-Aldrich, 142387)

- Undecanethiol, 98% (Sigma-Aldrich, 510467)

- Zinc acetate dihydrate, 99.999% (Sigma-Aldrich, Z0625)

2. Procedures and fabrication methods

a) **Cleaning of substrates and glassware**

Glass coverslips or silicon wafers for monolayer preparation experiments and glassware required for clean reaction conditions were deep-cleaned with piranha solution (**WARNING:** *piranha solution is highly corrosive and explosive with large amounts of*

organic material – implement adequate precautions). Glass sample tubes were cleaned with

sodium dodecyl sulphate beforehand to remove any excess organic contaminants. If required,

the substrates to be cleaned were then placed in the appropriately-sized tubes. Once placed

within a larger beaker, the piranha solution was mixed (30:70 hydrogen peroxide: sulfuric

acid) with the samples, upon which a vigorous fuming reaction occurred. Upon completion

and cooling (~ 1.5 h) the solution was poured into a large dilution tank followed by 7 cycles

of copious washing (complete filling of the tubes and the beaker) with deionised water. The

substrates/glassware were then placed in a thoroughly cleaned glassware oven (T = ~ 80 °C)

to dry before use.

b) *Preparation of metal substrates for monolayer formation*.

Dried substrates after piranha cleaning were placed in an Edwards Auto 306 Vacuum

bell jar evaporator (Edwards, Crawley, UK) along with two metal sources, typically a small

amount of chromium and gold in separated tungsten source boats. The interior pressure was

then reduced to $< 3 \times 10^{-6}$ Torr. Under optimal conditions a pressure of 8×10^{-7} mbar was

achieved. Current was then applied to the evaporation source, causing vaporisation of the

target metal which was then deposited onto the substrate. For typical samples, an adhesion

layer of chromium metal (Cr, thickness = 2-10 nm) was evaporated followed by gold (Au,

thickness = 15-30 nm) at a rate lower than 0.1 nm/s. After cooling of the bell jar interior

pressure was equalised to extract the samples. Prepared substrates for unpatterned monolayer

studies were kept in sealed piranha-cleaned glass vials until needed for monolayer formation.

For the fabrication of arrays of gold nanostructures, substrates with more specific thickness

ranges (2-5 nm Cr, 20 nm Au) were immersed in a solution of octadecanethiol (2 mM, EtOH)

for at least 48 hours before patterning.

c) *Preparation of self-assembled monolayers on gold.*

Gold substrates for monolayer formation were cut into sample sizes from the main glass coverslip substrates with a diamond-tipped cutting pen to a size appropriate for the function or analysis method to be performed. The solvent was degassed of dissolved oxygen with argon gas in a piranha-cleaned vessel for 10-30 min. The adsorbate thiol was then dissolved with the solution in a sterile sample tube to a typical concentration of 2 mM. The substrates were then immersed in up to 1.5 mL of the adsorbate solution (depending on sample size) in an appropriately sized sample tube and sealed. Samples were then placed in a fridge (T = 4 °C) and given at least 24 – 48 hours to assemble into surface monolayers. Until required, samples were kept in these solutions upon which they were washed with the solvent of choice and dried with nitrogen before use.

d) *Fabrication of arrays of plasmonic gold nanostructures by interferometric lithography.*

Large area patterning of a substrate can be accomplished using interferometric lithography as a variant of high-resolution photolithography. In general, photolithography is the top-down fabrication process of writing onto a substance by using light to expose a photosensitive resist layer, followed by a development process which removes the substrate either under the exposed areas or in the surrounding areas to produce surface features (130). Under normal circumstances however, such as typical mask-based lithography processes, the diffraction limit on the resolving power of visible light wavelengths prevents their use in writing nanometre-scale features coherently (131). Higher energy radiation has been employed to try and circumvent this limit using adapted techniques (132), but the costs associated with higher-energy sources, developing new photoresists and nanometre-scale masks for large area nanopatterning are high. Recently, near-field lithography was developed

to circumvent the diffraction limit by utilising the evanescent light component, which at short range, i.e. a few nanometres, does not exhibit diffraction when emitted through an aperture (131, 133). By exposing a sample to a laser-light source with an aperture extended only by a few nanometres above the surface, a resist layer such as a thiol monolayer can patterned at a resolution equal to the size of the aperture used, making features as small as 30 nm possible (134). However, the single-aperture requirement, small beam diameter and the writing speed required for well-defined features makes the large-scale patterning of a sample impractical using this method unless a larger-scale platform for parallel writing is utilised (135).

Interference lithography (IL) can circumvent these issues to produce large-area patterns of repeating structures, ideal for making regular arrays of plasmonic structures (135, 136, 117). It is well known that two polarised light beams with a phase separation produce a new radiating pattern of alternating intensity when they interact with each other at an incident point – constructive interference where the light waves amplitudes become in phase, resulting in greater intensity, and destructive where the amplitudes are 180 degrees out of phase, thus cancelling their intensity. The result is a series of lines of light intensity, and the period spacing between these lines is determined by:

$$d = \frac{\lambda}{2n.\sin\theta}$$

$$\text{(2.1)}$$

where λ is the light wavelength, n is the refractive index of the medium and θ is the angle of incidence of the light beams. The resulting interferogram consists of bands of constructive and destructive interference, yielding regions of high and low intensity exposure respectively. On gold surfaces, thiols are used as resist layers. Upon exposure to light wavelengths in the ultraviolet range, the sulphur-gold bond tethering the molecules to the substrate can be broken by a photocatalysed oxidation environment in ambient conditions (137, 138, 139):

$$AuSR + {}^3/_2\, O_2 + e^- \longrightarrow Au + RSO_3^- \hspace{3cm} (2.2)$$

Once removed, an etching process can then be used to develop the features in the exposed areas.

      For the fabrication of arrays of plasmonic gold nanostructures for our experiments (figure 2.1), octadecanethiol SAM samples were cut into samples of approximately 1 x 2 cm dimensions. An individual sample for exposure was then mounted on a custom-built Lloyds's mirror interferometer, a simple corner cube with two walls, one on which the sample is held in place with a low vacuum pump and the other has a mounted mirror. A Coherent Innova 300C frequency-doubled argon ion laser ($\lambda = 244$ nm, Coherent, Ely, UK) was used as the light source. During operation, the laser beam was fired at the interferometer, after first having been passed through a spatial filter to ensure a coherent, collimated beam and through a lens and aperture to expand the beam size. The size of the beam encompassed both the mounted sample and the mirror on the adjacent wall – one part of the beam illuminated the sample surface unhindered while the other part was reflected from the mirror towards the sample at an angle θ, resulting in an interference pattern at the sample surface over an area of approximately 1 cm^2. To produce parallel lines on the surface, a single exposure was used at a dose of 35 – 45 J cm^{-2} before etching. To produce arrays of nanodots, the sample was rotated through angle φ and exposed to a second dose of 20 cm^{-2}. Once the desired exposures were completed, the gold substrate under the exposed areas was etched using an ethanolic solution of cysteamine (0.2 M, EtOH/ 8% ammonia solution) until there was no gold present between the unexposed islands (as evaluated by atomic force microscopy), thus fabricating a regular series of features. The samples were then rinsed with ethanol and dried with nitrogen.
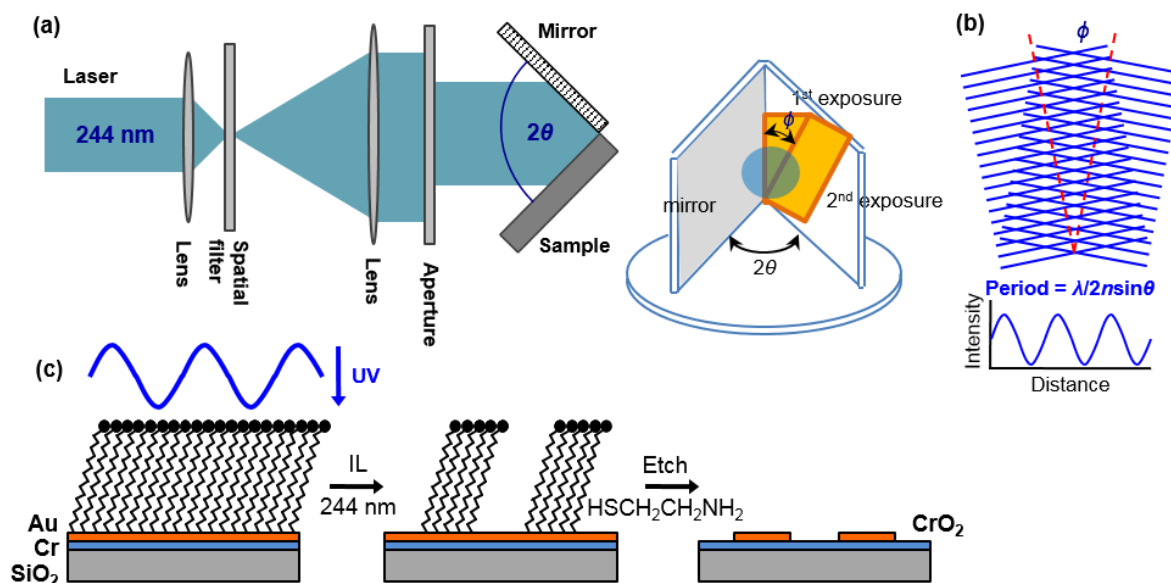
Figure 2.1: The set-up used for interferometric lithography to fabricate arrays of gold nanostructures. **a)** The laser beam is passed through a spatial filter before focusing by a lens and then passed through an aperture towards a Lloyd's mirror interferometer. The mirror and sample are arranged at an angle 2θ to each other. The sample is mounted on the interferometer and rotated about angle ϕ between two exposures. **b)** The interference of the straight and reflected components of the beam generates a series on lines with a given periodicity dependent on λ and θ. As a consequence of two exposures about ϕ, a pattern of criss-crossing lines results in island of no exposure, allowing for formation of arrays of separated nanostructures. **c)** A monolayer of octadecanethiol on a gold substrate is exposed to the interferometric light pattern. The photo-oxidized molecules are removed to expose the gold substrate, and a cysteamine etch removes these deprotected areas to produce the separated gold nanostructures.

For gold nanodots, annealing of the samples was necessary in most cases to optimise the plasmon extinction spectrum by modifying the shape and crystallinity of the gold aggregates after fabrication. For this, samples were placed in air in a muffle furnace (Keison International Ltd., UK) and heated gradually at a rate of $7 \ ^{\circ}C.min^{-1}$ up to a $490 – 525 \ ^{\circ}C$ standing temperature range (depending on sample dimensions) for $90 – 120$ minutes, before gradual cooling back to room temperature. Samples were then evaluated by atomic force microscopy and UV/Vis absorption before use.

All fabrication and measurements steps were carried out by Dr. Anna Lishchuk, and a mix of samples previously shown to display strong coupling with light-harvesting proteins (116) and newly fabricated samples were used.

e) *Cleaning of plasmonic nanostructure arrays*.

Nanostructure arrays were durable enough to be cleaned of previously adsorbed organic material and then re-used with adsorption of new material. To do this, a small glass petri dish was used to mix a small amount of piranha solution which was left to cool down for approximately 30 minutes to 1 hour. Once cooled, plasmonic samples were immersed in the solution for 2 – 5 min, after which they were washed thoroughly with deionised water and dried with nitrogen. While piranha solution is specifically reactive with organic material the acid conditions may impart some damage to the substrate or nanostructures, so the samples were then re-examined with atomic force microscopy and UV/Vis spectroscopy to record any changes to the structure or absorption profile of the samples before reuse.

3. Analytical methods

a) *Nuclear Magnetic Resonance (NMR) spectroscopy*

^{1}H and ^{13}C NMR spectra were collected on Bruker Avance and Avance III HD NMR spectrometers operating at a 400 MHz radio frequency. Samples were prepared in multi-gram quantities and dissolved in approximately 5 mL of the appropriate deuterated solvent and filtered before measurement. Details of chemical shift results and solvents used may be found in the experimental sections of the subsequent chapters.

b) *Mass Spectrometry*

Samples submitted for mass spectrometry were analysed with a Waters LCT classic ToF liquid-chromatography mass spectrometer for both direct EI and LC-MS measurements. Further details and results may be found in the relevant experimental section of subsequent chapters.

c) *Ultraviolet/Visible spectroscopy of solutions and plasmonic nanostructures*

For measurements of compounds dissolved in liquids, the analysis was carried out using an Agilent Technologies Cary 50 spectrophotometer, with a wavelength scanning range of 350 – 800 nm. Solutions were analysed in a 2 mL cuvette with a 1 cm path length. For plasmonic arrays before and after functionalisation with materials, measurements were carried out with a Cary 5000 spectrophotometer between 350 – 850 nm. For dry measurements a customised holder was used to hold the samples perpendicular to the beam direction, with a pinhole allowing the sample to be aligned to ensure the same area was being scanned between surface functionalisation steps. For liquid measurements of these, a custom holder was used in conjunction with a standard cuvette to allow reliable measurements in the medium of choice.

d) *High Performance Liquid Chromatography (HPLC)*

Samples were submitted to the Sheffield Department of Chemistry Chromatography Service for purity determination, via analytical HPLC with single-wavelength detection. Further details for purity, retention times and solvents used may be found for the relevant compounds in the experimental sections of the subsequent chapters.

e) X-ray Photoelectron Spectroscopy (XPS)

X-ray photoelectron spectroscopy is a surface analysis technique which provides elemental compositional and quantitative analysis of a material, whether it is a bulk material or a layered composite (141). In XPS, a sample is exposed to a beam of energetic x-rays, causing emission of electrons from core shells. These photoelectrons have kinetic energies that are characteristic of the elements from which they are emitted, and these are used to identify the chemical elements present on the surface. The simplified experimental principles are illustrated in figure 2.2.

In a typical XPS machine, the samples to be analysed are placed in an ultra-high vacuum chamber (p ~ 10^{-9} mbar) This is required to prevent scattering of the emitted photoelectrons in the experiment from any air molecules in the chamber, as well as to preserve the sensitivity of the analysis by preventing the adsorption of gas molecules to the sample surface. Once the samples are in place, X-rays are generated by firing electrons at a water-cooled metal anode and the emitted radiation has a specific energy – for example, aluminium is commonly used as an anode and generates K_α radiation with an energy of 1486.6 eV. This known quantity is essential for the determination of the photoelectron binding energies later on. The efficiency of x-ray generation also increases with increasing electron energy used to bombard the anode. The "raw" X-rays are then reflected from a monochromator, essentially a quartz crystal to give first order diffraction. This serves multiple functions – to reduce the X-ray linewidth to give higher resolution spectra, to remove any unwanted portions of the X-ray spectrum, to enable a remote distance between the anode (a potentially damaging heat source) and the sample, and as a focusing device to enable a small analysis area (down to the micrometre scale) which also limits potential x-ray damage on the sample and adjacent ones also.
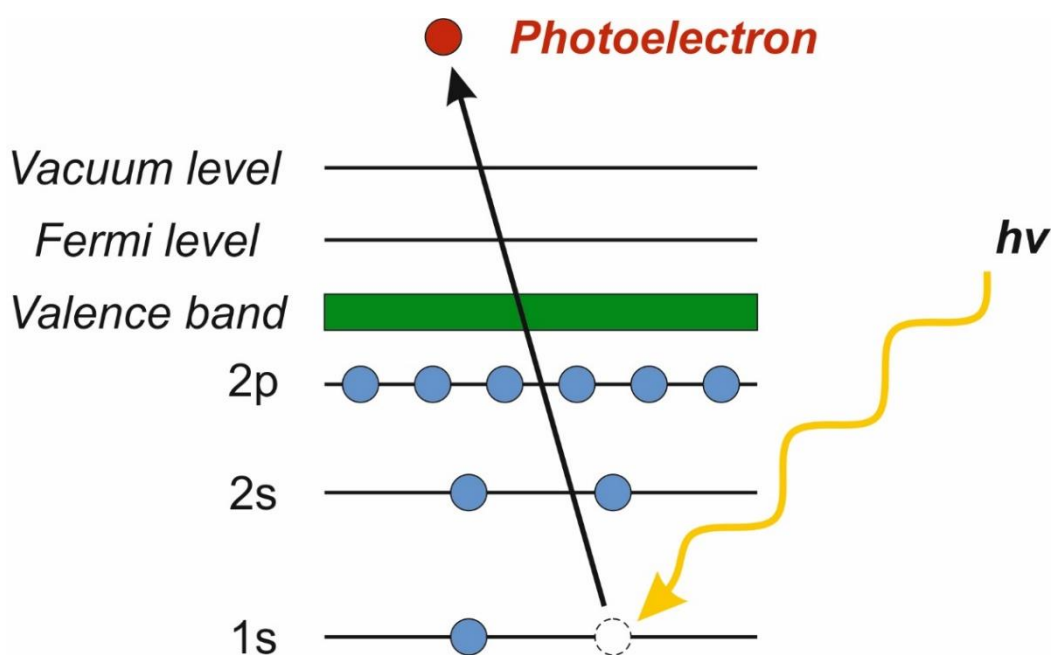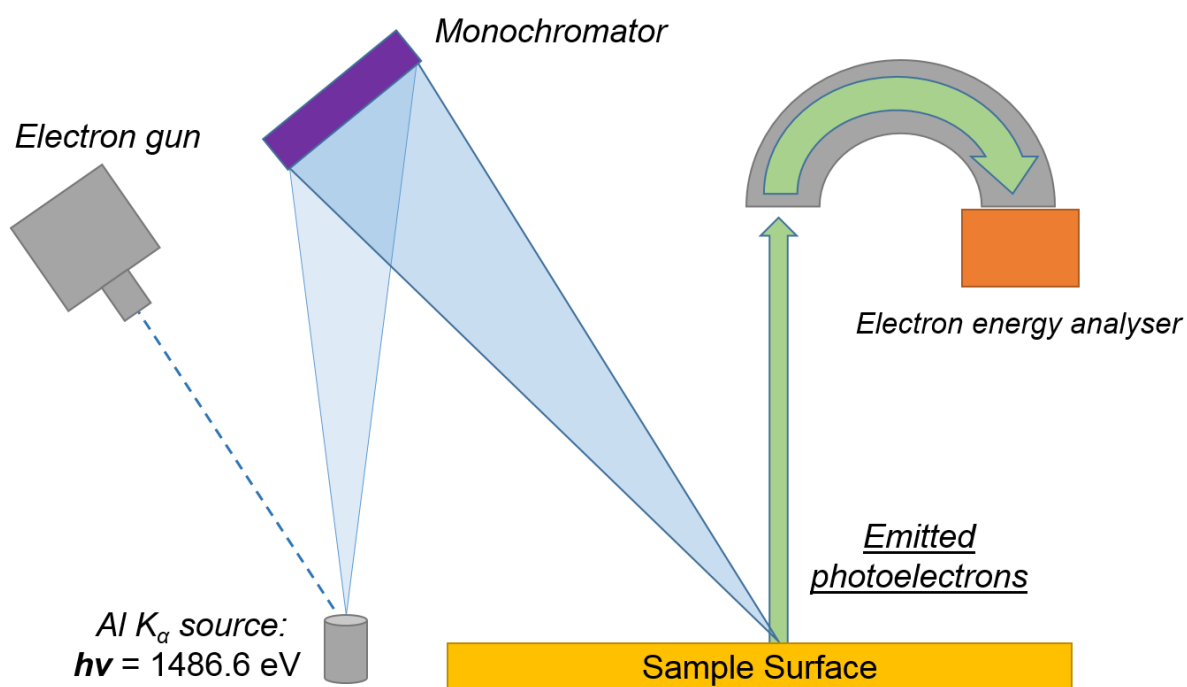
Figure 2.2: (**Top**) *The general operating principle behind X-ray photoelectron spectroscopy – X-rays by an anode excited by electrons are monochromated and focused onto the sample surface, where photoelectrons are generated. These are then detected by an electron energy analyser to catalogue their kinetic energies.* (**Bottom**) *The X-rays collide with an electron in an atomic orbital, for example the 1s orbital here. If the energy is enough to knock the electron from the shell and to overcome the vacuum level, the photoelectron is now able to travel through free space.*

When the x-ray photons irradiate the sample, they interact with the electrons within the atoms and can impart energy to excite them (figure 2.2). For an electron to be emitted from the atom, the binding energy E_b must be overcome by the energy of the photon in the collision. This photoelectron must also have enough energy to be ejected beyond the Fermi band energy and into the vacuum of the chamber – the work function W. Once accomplished, the photoelectrons move around freely in the vacuum with a kinetic energy E_k which varies with the binding energy for each elemental energy level of origin. These photoelectrons are then analysed by an electron spectrometer positioned above the sample where their kinetic energies are measured. From the known values of the x-ray energy, the measured kinetic energy and the work function specific for the spectrometer, the binding energy can be calculated as:

$$E_b = h\nu - E_k - W \tag{2.3}$$

This calculation is done automatically by the attached software package to the spectrometer, which this accumulates the data into a spectrum of count intensity versus the binding energies calculated for the photoelectrons. This allows for peak assignments to elements found in the sample, with the peak intensities and areas in general representing the relative amounts of each element found. However, direct comparison of peak areas can be misleading as the probability of producing a photoelectron, known as the emission cross-section, is different between the analysed elements as well as the orbitals of origin for the photoelectrons. The intensity I of a peak is related to this by:

$$I = J\rho\sigma K\lambda \tag{2.4}$$

Where *J* is the photon flux, ρ is the atomic concentration and σ is the emission cross-section. *K* is a constant taking several instrumental factors into account such as the proportion of electrons transmitted as a function of kinetic energy (the transmission function), the detector efficiency and the effect of stray magnetic fields on the transmission of low-energy electrons. λ is the attenuation length of the electron – as the spectrometer can penetrate through the sample surface by multiple nanometres, photoelectrons can be generated within the three-dimensional depth of the sample. However, these photoelectrons may not only be generated with less efficiency than those at the surface but collisions and recombination of these with the surrounding matter above reduces the number that reach the detector and thus can lower peak intensity. All of these factors thus make the direct comparison of peak areas extremely complex. However, the comparison can be simplified greatly by compiling these factors into an experimentally-determined sensitivity factor *F* for each element. Thus, once peak intensities have been recorded and ensuring that the X-ray photon flux was constant during the measurements, expressing the individual peak intensities as ratios to their sensitivity factors and then as percentages of the sum of these new normalized intensities gives the atomic concentration percentage which can then be used for direct quantification of elemental composition:

$$[A] atomic\ \% = \left\{ \frac{\left(\frac{I_A}{F_A}\right)}{\Sigma \frac{I}{F}} \right\} X\ 100\% \qquad (2.5)$$

Depending on the sample composition, especially on insulating materials, positive electrostatic charging can occur on the substrate, especially where a monochromated X-ray beam is used. This results in a uniform shift of the peak positions of the spectra towards higher energy. This can be counteracted using a low-energy electron source (< 5 eV) to

neutralize the surface during measurement. Typically, the spectra acquired will still be shifted uniformly by a few eV as a known excess of electrons is used to ensure complete neutralisation of the positive charge. In these cases, the spectra are calibrated to a peak with a well-referenced signature energy to ensure the correct assignment of the other elements. For example, the hydrocarbon C-C peak can be used as a reference, with manifest examples in the surrounding literature placing its binding energy at 285 eV.

For a sample two kinds of spectra can be collected. The wide scan spectrum is collected from the whole range of electron binding energies below that of the X-ray energy used – practically speaking this gives a range from 0 – 1200 eV. This provides the largest range of quantification of elemental composition but has low resolution and so only give broad peak quantification. Spectra can also be collected on specific regions where elements are expected, with longer acquisition time in these areas giving higher resolution lineshapes of the spectrum. These high-resolution scans give the ability to examine the binding energies more closely and assign functional group composition for elements such as carbon. This is because the binding energies of inner shell electrons can be modified by the bond environment around the atom. Where a comparatively electronegative atom or ion is bonded to the atom being analysed, such as oxygen to carbon in alcohols and carboxylate groups, the shift in electron density around it results in a partial positive charge which increases the attractive force on the inner shell electrons and thus increasing the binding energy to be overcome by the X-ray collisions. Conversely, electropositive groups or ions shift electron density towards the atom and thus reduce the binding energies slightly. In this way, detailed chemical environment information can be obtained from high resolution XPS scans.

For our experiments with chlorophyllides attached to polymer brushes, we found that angle-resolved XPS was a useful additional tool for characterisation. Typical XPS analysis has the detector at a perpendicular orientation to the sample plane (the direction of the largest

photoelectron mean free path) to allow for maximum depth penetration, which can be around 10 nm. The analysis depth can be changed however by modifying the angle of either the detector or the sample while keeping the X-ray source in the same position. At angles close to the plane, the number of photoelectrons emitted is reduced as a function of the cosine of the new angle from the surface normal. As the photoelectrons at lower depth have a longer path to travel to escape the surrounding sample material at these angles, proportionately more of the chemical information conveyed by the remaining photoelectrons originates from the material closer to the sample surface. In this way, a comparison of the data collected from the normal angle and increased angles can give a compositional comparison of the "bulk" and "surface" compositions of the material. This can be useful for analysing X-ray-sensitive materials such as organic materials and polymer brushes without significant sample damage and assessing the functionalisation of porous samples which may be diffusion controlled.

Experimental Set-up. XPS analysis of prepared samples was carried out using a Kratos Axis SUPRA X-ray photoelectron spectrometer. X-rays were generated from an Al Kα monochromatized source with an operating power of 225 W and an energy of 1486.6 eV. The typical chamber pressure was maintained to a minimum of 10^{-10} mbar. Survey scans were collected over a 1200 eV range - a 160 eV pass energy with 1 eV steps was used, with a total acquisition time of 4 minutes 60 seconds consisting of 248 ms dwell times for 1206 steps. High resolution spectra were collected over a 20 eV pass energy with 0.1 eV steps. Typical collection times for elemental regions were as follows: C 1s = 5 min (1298.7 ms x 1 x 231), N 1s = 10 min (1492.5 ms x 2 x 201), O 1s = 5 min (1657.5 ms x 1 x 181), S 2p = 20 min (2127.7 ms x 4 x 141), Au 4f = 5 min (1863.4 ms x 1 x 161). All spectra were analysed by the CasaXPS software package, version 2.3.18PR1.0. Wide spectra were fitted by automatic elemental line identification and narrow spectra were peak-fitted manually, with all

binding energies referenced to the hydrocarbon C 1s peak energy at 285 eV. For angle-resolved spectroscopy, measurements were first taken at normal orientation to the sample plane (0º) followed by successive measurements at detector angles of 37º, 53º, 66º and 78º to that normal.

f) Secondary Ion Mass Spectrometry (SIMS)

Secondary ion mass spectrometry is a surface-specific mass spectrometry technique utilising heavy ions as a means of fragmenting the surface sample to analyse the ejected components (142). Much like XPS, it can be used for qualitative elemental analysis but has the added benefit of identifying isotopic and molecular fragments by mass and the capability of imaging to observe elemental distributions across a sample. The simplified operating principle of this techniques is illustrated in figure 2.3.

In a typical experiment, the sample is placed in the instrument analysis chamber and the pressure is then reduced to ~ 10^{-10} mbar. After this, the sample is bombarded by energetic ions. The energy imparted by the impact results in a cascade of collisions between the surface atoms and eventually fragments the surface material into secondary ions, molecular particles and smaller fragments. The yield of ions for species m from a primary beam impact is given as:

$$I_s^m = I_p y_m \alpha^+ \theta_m \eta \tag{2.6}$$

Where I_s^m is the secondary ion current for m, I_p is the flux of the incoming primary ions, y_m is the sputtering yield of all the fragments produced (neutral, positive or negative), α^+ is the probability of producing positive ions from the collision, θ_m is the surface fractional concentration of m and η is the transmission of the analyser used.

The sampling depth is surface specific, estimated to $1 - 3$ nm. This is because while the high energy of the primary ion is transferred deep into the substrate, the energy density which returns to the surface is typically low. Once the secondary ion fragments are generated, much like in typical mass spectrometry they are accelerated through a magnetic field towards a mass analyser which detects the masses of the various fragments. Various kinds of analyser commonly used for standard instruments are compatible with the SIMS instrument, including magnetic sector, quadrupole and time-of-flight (ToF) configurations (141). ToF-SIMS instruments in particular have become widely used as standard for surface analysis as the entire fragment library produced by the ion impact is collected, a very high range of atomic masses can be detected up to 10,000 atomic mass units and the transmission efficiency at 10 – 50% is comparatively high compared to other types of analyser (for example, quadrupole analysers only have a 1% efficiency). The mass detector is also capable of differentiating the charges of the ions in positive and negative, thus allowing the collection of two separate spectra the positive and negative ions collected per analysis.

The primary type of SIMS used here is Static SIMS. As SIMS is a destructive technique which damages the substrate during the analysis, the static analysis method was developed to preserve the sample substrate as much as possible during the analysis time period by using a low flux of primary ions to bombard the surface while still receiving a compositional analysis of the surface. The flux is usually reduced to around 10^{12} impacts per centimetre squared, and the primary ions become statistically more likely to impact undamaged parts of the surface over previous impact sites. As per the SIMS equation, this lower flux also lowers the potential yield of secondary ions and so high sensitivity analysers such as ToF instruments are preferred for static-SIMS.

Experimental Set-up.* SIMS analysis of prepared monolayers was carried out using a ToF-SIMS 5 spectrometer. Positive and negative ion fragments were generated using a Bi^{3+} primary cluster source over a 300 x 300 μm^2 area with a 1.46 x 108 eV dose at a minimum pressure of 10-10 mbar. Positive and negative spectra were collected over a range of 1000 m/z. Surfacelab 6 software was used for peak picking and spectra output in both positive and negative.
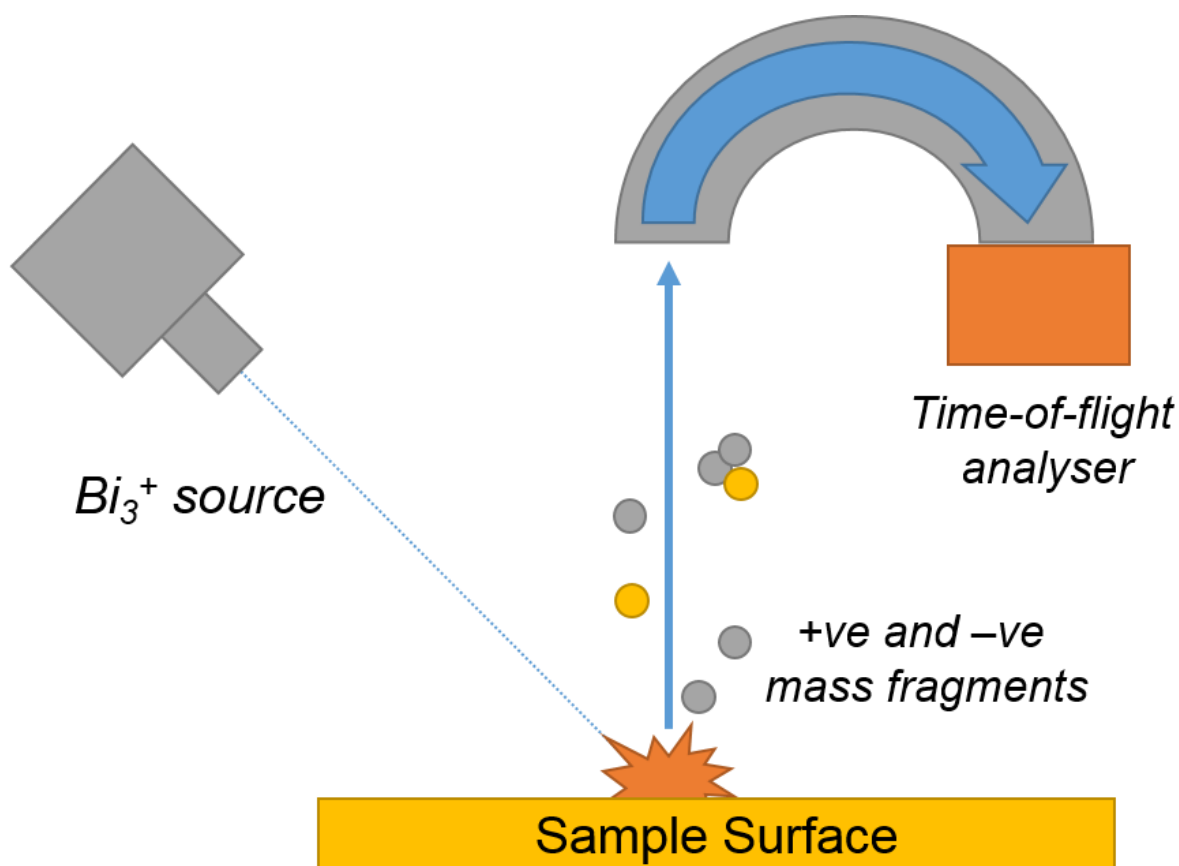
Figure 2.3: *A simple representation of the operating principles of SIMS – a primary ion source fires energetic particles at the surface, where the energy is transferred to the surface molecules. This results in fragmentation and produces free ions in the vacuum, which are then collected and run through a standard time-of-flight mass analyser to give spectra of the negative and positive mass fragments produced.*

g) Ellipsometry

Ellipsometry is a technique for the measurement of the optical properties of a surface material or composite using polarized light so that properties of the material such as layer thickness, refractive index, optical constants and composition can be determined (143).

In spectroscopic ellipsometry, a typical experimental instrument consists of a light source and polarizer mounted at one end, a stage which can be manipulated by height and tilt angle, and a polarized light detector at the other end (figure 2.4). The light source and detector are angled with respect to the stage, typically between $70 - 75^o$ from a normal orientation. The principle of the technique is that the optical properties of a surface material, either thin film or bulk, can alter the properties of polarized light when it is reflected from said surface, and that these altered properties can be used to model the surface composition computationally and determine its characteristics. First, a sample is placed on the centre stage where alignment can be carried out to ensure the reflected light beam will enter the detector correctly. A continuous beam of linearly polarized light, consisting of two combined polarized light beams in phase with each other, is then fired at the sample at an incident angle across a defined wavelength range. This has a polarization function χ_i is defined by the combination of the electric field vectors of the two beams, $\tilde{E}^i_p$ and $\tilde{E}^i_s$. These vectors are orthogonal to the beam propagation direction along two planes, p and s, orientated 90° apart. The polarization function is expressed as:

$$\chi_i = \tilde{\mathrm{E}}^i_p / \tilde{\mathrm{E}}^i_s \qquad\qquad (2.7)$$

When the light is reflected from the surface, interaction of the light with the material in the sample is dependent on the optical properties of the material, and results in a change in

the polarization characteristics of the reflected light. When it reaches the detector at the other

end of the instrument the polarization function is now:

$$\chi_r = \tilde{E}_p^r / \tilde{E}_s^r \tag{2.8}$$

The p and s components also now gain two new reflection coefficients, R_p and R_s. These

functions however are different from each other, as their different electric field vectors mean

that the two light beams are reflected differently upon contact with the sample. The resulting

reflected light is now elliptically polarized instead of linearly. In linearly polarized light, the

two components are in-phase and of equal amplitude, but the reflection results in a new phase

difference between them and a change in amplitude in each of the two components, the

magnitude of which can be expressed as a ratio. These can be put into a relationship with the

reflection coefficient to create a new complex reflectance ratio parameter ρ:

$$\rho = \frac{R_p}{R_s} = tan(\psi).e^{i\Delta} \tag{2.9}$$

where ψ is the amplitude change ratio and Δ is the phase difference. During the

measurement, these two factors are recorded and displayed as a spectrum in respect to the

wavelength of light.

This in itself does not provide any useful information directly, however. Instead, the

data has to be replicated using a computer-modelled spectrum which takes into account the

anticipated layer structure of the sample, the types of materials in the sample with their

optical properties included and the thicknesses of the layers. By knowing which materials

which have been layered onto the substrate in which order with an estimated thickness an

accurate model can be constructed to give additional information on optical properties, as well as determining the true thickness of a layer of interest on the surface, for example a self-assembled monolayer. A simple goodness of fit is used to evaluate the reliability of the model to the raw data, but one must be careful to make sure the model is constructed to accurately replicate the known optical properties and layer structure of the known materials used – a well fitted model does not necessarily describe the surface accurately if the wrong components are used or if the organisation of layers used is incorrect.
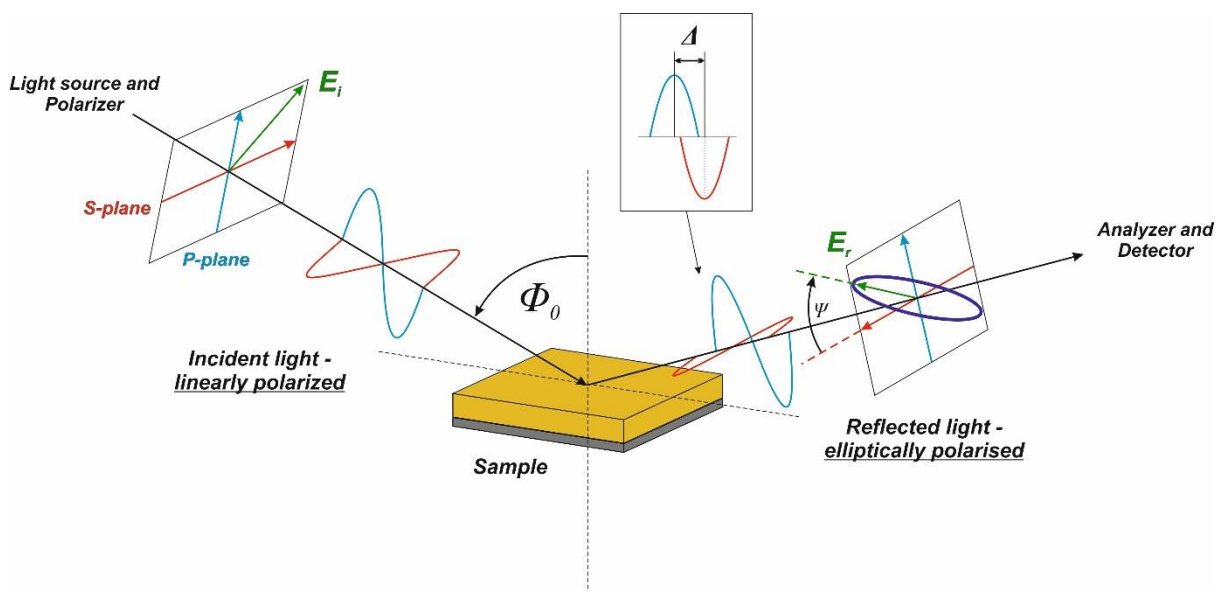
Figure 2.4: In ellipsometry analysis, light from a source is linearly polarized (no phase or amplitude differences between the orthogonal s-and p-components) and emitted towards a surface sample at an incidence angle Φ_0. Once the light interacts with the sample and is reflected, it becomes elliptically polarised with a phase difference Δ as well as an amplitude ratio Ψ between the two components in the newly polarized light. These two factors are measured by the detector and a model is calculated to fit the resulting spectrum and estimate the thickness or optical properties of the composite sample.

Experimental set-up. Two ellipsometers were used to carry out the analysis for this work. For the measurements on non-photopatterned monolayer samples for chapter 3, a J. A. Wollam Co. Inc M-2000^{TM}-V variable angle ellipsometer was used at an incidence angle of 70° over a spectral range of 371 – 1600 nm. For unpatterned polymer brush samples in

chapter 4, measurements of unpatterned samples were collected with an Alph-SE ellipsometer operating over a range of wavelengths between 370 – 1000 nm. The incident angle here was 75.238^o. Measurements in air were carried out on the stage baseplate or with a metal block in ambient conditions. For measurements in liquid media, a liquid cell with angled portholes at ~ 70° to normal was used. Corrections for window effects were applied during the measurement. The measurements and subsequent modelling were carried out using CompleteEASE software, version 5.14. Additional descriptions of the models used may be found in the relevant subsequent chapters.

h) *Atomic Force Microscopy (AFM)*

Atomic force microscopy was used to evaluate the surface structure of plasmonic nanoarrays after fabrication and after cleaning with piranha solution to ensure quality control of the samples between different uses.

AFM (or alternatively scanning force microscopy) is a variant technique of scanning probe microscopy in which the interaction force between a probe and surface is measured by observing the deflection of a force-measuring spring (a cantilever) (142, 144, 145). AFM has been proven useful in measuring properties of a variety of non-conducting surfaces and also of biological structures, especially using "soft" techniques.

A typical experimental apparatus for AFM is simply illustrated in figure 2.5. A micro-fabricated cantilever is used as the scanning probe, with a sharp tip fabricated at the end. This tip ultimately limits the resolution of the imaging and can be fabricated down to a sharpness of below 10 nm at the very end. The cantilever is mounted on an electronic controller which is attached to a variable-voltage piezoelectric micropositioner. A laser beam is then reflected off the flat head of the probe out to a position-sensitive photodiode and detector system which is connected to the piezoelectric system – this is a feedback circuit which allows the

micropositioner to react with the changes in voltage detected from the photodiode. To image the desired sample placed on a motorized stage, the cantilever is brought down towards the surface until a voltage selected as a setpoint is detected from the photodiode. At the surface, this represents the cantilever bending once the tip is in contact with the surface, and this changes the laser's reflection onto the photodiode and thus a change in voltage. The setpoint voltage thus determines the set force which acts on the tip from its interaction with the sample. Force is simply given by Hooke's Law:

$$F = -k.x \tag{2.10}$$

where k is the spring constant of the cantilever (determined by its material and thickness) and x is the measured displacement from the normal position. In contact-mode AFM, the voltage setpoint determines the set deflection of the cantilever. This is then drawn across the sample surface over a certain area. When a topographical feature such as a peak or a trough meets the cantilever tip, this invariably results in a change in the cantilever deflection. This changes the reflected angle of the laser and thus the voltage on the photodiode. While the change in deflection can be related to the force and used to measure the topography as a measure of force detected, more commonly on modern instruments the feedback system allows the micropositioner to change the height of the cantilever to keep the deflection constant, thus keeping as close to the set-voltage as possible. The change of the voltage or current in the micropositioner can therefore be mapped across the surface area to give imaging and topography data.

While contact-mode AFM is widely used and accurate, tapping-mode is an alternative that has been found useful for imaging of soft matter and biological samples which are susceptible to damage if the force exerted by a tip in contact is too high and also to preserve the tip sharpness. In this instance, the piezoelectric controller is used to induce a vertical

oscillation into the cantilever with an oscillation frequency close to its point of resonance, thus making it behave as a single harmonic oscillator:

$$x(t) = A \, cos(\omega t + \, \varphi) \tag{2.11}$$

Where A is the amplitude of the displacement of position x, ω is the frequency, t is the time period and φ is the phase of the oscillation. ω is related to the tip's spring constant k:

$$\omega = \sqrt{\frac{k}{m}} \tag{2.12}$$

When the cantilever is brought down to the surface it therefore "taps" the surface rapidly, making short and intermittent contacts. In doing so, surface forces such as Van der Waals interact with the tip and this new force reduces the amplitude of the cantilever's oscillation. This amplitude change can be measured using the laser reflection in much the same way as deflection in contact mode, and so this can be used as the feedback parameter for the micropositioner - the height changes to keep the amplitude constant in order to gain topographical information.

Experimental set-up. AFM measurements were carried out using a Nanoscope Multimode 8 atomic force microscope (Bruker). Measurements were carried out in air under ambient conditions using tapping mode. The probes used were OTESPA-R3 tapping mode cantilevers (Bruker, ~ 300 kHz frequency, 7 nm nominal tip radius). Analysis and processing of the images produced was carried out using Bruker Nanoscope Analysis software (v. 1.5).
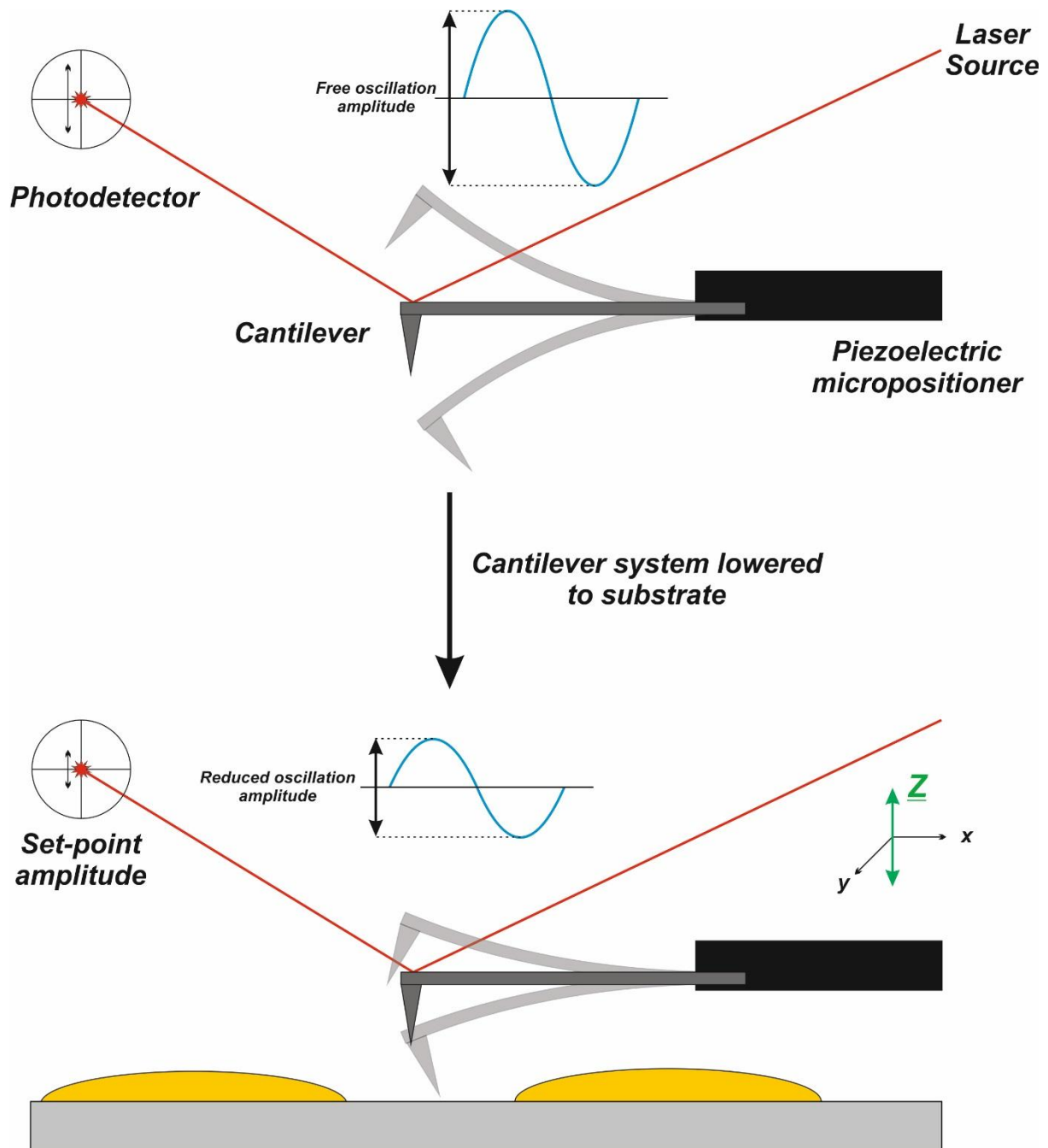
Figure 2.5: In tapping mode AFM, an oscillating cantilever is lowered to the surface until a set oscillation amplitude is detected, measured by a reflected laser beam from the cantilever head. The piezoelectric scanner then draws the tip across the surface. When an obstacle of increasing or decreasing height meets the tip, the resulting change in amplitude causes a feedback circuit to change the height of the scanner in the Z-plane to return to the set-point, thus allowing surface topography to be recorded.

i) *Modelling of the extinction spectra for chlorin-functionalised plasmonic samples*

In order to determine the energies of the exciton states in the bacteriochlorin and chlorophyll derivatives adsorbed to the plasmonic arrays, a model was needed to describe the phenomena and obtain a fit to the experimental extinction data obtained. This model, as explained in the background information provided in chapter 1, is derived from the consideration of the plasmon band and the exciton state in the chlorophylls as coupled harmonic oscillators, with the plasmon acting as the driven oscillator due to its interaction of light to give localised surface plasmon resonance. The construction of the model is given in more detail in previous work with LH2 and 1- and 2-chlorin maquettes adsorbed to these plasmonic arrays, and the considerations and criteria used there were applied here also (116, 129) as derived from Törmä *et al* (123). In simple terms, a model spectrum was overlaid with the experimental data, changing parameters until a close goodness of fit was achieved. For coupled harmonic oscillators with frequency ω the coupling strength is given by g (in units of frequency squared) and the splitting of the two frequency modes is approximate to g/ω. In the extinction spectrum expressed in terms of energy (eV), the energy difference between the two normal modes observed in strong coupling gives the coupling energy E_C. The frequency splitting can therefore be expressed in terms of energy by the converted coupling constant $G = \hbar^2 g$ and the plasmon energy as E_{LSPR}, thus giving $E_C = G/E_{LSPR}$. This can then be related to the exciton energy E_{mol} and the number N of dipoles present:

$$E_C \cong \sqrt{\frac{\mu^2 E_{mol}^2}{\varepsilon_0 \varepsilon_b E_{LSPR}} \frac{N}{V_{LSPR}}} \tag{2.13}$$

where μ is the transition dipole moment for N dipoles, ε_o is the permittivity of free space, ε_b is the relative permittivity of the background medium (most likely being air) and V_{LSPR} is the

volume of the plasmon mode. For a plasmonic array then E_C should therefore be proportional to the square root of dipoles present in the plasmon mode volume, which may range from approximately 10 to 35 nm. To determine if the coupling was within the strong coupling regime, the normal mode Rabi splitting required E_C to be greater than the linewidths of the two oscillator modes, γ_{lspr} and γ_{mol}:

$$E_C \geq \frac{1}{2} \left(\gamma_{lspr} - \gamma_{mol} \right) \qquad (2.14)$$

In practical terms derived from previous LHC experimentation, the boundary of the strong coupling regime is considered to be $E_C \approx 0.24$ eV (129).

A consideration to bear in mind is that the exact coupling energy is determined by factors which may not be determined precisely with the analysis techniques used here, such as the fine details of the mode structures and the precise orientations of dipoles (especially where it is highly likely a mixture of orientations is present such as in chlorophylls bound to polymer brushes). As these could not be taken into account then the model will only produce an order of magnitude estimate, and therefore this is the level of correlation needed to interpret its closeness to the experimental data observed.

Modelling was calculated using Wolfram Mathmatica software, version 10. The models were constructed and fitted to the obtained extinction spectra by Dr. Anna Lishchuk.

Chapter 3: Synthesis, characterisation and exciton-plasmon interaction of an artificial bacteriochlorin anchored to gold surfaces

1. Introduction

In this chapter, a minimal form of organisation is explored. Instead of assembling pigments in protein scaffold, chlorins can be designed to self-assemble into organised layers, independent of a secondary arranging element. Self-assembled monolayers (SAMs) are a simple form of close-packed organised nanomaterials that can be formed on substrates such as gold and silicon (41). Such assemblies serve as an analogy for the organisation of chlorophylls found in the chlorosomes of green sulfur bacteria, which densely stack in antiparallel arrangements held together by hydroxyl-magnesium ligation (146). With this biologically inspired approach, highly efficient energy transfer may be achieved in these dense surface assemblies using our plasmon-exciton strong coupling system.

In the strong coupling experiments of LH2 with gold nanoparticle arrays (116), bacteriochlorophyll *a* (BChl *a*) is the other major pigment apart from the sphaeroidenone carotenoid which couples to the plasmon field as it has a well-defined Q_x transition dipole which is orientated optimally with the plasmonic field. However, as the total dipole strength of the LH2 complex is dominated by the contribution of the carotenoids, the total contribution of the BChl *a* in strong coupling is unclear. As these are the major pigments used to transport exciton energy across bacterial vesicles, it would thus be beneficial to study bacteriochlorophylls in isolation from the protein matrix and determine if strong coupling can be achieved for close-packed layers of these pigments.

While natural BChl *a* may be extracted from natural photosynthetic bacteria and modified for this purpose, the sensitivity of the molecule to oxidative damage and side-reactions may be synthetically challenging (147 - 151). An alternative strategy however is to utilise an artificial analogue of bacteriochlorophylls which replicates most of the absorption characteristics but without the drawbacks of sensitivity. This also makes it possible to design the molecule from the ground up to incorporate the desired functional groups to allow self-assembly, as well as modifying the characteristics of the exciton transitions of the molecule. This provides an opportunity to make a tailored bacteriochlorin with properties not found in nature which may be exploited for our plasmon-exciton energy transport system.

a) *Synthesis and functionality of artificial bacteriochlorophyll-type molecules*

For several decades, the production of bacteriochlorins entailed the reduction of the alkene groups of porphyrins using *in-situ* generated diimide as the reducing agent (152, 153). However, there was very poor control over these reactions, producing both bacteriochlorins and chlorins which were difficult to separate chemically with very low yield. The total organic synthesis of bacteriochlorins however was developed more recently. Jonathan Lindsay's group for several years has produced *de novo* synthetic routes for a range of stable bacteriochlorins incorporating multiple functional groups from simple organic molecules (154, 155). The most significant characteristic of these bacteriochlorins is the incorporation of dialkyl groups at the C8 and C18 positions by the reduced bonds – this protects these positions from the dehydrogenation mechanism and so prevents conversion to the corresponding chlorin or porphyrin. Their absorption spectrum is also very characteristic of this class of molecules, with well-defined Q_x and Q_y absorption bands. This has been shown to be tunable depending on the incorporated substituents. This method therefore not only allows synthesis of stable bacteriochlorins of practical use, but also the tuning of absorption

possible can be used to access the near-infrared spectral region for the purposes of artificial photosynthesis or photo-medicinal applications (156).

Generally, this synthesis is summarised by the formation of a pyrrole incorporating the functional groups that are to be included in the final bacteriochlorin, followed by multiple chemical reactions to form a functional dihydropyrrin (155). This is then capable of undergoing an acid-catalysed self-condensation reaction, where two molecules act as both western and eastern halves and produce the bacteriochlorin, which incorporates two sets of the functional groups present in the beginning pyrrole molecule (figure 3.1).
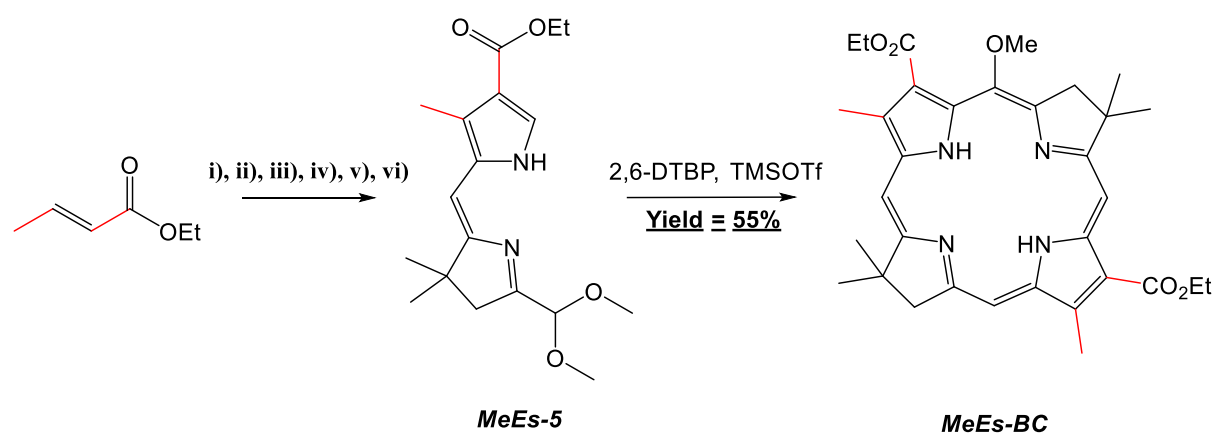
*Figure 3.1: The de novo synthesis for the bacteriochlorin **MeEs-BC** (**MeEs-OMe BC** in the original study) from a simple α, β-unsaturated ester (155). Red bonds indicate the functional groups retained form the initial ester into the final bacteriochlorin product. Reactions i) - vi) are described below and in section 2 of this chapter.*

The synthesis typically begins with a pyrrole incorporating the desired side-groups to be introduced into the bacteriochlorin. These can be commercially sourced or starting from a functional α, β – unsaturated ester. Reaction of these molecules with p-toluenesulfonylmethyl isocyanide (TosMIC) (**i**) in figure 3.1) results in a ring forming reaction across the isocyanide group with loss of p-toluenesulfonic acid to produce the corresponding pyrrole (157). Next, there is a series of transformations to be performed to produce the dihydryopyrrin. A formylation (**ii**)) is performed via a typical Vilsmeier-Haack reaction for aromatic compounds

using phosphorous oxychloride and dimethylformamide. A two-step reaction (**iii)**) is next –

condensation of the carboxaldehyde group with excess nitromethane produces a 2-(2-

nitrovinyl)pyrrole followed by a necessary reduction of the alkene using lithium borohydride

to give the nitroethylpyrrole. This can then undergo Michael addition (**v)**) with 11-

dimethoxy-4-methyl-penten-2-one (synthesised in a parallel reaction (**iv)**). This Michael

addition is important for three reasons – it enables another ring closing to form the

dihydropyrrin, the included dimethoxy group is required for the eventual self-condensation

reaction, and this also introduces the alkyl groups which protect the end bacteriochlorin

product from dehydrogenation. Finally, a reductive cyclization reaction (**vi)**) is performed

first by treatment with sodium methoxide followed by stirring in a heavily-buffered titanium

trichloride solution under oxygen-free conditions to afford the dihydropyrrin.

The self-condensation of the dihydropyrrin is possible due to its dual electrophilic and

nucleophilic behaviour. The aromatic electrons of the original pyrrole ring acts as a

nucleophile which can attack the electrophilic dimethoxy group of another dihydropyrrin

molecule, but this requires a Lewis acid catalyst to enable formation of the macrocycle

followed by oxidation to form the aromatic system. This is typical of porphyrinic

condensations such as the Rothemund synthesis (158), which is compatible with a wide range

of acids (159). An initial investigation used trifluoroboron etherate, $BF_3.OEt_2$ (154), which

resulted in a mixture of bacteriochlorins either with no substituent (**H-BC**) or a methoxy

group (**MeO-BC**) at the meso position of the cycle. In later work, improvement of this

synthesis with another survey of acid catalysis conditions led to the use of trimethylsilyl

trifluoromethanesulfonate (TMSOTf) with 2,6-di-*tert*-butylpyridine (2,6-DTBP), which

produces only the **MeO-BC** variant at higher yield with no perceptible production of the non-

substituted bacteriochlorin (155).

One primary interest of these artificial bacteriochlorins is their absorption profiles, as this determines their usefulness as analogues for natural bacteriochlorophylls. These analogues have well defined absorption bands for the Soret, Q_x and Q_y transitions (154). Both the Q_x and Q_y bands were both found to vary depending on the substituents included in the original pyrrole (155). In the Q_y especially, it was observed that bacteriochlorins with electron-withdrawing groups such as bromine or ethyl esters red-shifted the absorption closer to the near-infrared region. This feature lends flexibility to this synthetic route as the specific absorption profile desired for an application is accessible by changing the substituents incorporated. In general, the Q absorptions of these compounds are blue-shifted from the absorptions of isolated bacteriochlorophyll a in solution (160).

The potential for chemical modification of the bacteriochlorin once synthesised can make them more functionally useful as new materials. Rigid alkyne tethers terminated in reactive groups can be used for controllable adsorption onto functional surfaces for use as sensitizers (161, 162), while bromine substituents could be utilised to give phenyl, vinyl and acetyl groups (163). The 5 and 15 positions at the top and bottom of the macrocycle can also be utilised. Appended bromines have become useful precursors in producing annulated bacteriochlorins with an extra five- or six-membered ring to produce an analogue which more closely resembles the structure of a naturally occurring bacteriochlorin (164). This molecule, and the six-membered ring variant, showed Q_y absorbances which were close to that shown for bacteriochlorophyll a.

Artificial bacteriochlorins have been studied for their energy transport properties. A brominated bacteriochlorin can be conjugated to an artificial chlorin which incorporates an alkyne, producing a rigid connection which allows the study of energy transfer characteristics between them. Further chemical modification has been utilised modify the relative absorption energies in these dyads, such as metallochlorins (165), addition of extended aromatic dyes

(166), tetraalkyl substituents (167), aryl groups incorporated into the meso positions (168), and conversion to oxobacteriochlorins (169), as well as the tailoring of the hydrodipyrrin precursors (170). Artificial bacteriochlorins can even be bioconjugated to make new artificial protein-chromophore systems.

Recently, introduction of carboxylic acids, N-hydroxysuccinimidyl reactive esters and maleimides, known to bind with protein residues such as amines or sulfhydryl groups, was reported (171). By tailoring some varieties of NHS-bacteriochlorins to be hydrophilic, they were able to bioconjugate to the accessible primary amines of myoglobin. Other modifications have included polar groups for improved solubility in aqueous media for bioconjugation studies (172, 173). Incorporation of these artificial chromophores into biologically-inspired structures is also possible. With a selection of NHS-bacteriochlorins attached to β-peptides and assembled into LH1-type structures, energy transfer approaching 95% efficiency was observed (174). Similar results can be achieved using lipid vesicles as the encapsulating structure, showing that simple organisation without complex protein engineering can give structures with near-saturated transfer efficiency (175). A more complex photosynthetic structure containing several varieties of tetrapyrroles like bilins and chlorins in addition to bacteriochlorins is the closest attempt so far to make a completely synthetic functional light-harvesting complex with interchromophore transfer between different absorbers (176).

The literature thus indicates that not only can artificial chlorophyllous pigments be produced within the desired spectral ranges for potential applications, but also that they can be arranged in mimic structures inspired by photosynthetic complexes that can receive and transfer energy. When immobilising a synthetic bacteriochlorin monolayer on a surface of nanoparticles with a plasmonic field, it is therefore possible that plasmon-exciton coupling resulting in fast energy transfer will be observed. As the arrays in question will be fabricated

from gold substrates, modification must be carried out to incorporate alkanethiol groups for attachment.

b) *Gold-thiol self-assembled monolayers (SAMs), and a strategy for synthesis*

The assembly of thiol molecules on gold substrates is due to the specific affinity of sulfur groups to interact with the gold atoms at the surface-medium interface. For alkanethiols, the most commonly used sulfur-containing groups for this field, an oxidative addition occurs at the substrate with the elimination of hydrogen to form a strong gold-sulfur bond (41):

$$R\text{-}S\text{-}H + Au_n^0 \longrightarrow R\text{-}S^-Au^+. Au_n^0 + \tfrac{1}{2}H_2$$

Alkanethiolates assemble spontaneously on substrates which are immersed in a dilute solution containing the thiol or by lithographic "inking" approaches and can be characterised with surface techniques such as optical ellipsometry, X-ray photoelectron spectroscopy, secondary ion mass spectrometry, scanning probe microscopy, electron microscopy and measurement of water-droplet contact angles (177 - 180).

For typical long chain alkanethiols, the surface assembly has two distinct phases. First, the molecules adsorb onto the substrate from solution. Ellipsometric evidence of substrates immersed at varying time intervals suggests this step begins with initial adsorption of thiols lying flat in plane of the surface followed by a "standing up" phase once more molecules start adsorbing. Up to 90% of the maximum measured thickness can be achieved within a few minutes. Second, organisation of the adsorbates into a crystalline long-range order takes place, mediated by additional adsorption, desorption, expulsion of solvent molecules and rearrangement to reach the maximum packing density for the system. Standard

practice for these systems is to leave a sample immersed for 24 to 48 hours to ensure

complete monolayer formation. Once achieved, the alkanethiols adopt a tilted structure where

the hydrocarbon chains point upwards and the sulfur head group is chemisorbed to the gold

surface (figure 3.2). The tilt of the chains maximises the van der Waals interactions between

the molecules and acts as a stabilising force for the layer, with a $10 – 40^o$ angle depending on

the adsorbate structure (178). Au(111) is the most common substrate used for alkanethiols,

making a simple atomically-rough surface with a rhombic arrangement. Thiols of several

lengths have been adsorbed to these surfaces and examined by scanning tunnelling

microscopy, confirming that their crystalline structure adopts a ($\sqrt{3}$ x $\sqrt{3}$)R30^o orientation

(181).
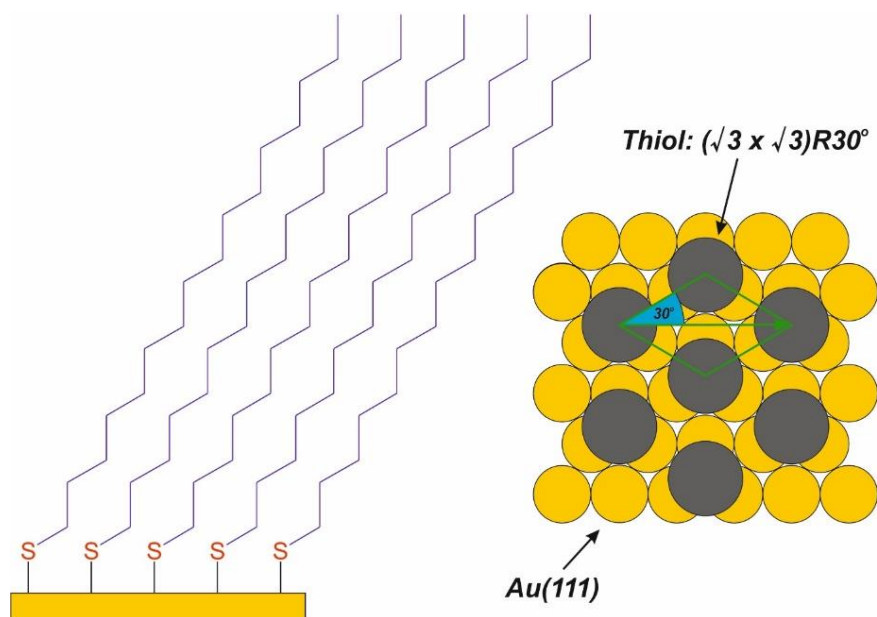
*Figure 3.2: (**Left**) Simple alkanethiols attach to the surface via the sulfur head group (red) with the hydrocarbon "tail" group providing stabilisation by Vane der Waals intermolecular interactions, making a semi-crystalline layer structure. (**Right**) Close-packed thiols on Au(111) substrates adopt a (√3 x √3)R30º unit cell arrangement (42).*

Thiolate SAMs are popular for functionalisation of several forms of gold materials or

other noble metals such as silver. One reason is the large variety of terminating functional

groups which are available, which can be used to make functional surface coatings on metal structures. Goals include changing the surface wetting properties, the design of model biological surfaces for protein and cell analysis, or as a base for surface-based reactions in the fields of molecular recognition or electronics (178, 180). These SAMs are also used to interact with nanostructures, with multiple examples in the literature of monolayers formed on materials such as gold nanoparticles or metallic colloids in solution and on nanorods, wires, quantum dots and nanostructured arrays on substrates. Specifically, SAMs have been used in conjunction with arrays that display LSPR. When successfully adsorbed to the surface of silver nanoparticles for example, the wavelength of the LSPR extinction maximum shifts due to the localised change of refractive index at the gold-medium interface (182). Thiolate SAMS have proven useful as anchoring structures for a plasmonic sensor for biological molecules (183, 184). This was the approach used where LH2 was anchored to gold nanoarrays and displayed strong coupling as a result (116).

Incorporation of a thiol group in a bacteriochlorin would enable it to be attached to the surface. As noted above, Lindsey *et al* produced a very large library of porphyrinic molecules incorporating many groups which are alien to natural chlorophyllous pigments. For a model system analogous to natural BChl *a,* it is best to choose a variant which as closely resembles their physical characteristics as is reasonable. For all the natural bacteriochlorophylls, most of the side groups present are simple hydrocarbons but also with some carboxyl groups present around the ring structure and as a linker for the phytyl tail (1). As such, one of a variety of bacteriochlorins produced in the original *de novo* synthesis route would be suitable (155). In addition, the ester groups incorporated in this way provide a convenient target group for further functionalisation.

Several strategies are available, in principle, for attachment of the bacteriochlorin to the gold surface. Firstly, the hydrocarbon chain length has been identified as a major factor in

the packing density and quality of thiolate monolayers (178, 185). Where assemblies are made of thiols with a carbon chain length of $n \geq 9$, the monolayers achieve their optimum surface density and crystallinity, but where n is lower than this thickness measurements have suggested a disordered structure with poor packing. Using a longer chain of 10 carbons and above would thus be favourable for producing the densest structures of these bacteriochlorins. The other synthetic consideration is the incorporation of the thiol group itself into the structure. Using a thiolated molecule itself in a reaction is inadvisable, due to the propensity of thiols in oxygenated solutions to undergo oxidative reactions over time to produce disulfides or sulfonates (178 - 180). It would therefore be more favourable to only introduce the thiol functionality at the end of the synthesis route just before the assembly experiments are attempted. In this case a thiol protecting group is called for, of which there are several possibilities (186 - 188).

Thioacetate derivatives of thiols can be trivially produced from the nucleophilic addition of potassium thioacetate to an alkyl halide (186). Thioacetates can form thiolate monolayers in contact with gold substrates upon addition of a mild base such as ammonium hydroxide (189 - 194) (figure 3.3). This deprotection results in a thiolate ion which is rapidly protonated by the quaternary ammonium ion in solution, with acetic acid and ammonia as the by-products. The resulting thiol can then react quickly with the gold surface to produce the monolayer. Ellipsometric measurements of surfaces exposed to several thioacetate-derived molecules with addition of NH_4OH gave consistent monolayer thicknesses after several days of immersion compared to their thiol counterparts at the same concentration, suggesting this is a viable method of monolayer formation (189).
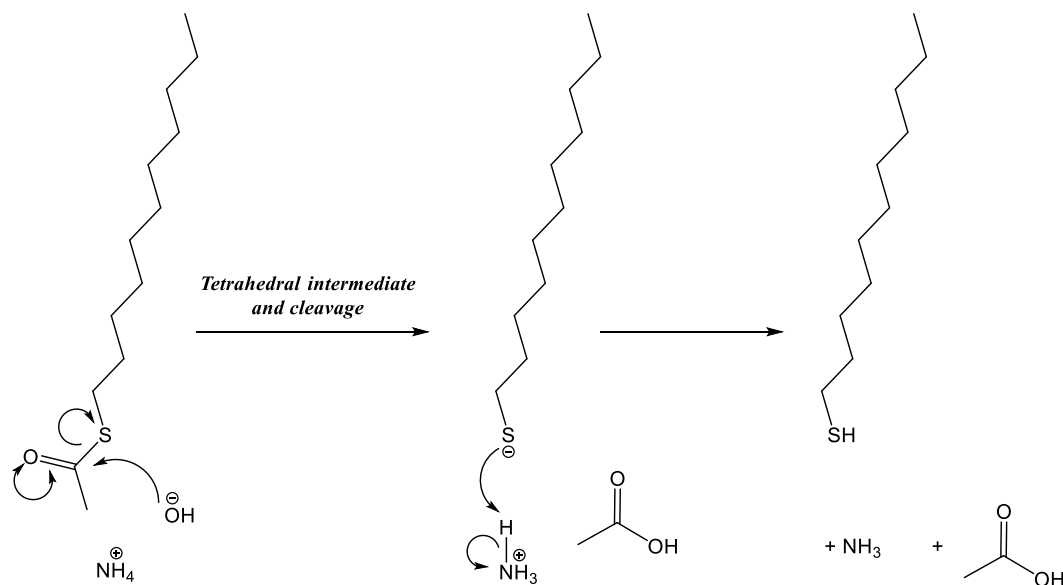
Figure 3.3: The deprotection mechanism of a thioacetate group with ammonium hydroxide, producing a thiol ready for self-assembly (57).

c) *Aims*

The first aim of this chapter is to synthesise a bacteriochlorin molecule which can be self-assembled onto a gold substrate as a self-assembled monolayer, to form close-packed arrays of excitons for studies of strong plasmon-exciton coupling. A previously-known bacteriochlorin, 3,13-bis(ethoxycarbonyl)-5-methoxy-2,8,8,12,18,18-hexamethylbacteriochlorin **(MeEs-BC)** (14), will be synthesized. The ethyl ester groups will be modified to introduce a surface-binding group, by first reducing the ethyl esters to primary alcohols, which will then be coupled to an α, ω-bromoalkyl acyl chloride. The bromine can then be derivatised with sodium thioacetate to give a thioacetyl terminus for the bacteriochlorin, producing a new gold-anchoring molecule **AcS-12C-BC** (figure 3.4). SAM formation of this will be enabled via in-situ cleavage of the thioester in the presence of the gold substrate. The resulting monolayers will be characterised by surface ellipsometry, x-ray photoelectron spectroscopy and secondary ion mass spectrometry. The bacteriochlorins will

then be assembled to arrays of gold nanostructures and the extinction spectra will be obtained

and modelled using a coupled harmonic oscillator model.
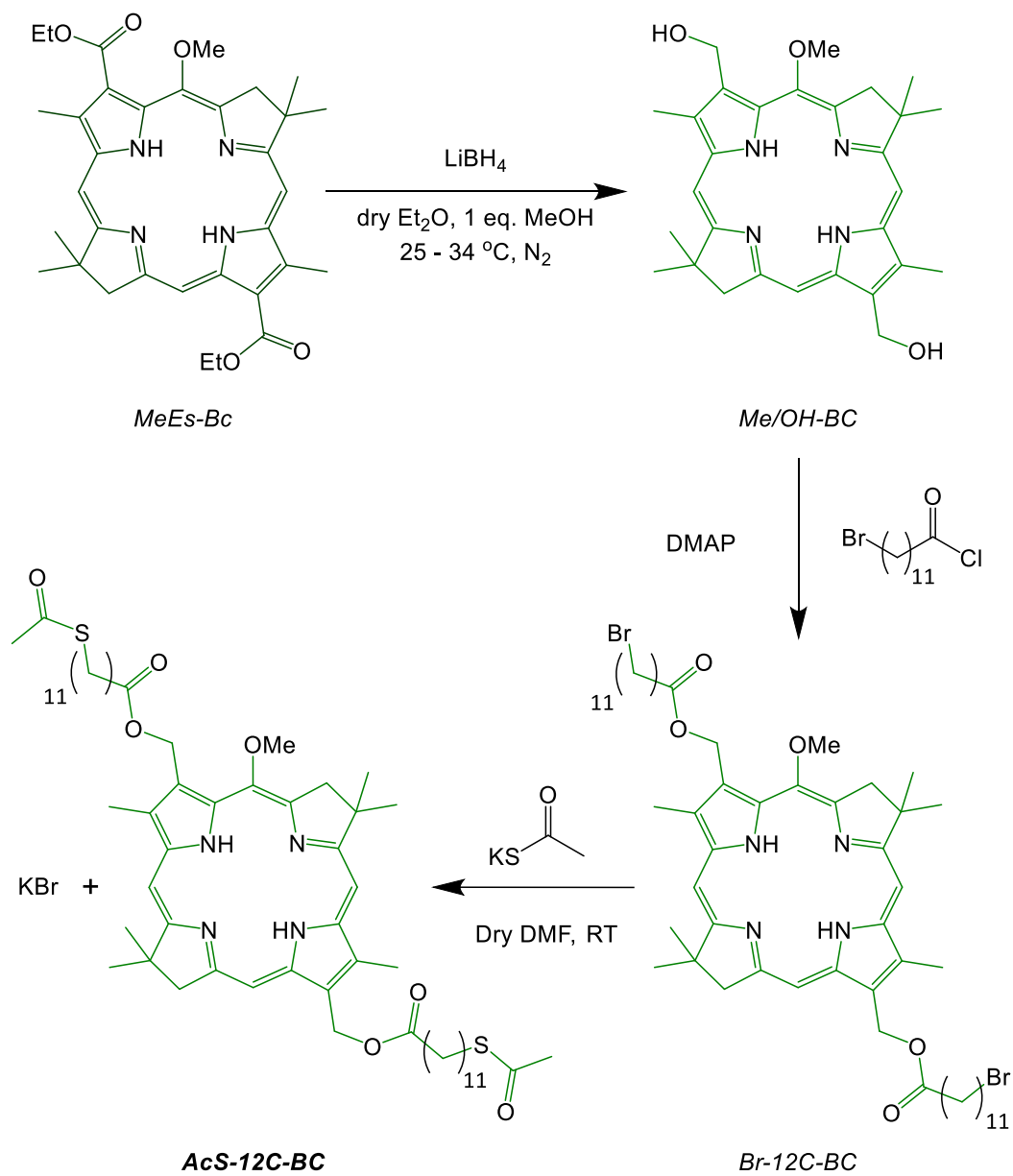
Figure 3.4: The planned synthesis scheme for producing AcS-12C-BC, a bacteriochlorin with thioacetate groups.

2. Experimental Section

a) Synthesis

i. **3-Ethoxycarbonyl-4-methylpyrrole (MeEs-1).** A suspension of sodium hydride (NaH, 60% wt. dispersion in mineral oil, 5.55 g, 139 mmol) under an N_2 atmosphere was prepared in 100 mL of dry Et_2O. A separate solution was then prepared of ethyl trans-2-butenoate (7.9 mL, 64 mmol) and *p*-toluenesulfonylmethyl isocyanide (TosMIC, 12.59 g, 64 mmol) in a 2:1 Et_2O: DMSO mixture (300 mL). This was then added to the NaH suspension dropwise, with attention paid to the effervescence resulting from the reaction. Once all of the reagent solution was added, the reaction mixture was stirred at room temperature for 20 hours. After the reaction was complete an orange suspension resulted. To this, distilled water was added slowly to neutralise the remaining NaH, until no more effervescence was observed (~ 400 -500 mL). The resulting mixture was then extracted with Et_2O (100 mL) and distilled water (3 x 200 mL), followed by washing with saturated brine (200 mL). The organic layer was dried with anhydrous $MgSO_4$, filtered and the solvent was removed by rotary evaporation, affording an orange solid. This product was then dissolved in CH_2Cl_2 and purified by column chromatography (Silica, CH_2Cl_2) to provide an orange-white solid (5.866 g, 38.29 mmol, 60%): ^1H NMR (400 MHz, $CDCl_3$) δ (ppm) = 1.36 (t, J = 7.16 Hz, 3H), 2.31 (s, 3H), 4.29 (q, J = 7.16 Hz, 2H), 6.56 (s, 1H), 7.40 (broad t, 1H), 8.25 (broad s, 1H); ^{13}C NMR (400 MHz, $CDCl_3$) δ (ppm) = 11.72, 14.49, 59.42, 114.78, 117.39, 120.96, 124.44, 165.91; TOF-MS ES+ obsd = 154.1, calcd = 154.1879 [$(M + H)^+$, M = $C_8H_{11}N_1O_2$].

ii. **4-Ethoxycarbonyl-2-formyl-3-methylpyrrole (MeEs-2).** Vilsmeir reagent was first prepared by stirring phosphorous (V) oxychloride ($POCl_3$, 1.6 mL, 17 mmol) in dry DMF (10 mL) at 0 °C for 10 minutes under inert N_2. MeEs-1 (2.217 g, 14.47 mmol) was dissolved in dry DMF (113 mL) and also stirred for 10 minutes at 0 °C. To this solution, the cold Vilsmeir reagent was added dropwise with stirring. After 5 minutes, a thick white precipitate formed in the solution, to which a further 150 mL of DMF was added to facilitate further stirring of the reaction for 1 hour at 0 °C and for 2 hours at room temperature. A 1:1 solution of CH_2Cl_2 and saturated aqueous NaOAc (150 mL) was added and stirred for 1 hour, upon which the precipitate dissolved to produce a clear straw-coloured solution. The organic layer was extracted with CH_2Cl_2 (100 mL) and washed with water (3 x 200 mL), followed once by brine. The organic layer was then dried with $MgSO_4$ and the solvent removed. The crude product was then dissolved in CH_2Cl_2 and purified by column chromatography [silica, 4:1 CH_2Cl_2: EtOAc] to produce a beige solid (2.124 g, 11.72 mmol, 81%): ^{1}H NMR (400 MHz, $CDCl_3$) δ (ppm) = 1.38 (t, J = 7.05 Hz, 3H), 2.62 (s, 3H), 4.33 (q, J = 7.05 Hz, 2H), 7.64 (s, 1H), 9.40 (s, 1H), 9.74 (s, 1H); ^{13}C NMR (400 MHz, $CDCl_3$) δ (ppm) = 9.93, 14.42, 59.99, 117.44, 130.10, 13.51, 133.86, 164.14, 178.37; TOF MS ES+ obsd = 182.1, calcd = 182.1979 [$(M + H)^+$, M = $C_9H_{11}NO_3$].

iii. **4-(Ethoxycarbonyl)-3-methyl-2-(2-nitroethyl)pyrrole (MeEs-3).** MeEs-2 (1.015g, 5.6 mmol) was mixed with methylamine hydrochloride ($CH_3NH_2.HCl$, 0.405 g, 6 mmol) and potassium acetate (KOAc, 0.589 g, 6 mmol) and dissolved in nitromethane (51 mL). This solution was stirred for 3 hours at room temperature until a yellow precipitate was formed. This precipitate was then filtered by vacuum, with washing using ice-cold water followed by ice-cold methanol. This precipitate was then dried under reduced pressure

overnight. The resulting yellow solid was used directly in the next step. This was dissolved in dry THF (68 mL) under N_2 and stirred at 0 °C for 10 minutes. Lithium borohydride ($LiBH_4$, 0.176 g, 8.08 mmol) was added to this solution, upon which some effervescence was observed. Once the solution was calmed it was stirred at 0 °C for 2 hours, after which the solution became pale yellow in colour. Here, saturated aqueous ammonium chloride (NH_4Cl) was added slowly to the reaction to neutralise the unreacted $LiBH_4$. When no more effervescence was observed, the organic layer was extracted with a washing of water (100 mL) followed by separation with saturated brine (100 mL). The organic layer was then dried with $MgSO_4$ and the solvent evaporated. The crude product was purified by column chromatography (silica, 4:1 CH_2Cl_2: EtOAc), resulting in a pale yellow solid (0.492 g, 2.17 mmol, 39%): ^{1}H NMR (400 MHz, $CDCl_3$) δ = 1.35 (t, J = 7.14 Hz, 3H), 2.25 (s, 3H), 3.27 (t, J = 6.42 Hz, 2H), 4.28 (q, J = 7.14 Hz, 2H), 4.55 (t, J = 6.42 Hz, 2H), 7.33 (d, J = 3.18 Hz, 1H), 8.31 (broad s, 1H); ^{13}C NMR (400 MHz, $CDCl_3$) δ (ppm) = 10.11, 14.48, 23.28, 59.45, 74.92, 115.48, 118.08, 123.53, 123.65, 165.33; TOF MS ES+ obsd = 227 .1, calcd = 227.24 [$(M + H)^+$, M = $C_{10}H_{14}N_2O_4$].

iv. **11-Dimethoxy-4-methyl-3-penten-2-one (R4).** Mesityl oxide (6.5 mL = 5.577 g, 56.8 mmol), diphenyl diselenide (1.336 g, 4.28 mmol) and ammonium peroxydisulfate (27.684 g, 121 mmol) were dissolved in MeOH (250 mL) and degassed roughly under cycles of vacuum followed by backfilling with inert N_2. The reaction mixture was then refluxed under an inert atmosphere with an oil bath (T= 74 – 76 °C) with stirring for 24 hours. Upon returning to the reaction, the solution had turned a dark brown colour. Once drawn off the heat and cooled, distilled water (250 mL) was added, and the organic layer was extracted with CH_2Cl_2 (250 mL). The layer was washed three times with water, dried with $MgSO_4$ and the solvent evaporated to give a dark brown oil. Before column

chromatography could be performed, the product was distilled from the oily side products by Kügelrohr distillation (P = 4 mbar, T = 170 – 175 $^{\circ}$C). This resulted in a yellow oil which was purified by column chromatography (silica, 3:1 Hexane: EtOAc) to afford the desired product (1.975 g, 12.48 mmol, 32%). ^{1}H NMR (400 MHz, CDCl$_3$) δ (ppm) = 1.96 (d, J = 1.14 Hz, 3H), 2.21 (d, 1.14 Hz, 3H), 3.42 (s, 6H), 4.49 (s, 1H), 6.37 (qt, J = 1.14 Hz, 1H); ^{13}C NMR (400 MHz, CDCl$_3$) δ (ppm) = 21.16, 28.04, 54.38, 104.4, 119.02, 159.98, 194.06; TOF MS ES+ obsd = 159, calcd = 159.19 [(M + H)$^{+}$, M = C$_8$H$_{14}$O$_3$].

v. **6-(4-Ethoxycarbonyl-3-methylpyrrol-2-yl)-1,1-dimethoxy-4,4-dimethyl-5-nitrohexan-2-one (MeEs-4).** MeEs-3 (0.492 g, 2.17 mmol), R4 (0.704g, 4.45 mmol) and 1,8-diazabicyclo[5.4.0]undec-7-ene (DBU, 1.214 g, 7.97 mmol) were stirred together to form a viscous orange solution. This was stirred without additional solvent for 20 hours. After this time, the solution was diluted with EtOAc (20 mL). The organic components were extracted with distilled water (3 x 50 mL) and saturated brine (50 mL), followed by drying with MgSO$_4$ and rotary evaporation. Subsequent purification by column chromatography (silica, 10:1 CH$_2$Cl$_2$: EtOAc) gave an orange oil which crystallised to an orange solid (0.774 g, 2.01 mmol, 93%). ^{1}H NMR (400 MHz, CDCl$_3$) δ (ppm) = 1.17 (s, 3H), 1.27 (s, 3H), 1.34 (t, J = 7.12 Hz, 3H), 2.23 (s, 3H), 2.64 (m, 1H), 2.78 (m, 1H), 3.02 (dd, J = 2.48 Hz, 1H), 3.30 (d, J = 3.37 Hz, 1H), 3.45, 3.47 (2 x s, 6H), 4.26 (q, 7.12 Hz, 2H), 4.39 (s, 1H), 5.12 (dd, J = 2.41 Hz, 1H), 7.27 (s, 1H), 8.19 (s, 1H); ^{13}C NMR (400 MHz, CDCl$_3$) δ (ppm) = 9.98, 14.48, 21.06, 24.23, 24.32, 24.47, 36.51, 45.03, 55.30, 59.32, 94.12, 104.80, 115.35, 118.25, 123.55, 165.30, 203.78; TOF MS ES+ obsd = 385.2, calcd = 385.4341 [(M + H)+, M = C$_{18}$H$_{28}$N$_2$O$_7$].

vi. **8-Ethoxycarbonyl-1-(1,1-dimethoxymethyl)-3,3,7-trimethyldipyrrin (MeEs-5).**

MeEs-4 (2.287 g, 5.95 mmol) was dissolved in dry THF (30 mL) under argon, to which

sodium methoxide (NaOMe, 25 wt% in MeOH, 3.86 mL, 17.85 mmol) was added and

stirred for 30 minutes at room temperature under argon. This formed a dark brown

solution over the course of the reaction. In a separate flask, ammonium acetate (NH_4OAc,

75.427 g, 978.6 mmol) was dissolved in distilled water (200 mL), followed by THF (150

mL), and degassed with argon for 15 minutes. In a separate flask from this, titanium

trichloride solution (30% $TiCl_3$ in 10% HCl, 18.35 mL, 3.6 mmol) was degassed with

argon for 15 minutes. Once degassed, the $TiCl_3$ reagent was added to the base solution

and further degassing performed for 30 minutes with stirring. After this, the MeEs-4

reagent was added, and the resulting solution was stirred for 15 hours under argon at

room temperature. Once complete, saturated sodium bicarbonate ($NaHCO_3$) was added,

upon which some effervescence was observed. Once enough was added for this to cease,

the organic phase was extracted with EtOAc (200 mL) and washed with distilled water (3

x 200 mL) and then with saturated brine (3 x 200 mL). This was then dried with $MgSO_4$

and the solvent evaporate as before. Purification with column chromatography (silica,

10:1 CH_2Cl_2: EtOAc) gave an orange solid (0.929 g, 2.78 mmol, 47%). ^{1}H NMR (400

MHz, $CDCl_3$) δ (ppm) = 1.25 (s, 6H), 1.37 (t, J = 7.12 Hz, 3H), 2.37 (s, 3H), 2.65 (s, 2H),

3.48 (s, 6H), 4.29 (q, J = 7.12 Hz, 2H), 5.05 (s, 1H), 5.89 (s, 1H), 7.45 (d, J = 2.99 Hz),

10.95 (broad s, 1H); ^{13}C NMR (400 MHz, $CDCl_3$) δ (ppm) = 10.28, 14.25, 29.17, 40.28,

48.27, 54.57, 59.23, 102.59, 104.51, 114.92, 119.35, 124.87, 128.66,159.89, 165.73,

174.63; TOF MS ES+ obsd = 335, calcd = 335.4213 [(M + H)+, M = $C_{18}H_{26}N_2O_4$].

vii. **3,13-Bis(ethoxycarbonyl)-5-methoxy-2,8,8,12,18,18-hexamethylbacteriochlorin**

(MeEs-BC). MeEs-5 (0.163 g, 0.49 mmol) was dissolved in dry CH_2Cl_2 (84 mL) under

argon and stirred. To this was added 2,6-di-tert-butylpyridine (2,6-DTBP, 2.2 mL, 1.87 g, 9.80 mmol) first, followed by trimethylsilyl trifluormethanesulfonate (TMSOTf, 0.45 mL, 0.55 g, 2.48 mmol). Once added a rapid colour change from orange to dark green to black-purple was observed. This solution was stirred at room temperature for 15 hours under argon. Once complete, the solvent was removed by rotary evaporation, with careful flushes and evacuation to remove TMSOTf which was unreacted. The 2,6-DTBP could be removed at this stage by evaporation at high vacuum (4 mbar, $\sim 80\ ^{\circ}$C). The crude product was then purified by column chromatography (silica, CH_2Cl_2) to produce a black-purple solid with a dark green colouration in solution (77 mg, 0.136 mmol, 55%). ^{1}H NMR (400 MHz, CDCl$_3$) δ (ppm) = - 1.84 (broad s, 1H), - 1.58 (broad s, 1H), 1.65 (t, J = 7.16 Hz, 3H), 1.73 (t, J = 7.16 Hz, 3H), 1.95, 1.96 (2 x s, 12H), 3.40 (s, 3H), 3.66 (s, 3H), 4.24 (s, 3H), 4.38 (s, 2H), 4.42 (s, 2H), 4.80 (q, J = 7.16 Hz, 4H), 8.52 (s, 1H), 8.67 (s, 1H), 9.62 (s, 1H); ^{13}C NMR (400 MHz, CDCl$_3$) δ (ppm) = 11.60, 13.37, 14.61, 14.75, 30.96, 31.12, 45.58, 45.88, 47.92, 51.74, 60.75, 61.82, 64.33, 93.68, 95.36, 97.54, 115.2, 124.94, 132.77, 134.77, 134.84, 135.03, 135.35, 135.95, 155.74, 160.52, 167.95, 168.78, 171.46; TOF MS ES+ obsd = 573, calcd = 573.714 [(M +H)+, M = $C_{33}H_{40}N_4O_5$]; UV/Vis λ_{max} (nm) = 354 & 376 (Soret), 518 (Q$_x$), 735 (Q$_y$).

viii. **3,13-Bis(hydroxymethyl)-5-methoxy-2,8,8,12,18,18-hexamethylbacteriochlorin (Me/OH-BC).** MeEs-BC (55 mg, 96 µmol) was mixed with a large excess of LiBH$_4$ (78 mg, 3.6 mmol) under argon, dissolved in dry Et$_2$O (100 mL) and stirred. To this was added an approximate 1 molar equivalent of MeOH with respect to the molar amount of LiBH$_4$ used (0.15 mL, 3.7 mmol), upon which some effervescence was observed. The solution was then stirred under argon for 18 hours at room temperature. Once complete, a green precipitate was observed to have formed on the wall

of the reaction vessel. 3M aqueous HCl was added in drops to neutralise the unreacted

reducing agent, upon which vigorous effervescence was observed and the precipitate

dissolved into the organic layer. Once neutralisation was complete, the organic layer was

extracted with distilled water (100 mL) and washed further with water (3 x 50 mL) and

then with saturated brine (100 mL). The organic layer was then dried with $MgSO_4$

followed by evaporation of the solvent. The crude product was then purified by column

chromatography (4:1 Et_2O: THF) to give a green solid (43 mg, 88 µmol, 91%). ^{1}H NMR

(400 MHz, $CDCl_3$) δ (ppm) = -2.22 (s, 1H), -1.98 (s, 1H), 1.97, 1.99 (2 x s, 12H), 3.44,

3.46 (2 x s, 6H), 4.40 (s, 3H), 4.43, 4.46 (2 x s, 4H), 5.77 (s, 2H), 5.85 (s, 2H), 8.62 (s,

2H), 8.80 (s, 1H); ^{13}C NMR (400 MHz, $CDCl_3$) δ (ppm) = 11.08, 11.18, 23.93, 29.15,

29.24, 30.99, 31.06, 31.20, 45.78, 45.82, 47.77, 51.77, 53.74, 56.39, 57.81, 62.59, 62.61,

64.23, 67.71, 93.70, 93.81, 94.72, 98.46, 100.81, 101.85, 107.40, 107.48, 107.98, 125.55,

127.92, 128.37, 129.52, 130.25, 130.65, 133.39, 134.38, 134.66, 153.00, 154.11, 159.33,

168.47, 168.91; TOF MS ES+ obsd = 489.2, calcd = 489.64 [(M + H)$^+$, M =

$C_{29}H_{36}N_4O_3$].

ix. **3,13-Bis(methyl 12-bromododecanoate)-5-methoxy-2,8,8,12,18,18-hexamethylbacteriochlorin (Br-12C-BC).** 12-Bromododecanoic acid (12-BDDA, 121

mg, 0.43 mmol) was dissolved in dry CH_2Cl_2 (20 mL) under argon, upon which oxalyl

chloride (1 mL, 1.5 g, 11.82 mmol) was added and stirred under argon at room

temperature for 2 hours. Upon completion, the solvent was evaporated along with any

unreacted oxalyl chloride to produce 12-bromododecanoyl chloride (12-BDDC). This

reagent was immediately used once prepared. Next, 4-dimethylaminopyridine (DMAP, 13

mg, 0.11 mmol) was added to the first reagent, and Me/OH-BC (14 mg, 28.7 µmol) was

dissolved with sonication in dry Et_2O (100 mL) under argon and added to the first reagent

via cannula. This mixture was then stirred at room temperature under argon for 16 hours. Once complete the solution was observed to change to a lilac/bright green colouration. Distilled water (100 mL) was then added to extract the organic layer followed by washing with water (50 mL) and then with saturated brine (100 mL). Once dried with $MgSO_4$ and the solvent evaporated, column chromatography (silica, Et_2O) produced a green solid (29 mg, 28.7 µmol, complete conversion). ^1H NMR (400 MHz, $CDCl_3$) δ (ppm) = -1.98 (s, 1H), -1.77 (s, 1H), 1.30 (s, 28H), 1.79 (qt, J = 7.52 Hz, 4H), 1.87 (qt, J = 7.30 Hz, 4H), 1.96, 1.97 (2 x s, 12H), 2.47 (t, J = 7.52 Hz, 4H), 3.42, 3.43, 3.44 (2 x s + 1 x t, J (t) = 7.30 Hz, 10H total), 4.26 (s, 3H), 4.40, 4.41 (2 x s, 4H), 6.28 (s, 2H), 6.48 (s, 2H), 8.57, 8.59 (2 x s, 2H), 8.66 (s, 1H); ^{13}C NMR (400 MHz, $CDCl_3$) δ (ppm) = 1.06, 11.20, 14.23, 22.73, 24.74, 25.09, 25.18, 28.06, 28.12, 28.19, 28.63, 28.71, 28.78, 29.07, 29.13, 29.21, 29.23, 29.28, 29.35, 29.39, 29.42, 29.46, 29.74, 30.33, 30.99, 31.32, 32.74, 32.79, 32.84, 33.83, 34.06, 34.09, 34.13, 34.53, 34.65, 45.58, 45.85, 47.55, 51.98, 57.42, 59.57, 93.70, 93.94, 94.52, 122.70, 123.22, 125.56, 126.10, 127.57, 130.50, 132.70, 135.07, 135.28, 135.83, 153.30, 160.09, 168.44, 169.10, 174.16, 174.31, 178.60; TOF MS ES+ obsd = 1011, calcd = 1011.038 [(M)+, M = $C_{53}H_{78}N_4O_5Br_2$].

x. **3,13-Bis(methyl 12-thioacetyldodecanoate)-5-methoxy-2,8,8,12,18,18-hexamethylbacteriochlorin (AsC-12C-BC).** Br-12C-BC (31 mg, 30.6 µmol) was mixed with potassium thioacetate (KSAc, 62 mg, 0.54 mmol) under argon. The reagents were then mixed in dry DMF (30 mL) and stirred under argon at room temperature for 16 hours. Once complete, the organic layer was extracted with Et_2O (50 mL) and washed with water (5 x 50 mL) to remove the DMF. Once a clear separation between the aqueous and organic layers was achieved the solution was washed once again with saturated brine (50 mL), dried with $MgSO_4$ and the solvent removed by evaporation to result in a green

solid (30 mg, 29.96 µmol, 98%): ^{1}H NMR (400 MHz, CDCl$_3$) δ (ppm) = -1.99 (s, 1H), -1.77 (s, 1H), 1.30 (s, 28H), 1.58 (qt, J = 7.38 Hz, 4H), 1.73 (m, 4H), 1.96, 1.97 (2 x s, 12H), 2.3 (s, 6H), 2.63 (t, J = 7.59 Hz, 4H), 2.88 (t, J = 7.38 Hz, 4H), 3.42, 3.44 (2 x s, 6H), 4.26 (s, 3H), 4.40, 4.41 (2 x s, 4H), 6.28 (s, 2H), 6.48 (s, 2H), 8.57, 8.59 (2 x s, 2H), 8.67 (s, 1H); ^{13}C NMR (400 MHz, CDCl$_3$) δ (ppm) = 1.01, 11.15, 14.10, 19.74, 21.18, 22.69, 24.70, 25.46, 28.79, 28.84, 29.04, 29.08, 29.13, 29.16, 29.31, 29.36, 29.39, 29.42, 29.49, 29.70, 30.33, 30.62, 30.96, 31.26, 31.92, 33.58, 34.52, 34.64, 37.11, 37.46, 42.88, 43.79, 45.82, 48.16, 48.62, 51.98, 57.38, 59.93, 63.75, 64.35, 64.80, 66.79, 93.66, 125.50, 129.90, 132.58; TOF MS ES+ obsd = 1001.3, calcd = 1001.452 [(M)+, M = C$_{57}$H$_{84}$N$_4$O$_7$S$_2$]; UV/Vis (nm) (DMF, 50 µM) = 352 & 374 (Soret), 505 (Q_x), 723 (Q_y); HPLC (30 min, 60 – 100% THF in H$_2$O over 20 min, detection = 350 nm) = 10.8 min, 99.1%.

b) Formation of self-assembled monolayers and multilayers of AcS-12C-BC

xi. **Self-Assembly of AcS-12C-BC monolayers on gold substrates.** Samples of prepared Au/Cr substrates were cut into 5 x 5 mm squares and placed in Eppendorf tubes. AcS-12C-BC solutions was typically made to 1 mM concentrations in a separate flask with argon-degassed 1:1 CH$_2$Cl$_2$: EtOH as the solvent mixture. To each sample, the AcS-12C-BC solution was added (0.3 mL, 3 x 10^{-7} mol). To this, degassed aqueous NH$_4$OH (0.05 mL) was added followed by agitation of the sample to effectively mix the solutions. The resulting mixtures were then stored at 4 °C in excess of 48 hours to allow for monolayer assembly. Once assembly was completed for the required time and analysis was needed,

the samples were removed from solution and rinsed three times with CH_2Cl_2 and three times with EtOH to ensure any physisorbed multilayers were removed from the sample surface, followed by drying with a stream of N_2. Samples functionalised with mercaptoundecanoic acid (MUA, 2 mM in EtOH) were also prepared as analysis references. Surface analysis on these monolayers were carried out by XPS, SIMS and ellipsometry techniques as described in chapter 2.

xii. **Adsorption Isotherm study for AcS-12C-BC.** Sample substrates were prepared as before as 5 x 5 mm squares. Two sets of measurements were carried out – Set 1 was measured by ellipsometry while Set 2 was measured by XPS. In Set 1, 20 samples were functionalised with AcS-12C-BC solution at varying concentrations and split into two sets of 12 for adsorption of two separate time periods – 8 samples for 2 hours and 12 samples for 65 hours. Once complete, the samples were rinsed with CH_2Cl_2 and EtOH as before and placed in argon-degassed EtOH for storage immediately before ellipsometric analysis. In Set 2, two sets of 8 samples were adsorbed for 48 hours and washed in the same way before XPS analysis. Tables of the concentrations used and measured parameters may be found in **Appendix 1 ii)**.

xiii. **Self-assembly of AcS-12C-BC monolayers on plasmonic nanoarrays.** Nanoarrays which had been used in previous studies of strong coupling with LH2 proteins were selected for coupling studies with AcS-12C-BC. The arrays were piranha-cleaned as described in chapter two before use and examined with AFM and UV/Vis spectroscopy (**Appendix 3 i)**). AcS-12C-BC solutions were prepared to 1 mM concentrations in argon-degassed 1:1 EtOH: CH_2Cl_2. The samples were then immersed in this solution (1 mL), followed by addition of NH_4OH (0.05 mL) and agitation to mix the solution. After 48

hours, the samples were washed with three washings of CH_2Cl_2 and three washing of EtOH followed by drying with nitrogen. These samples were then measured with UV/Vis spectroscopy and ellipsometry.

For samples with physisorbed layers, the arrays used were immersed in 2 mM solutions of AcS-12C-BC with 0.05 mL of NH_4OH added as before. These were left in the solutions for 120 hours before measurement. The samples were lightly washed with CH_2Cl_2 and EtOH just before measurement by UV/Vis absorption spectroscopy.

3. Results and discussion

a) Synthesis of AcS-12C-BC

i. De Novo synthesis of MeEs-BC

The *De Novo* synthesis of the central bacteriochlorin (illustrated in figure 3.5) was carried out by the same method developed by Lindsey *et al* to produce stable and multivariant bacteriochlorins (155). Here, the ethyl ester-substituted variant MeEs-BC was used, primarily as the esters provided the best incorporated functional groups which could be modified immediately after the central synthesis with the minimal amount of interference of the macrocycle structure possible, which would also have a large effect on the absorbance properties. Another factor is that the other substituents are mostly methyl carbon groups apart from the methyl ether on the top of the cycle – with their unreactive nature, it was felt that these groups would a) have minimal interference on reactivity at the later stages and b) would provide as close a model to the natural bacteriochlorophyll as possible with this synthesis
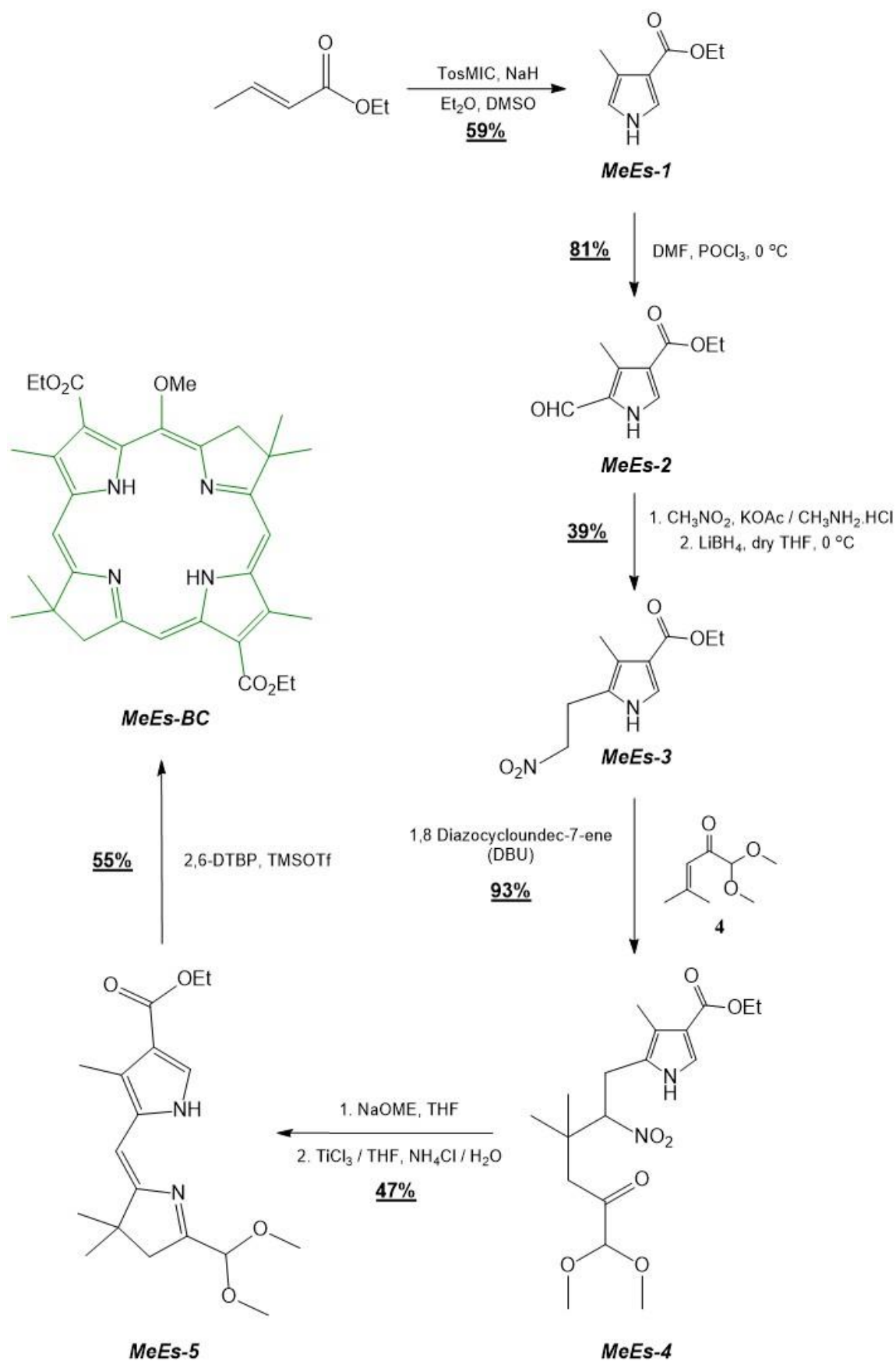
*Figure 3.5: The De Novo synthesis scheme for producing **MeEs-BC**.*

route. All synthesis steps, observations, product yields and characterisation were very similar as described in the previous report. One modification was made to the published method. In the previously published procedure, solid $TiCl_3$ and NH_4Cl solution was used as the buffer solution for the production of MeEs-5 from MeEs-4. This was not only cumbersome here, as the high reactivity of $TiCl_3$ with oxygen required handling in an inert atmosphere of nitrogen or argon, but the degassing requirements and pH balancing with the buffer solution were difficult to achieve. As such, for a typical reaction here only a 15% yield was achieved. The pH requirements are particularly important for the purported reaction mechanism to occur successfully (195). When the pH is almost neutral the ring-closing reaction is thought to occur due to a reduction in the rate of tautomerism of the nitroso group generated by the $TiCl_3$ catalyst, but at low pH a rapid tautomerism to form an oxime group results in reduction to a ketone. As $TiCl_3$ in aqueous solution has an equilibrium of HCl formation and more is produced when more catalyst reacts, tight control of pH is necessary with a buffer solution to maintain the pH above 6 during the reaction. As an alternative method, using stabilised $TiCl_3$ solution in an HCl solution buffered with aqueous NH_4OAc prepared with guidance from a later study by the Lindsey group (196) gave much better results – using 200 molar equivalents or more of NH_4OAc helped much to stabilise the pH at 6 throughout the reaction. The solution mixtures were also much easier to degas with argon using this method, where introduction before and after mixing helped to effectively eliminate oxygen from the reaction. A reaction yield of 47% was as achieved here, which helped to alleviate a bottleneck in the production of reasonable amounts of MeEs-BC for further work.

ii. *Modification of MeEs-BC to produce AcS-12C-BC*

For the incorporation of new chemical groups into the resulting bacteriochlorin, a reduction of the starting esters followed by reconstitution of new ester linkages was

performed to add long functional chains. At first however, there were attempts to convert the ethyl esters to the respective carboxylic acids in order to make them receptive to carbodiimide-mediated coupling with amines. An attempt at hydrolysis in THF using aqueous LiOH resulted in no change to the starting MeEs-BC, even with the addition of tetrabutylammonium bromide as a phase transfer agent, indicating that there was little driving force for the reaction (the pKa of ethyl alkoxides and hydroxides of leaving groups is almost identical). Alternatives were tried using other agents, namely lanthanum triflate, which has been used for direct amidation of ethyl esters in the literature at high yields (197), and potassium trimethylsilanolate which has been reported to capture the ethyl group from the ester and produce the carboxylate salt (198). Both approaches however also only produced the original bacteriochlorin as well as unidentifiable side-products (possibly degradation products due to oxidation).

It became apparent that hydrolysing the ethyl ester was impractical. Instead of preserving the original carboxyl group on MeEs-BC as a linker, the new molecule to be introduced was selected to provide the linking ester group. The most efficient method for this was to reduce the esters on MeEs-BC to primary alcohols and then react this with a molecule with a highly reactive carboxyl nucleophile, i.e. an acyl halide. For the reduction (figure 3.6), LiBH$_4$ was used as a standard reducing agent for esters in dry Et$_2$O under argon. On its own however LiBH$_4$ did not reduce the ester groups effectively at room temperature or when heated in Et$_2$O, as observed during the synthesis of MeEs-3. Significant enhancement of these reductions has been reported in the past where 1 molar equivalent of MeOH with respect to LiBH$_4$ was added as a catalyst (199), and here this resulted in a more rapid and visible reduction. The reaction was completed at room temperature over an extended period under argon (typically over 16 hours) but can be completed at reflux temperature (~35 $^\text{O}$C) in 2-4 hours. However, it was found that refluxing the mixture can result in a side reaction which

gives an unknown bacteriochlorin product with a mass of 456 g.mol^{-1} that does not react in the subsequent coupling step. The room temperature reaction was thus preferred as it gave a reasonable yield of the expected reduced bacteriochlorin Me/OH-BC. The resulting product was fairly straightforward to characterise. The ^{1}H NMR peaks at 1.65, 1.73 and 4.79 ppm corresponding to the ethyl ester protons in MeEs-BC disappear in Me/OH-BC while the shielded pyrrole nitrogen protons at -1.58 and -1.84 are further shielded, likely due to the reduced electron-withdrawing effect on the ring system by the removal of the esters. The colour of the molecule also became a much lighter green than observed in the original, indicating the esters had a large effect on the absorption profile of the bacteriochlorin.
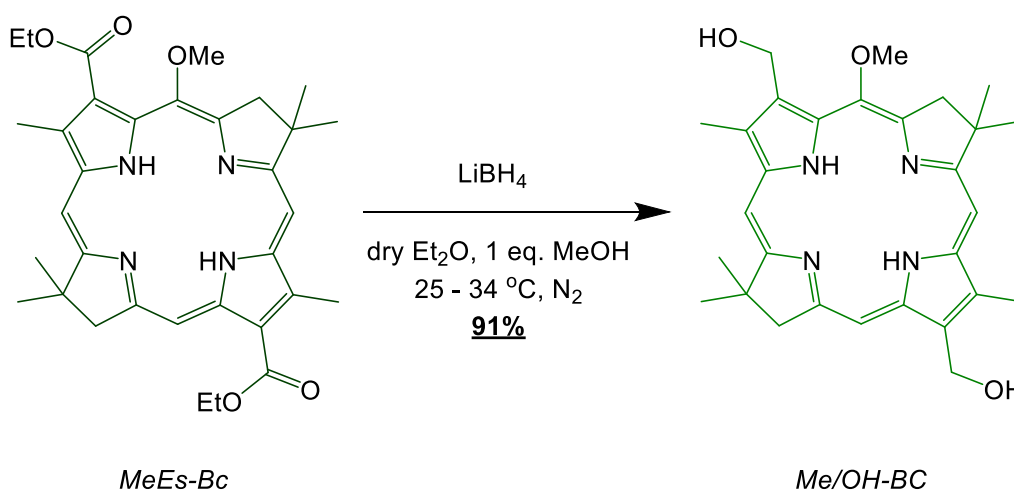
*Figure 3.6: The conversion of **MeEs-BC to Me/OH-BC**, bearing reactive primary alcohols.*

The coupling was then carried out by converting 12-BDDA to the corresponding acyl chloride by stirring with an excess of oxalyl chloride, in a standard acylation reaction, followed by the immediate reaction of this to Me/OH-BC to give Br-12C-BC (figure 3.7). Upon completion and purification, ^{1}H NMR examination confirmed another shift in the nitrogen protons but this time in a deshielded direction due to the reintroduction of the esters, albeit now separated from the macrocycle by one carbon. In addition, a large peak appears at

1.30 ppm, which can be attributed to a large number of the alkyl protons in the hydrocarbon chain, along with the appearance of the more deshielded protons adjacent to the electronegative bromine and ester groups. In combination with the mass spectrum obtained of m/z = 1011, the analysis indicates that the reaction results in substitution of both alcohols with the equivalent of two molecules of 12-BDDA being attached to the bacteriochlorin. The peripheral methoxy group on the macrocycle therefore does not appear to provide steric hindrance for the coupling on the same side.
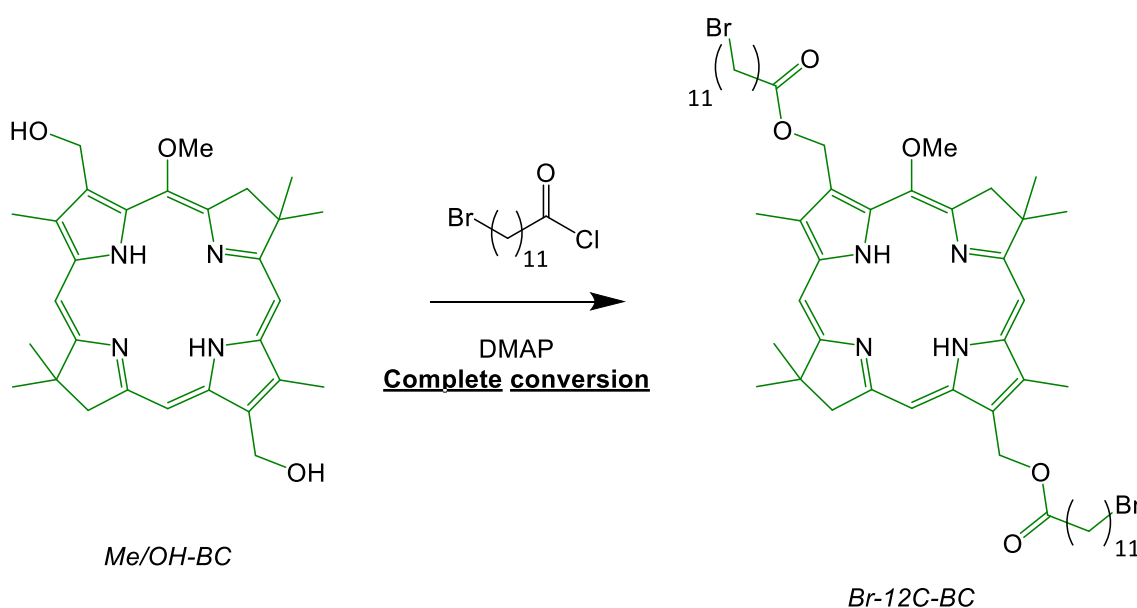
*Figure 3.7: The conversion of **Me/OH-BC** to **Br-12C-BC**, incorporating long-chain bromoalkyl side-chains to the bacteriochlorin.*

For the final step, the incorporated bromine was the target to be converted to a thioacetyl terminating group as a protecting group for the thiol moiety capable of attachment to gold surfaces (figure 3.8). Here, KSAc in DMF was used as the coupling agent (186) in excess to ensure as complete a reaction as possible, with an argon atmosphere to ensure no sulfur oxidation during this step. Typically, this results in the thioacetate replacing the bromide in a nucleophilic substitution with the bromide leaving group forming the KBr salt which can easily be separated from the organic layer by water washing. In the analysis, a

reduction in mass to m/z = 1001 suggests that both bromides were substituted with the lighter thioesters, while a new ^{1}H NMR peak at 2.35 ppm conforms to the protons associated with the thioacetyl group. At this stage, no further synthesis was strictly required, as the thioacetate moiety has been used in surface attachment studies with a suitable deprotecting agent such as ammonium hydroxide. Cleaving of these groups to form thiols was attempted at first using aqueous NaOH as described (186). However, for this molecule this deprotection method proved difficult, and either there was no reaction observed following careful neutralisation or, when a larger amount of base was used, a rapid colour change was observed to orange or pink accompanied by heat generation. Analysis revealed the isolated products in the latter case contained no bacteriochlorin and contained a mixture of unidentified mass fragments. This may suggest that there was some oxidative damage which broke apart the macrocycle structure, which is possible given the vulnerability of natural chlorophylls to oxidation. However, as a surface-anchoring group had now been incorporated, the cleavage of the thioester was determined to be best carried out in-situ using a mild-deprotection protocol which has been previously shown to produce monolayer systems.
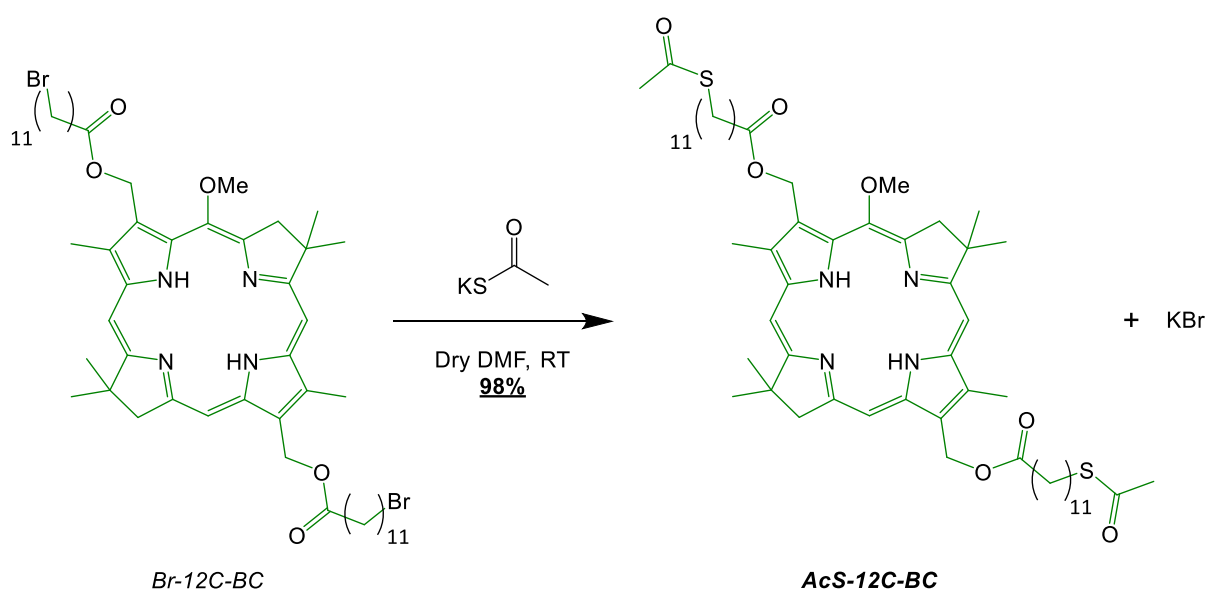
*Figure 3.8: The conversion of **Br-12C-BC** to **AcS-12C-BC**, incorporating thioacetyl groups to the long-chain substituents as groups capable of anchoring to gold substrates.*

iii.   *Absorption spectrum of AcS-12C-BC*

For additional characterisation of the final AcS-12C-BC molecule, a UV/Vis absorption measurement was taken in dimethylformamide (figure 3.9). The spectrum characteristics are very similar to what would be expected for a bacteriochlorophyll with a prominent split Soret band and distinguished Q_x and Q_y bands. In terms of the absorbance maxima compared to the original MeEs-BC molecule (14), there is a clear blue-shift of the Q_x and Q_y bands from 519 to 505 nm and 738 to 723 nm respectively. This would be very likely to be due to the change of functional group during the synthesis, and probably due to the repositioning of the ester group further from the macrocycle by one carbon and reducing its effect on the electronic structure. Apart from this, this measurement also gave additional confirmation that the final product is still a bacteriochlorophyll-type molecule.
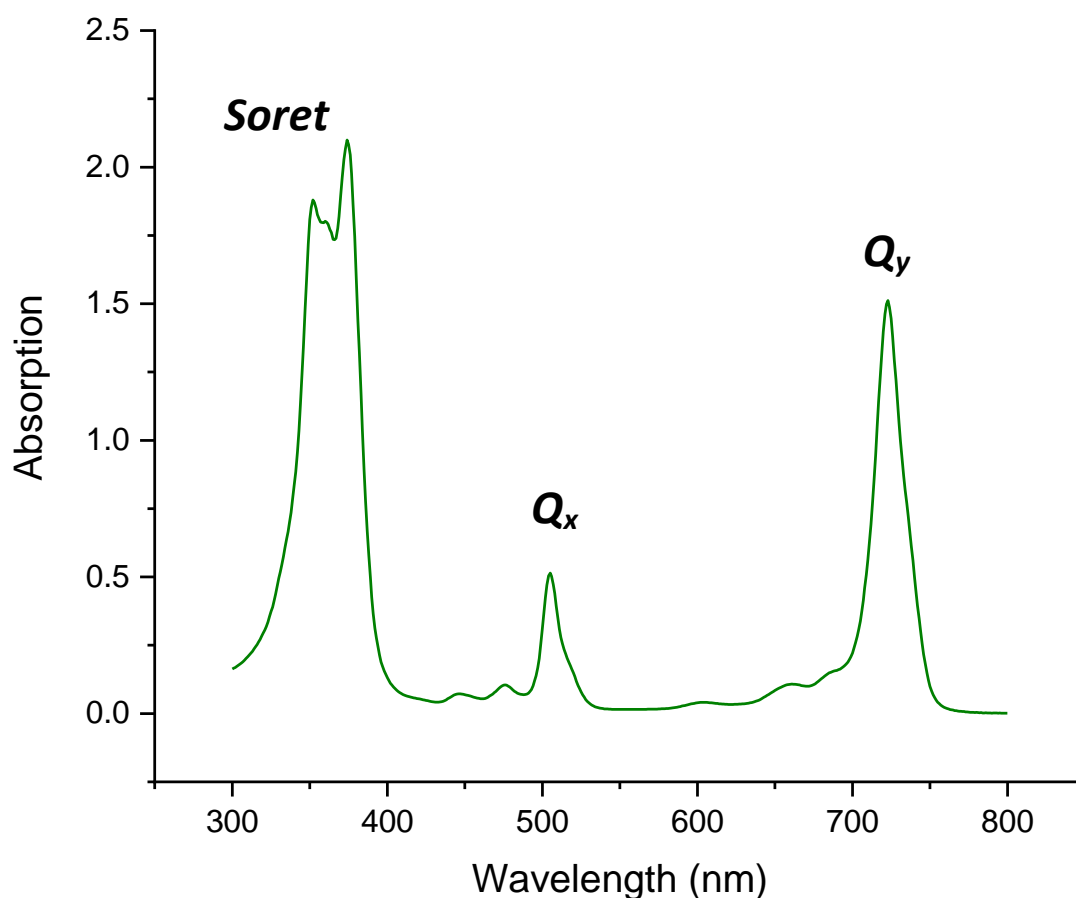
Figure 3.9: The UV/Vis absorptions spectrum for AcS-12C-BC at a 50 µM concentration in DMF.

From this spectrum, the approximate values for the transition dipole moments of the Q_x and Q_y bands were calculated. The dipole strength for a peak across a wavelength range $\Delta\lambda$ can be related to the absorption coefficient of the analyte and the refractive index of the solvent medium by (200):

$$D(n)^2 \ (debye^2) = 9.186 \text{ x } 10^{-3}n \ \int \frac{\varepsilon\,(\lambda)}{\lambda} \,.\, d\lambda \qquad (3.1)$$

For this absorption profile however, the vibronic sub-bands adjacent to the absorption bands may lead to an underestimation of the integrated area of the peaks and thus the dipole strength. The approximation was therefore used accounting for the maximum absorption coefficient and the full width half maximum δ of the peak:

$$D(n)^2 \sim 9.19 \text{ x } 10^{-3}n \left(2.13 \text{ x } \frac{\varepsilon_{max}\delta}{\lambda_{max}}\right) = 1.96 \text{ x } 10^{-2}n \left(\frac{\varepsilon_{max}\delta}{\lambda_{max}}\right) \qquad (3.2)$$

For the molecule dissolved in DMF ($n = 1.4305$) to a concentration of 50 µM, the Q_y band with $\varepsilon_{max} = 30237.6$ dm^3.mol^{-1}.cm^{-1} and $\delta = 22.39$ nm has an approximate dipole strength of 26.26 D^2 giving a transition dipole moment of 5.12 D. This is at least in the correct order of magnitude compared to the calculated strengths for the chlorophylls but is less than the values obtained for bacteriochlorophylls a and b (201). The Q_x dipole strength was also obtained from the spectrum to be approximately 7.83 D^2 ($\varepsilon_{max} = 10290.4$ dm^3.mol^{-1}.cm^{-1}, $\delta = 13.7$ nm) giving the transition dipole moment as 2.80 D. This is in the correct order of magnitude for Q_x dipoles, which can differ in the literature depending on the calculation method (126, 201, 202).

iv.   Summary

Overall, this synthesis provides a route which can be used to derive functional bacteriochlorins from a simple unsaturated ester for surface studies by modification using relatively simple chemistry. As far as our knowledge goes at the time of writing, the esters of this bacteriochlorin had not been exploited as potentially reactive groups for further synthesis. Here, the first known incorporation of the thiol moiety into these types of artificial bacteriochlorins is reported. This shows that a) these molecules can be synthetically flexible to enough to be given new functionality beyond photosensitizer studies and b) interaction with gold or other potential metal-based substrates raises the prospect of the use of the molecules in conductance, plasmonic and optical materials and devices. Because the synthesis involves multiple steps, the yield of MeEs-BC is only a few hundred milligrams from a multigram starting mass of the unsaturated ester. However, this can be ameliorated by appropriate scaling of the reactions (which is made easier in step 5 by using liquid buffered TiCl$_3$ solution) and the subsequent reactive modifications to MeEs-BC are all high yielding, allowing a large proportion of the new pigment to be fully functionalised for our purposes. UV/Vis characterisation also confirms the absorption properties of the new molecule including the approximate dipole strengths of the Q_y and Q_x bands, which will play a role in the strength of coupling with surface plasmons.

## b) *Surface characterisation of AcS-12C-BC monolayers*

i.   Potential models of the assembly of AcS-12C-BC monolayers

To produce monolayers of AcS-12C-BC, solutions of AcS-12C-BC were made, to which evaporated thin-film gold substrates were introduced. To activate the thiol-gold reaction, NH$_4$OH was added as the cleavage agent for the thioester as used before in the

earlier literature (189 – 194). At least 48 hours was given for the monolayer formation to allow for the optimisation of organisation between the molecules in the layer.

Two aspects of the AcS-12C-BC molecule may affect the organisation of its monolayers in contrast to simpler alkyl monolayer systems. The first is the large planar dimensions of the central bacteriochlorin, which can measure 8.5 Å along the longest dimension (using a simple optimised 3D model). This means that the molecules, if stacked face-to-face like the chlorophylls in bacterial chlorosomes, may not organise as effectively in the planar direction. It is likely that this will result in a lower density of molecules across the surface than densely-packed alkanethiol monolayers. The second is the bifunctional nature of the molecule, with two thioacetyl groups appended to either end of the bacteriochlorin as a consequence of the synthesis method. With the cleavage of these groups, this gives two possible binding modes where one (monodentate) or two (bidentate) of the thiols may react with the substrate (figure 3.10). This may also affect organisation along the planar direction.

Including two thioacetate groups into the molecule was a consequence of the synthesis method that was initially chosen, as the self-condensation resulted in two identical set of functional groups on the macrocycle. It was therefore expected that the ester group would not provide the steric hindrance for any large degree of preferential derivatisation of one ester group over the other. This however does confer a benefit with this molecule – if one thioacetate is bound to the surface while the other is free to form a surface terminus, this presents another reactive group to which new molecules may be attached. There is therefore some potential to create three-dimensional hierarchical structures of bacteriochlorins. However, this is dependent on the binding mode of the molecule to the substrate. At a first glance of the molecular structure, it is not obvious which binding mode would be preferred. In the ideal case, a monodentate attachment may be preferred to afford a slightly greater packing density, as the large alkyl chains and their ester linkages would be less likely to

extend further from the planar dimension of the central macrocycle. To give some insight into this as well as general chemical characterisation of the assembled AcS-12C-BC molecules on the surface, x-ray photoelectron spectroscopy, secondary ion mass spectrometry and ellipsometry were employed. Elemental and layer thickness analysis would be especially beneficial to give an indication of the likely assembly mode of the monolayer. For a monodentate-bound molecule, XPS analysis would give an indication of any terminal thiol or thioacetate groups, while ellipsometry would show a layer thickness which is approximate to the ideal end-to-end dimensions.
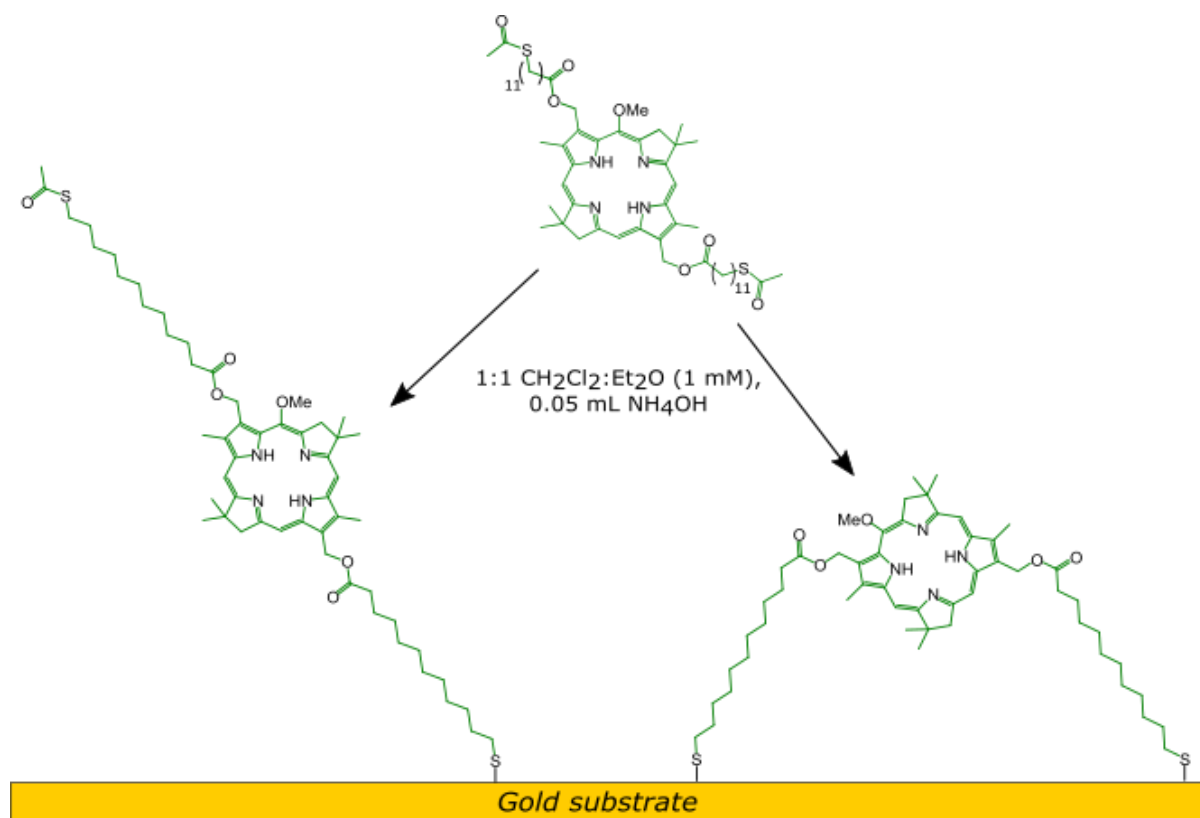
*Figure 3.10: Attachment of AcS-12C-BC to the gold substrate may occur either in a monodentate **(left)** or a bidentate **(right)** fashion.*

ii. X-Ray Photoelectron Spectroscopy

The XPS spectra of the C 1s, N1s, S 2p and O 1s regions for AcS-12C-BC adsorbed to a gold substrate, via mild cleavage of the thioacetyl group, are shown in figure 3.11. A summary of the compositional analysis of each region is given in table 1.
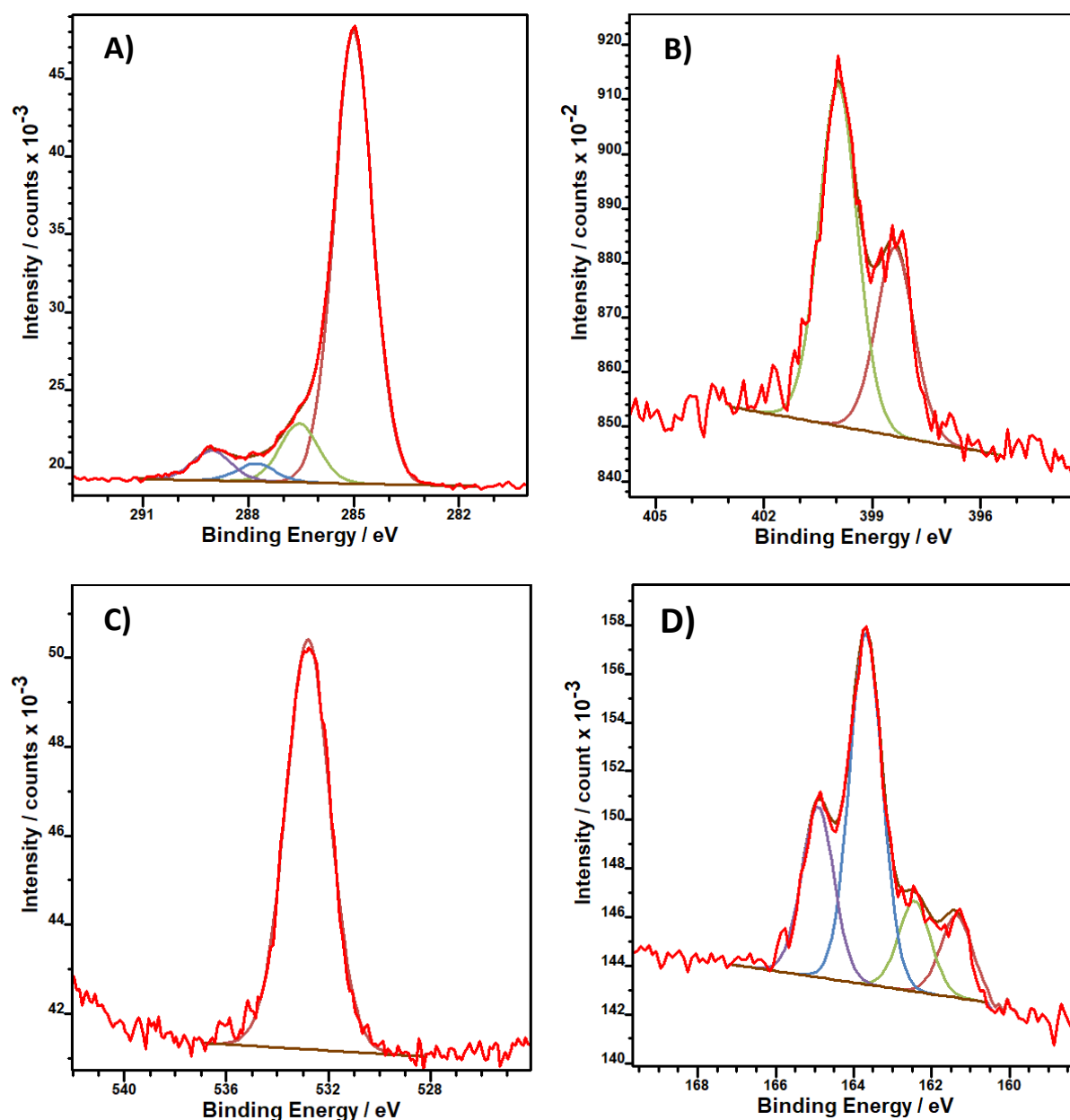
*Figure 3.11: XPS narrow spectra for the **A)** C 1s, **B)** S 2p, **C)** N 1s and **D)** O 1s regions for AcS-12C-BC adsorbed to a gold substrate.*

Table 1: XPS narrow spectra peak assignments for AcS-12C-BC monolayers adsorbed to a gold substrate.

Functional Group	Binding Energy (eV)	FWHM	% Total Area
S 2p			
C-<u>S</u>-Au	161.4, 162.4	0.96	11.91, 13.02
C-<u>S</u>-OAc	163.7, 164.9	0.96	50.52, 24.55
C 1s			
<u>C</u>-C, <u>C</u>-S, <u>C</u>-N	285.0	1.29	81.00
C-<u>C</u>-O	286.5	1.29	10.49
O=<u>C</u>-S	287.8	1.29	3.17
O=<u>C</u>-O	289.0	1.29	5.34
N 1s			
C=<u>N</u>-C	398.4	1.24	35.67
C-<u>NH</u>-C	400.0	1.24	64.33
O 1s			
C-<u>O</u>, C=<u>O</u>	532.8	2.04	100

In the C 1s region the optimal fitting of the lineshape produces four components. The peak at 285 eV shows contributions from the hydrocarbons of the macrocycle and the long-chain substituents at either side. The fitting did not include a separate component for C-<u>C</u>-S however, because this has a chemical shift of only 0.3 eV and so cannot be resolved from the main hydrocarbon peak. The C-<u>C</u>-N and C-<u>C</u>=N bonds associated with the central nitrogen atoms of the bacteriochlorin also could not be resolved as they are part of the aromatic system – evidence in the literature for related porphyrin structures suggests that the additional electron density reduces the chemical shift from the main peak (203). The peaks found at 286.5 and 289 eV correspond to the C-<u>C</u>-O and -O-<u>C</u>=O bond environments respectively. The C-<u>C</u>-O/O-<u>C</u>=O ratio is ~ 2, consistent with the expected ratio of 4:2 based on the bacteriochlorin structure. In addition, a peak is observed at 287.7 eV. This is usually the

region occupied by ketone groups, but here it can be assigned to a thioacetate group as sulfur's lack of electronegativity does not produce a shift as large as seen for the ester groups. A binding energy of 288.2 eV was reported previously for thioacetate-terminated monolayers on silicon (204). The peak area for this component is ~0.5 times that of the O-$\underline{C}$=O component ~ 0.25 times that of the C-$\underline{C}$-O component. This indicates that there is one less thioacetate group in the structure than expected for the original molecule, suggesting that one thioacetate has been cleaved while the other is unaffected.

The S 2p region shows two different sulfur environments as two separated doublets are present (as the S 2p shell gives spin-orbit coupling components for each sulphur atom). A doublet at 161.4/162.4 eV corresponds to sulfur bonded to the gold surface, while the doublet at 163.7/164.9 eV can be attributed to the thioacetate group. Although there are equal amounts of the two S-bonding environments in the adsorbate, the photoelectrons emitted from them experience very different amounts of attenuation. This suggests that the S-Au bond is a few nanometres below the thioacetate group at the upper end of the adsorbate when it is orientated perpendicular to the gold surface. Both spectra support the hypothesis that the bacteriochlorins are attached by only one thiol group to the gold surface, while the thioacetate remaining is close to the monolayer-medium interface.

The N 1s region shows two distinct types of nitrogen present, attributable to the two nitrogen groups found in the macrocycle where no metal centre is found. This is supported by XPS assignments given for related porphyrin structures adsorbed on copper substrates prior to incorporation of metal centres (205).

Table 2: *The predicted atomic percentage concentrations for the observed elements in AcS-12C-BC by XPS, with the measured percentages observed for three samples analysed by XPS.*

Sample	C 1s	O 1s	N 1s	S 2p
Predicted	*82.09%*	*8.95%*	*5.97%*	*2.99%*
AcS-12C-BC (1)	80.68%	9.38%	5.41%	4.52%
AcS-12C-BC (2)	82.09%	8.61%	5.01%	4.30%
AcS-12C-BC (3)	78.59%	12.73%	5.17%	3.51%
Average + standard deviation	*80.45 ± 2.07%*	*10.24 ± 3.20%*	*5.20 ± 0.03%*	*4.11 ± 0.23%*

In terms of elemental analysis, table 2 gives the predicted and observed % atomic concentrations of the narrow regions studied for three separate samples. The relative ratios of each region were close to that expected by the molecular formula of Acs-12C-BC. The sulfur region made up a higher percentage than expected, likely due to some attenuation of the carbon, oxygen and nitrogen contributions compared to the terminal thioacetate group.

To quantify the level of attenuation of the photoelectron signal, the C 1s / Au 4f raw area ratio was studied for three samples of AcS-12C-BC and compared to a monolayer of mercaptoundecanoic acid (MUA). The ratio was found to increase by a factor of ~ 4.8 between MUA and AcS-12C-BC. This was close to the expected observation, as the number of carbons increases from 11 in MUA to 55 in Acs-12C-BC.

Table 3: The C1s /Au 4f ratios for a clean gold substrate, MUA and AcS-12C-BC adsorbed to gold, illustrating greater attenuation of the gold signal by AcS-12C-BC.

Sample	C 1s (raw area)	Au 4f (raw area)	C 1s/Au 4f ratio
Unfunctionalized Au	13584.53	391207.7	**0.035**
MUA	19953.51	311817.25	**0.064**
AcS-12C-BC (1)	38687.6	131113	**0.295**
AcS-12C-BC (2)	38579.6	141175	**0.273**
AcS-12C-BC (3)	39391.2	128245	**0.307**

To determine the monolayer density of AcS-12C-BC, the C 1s/Au 4f ratios were compared for MUA and AcS-12C-BC (table 3). The ratio for MUA was ~ 0.064, which attenuates the signal of clean gold by 1.84 times. Normalising the C/Au ratios by their attenuation factor, the molecule ratio of AcS-12C-BC to MUA was found to be ~0.079. AcS-12C-BC therefore produces monolayers of less than 10% of the surface density of molecules compared to typical alkanethiols like MUA. As most simple alkanethiols occupy a surface area of ~ 21.2 $Å^2$ per adsorbate (246), AcS-12C-BC therefore occupies an area of ~ 269.2 $Å^2$ per adsorbate here, or 0.0037 molecules $Å^{-2}$. This gives an approximate surface density of AcS-12C-BC as ~ 3.7 x 10^{17} m^{-2}. This reduction in packing is likely due to the large dimensions of the bacteriochlorin, which results in longer axial distance between molecules. This density is also lower than the surface area estimated for BChl *a* in LH2 (116).

### iii.   *Secondary Ion Mass Spectrometry*

SIMS was also used as a primary method for identifying AcS-12C-BC assembled on the gold surface. Here, the positive spectrum proved to be of primary importance for the breadth of chemical information. Between *m/z* = 200 and 450, a large series of peaks is

observed that is separated by $m/z = 14$. This indicates the ejection of mass fragments
containing nitrogen as well as possible sequential loss of $-CH_2$ from the central macrocycle,
or two overlapping sequences of elimination of $-CH_2CH_2$ units. This fragmentation pattern
has been observed for porphyrins adsorbed on surfaces in the past (206). A peak after this
series at $m/z = 455.2$ corresponds to ejection of an intact bacteriochlorin macrocycle
fragment. Between $m/z = 680 – 740$, large mass fragments were identified corresponding to
the side chains fragmenting from the macrocycle. In the region between $m/z = 900 – 1000$ the
largest fragments were observed, with peaks at $m/z = 914.5$ and 957.5 corresponding to
fragmentation of the remaining acetate group and intact AcS-12C-BC from the gold surface
respectively. The positive spectrum is displayed in figures 3.13 and 3.14.


$C_{55}H_{79}N_4O_6S_2$: m/z = <u>957.56 g.mol^{-1}</u>

Chain 1 = 273.1 g.mol^{-1}   *Chain 2 = 230.1 g.mol^{-1}*

Bacteriochlorin =
454.36 g.mol^{-1}
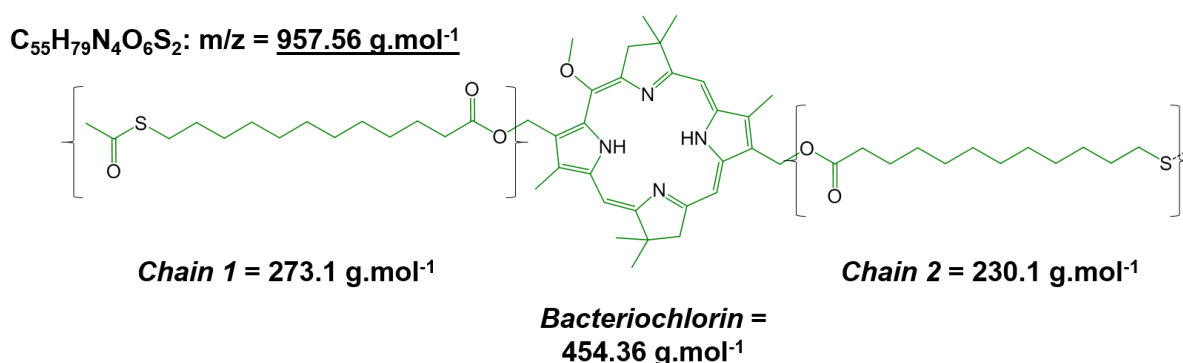
<u>Figure 3.12:</u> *Calculated atomic masses for intact surface-bound AcS-12C-BC as well as expected molecular fragments which may result.*
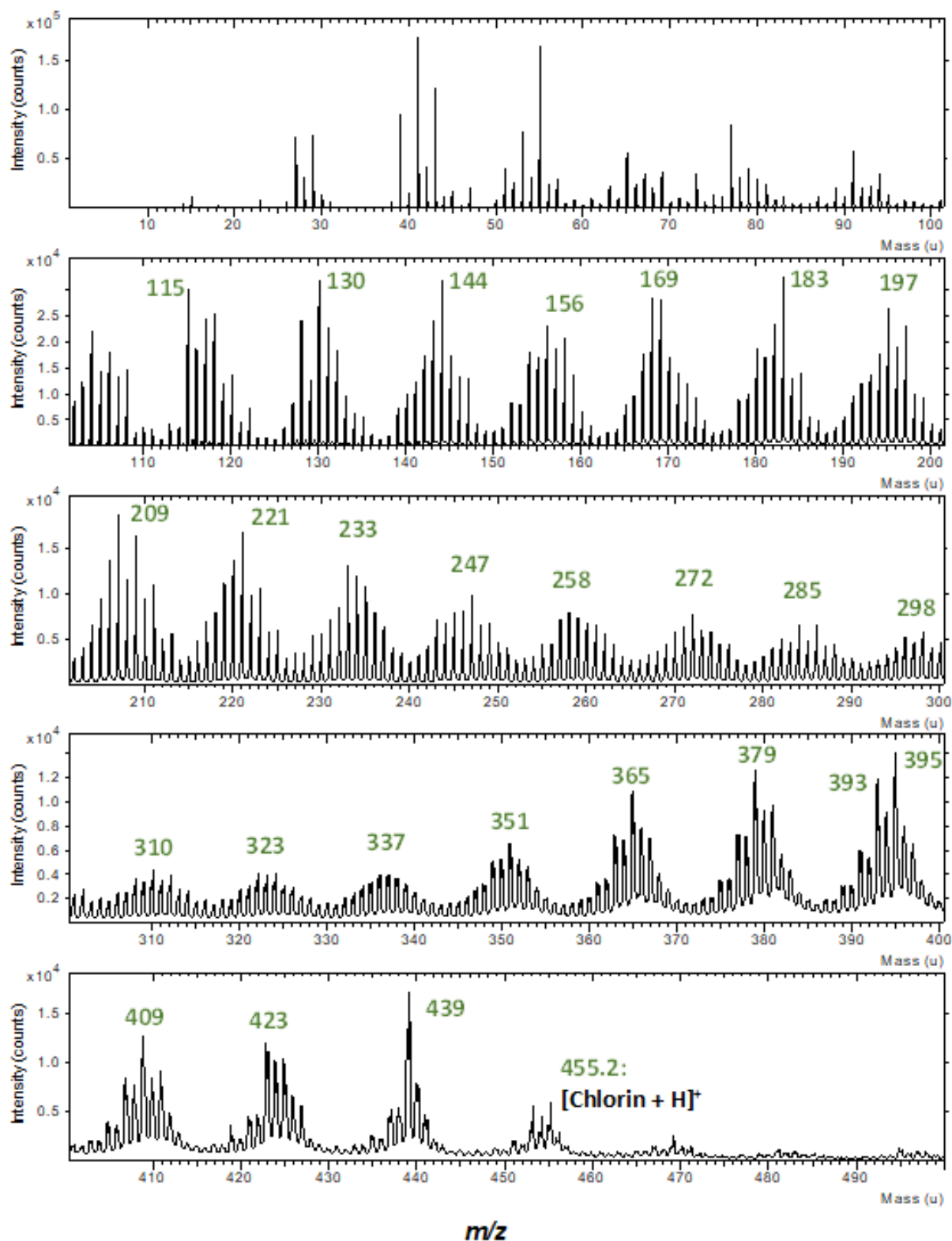
Figure 3.13: The SIMS spectrum for AcS-12C-BC adsorbed to a gold substrate, m/z = 0 – 500.
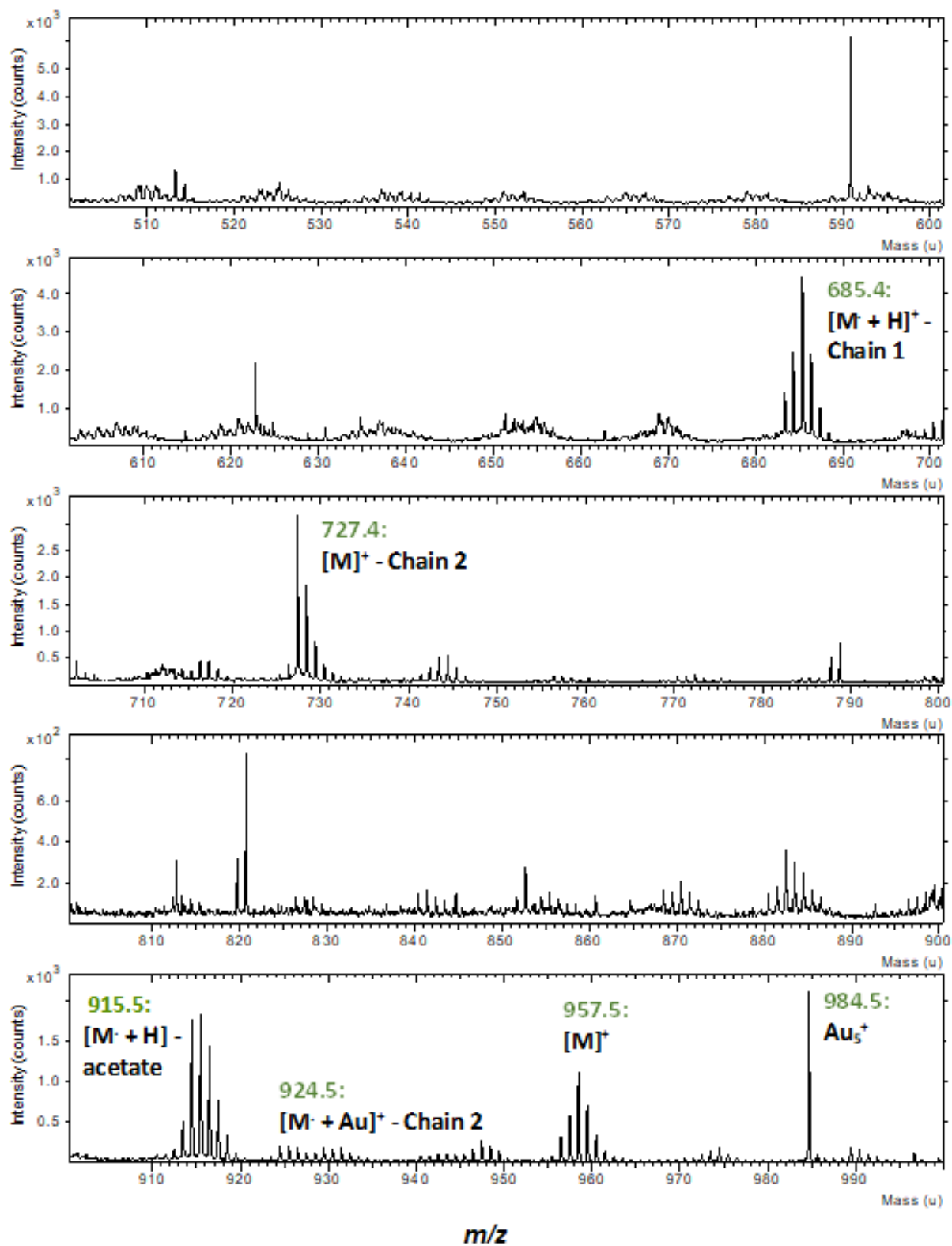
Figure 3.14: The SIMS spectrum for AcS-12C-BC adsorbed to a gold substrate, m/z = 500 – 1000.

The negative ion SIMS spectrum of AcS-12C-BC monolayers is shown in Figure 3.15. Few ions were observed above m/z = 300. However, several ions were observed between m/z = 200 – 300. Both the long-chain carbon fragments can be found in this region. Chain 1 is observed in a small peak at m/z = 272, with possibly fragmentation of single carbon and oxygen from the chain to give peaks at m/z = 262 and 256. Chain 2 appears at m/z = 231 relatively intact. At below m/z = 200, negative peaks were detected from m/z = 183.1 with regular intervals of 14 units, again suggesting a fragmentation pattern of the macrocycle. The peak positions here also appear to align in mass with the corrugated mass pattern observed in the positive spectrum.
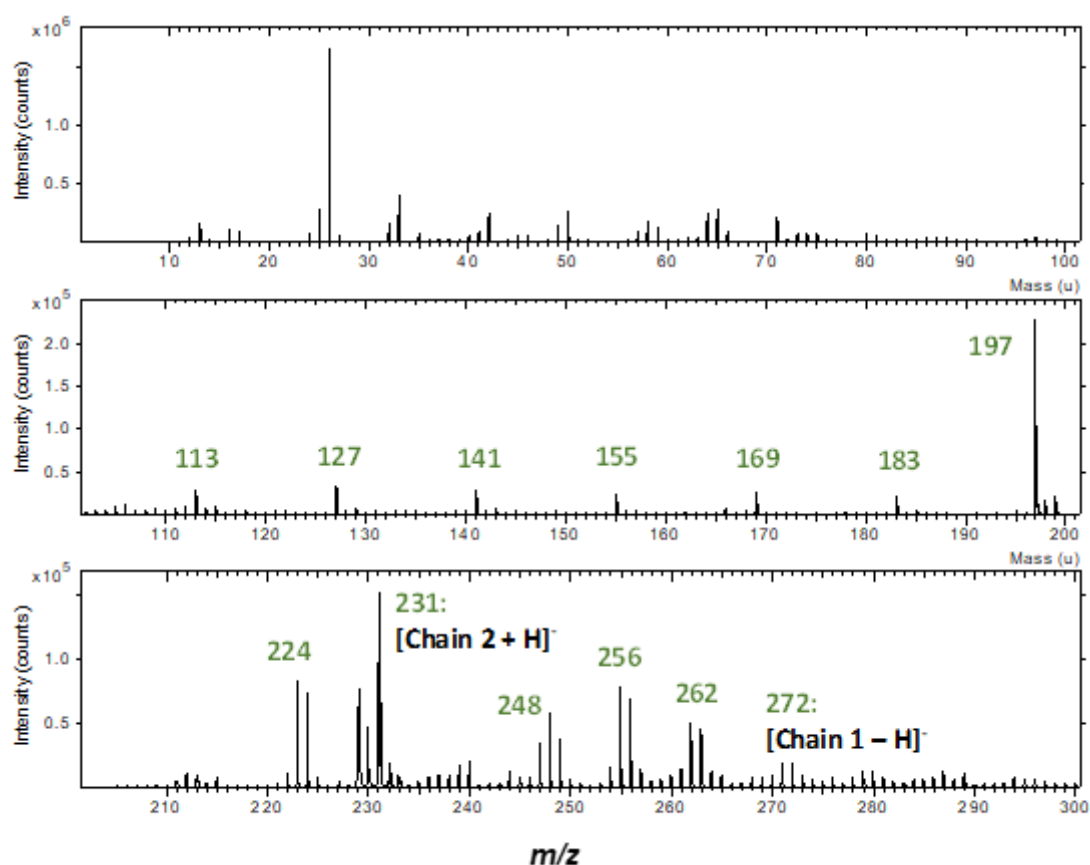
Figure 3.15: The m/z = 0 – 300 regions of the negative SIMS spectrum obtained for AcS-12C-BC adsorbed to gold substrates.

iv.   *Ellipsometry.*

For ellipsometry measurements, reference measurements were taken for unfunctionalized chromium/gold substrates before new measurements after adsorption of AcS-12C-BC. Both measurements were carried out under ambient conditions in air.
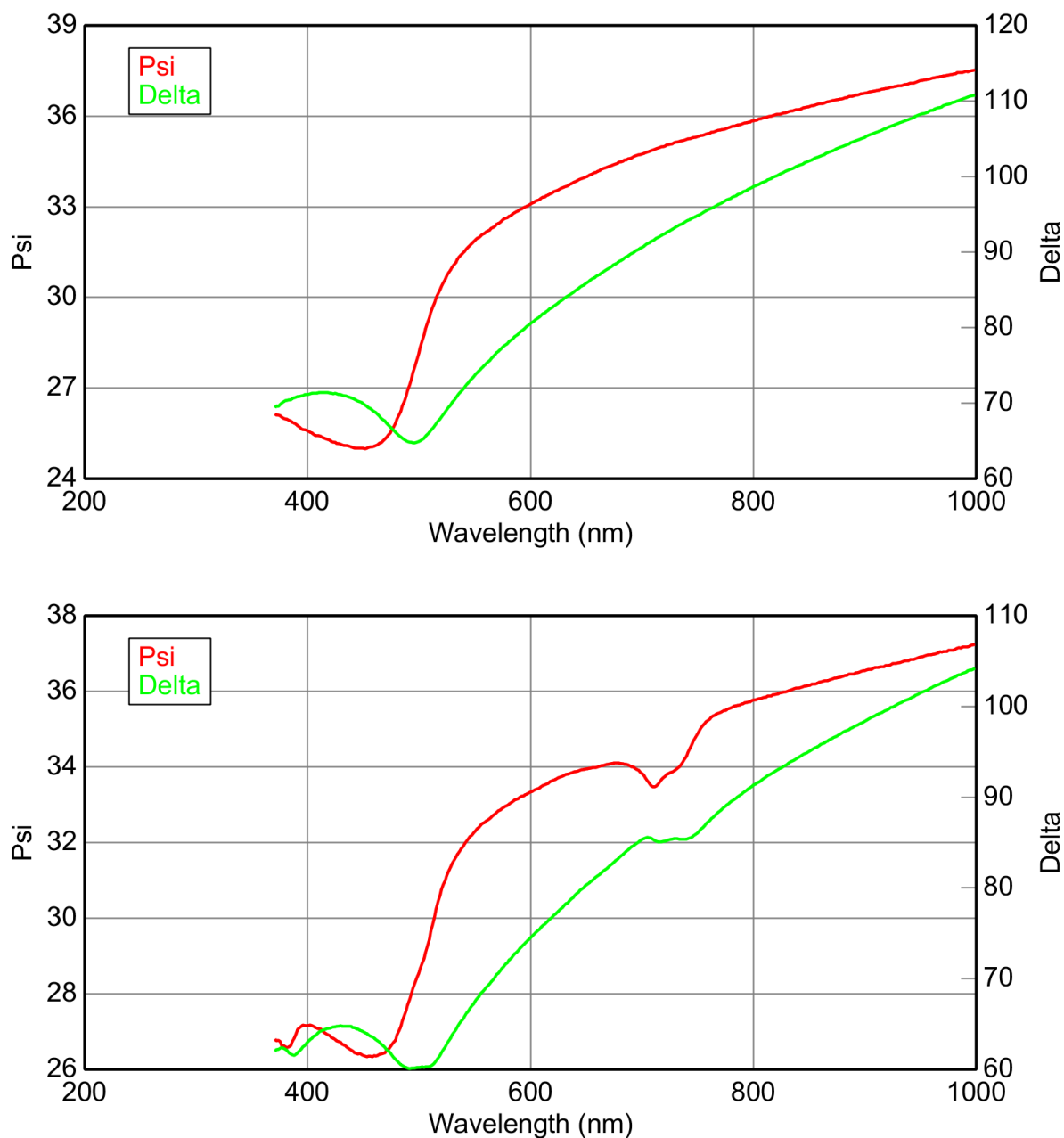

*Figure 3.16: (**Top**) A typical Ψ/**Δ** for a gold substrate with a chromium adhesive layer mounted on a glass coverslip. (**Bottom**) A repeated measurement after adsorption of AcS-12C-BC to the surface shows new features close to the absorption wavelengths of the molecule.*

What was immediately apparent after adsorption of the bacteriochlorin was the stark difference in the Ψ/Δ plot as shown in figure 3.16. The first plot shows a typical graph for a glass microscope slide with evaporated chromium (~ 5 nm) with a top layer of evaporated gold (~ 15 – 20 nm) with a smooth curvature. After adsorption, new features appear at specific wavelengths with the most prominent observed at ~ 714 nm. This feature is close to the absorption of the Q_y band of the molecule observed at 723 nm in solution, indicating that the absorption features of the assembled monolayer have a strong effect on the surface optical properties. Another feature at ~ 500 nm correlates to the Q_x adsorption and is not as intense, lining up with that band's lower intensity. In addition, these features had shoulders which were red-shifted by several nm. This may indicate the formation of aggregates which shift the transition energies of the dipoles. J- and H-aggregates can be formed between chlorins by intermolecular interactions such as π-π stacking (207, 208). Close packing in a monolayer system may produce similar arrangements across a two-dimensional plane.

These changes made the optical properties much different from a typical transparent organic layer for modelling purposes – when attempting to fit the organic layer with a standard Cauchy model (describing and organic thin film) the model could not take the absorption features into account. To model the spectrum correctly, a new profile for AcS-12C-BC was obtained by measuring extinction and ellipsometry spectra for the molecule physisorbed to a piranha-cleaned glass slide, of which the details can be found in the model description (**Appendix 1 i**)). When used, a much-improved mean squared error of between 1-2 on average was achieved (compared to 7-8 using the Cauchy model). For bulk gold samples, the thickness of a fully adsorbed monolayer of AcS-12C-BC was found to be on average 4.31 ± 0.515 nm. This puts the thickness range approximately 3 times higher than for monolayers of simple long chain thiols like undecanethiol (between ~ 1.3 – 1.7 nm). This

would not be entirely unexpected given the extended nature of the chain structure in AcS-12C-BC.

If an ideal extended conformation with a near-perfect crystalline arrangement was to be assumed, a tilt angle for the molecules in the monolayer could be determined (figure 3.17). The length between the gold-bound sulfur and the terminating carbon atom was measured in a simple optimised 3D model of the structure produced using ChemSketch^{TM} software, giving a molecular length of 4.936 nm. Applying simple trigonometry then gives us an angle of 29.17°: a value which has been observed commonly for alkanethiol monolayers.

_A_

_c_ = optimised length

= 4.936 nm

_b_ = layer thickness

= 4.31 nm

Gold substrate

Chromium adhesive layer
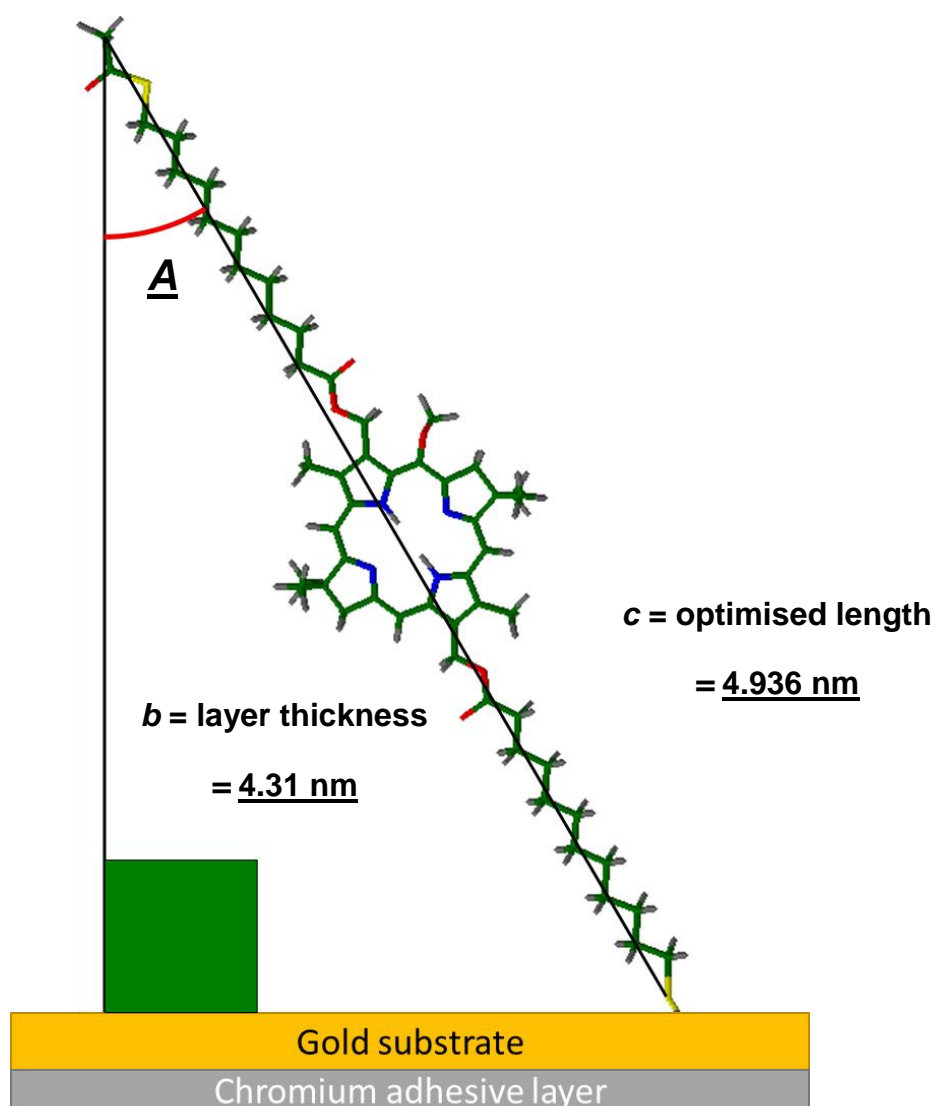
Figure 3.17: _Estimating the tilting angle of AcS-12C-BC molecules in an idealized monolayer from the thickness measured by ellipsometry and the optimised length of a simple 3D model structure._

The assumption used in the tilt angle estimation however is not a certainty. Typical alkanethiol monolayers, upon which this assumption would be based, tend to adopt their extended confirmations due to the high degree of intermolecular interactions between neighbouring chains, which provide maximum stabilisation when extended. This stabilisation originates in many directions on the two-dimensional planar surface in the crystalline, close-packed monolayers. For AcS-12C-BC however, the packing density was determined using XPS to be approximately 8% that of a typical alkanethiol like MUA. As the large molecule occupies more space on the surface, the alkyl chains, themselves of similar molecular dimensions compared to MUA are unlikely to be as closely packed. If there are *J*- or *H*-aggregates forming between the bacteriochlorins, it is feasible that there may be some interactions between neighbouring chains in the stacking direction. However, the separation of chains along the bacteriochlorin plane direction will be greater due to the much larger molecular size in that dimension. As a result, there is a possibility that there will be a much lower degree of stabilisation of the alkyl chain conformations than observed in smaller alkanethiols. The reduction in layer height from the optimized 3D model can therefore conceivably be due to the flexibility of the alkyl chains, which can bend and compress underneath and above the central bacteriochlorin (figure 3.18). The result would be a more amorphous layer structure than is typical for SAMs. This may be supported by the standard deviation in thickness of ± 0.515 nm recorded across the measured samples – while on the whole the monolayers are extended there may be enough space for variability in the chain conformations. However, with the intimation of *J-/H*-aggregation, it is possible that with the reduction of alkyl-alkyl intermolecular organisation, π-π stacking may conceivably be important in the organisation of the bacteriochlorins on the surface. However, with the surface analysis evidence this is not certain.
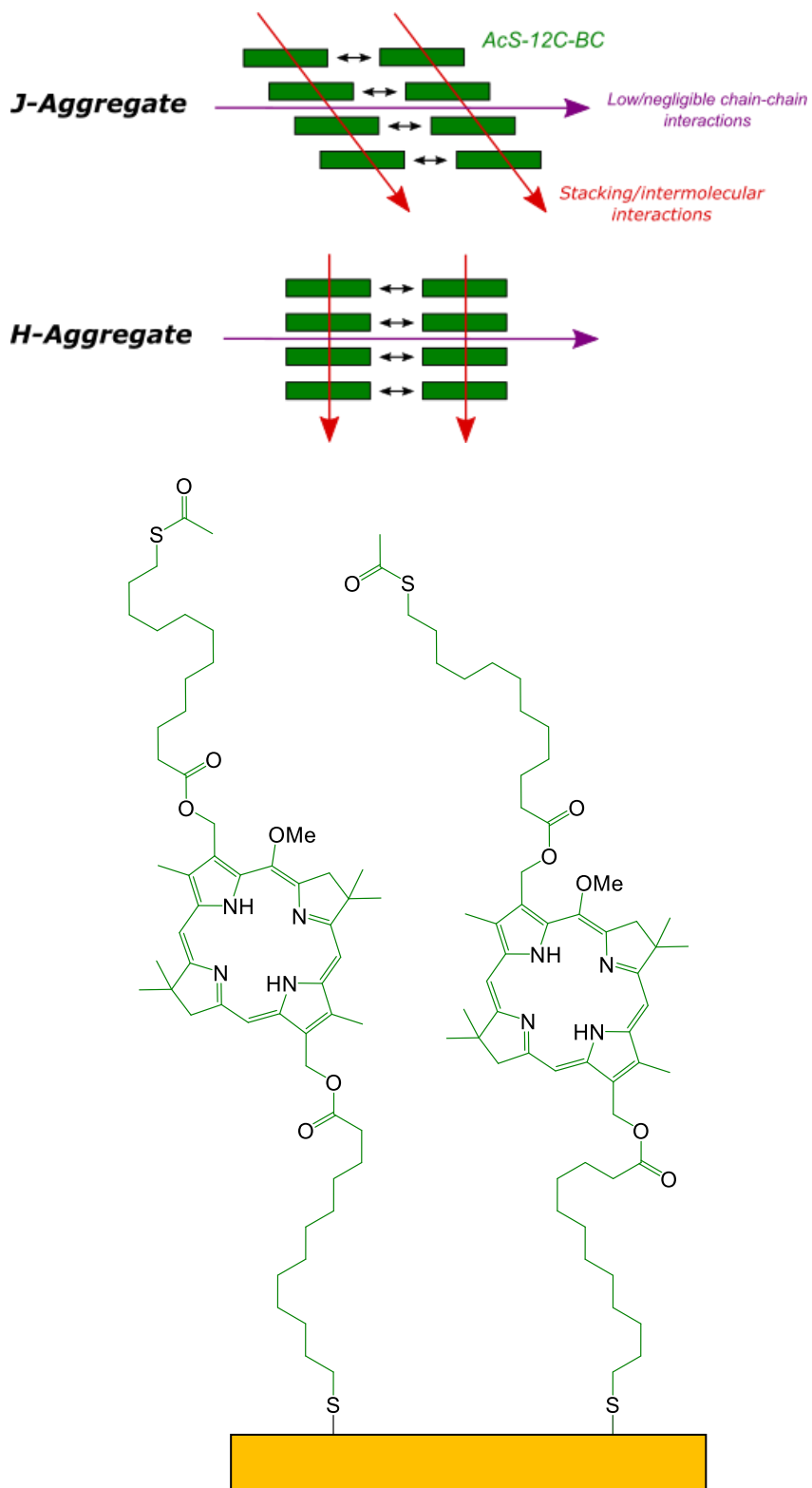
*Figure 3.18: (**Top**) A simple representation of the hypothetical structure of J- (staggered) and H- (face-to-face) aggregates of AcS-12C-BC. The larger separation between bacteriochlorins along their planar direction may reduce the total strength of intermolecular reactions between the long-chain alkyl substituents. (**Bottom**) A consequence of lower interchain packing may be greater conformational flexibility of the alkyl chains of each molecule.*

v. *Summary*

The surface analysis results appear to support the monodentate hypothetical model, with only one thiolate group bound to the substrate while the other forms the layer terminus. XPS shows a large difference in signal attenuation between the two sulfurs and a C 1s peak which can be interpreted as one remaining thioacetate group. The surface density was also estimated to be ~ 3.7 x 10^{17} m^2, around 8% that of typical alkanethiols. This was an expected due to the large physical dimensions of the molecule, which limits the packing density along the planar dimension. The positive ion SIMS spectrum indicates the fragmentation of the two chains of the bacteriochlorin and distinguishes them as two different mass fragments, which would suggest that one sulfur group was deprotected while the other was still intact. Finally, ellipsometry showed an adsorbate height which would suggest significant monodentate attachment. Spectral features in the ellipsometry measurements also suggest the potential formation of *J-/H-* aggregates between the bacteriochlorins. As the estimated surface density of these molecules is in the same order of magnitude as found in LH2 (116), it is possible that this stacking may help with the organisation of the monolayer.

These results would provisionally support the hypothetical model of monodentate attachment. The observation of thioacetate in the XPS and SIMS analysis would suggest that when one thioacetate group is cleaved by NH_4OH, immediate reaction of this with the substrate occurs. The kinetics of the cleavage may then be different at the medium/surface interface, which could preserve the thioacetate groups once AcS-12C-BC is on the substrate. The surface analysis alone however does not rule out however that there may be some thiols terminating the monolayer, or that simultaneous thioacetate deprotection in solution may occur in some molecules and result in some bidentate attachment in addition to the singly-bound molecules. In the SIMS analysis, a peak at 915.5 in the positive spectrum (see figure 3.14) could be attributed to either the fragmentation of the terminal thioacetate of a

monodentate molecule or an intact bidentate molecular fragment. However, consideration of the XPS and ellipsometry results would indicate that if there is a mixture of these two bonding modes, the bidentate molecules are likely to be a small minority of the overall monolayer structure. A potentially more significant conclusion to draw here is that the presence of free thioacetate protecting groups could allow post-assembly modification of the monolayer in future, allowing for three-dimensional architectures.

c) *Adsorption characteristics of AcS-12C-BC*
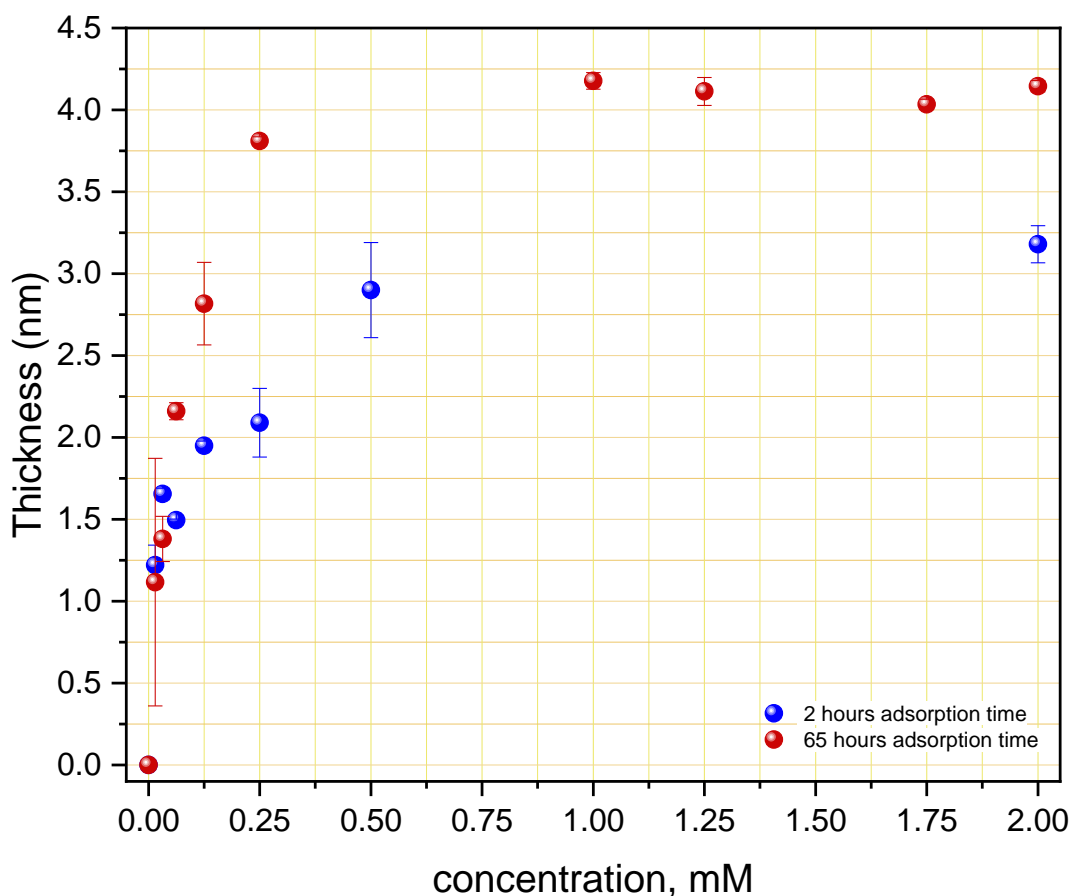
Figure 3.19: The measured thickness of a monolayer of AcS-12-BC by its concentration in solution. Two sets were produced for a short and long period of time for adsorption.

The kinetics of adsorption of AcS-12C-BC were studied by measuring the thickness of the adsorbed layer as a function of the concentration using ellipsometry. This was done for two reasons. The first was to determine if the adsorption exhibits similar behaviour to alkanethiols, or whether the potential bidentate nature of the molecule results in a different sequence of adsorption process. Secondly, from such a study the adsorption constant of the system could be studied for different time intervals, which may also provide some indication on the adsorption process.

Two sets were produced with various adsorption times of 2 hours and 65 hours (figure 3.19). The resulting thicknesses when plotted appear to show typical adsorption isotherm characteristics, with an initial sharp increase in thickness with concentration until a peak thickness is achieved. For the longest adsorption time allowed, the thickness reached a maximum of ~ 4.1 nm beyond 0.75 mM concentration, consistent with the previous ellipsometry measurements. After two hours, the adsorption isotherm showed a slower rate of increase and the maximum height achieved is almost a nanometre less. This kind of behaviour may be expected for thiol-derived adsorbates – as time increases, the monolayer structures becomes more organised as intermolecular forces between the hydrocarbon chains (and possible π-π stacking of the central macrocycles in this case) are given time to maximise the packing density of the molecules at the surface, hence why the apparent height of the molecules was lower after 2 hours than for 65 hours. However, for simple thiol species the typical adsorption profile achieved almost complete coverage after a few minutes, with reorganisation processes eventually increasing the coverage slowly until completion (178). Here, after 2 h the monolayer did not completely reach its maximum thickness even at 2 mM concentration. This would suggest that the potential rate of adsorption is much slower for AcS-12C-BC than for typical thiols. To test this, the thickness was measured as a function of a short period of time using Total Internal Reflection Ellipsometry (TIRE) with a liquid cell

containing a 2 mM solution of AcS-12C-BC (**Appendix 1 ii)**). Over a period of 55 minutes

the thickness of AcS-12C-BC increased more slowly than expected for a thiolate, reaching

just over 3.2 nm in under an hour. This indicates a slower adsorption process than expected.

As AcS-12C-BC has a larger molecular size than typical alkanethiols, adsorption of new

molecules between the bound adsorbates may have a higher energy barrier. Also, greater

spacing between the alkyl tails would mean less intermolecular stabilisation which would

likely increase the time needed for molecular organisation.

This study also gives some important indications of the molecular order on the surface

which may complement the surface analysis data. Firstly, the consistent growth profile of the

thickness with concentration over 65 hours suggests that there is one adsorption mode which

is preferred – the monodentate attachment. If bidentate attachment was to occur to a

significant degree, the resulting graph would likely display a plateau region of reduced height

at lower concentration which would indicate this. Also, the consistent maximum thickness

achieved for concentrations from ~ 0.75 – 2 mM suggests that the system has achieved a

maximum packing density, and that molecular organisation may have also optimized. It is

possible therefore that the conformation of the alkyl chains may be more regular than would

be expected for the calculated surface density of AcS-12C-BC. The *J-/H*-aggregation in the

monolayer may therefore provide enough stabilisation to suppress the large-scale

conformational bending of the alkyl chains. In contrast, after 2 hours of adsorption, the lower

maximum height achieved may indicate greater conformational flexibility of the molecules in

the less dense monolayer, depressing the height of the molecules. The lower height may be

due to formation of bidentate-bound AcS-12C-BC as well, but the lack of a corresponding

height plateau in the growth profile makes this unclear.

To determine the equilibrium constant of adsorption, K_{ads}, both data sets were

converted to fractional coverage to fit to a Langmuir adsorption isotherm (figure 3.20).

Fitting with a Langmuir isotherm produced approximate curves as a trend-line through the data sets. These were used to approximate values for K_{ads}.
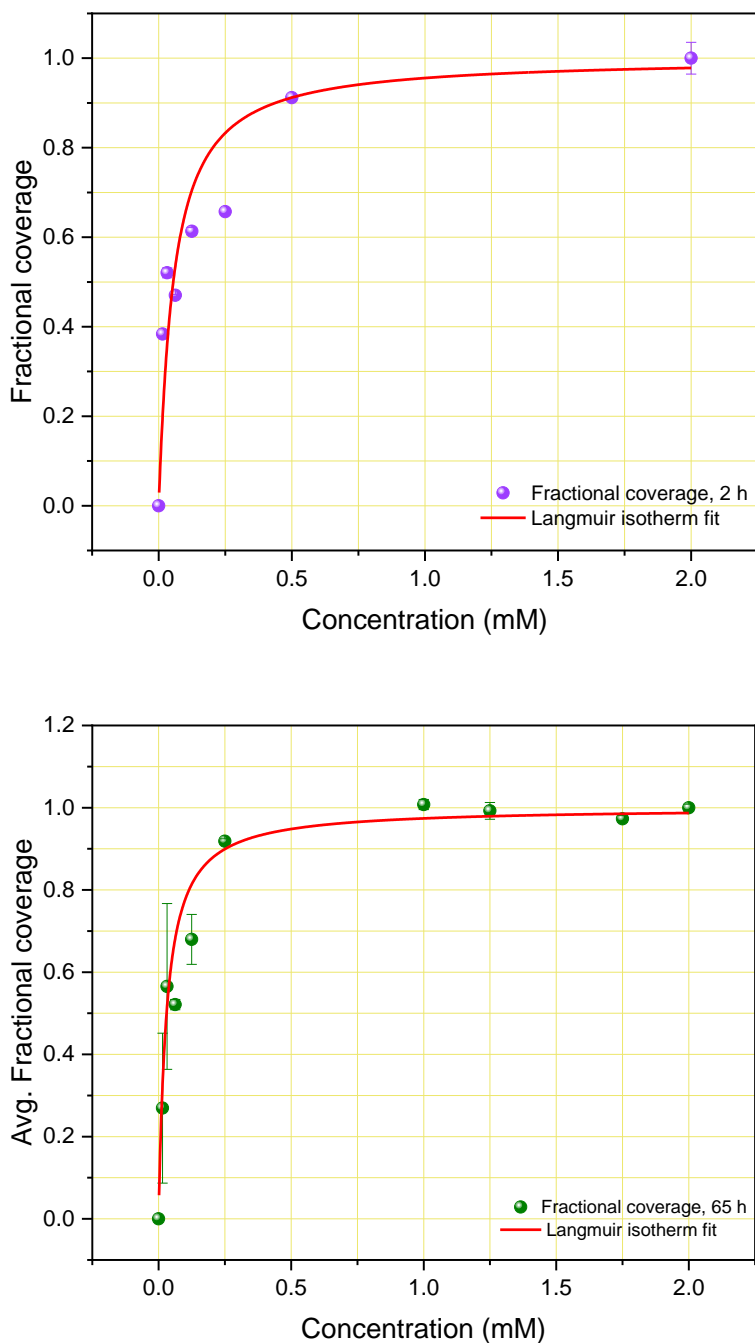
*Figure 3.20: The fractional coverage of AsC-12C-BC monolayers with increasing concentration as measured by ellipsometry after (**Top**) 2 h and (**Bottom**) 65 h adsorption time, fitted with Langmuir isotherms.*

For 65 h, 50% fractional coverage was reached with a concentration of ~ 0.0302 mM. This gave K_{ads} as 33112.6 M^{-1}. For 2 h, the concentration was higher at 0.0547 mM, therefore giving K_{ads} as 18281.5 M^{-1}. To corroborate the adsorption constant given for a period of 65 h, XPS measurements were carried out on samples adsorbed with various concentrations for 48 hours (which from past experiences was expected to give full coverage) (figure 3.21). From this, the approximate concentration of 50% coverage was 0.0399 mM, giving K_{ads} as 25062.7 M^{-1}.
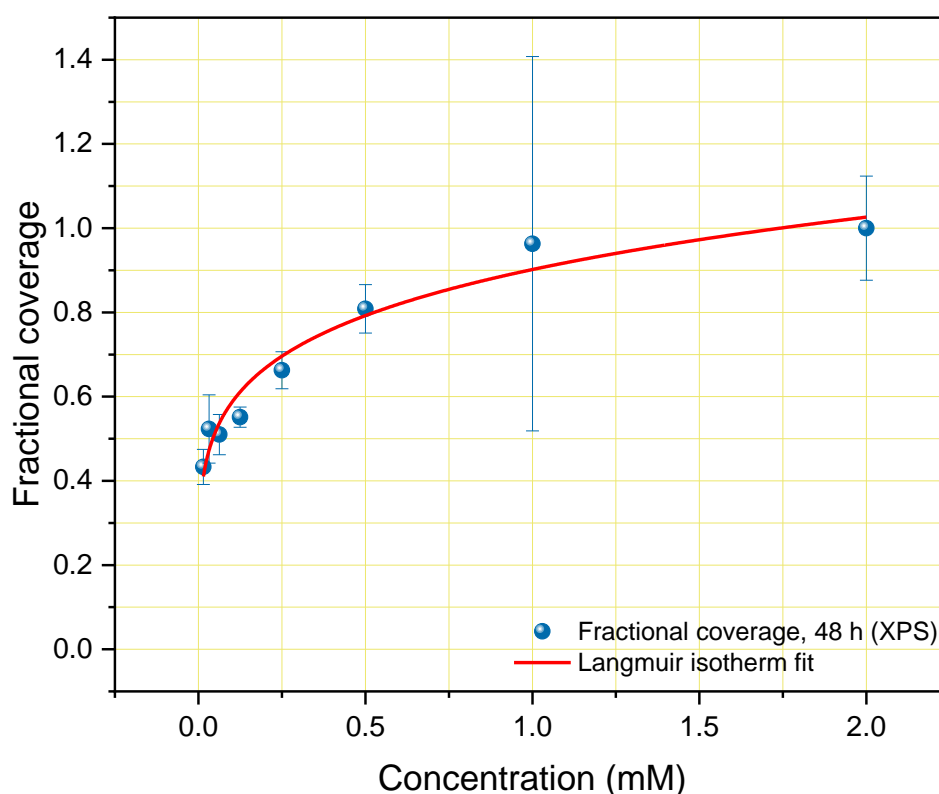
Figure 3.21: The fractional coverage of AsC-12C-BC monolayers adsorbed for 48 hours with increasing concentration as measured by XPS.

The difference in K_{ads} between 2 h and 65 h may be significant. These may point to a two-stage process of the monolayer formation which differs from typical thiolates. 2 h, adsorbates may assemble on the surface but are not close packed. A maximum thickness of this initial monolayer is reached at this time. However, for longer time periods the monolayer

may organize further in a long-form process. As *J-* or *H*-aggregates were suggested by the

ellipsometric spectra obtained earlier, this re-organization may be mediated toward the

maximisation of π-π interactions. As the number of inter-alkyl chain interactions between the

molecules is likely to be low as discussed earlier (page 130), these weak stacking interactions

may be crucial in imparting organisation into the monolayer during the adsorption process. In

order to form aggregates of large AcS-12C-BC molecules at the surface, this may therefore

take a significantly longer amount of time compared to simpler alkanethiol systems.

d) *Coupling of AcS-12C-BC to plasmonic gold nanostructures*

AcS-12C-BC was adsorbed to gold plasmonic nanostructures fabricated with

interferometric lithography. At first, four structures were selected exhibiting a range of

plasmon extinction maxima between 572 – 657 nm. These arrays were selected by their

previous use for the study of strong coupling in light harvesting proteins. The goal was to

determine what coupling, if any, might be observed if the protein was replaced with a

monolayer of bacteriochlorins. Before the experiment, the arrays were cleaned with cooled

piranha solution and evaluated with UV/Vis spectroscopy and AFM. After the cleaning

process, there was only a small shift in the extinction maxima and the array structures

themselves were largely intact. The arrays used are summarised in **Appendix 3 i).**

Adsorption was carried out in the same manner as with the unpatterned gold

substrates and the extinction spectrum was measured. In the resulting spectra, the position

and lineshape of the plasmon band was modified slightly, and a shoulder feature was

observed, poorly resolved from the more intense band (figure 3.22). This indicates the there

was some coupling of the excitons in AcS-12C-BC to the plasmon mode. The unresolved line widths for the new peaks however suggested that this may not be strong coupling.
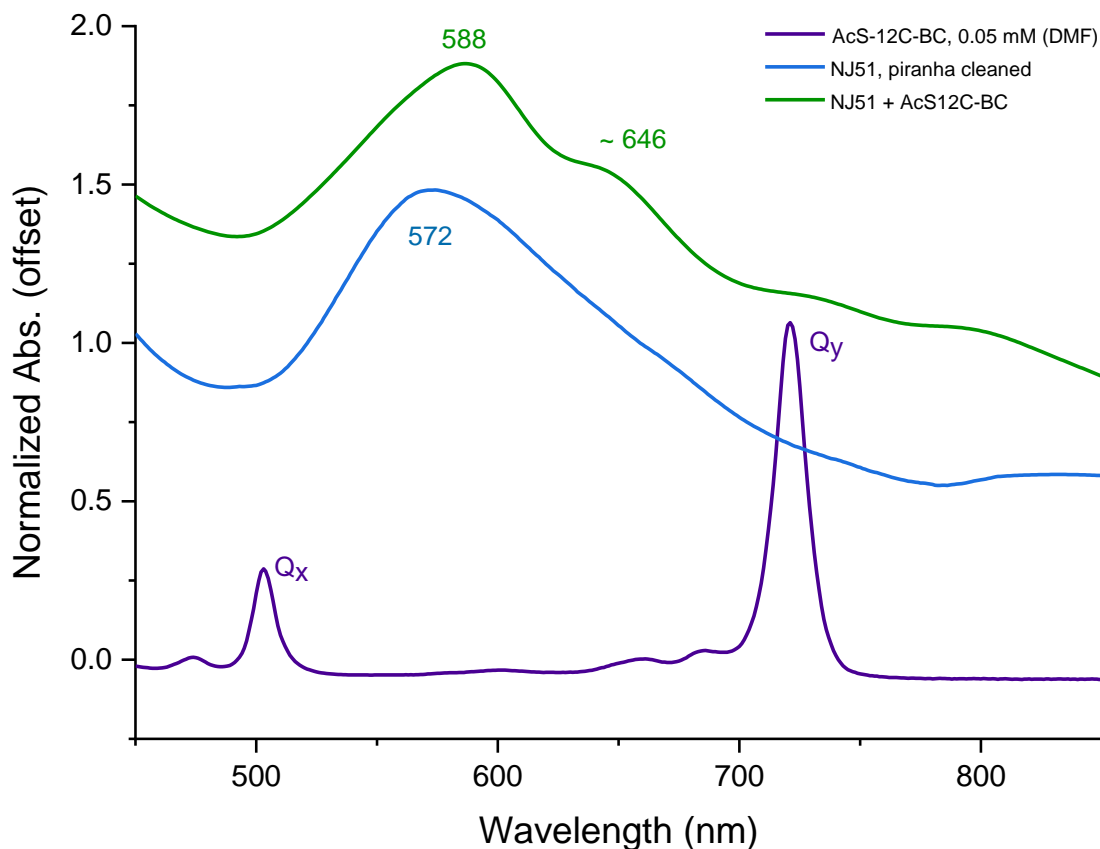
Figure 3.22: Extinction spectra for a plasmonic nanostructure array (NJ51) before and after adsorption of AcS-12C-BC. The extinction spectrum for AcS-12C-BC in solution is included for comparison.

Modelling of these spectra using the harmonic oscillator model gave an average exciton energy E_{mol} for AcS-12C-BC on these arrays of 1.93 ± 0.11 eV. This energy lies between the energies of the transition dipoles observed in the solution spectrum of AcS-12C-BC, which are 1.715 eV for Q_y and 2.455 for Q_x. This may be explained by misalignment of the molecular axes corresponding to these transitions compare to the plasmonic field propagation direction, which is perpendicular to the surface plane. The coupling interaction may therefore be the combination of interactions occurring between both the imperfectly

aligned transition bands. This may be expected due to the potential conformational flexibility of the alkyl chains in AcS-12C-BC. Even in the idealized case of a fully extended AcS-12C-BC molecule, the tilt angle calculated from the ellipsometry measurements would result in both the Q_x and Q_y dipoles being oriented differently from the plasmonic field direction (figure 3.23).
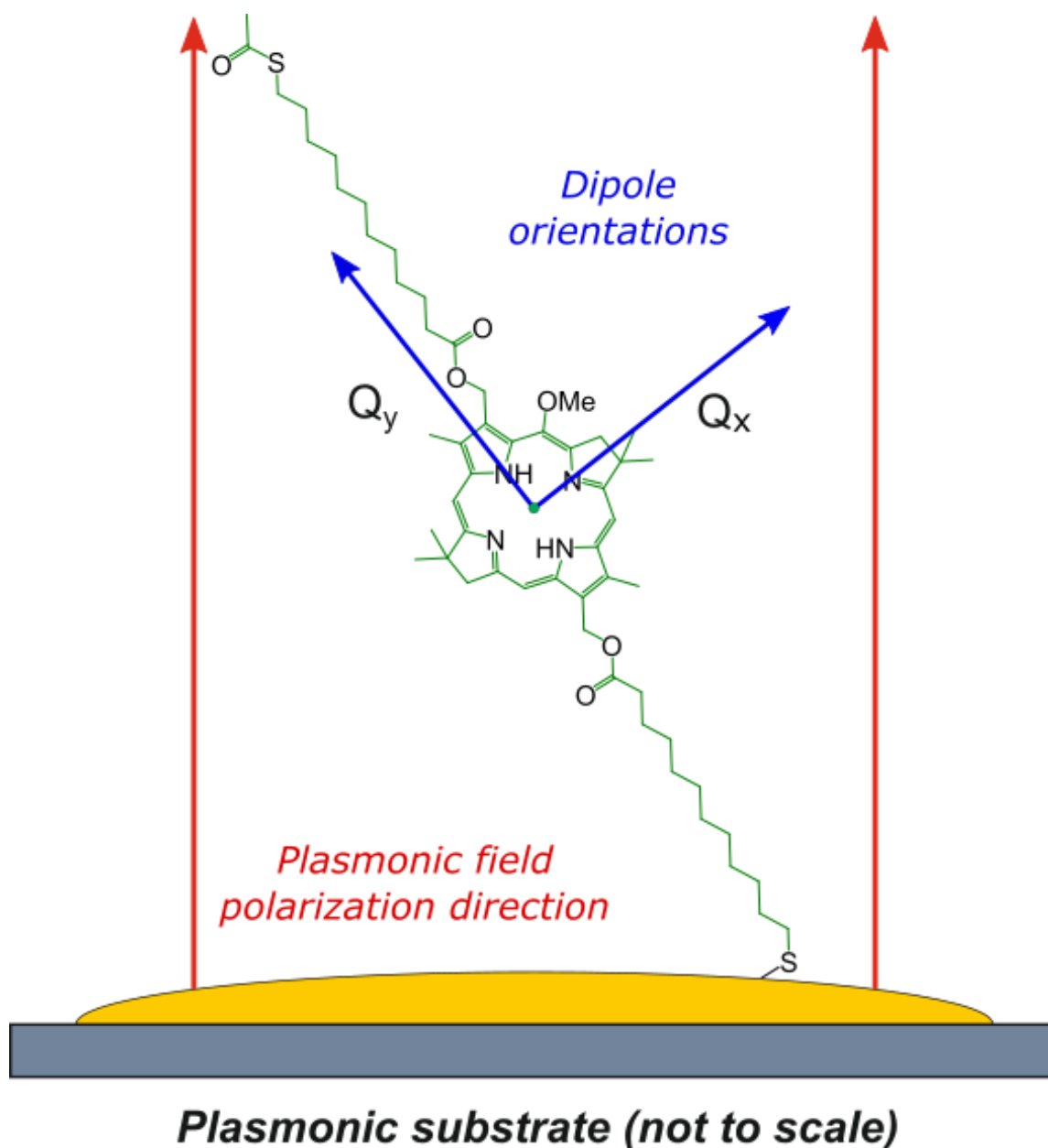
Figure 3.23: The mixed coupling of the Q_y and Q_x dipoles within the plasmonic field may be the result of angling of the transition dipoles (illustrated by the blue arrows) relative to the field polarization (the red arrows).

Using the same model to calculate the coupling energy E_c, the average energy

obtained was 0.12 ± 0.04 eV. If this was a case of the plasmon mode coupling to only one

exciton in the bacteriochlorin assembly this would be below the boundary of ~ 0.24 eV

hypothesised for strong coupling in light-harvesting complexes (129). However, this system

is likely to have both exciton transitions coupled to the plasmon mode simultaneously. As

such, the coupled harmonic oscillator used here may not describe the dynamics in the system

very effectively. It may be the case that the observed E_C is an average of the coupling

energies of the plasmon mode to both the dipoles. However, this may be unlikely because of

the wide energy gap that separates the transitions. The overall interaction of the plasmon

mode to the excitons in AcS-12-BC may therefore be more complex than can be described

using the current harmonic oscillator model.
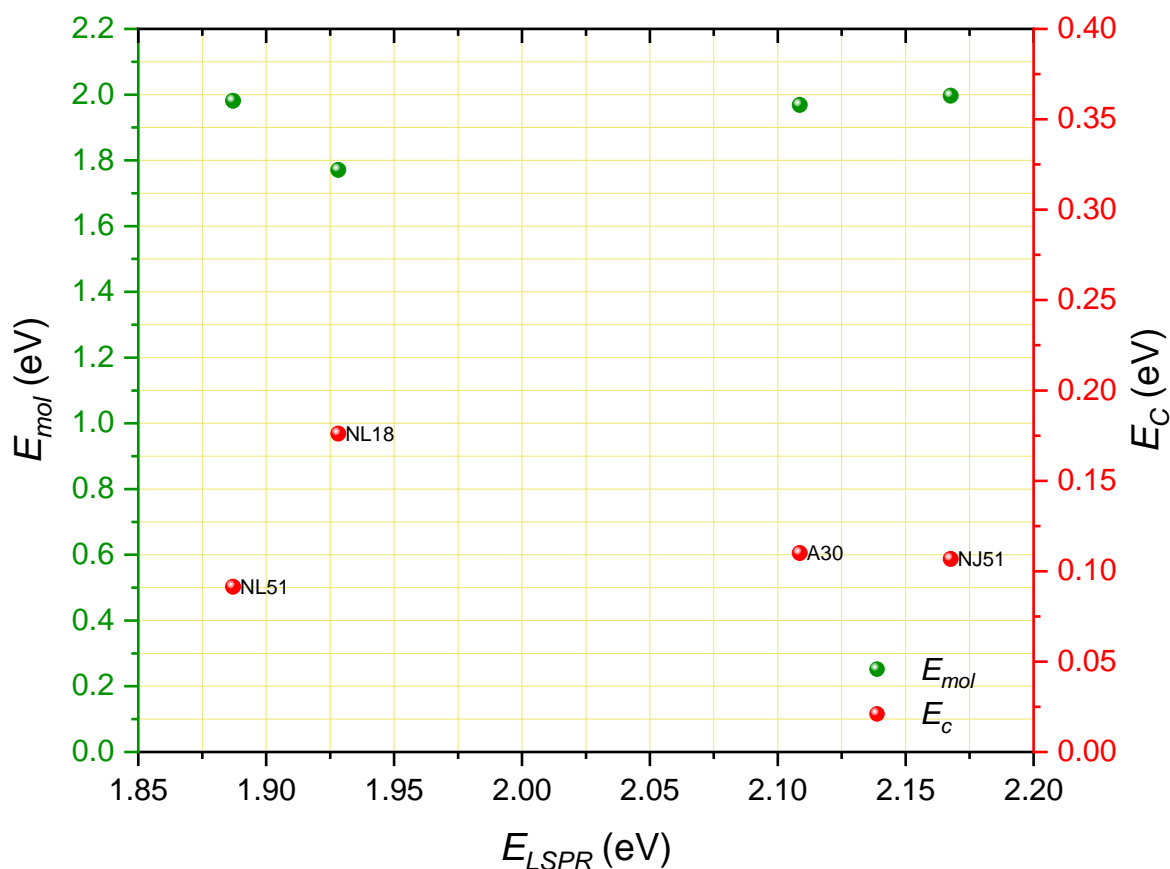
Figure 3.24: The exciton energy E_{mol} and the coupling energy E_c for AcS-12C-BC adsorbed to several plasmonic nanostructure arrays varying in E_{LSPR}.

Across the samples that were studied, E_{mol} and E_C was found to occupy a small range of energies (figure 3.24). This could reflect a degree of organisation in the AcS-12C-BC monolayers, perhaps due to *J-/H*-aggregation, which could restrict the orientations possible relative to the plasmon field polarization. Comparing the magnitude of these energies to the plasmon energies, E_{LSPR}, of the arrays used, no systematic relationship appeared to be observed. In one sample however, NL18, E_{mol} was found to dip below 1.8 eV, which resulted in a corresponding increase in E_c. There are two possibilities which may explain this. Firstly, a variability in the physical properties of the array compared to the others may have changed the coupling magnitude, but as of yet it is not clear how. In general, the main function of changing the physical parameters of the arrays is to control the LSPR energy by the size, shape and periodicity of the nanoparticles during the nanofabrication process (117). However, the annealing process which optimises the gold nanoparticles for these coupling studies can change these properties significantly and often unpredictably. Considering the characteristics of NL18 compared to the other nanoparticle arrays used here (**Appendix 3 i)**), there is no one obvious property of the sample which can be linked to the increased coupling. As such, the change in E_C could be treated as a variation within the range of energies that have been observed for other organized light-harvesting assemblies on a set of nanoparticle arrays (116, 129). Conversely, the change in E_{mol} observed in NL18 may indicate a variation in the monolayer arrangement, changing the relative orientation of the dipoles to the plasmon field. In this sample, an imperfect monolayer may have resulted in the Q_y dipole becoming more closely aligned to the plasmon mode, increasing its coupling contribution.

In the microscopic expression for energy in the harmonic oscillator model, the number of dipoles in the plasmon mode volume increases the coupling energy. AcS-12C-BC was estimated to have a surface density smaller than BChl *a* in LH2 (116). When coupled for the estimates of the dipole moments, which are lower than observed for carotenoids in LH2,

this suggests monolayers of this molecule are unlikely to strongly couple to the plasmon mode. While these AcS-12C-BC monolayers appear to exhibit a different coupling phenomenon, increasing the dipole number may have an impact on the coupling energy which could produce strong coupling. An attempt to increase the number of dipoles within the plasmon mode volume was performed by simple physisorption as a control experiment. The monolayers were prepared at 2 mM concentration with three plasmonic nanoparticle arrays, but after sample washing reintroduced them into the solution for an extended time, up to 120 hours. By doing this, it was aimed to make a monolayer with physisorbed AcS-12C-BC molecules resting on top, with the potential of dipole-dipole coupling.
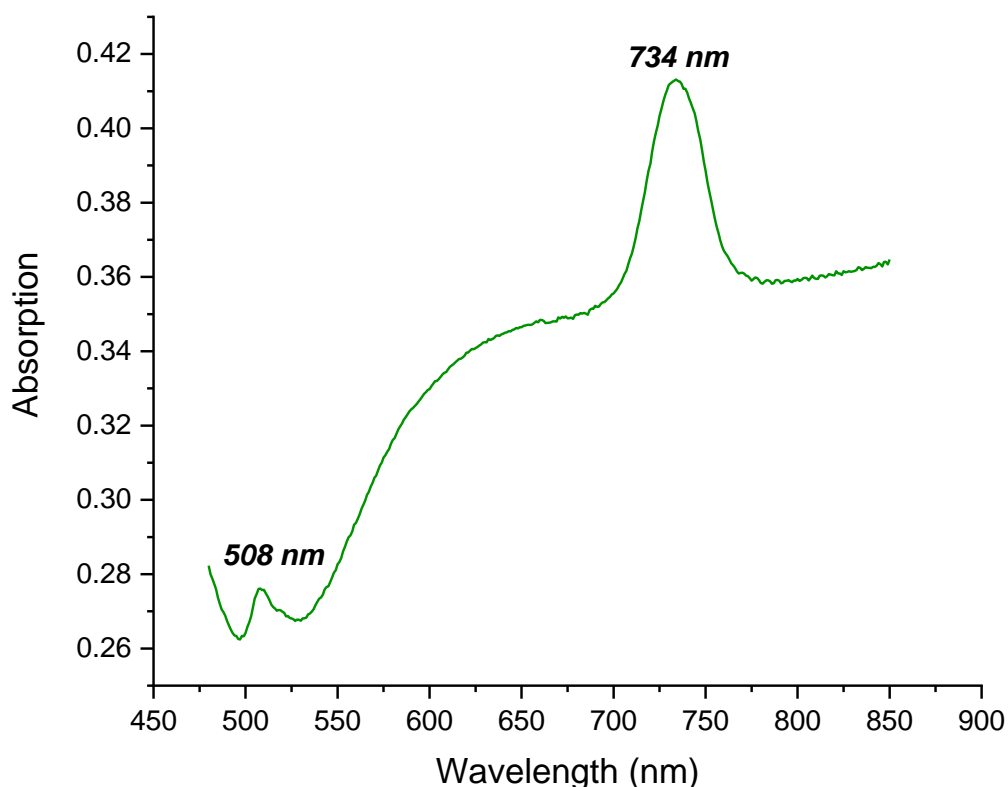
Figure 3.25: The physisorption of increased amounts of AcS-12C-BC results in the red shift of the absorption intensity for the Q_y and Q_x dipoles instead of increased coupling magnitude.

However, the resulting spectra did not show an increase in coupling, and instead large adsorption bands were detected correlating to the main absorption bands of AcS-12C-BC (figure 3.25). The most obvious visible band was the Q_y band, shifted from the normal peak maximum to 729 – 733 nm and observed at very high intensity, in some cases much higher than the plasmon band. The lack of coupling is likely due to the lack of control of the molecular orientation – after the formation of the perpendicular-standing monolayer, the extra molecules are more likely to adsorb in a flat orientation with respect to the macrocycle. This means that the majority of Q_y and Q_x dipoles are parallel to the surface which precludes them from coupling to the perpendicular-oriented plasmon field. This indicates that it is necessary to use careful design of the system synthetically to allow the dipoles to be positioned in a non-planar direction when forming multilayers. Also, the red shifting of the Q_y energy suggests the formation of *J-* or *H-* aggregates of AcS-12C-BC (207, 208). When compared to the extinction spectra for plasmon-exciton coupled AcS-12C-BC, some samples showed absorbance features in the same approximate spectral range. Whether they have any impact on the plasmon-exciton coupling dynamics however is not known.

To explore a synthetic strategy exploiting the unbound thioacetates, an attempt was made to produce multilayers of these molecules. A model molecule, dibromododecane, was used to try and make hierarchical chemically linked multilayers three-dimensionally above a gold substrate. After producing thioacetyl groups from the bromines as performed in the production of AcS-12C-BC, attempts were made to use the terminal thioacetate group as the basis of the linking strategy. Once a monolayer was formed, maleimide and disulfide chemistry was used, which had been used successfully in the past to immobilise thiolated DNA to thiol-terminated monolayers (209) (figure 3.26). However, XPS analysis showed poor results with 10 – 15% attachment of 1,4-di(maleimido)butane and no noticeable change in the sulfur ratio with the disulphide. In the experiment, deprotection of the terminal

thioacetate group is necessary to allow bond formations with the resulting sulfhydryl group.

XPS analysis here showed little change after an attempted deprotection in hydroxylamine

solution or with immersion in a concentrated solution of NH_4OH for over 16 hours. This may

indicate that thioacetate deprotection becomes less efficient when the molecule is constrained

to the substrate rather than floating in solution, possibly due to the likely close-packed

arrangement of the terminal groups with may provide steric hindrance to reactions. However,

as the surface density of AcS-12C-BC is lower than expected for alkanethiols, it is an open

question whether the strategy may yield better results with the anticipated greater distance

flexibility of the terminal thioacetates. This has not yet been explored further however, due to

the finite amounts of AcS-12C-BC synthesised, but the possibility remains for future

experiments.
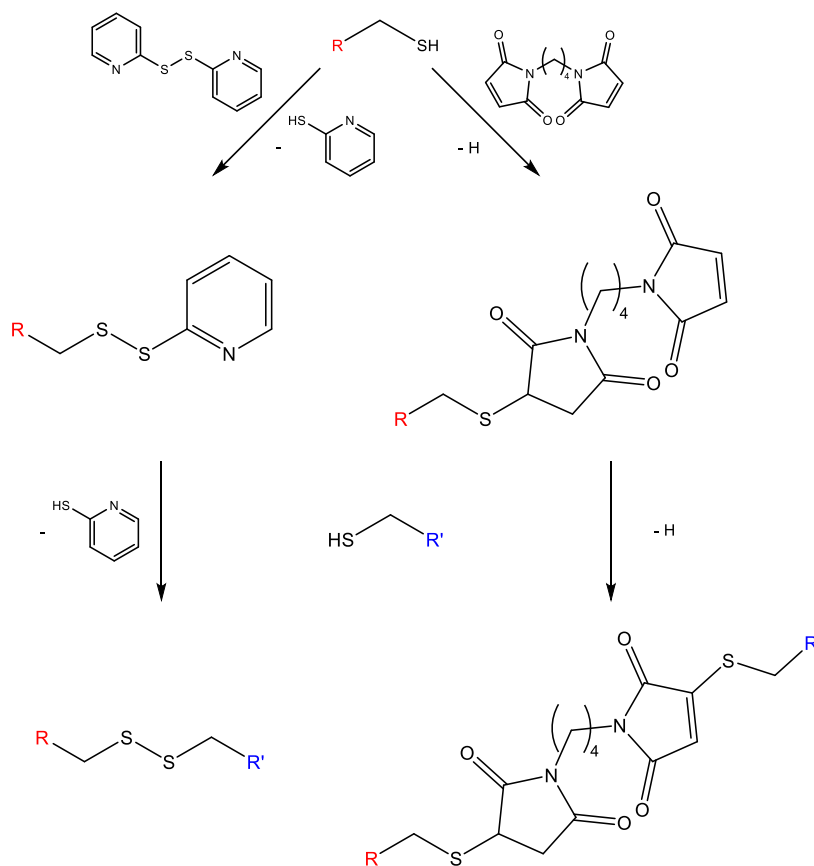
Figure 3.26: Potential strategies for linking thiol-functional molecules, such as the bifunctional AcS-12C-BC, using disulphide or maleimide crosslinking chemistry (209).

4. Conclusion

An artificial bacteriochlorin has been successfully derivatised with two long-chain anchoring groups terminated with alkanethiolate protecting groups and assembled into monolayer structures on gold substrates. While the conversion reactions from the synthesised macrocycle to the final product are efficient, the total synthetic scheme suffers from the drawback of an intensive number of transformations and the large-scale disparity between the original unsaturated ester and the new molecule, AcS-12C-BC. However, this route does allow the production of stable bacteriochlorophyll analogues with exploitable functional groups.

Using various surface characterisation techniques, this new molecule has been suggested to bind in a monodentate fashion to the gold substrate via one of these thiolates, leaving the other as a terminus to the monolayer. While it may be possible that bidentate attachment may also occur within this system, it is not indicated to occur by a significant degree by the XPS analysis or by the isotherm obtained by ellipsometry. The monodentate formation appears to be favoured, perhaps as it could give a slightly greater surface density of molecules than a bidentate binding mode. However, the calculated molecular surface density of AcS-12C-BC was found to be a significantly lower fraction of the commonly observed density for simpler alkanethiols in the literature. This is highly likely to be due to the large dimensions of the central bacteriochlorin. From ellipsometry measurements, an estimate for the tilt angle of an idealized conformational model is given as 29.17°. The measurements may also be explained by the lower density, which could reduce the stabilising intermolecular interactions between the anchoring alkyl chains which would increase their conformational flexibility. However, *J-/H*-aggregation of the bacteriochlorins could contribute to the molecular ordering. Using ellipsometry and XPS techniques, adsorption isotherms indicate

that the adsorption of AcS-12C-BC may include a longer re-organisation process than typically observed for alkanethiolates, possibly where maximization of the π-π stacking interactions resulting in aggregation takes place. The indication of a maximum monolayer thickness for AcS-12C-BC from the Langmuir isotherms also suggests an optimized packing of the final monolayer was also achieved. Despite the low surface density of molecules, it is therefore feasible that the organization is akin to the idealized model, perhaps with some limited conformational variability.

The coupling of the excitons corresponding the Q_x and Q_y dipoles with plasmonic fields associated with arrays of gold nanostructures results in a calculated exciton energy between these two dipoles and a coupling energy below the strong coupling regime. The former suggests that the dipoles of AcS-12C-BC are misaligned with the plasmon field direction when organized. The calculated exciton energy may therefore indicate a simultaneous coupling interaction between the two dipoles and the plasmonic field. The later result indicates this hybrid system may not breach the barrier for strong coupling. The lower density of dipoles in the plasmon mode compared to light-harvesting complexes may explain this. However, the harmonic oscillator model used here may not describe the full coupling dynamics between the plasmon mode and the two excitons in the bacteriochlorin. The relatively small range of E_{mol} and E_C in these systems however suggests that the bacteriochlorophylls are organized within the plasmonic field, so this method of emitter organisation may be useful with refinement. In future, co-adsorption of smaller-chain alkanethiols with AcS-12C-BC may also help with the conformational organisation of the resulting monolayer while maintaining the same surface density.

Subsequent attempts for study of multilayers of AcS-12C-BC also shows that a mere increase in the number of dipoles by physisorption does not result in an increase in coupling. For the design of strong coupling chlorophyll systems, control of the orientation of the

dipoles in relation to each other and the plasmonic field is all-important. To achieve this in future, the design of these systems can take two routes – the incorporation of efficiently-formed linkages between chlorins which will allow for correctly-oriented dipole-dipole coupling as well as increasing the number of dipoles within the plasmon field volume, and the use of a scaffold material which perform the same function. The potential to achieve these goals is available using artificial bacteriochlorin analogues, which could be accessible by a wide range of chemical approaches using the ester functional groups exploited here.

Chapter 4: Coupling of naturally-derived chlorophylls with three-dimensional polymer brushes as an excitonic composite material

1. Introduction

In strong coupling, the plasmon mode couples collectively to an array of emitters arranged within the plasmonic field volume. In light-harvesting complexes, these emitters are effectively organised in space by the protein structure. When these complexes are coupled to the plasmon mode, the arrangement of the excitons controls the coupling energy. In principle, the peptide scaffold may be replaced by an alternative scaffold by which the organisation can be controlled. A polymer scaffold could be used for this purpose, in particular polymer brushes.

In this chapter, the possibility of using a polymer brush as a scaffold to organise chlorophylls within the plasmon mode is investigated. Polymer brushes are surface-grafted polymers. In the grafting-to method, the polymer is pre-formed and attached to a surface. In the grafting-from method, however, the surface is modified to introduce an initiator and the polymer is grown by surface-initiated graft polymerization (figure 4.1). The brush thickness is controlled by the degree of polymerization but may also depend on the nature and density of any pedant groups, the presence of charged group and the nature of the polymer-solvent interactions. Polymer brushes are a well-understood system that has been studied for many years utilising a high variety of monomers (210, 211).

For immobilization of chlorophylls to a substrate, there may be advantages to using brushes as scaffolds. One is the controllable thickness of the brush layer. Chlorophyll monolayers are two-dimensional structures. However, if chlorophylls could be attached to the

Polymer/oligomer bound to substrate

Monomer

Initiator

Catalyzed polymerization
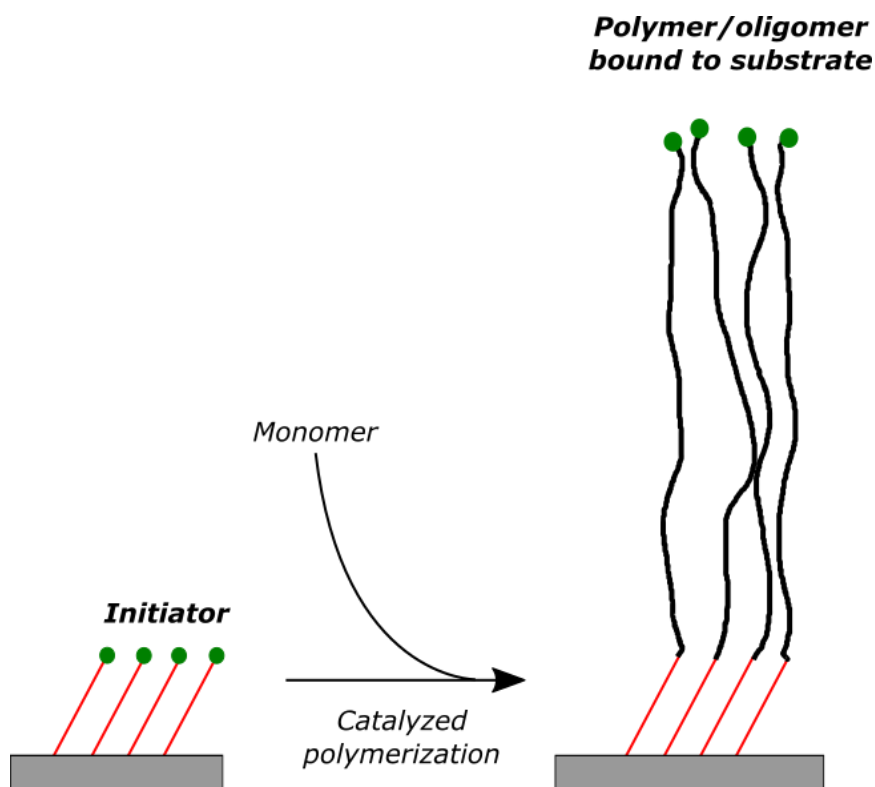
Figure 4.1: A general scheme for the growth of brush structures on a substrate using surface-initiated graft polymerization. The initiator groups for the polymerization are indicated in green.

pedant groups of a polymer brush then three-dimensional control of their organisation would be possible. This may allow stronger coupling of the plasmonic field to the exciton states of the chlorophylls, because according to the microscopic theory of strong coupling the coupling energy is proportional to the density of the dipoles in the mode volume. Another characteristic of interest could be the branched nature of brush materials. Most brush functional groups are present in a side-chain which stretches away from the main polymer "stem", especially of a brush is fully extended perpendicular to the plane of the substrate. It could be possible that this geometry allows the coupling of exciton bands which are not observed in the LH2 strong coupling experiment, i.e. the Q_y band, and thus allow coupling of its exciton state with the plasmonic field. There is also the possibility of studying the distance dependence of strong coupling by exploiting the controlled thickness of brush layers. There are numerous examples of brushes which are responsive to various conditions such as

changing solvents, temperature, pH and ionic strength (212). These characteristics thus make nanostructured brushes an attractive material to couple chlorophylls to plasmonic arrays on gold, where solvent responsive changes could be observed.

a) *Synthesis of polymer brushes*

The most widely used grafting-from approach of polymer brush synthesis is surface-initiated atom transfer radical polymerization (SI-ATRP). This is based on a well-studied "living" polymerization method utilising the transition metal-catalysed generation of reactive radical initiators, which then react with monomers to propagate radical chain growth (figure 4.2) (211, 213).

In SI-ATRP, the surface is modified to introduce initiators for ATRP. In the most wide-used approach, the initiator has a halogen leaving group and a Cu^I catalyst is used to generate radicals at the surface. Monomer chains containing vinyl groups then react with the radicals, adding the molecule to the initiator and forming a new radical on the chain end. These radical reactions are self-propagating, adding more monomer units over time to produce polymer chains. These reactions can then be terminated by reversible deactivation by the Cu^{II} complex generated from the initiation, re-inserting the halogen leaving group to the chain end. ATRP is compatible with a large family of monomers with both charged and neutral species capable of using the mechanism (211). One inconvenient aspect of this method however is that oxygen must be rigorously excluded from the reaction mixture. Free carbon radicals are well known to react rapidly with oxygen to produce oxidised species (214), as well as poisoning the Cu^I catalyst to reduce the efficiency of its catalytic activity. This results in poorly controlled surface polymerizations.

However, using in-situ reduction mechanisms enable the synthesis to be carried out in the presence of air, in a process known as Activators (Re)Generated by Electron Transfer
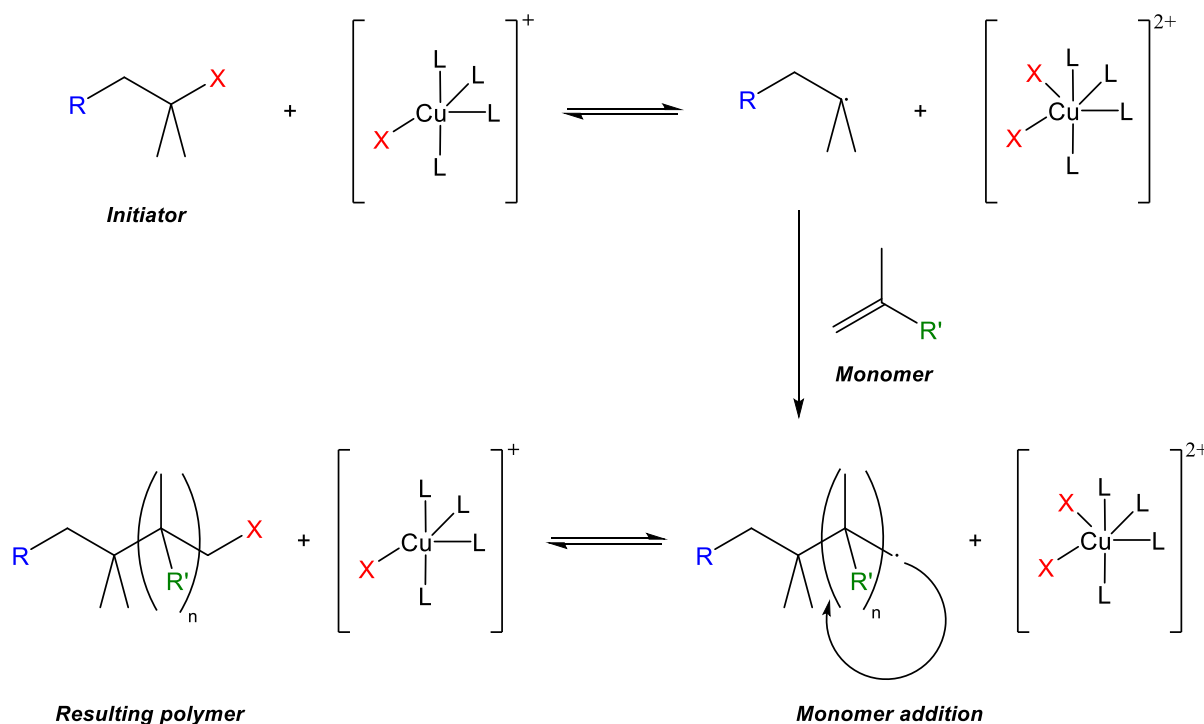
Figure 4.2: The general scheme of the ATRP mechanism, illustrating the generation of radicals and continual addition of monomer units before reversible deactivation of the process.

ATRP (AGET/ARGET ATRP) (215 - 217). In AGET-ATRP, the reaction solution is prepared only using a Cu^{II} catalyst complex, which is air-stable in solution. This mixture is then activated by the addition of a reducing agent, such as ascorbic acid. This agent reduces the Cu^{II} species to the active Cu^{I} species, which then activates the initiator to start the polymerization, with the oxidised side-product as a result. The amount of Cu^{I} generated can be controlled by the molar amount of reducing agent, thus a small number of initiators can by activated and give a controlled polymerization. The reducing agent also scavenges the oxygen present in the reaction solution, eliminating the need for deoxygenation. The polymerization is tolerant to a range of concentrations of reducing agent, but it must be effectively controlled as excess agent can result in excess Cu^{I} generation, and therefore an uncontrolled polymerization. For this reason, the ARGET modification was developed, where a reduced amount of catalyst (down to less than 1000 ppm) with a slow-reacting reducing

agent results in continual regeneration and consumption of Cu^I in a controlled manner with larger excesses of reducing agent (figure 4.3) (216, 217).
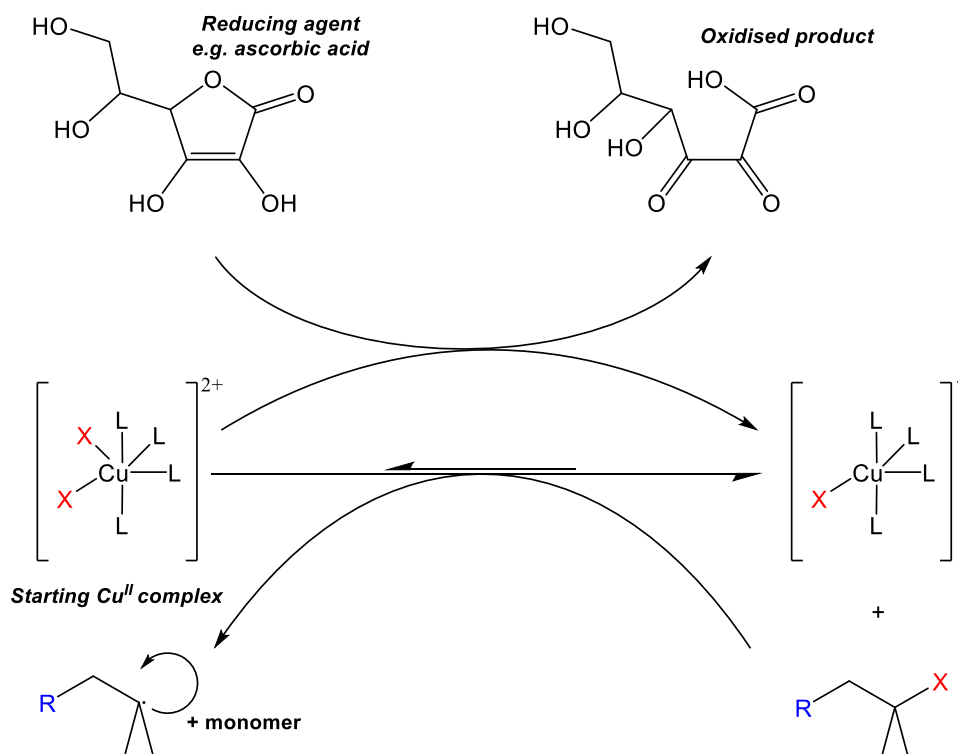
Figure 4.3: The ARGET-ATRP mechanism entails the continuous slow generation of the Cu(I) complex by reduction with small amounts of ascorbic acid, which then generates the initiator radicals in a controlled manner.

### b) *Brush behaviour with solvent and pH conditions*

Most brushes experience changes in layer thickness and conformation depending on the solvent in their environment, mediated by any favourable (or unfavourable) interactions of the brush with the solvent molecules. Where there is no solvent, in air for example, the lack of interactions makes the brush adopt a collapsed formation defined by inter-polymer interactions. In a good solvent, the maximization of polymer/solvent interactions will result in a swelling of the brush away from the surface, solvating the individual polymer chains (figure 4.4). In a poor solvent, the unfavourable interactions result in the collapse of the brush, where

no solvent can penetrate into the organic layer. These surface changes can be measured by surface analysis techniques such as ellipsometry and atomic force microscopy carried out under liquids. For example, poly(methyl methacrylate) (PMMA), containing hydrophobic methyl and methyl ester groups, collapses when exposed to water, but a non-polar solvent like THF solvates the brush well and it swells (218).
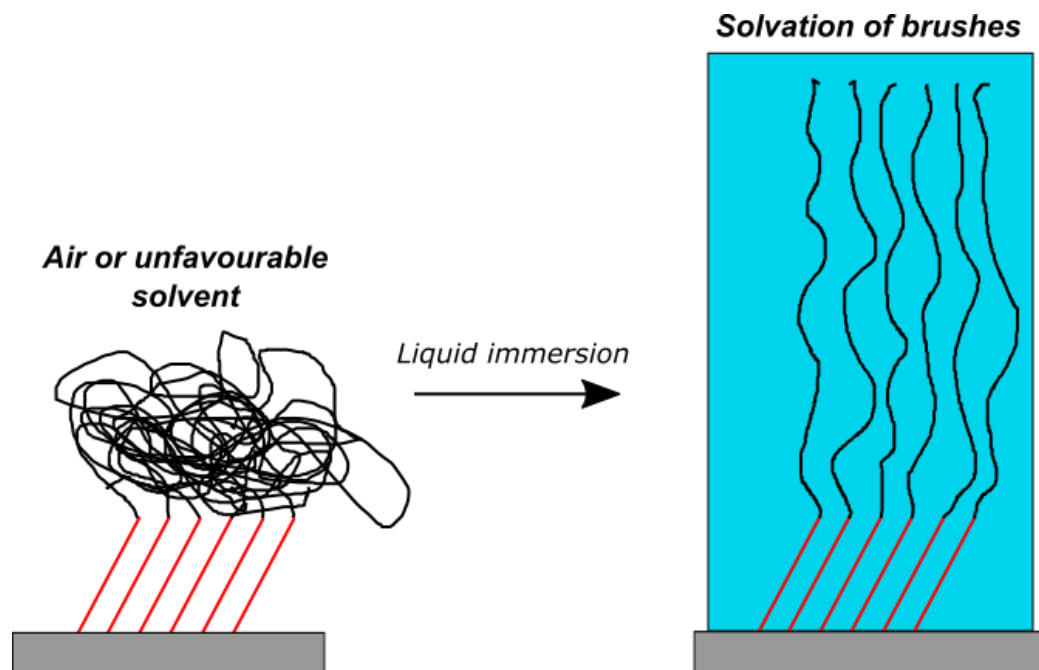
Figure 4.4: Polymer brushes can adopt different conformations depending on environmental conditions. In air, most brushes are collapsed in a "mushroom" shape. Using a solvent with favourable interactions with the brushes' side groups then causes expansion of the brush, increasing the apparent height.

There are many brushes which have been synthesised with polar groups capable of hydrogen bonding, such as hydroxyls, and with charged groups such as carboxylates, ammonium ions and sulfonates (211). These brushes tend to swell in polar solvents such as water, and collapse in non-polar liquids (219, 220). Polyelectrolyte brushes have been useful for applications in aqueous conditions, particularly when studying biological entities and their interactions with functionalised surfaces. Poly(cysteine methacrylate) (poly(CysMA)) is a

new poly(amino acid methacrylate) that can be grown from surface-bound initiators by ATRP (221). The monomer is produced by coupling cysteine to a methacrylate acrylate via a thiol-Michael addition; consequently, the pedant group is zwitterionic. When immersed in water, the height of the brush layer measured by AFM and ellipsometry under liquid increases to approximately twice the dry thickness. The brush is also pH responsive due to its zwitterionic properties (figure 4.5). Between pH 2 – 9, the brush layer height remains within a narrow range. However, at pH < 2, the brush becomes cationic in overall charge and swells by a further 50%, while at pH > 9 it is anionic and swells by the same degree. Repulsive forces between the charges at these pH extremes therefore cause the brush layer to expand to approximately 3 times the dry thickness.
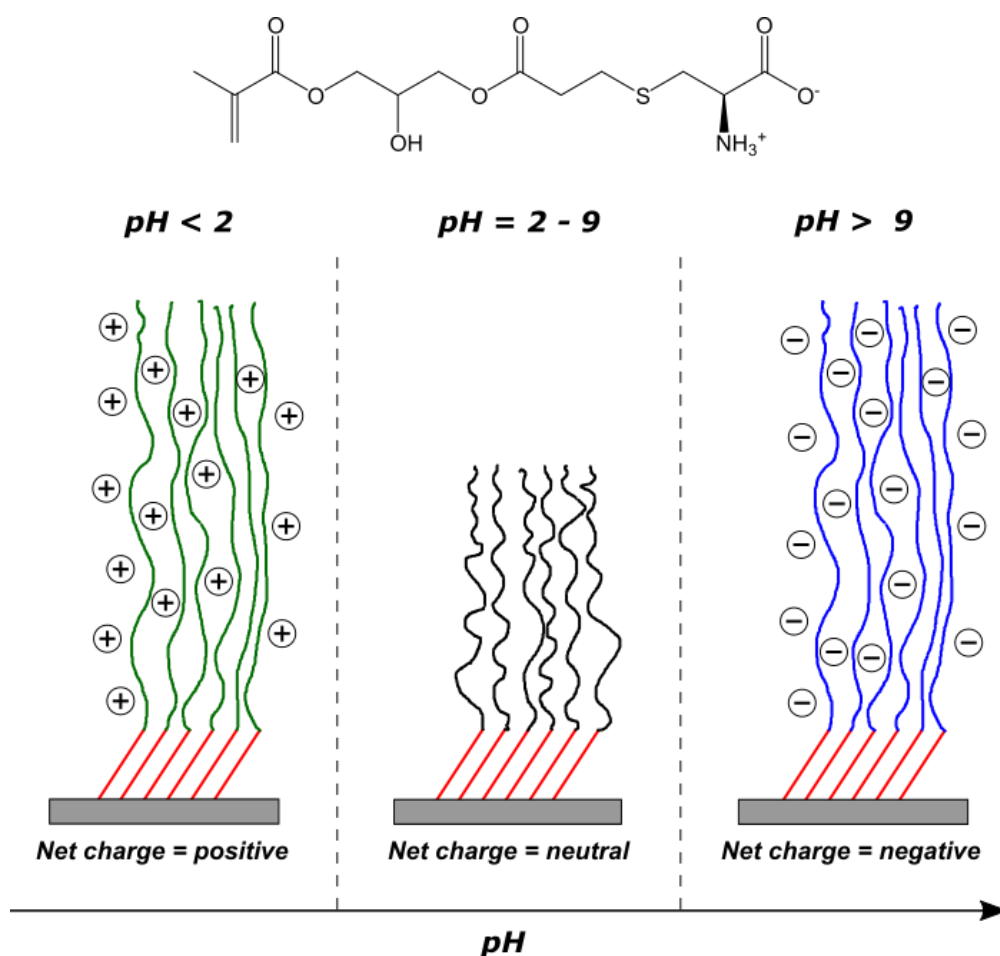
Figure 4.5: *The pH response of surface-bound poly(CysMA). Zwitterionic characteristics inherent in the monomer result in net cationic or anionic charge in extreme pH. This leads to electrostatic repulsion between polymer chains and therefor brush expansion.*

Swelling behaviour will influence the strategy used to attach the chlorophylls to the brushes. The amount of swelling of the brush is an important factor when considering the access that a coupling reagent will have to the brush's functional groups. An extended brush layer will allow a molecule better access to compatible groups, but a collapsed brush will only show derivatisation at the surface of the brush layer (222).

c) *Postpolymerization functionalisation*

Polymer brushes incorporating functional groups as side chains can be modified after polymerization, imparting new properties on the bush or as a scaffold for a molecule of interest. The degree of derivatisation can be dependent on the swelling of the brush in the solvent medium as well as the density of the polymers in the brush layer (figure 4.6).

A large variety of polymer brushes with oxygen-derived organic side groups such as hydroxyls, carboxyls and epoxides have been modified in the past (211). Hydroxyl modification on a brush such as poly(hydroxyethyl methacrylate) (poly(HEMA)) utilises simple well-understood organic reactions (223). However, the sensitivity of these reactions to water precludes aqueous solvents. By contrast, carboxylates can be derivatised in very mild conditions (224, 226). Recently, the modification of poly(CysMA) brushes was reported (222). The pedant amines on the brush can be derivatised in mild conditions, due to the zwitterionic equilibrium between the charged and neutral forms. As such, the surface amines were derivatised with glutaraldehyde and N_α,N_α-bis(carboxymethyl)-L-lysine hydrate to give a brush-terminating Ni-nitrilotriacetic acid complex, capable of chemisorbing proteins by binding to histidine residues. The properties of poly(CysMA) can therefore be changed using a postpolymerization modification strategy targeting the functional amines in the brush.

Once new groups are attached, the quantification of attachment to the brush can be performed using surface analysis such as XPS. For example, PGMA postmodified both with

propylamine and BSA protein was analysed to compare the relative degrees of incorporation through the brush layer as a function of depth (226). It was found that the amount of derivatisation depended on molecular size. Propylamine, a small and simple molecule, was able to diffuse evenly through the brush structure to give homogeneous distribution of attached groups. For BSA however, its large macromolecular size means only the uppermost layer of the brush was derivatised. This illustrates that size does indeed matter at two extremes – the smallest molecules will diffuse throughout the brush while large biomolecules are diffusion limited. However, large structures can be diffused into polymer brush layers by lowering the density of the polymers on the surface (the grafting density). Increasing the separation between polymer chains reduces the frictional force on the additives, thereby increasing the diffusion coefficient of the additives (227, 228). XPS techniques analysing composition as a function of depth can be used to determine the distribution of additives diffused through the polymer layer (226, 229, 230).
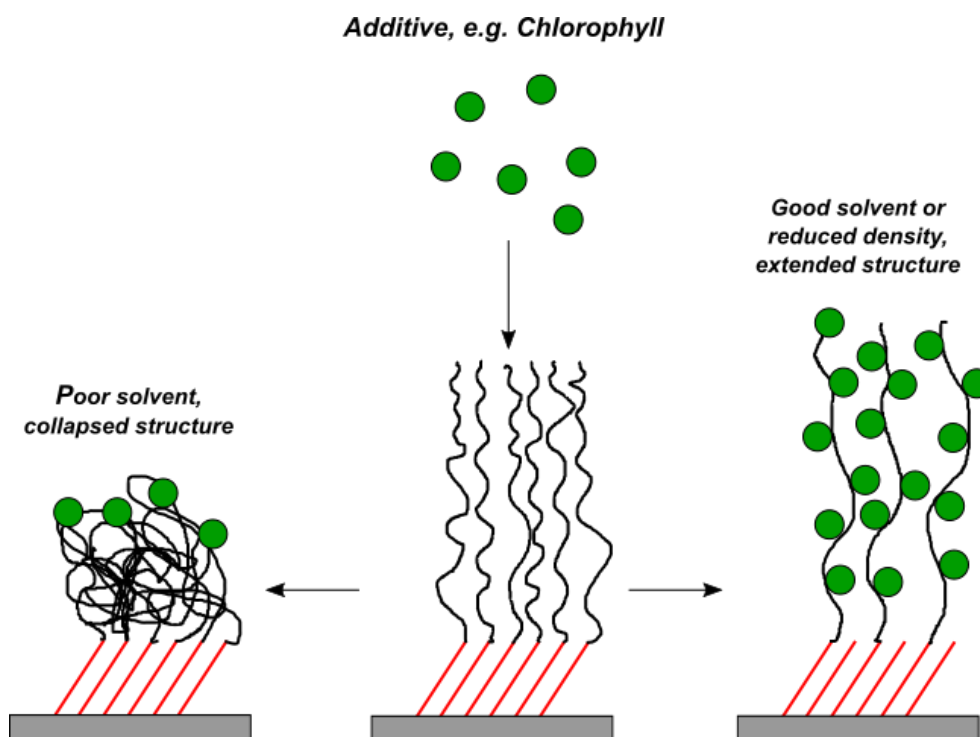
Figure 4.6: *The post-polymerization of polymer brushes with additives. Tightly-packed brush layers result in "capping" of the surface, whereas extended conformations or reduced brush density allows access down the length of the brushes.*

d) ***A synthetic strategy for attaching chlorophylls to responsive polymer brush***

scaffolds

After extraction of the pigment from a natural source, chlorophyll *a* can be modified

by a series of reactions to give a reactive carboxylic acid group for conjugation to other

species and structures (231, 232). This group has been used previously to graft derivatives of

chlorophyll *a* to structured surface systems.

In studies carried out by Furukawa and co-workers, chlorophyll *a* and the modified

pyrochlorophyllide *a* were deposited onto mesoporous silica films to construct an energy

transfer system (233, 234). Here, the modified chlorins were reacted with 1-(3-

dimethylaminopropyl)-3-ethylcarbodiimide hydrochloride (EDC) in the presence of 3-

aminopropyltriethoxysilane (APTES) – the carboxylic acid is made more reactive via EDC

coupling to form an acylisourea active ester, which is then receptive to nucleophilic attack by

the amine functional group on APTES to form a stable amide and an isourea by-product.

Attached to a reactive group for monolayer formation on hydroxyl-terminated silicon

surfaces, these chlorophylls could then be self-assembled into the films. Using the same

chemistry, these pyro-chlorophyllides could be attached to systems containing amine

residues, including polymer brushes.

One disadvantage of this direct coupling via the use of carbodiimides is the high

susceptibility of the intermediate to hydrolysis. A much higher efficiency can be achieved by

the formation of an active ester by introducing N-hydroxysuccinimide (NHS) to the reaction

mixture (235, 236). In dry solution, the hydroxyl group on NHS can act as a nucleophile to

attack the acylisourea ester, forming an N-hydroxysuccinimidyl ester. These esters exhibit a

similar reactivity towards amines, while being more selective for them over hydroxyls and

have a longer lifetime in aqueous solutions. This has made these reactions popular for

chemistry occurring in physiological conditions such as protein crosslinking (237) and

protein specific immobilization on carboxylic acid-terminated monolayers (238).
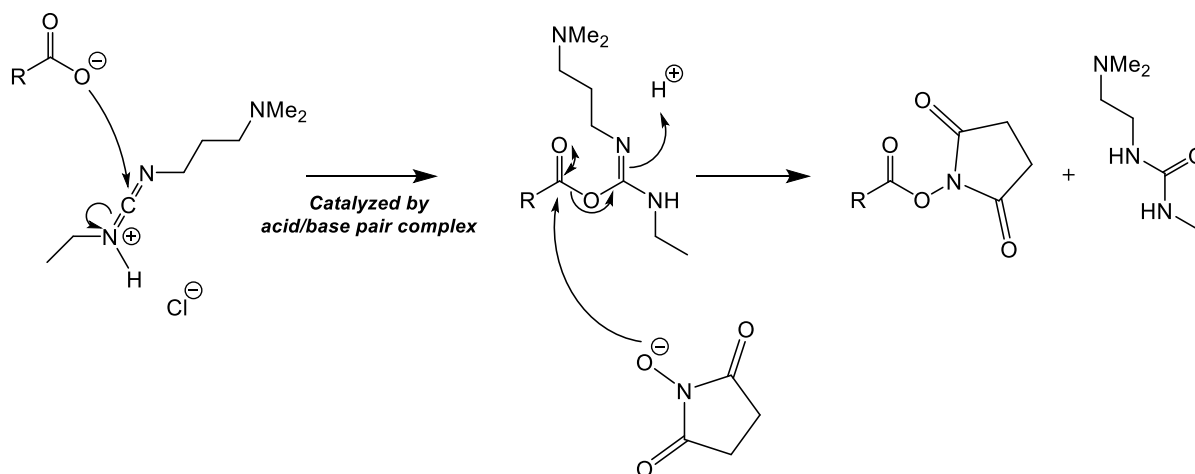
Figure 4.7: The mechanism of EDC-mediated cross coupling to give a succinimidyl active ester.

For such a coupling, an amine-functional polymer brush would be ideal for the most

efficient attachment possible, preferably in the form of the most nucleophilic primary amine.

Poly(CysMA) is compatible with such a coupling reaction, because in water the amine is in

equilibrium between the neutral and cationic forms. In its uncharged form, the amine is a

good nucleophile and can attack an active ester to yield an amide bond.

e) Aims

A modified chlorophyll *a* derivative will be produced, extracted from spinach leaves

followed by a series of simple transformation steps, with an accessible carboxylic acid

reactive group. This will be converted to an N-hydroxysuccinimidyl ester for attachment to

poly(CysMA) brushes grown from surface by ARGET-ATRP (figure 4.8). To determine the

optimum coupling conditions, the derivatisation of the brushes will be performed in solvents

of varying composition. To control steric factors, brushes will be used that exhibit a range of

densities. Exciton spectra for brushes grown on gold nanoparticles will be analysed to test for

plasmon-exciton coupling in these systems.
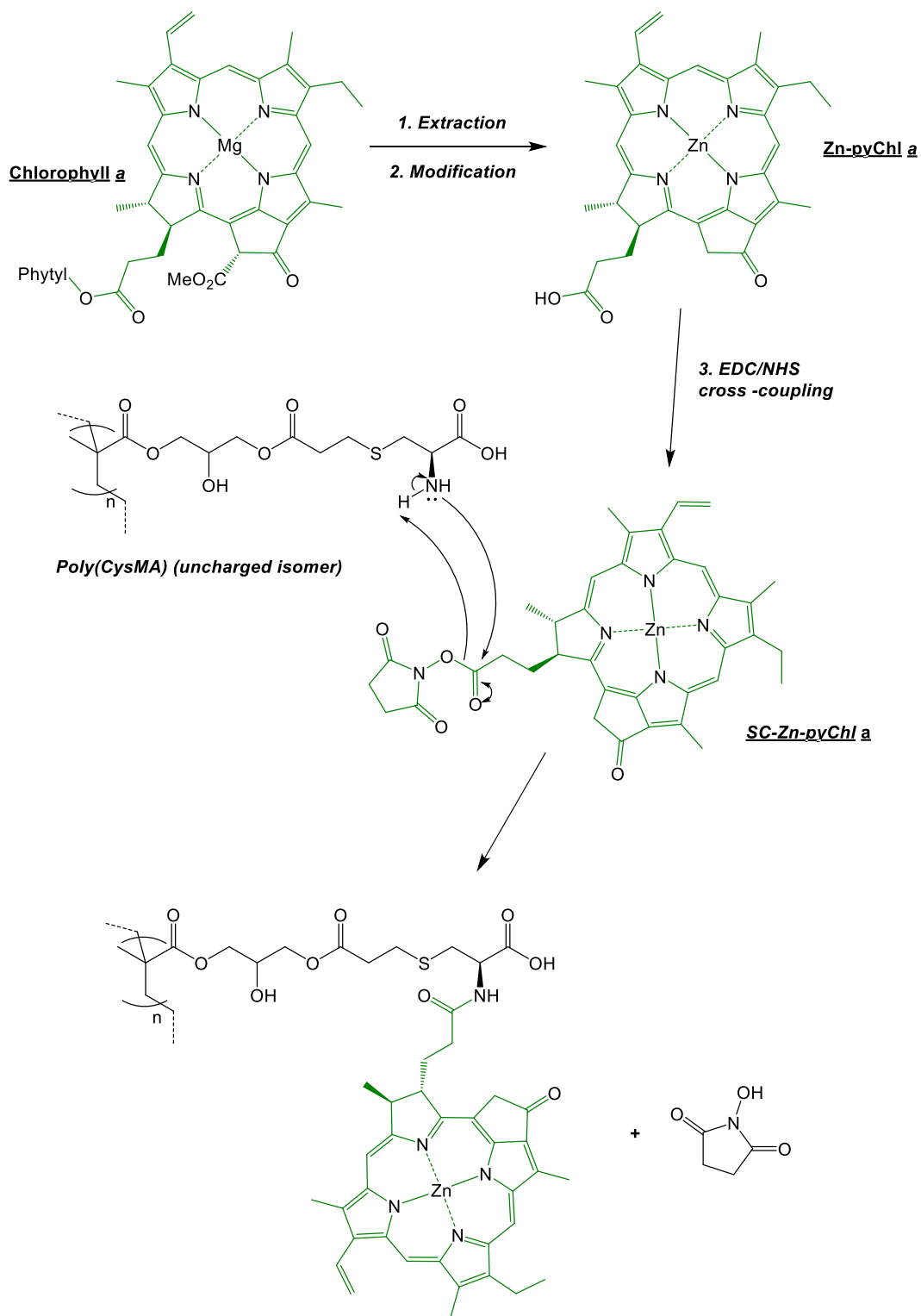
Figure 4.8: The proposed reaction scheme for conversion of chlorophyll a *into pyrochlorophyllides with an active ester, for reaction to the pedant amine groups of poly(CysMA) brushes.*

2. Experimental Section

a) *Extraction and synthesis of n-hydroxysuccinimidyl zinc-pyrochlorophyllide a*

i. **Extraction of pheophytin *a*.** Spinach leaves (500 g) were procured from a local supermarket retailer. These leaves were prepared by cutting the stems and mid-veins from the leaves and discarding them, followed by washing with deionised water. These were then dried on paper and then frozen for 16 hours at -20 °C. This matter was then macerated in 6 instalments by placing the leaves in a blender with acetone (250 mL) and stirring on a pulse setting for several minutes until a dark green slurry was obtained. The extract was then filtered by standard vacuum filtration to separate the dark green liquid from the leftover pulp. The acetone and some remaining water were then removed by rotary evaporation to give a dark green substance. This was extracted from remaining water first using petroleum ether 40-60°C (3 x 200 mL) followed by washing with 60% aqueous MeOH (1 x 250 mL, 2 x 100 mL). The resulting organic layer was dried over $MgSO_4$, filtered and the solvent removed, leaving a green solid.

To simplify the separation process, all the chlorophylls present in this initial mixture were reduced to their non-metallated pheophytin variants. Here, the solid was dissolved in glacial acetic acid (25 mL) and stirred for 3 hours at room temperature. The solution was then neutralised to pH 7 with careful addition of saturated aqueous sodium hydrogen carbonate solution. A brown precipitate was formed in this solution. This precipitate was then extracted from the water layer using CH_2Cl_2 (3 x 100 mL) and the combined organic layer washed with water (3 x 100 mL) before drying and solvent removal as before. The resulting brown solid was then purified by column chromatography (silica, 6:3:2 n-

hexane: Et$_2$O: acetone) to give pheophytin *a* as a black solid (235 mg, 0.288 mmol). R$_f$ = 0.33 (6:3:1 hexane: Et$_2$O: acetone); LC-TOF-MS ES+, obsd *m/z* = 872 (17.191 minutes), calcd = 871.22 [(M + H)$^+$, M = C$_{55}$H$_{74}$N$_4$O$_5$].

ii. **Methyl pyropheophorbide *a* (Me-PyPh *a*).** Extracted pheophytin *a* (312 mg, 0.358 mmol) was dissolved in pure 2,4,6-collidine (20 mL) and the vessel backfilled with an argon atmosphere. This solution was then stirred at 130 °C with a reflux condenser under argon for 16 hours. Once complete, the collidine was removed using a high-vacuum rotary evaporator (70 – 80 °C, 1 – 4 mbar) to give a brown solid. This solid was then immediately dissolved in CH$_2$Cl$_2$ (20 mL) with the addition of H$_2$SO$_4$ solution (5% in MeOH, 20 mL) and stirred at room temperature, again under argon, for another 16 hours. The organic mixture was then diluted with CH$_2$Cl$_2$ (100 mL), washed with water (3 x 100 mL) and once with 10% aqueous NaHCO$_3$ (100 mL), followed with drying with MgSO$_4$ and solvent removal as before. The resulting solid was then purified by column chromatography (silica, 6:3:2 n-hexane: Et$_2$O: acetone) to give a brown solid (102 mg, 0.186 mmol, 52%): R$_f$ = 0.48; LC-TOF-MS ES+, obsd = 549 (14.006 minutes), calcd = 548.69 [(M)$^+$, M = C$_{34}$H$_{36}$N$_4$O$_3$].

iii. **Pyropheophorbide *a* (PyPh *a*).** Me-PyPh *a* (102 mg, 0.186 mmol) was dissolved in THF (25 mL) to which aqueous lithium hydroxide monohydrate (3 M, 10 mL) was added. This mixture was stirred under argon at room temperature for 18 hours. Once complete, the solution was neutralised with addition of 3 M aqueous HCl dropwise until pH 7 was reached according to universal indicator paper. The organic layer was then extracted with CH$_2$Cl$_2$ (3 x 50 mL), washed with water (3 x 100 mL) followed by brine (100 mL), then dried with MgSO$_4$, filtered and evaporated as before. This resulted in a black solid (71

mg, 0.138 mmol, 74%): TOF-MS ES+, obsd = 535.1, calcd = 534.66 [(M + H)$^+$, M = $C_{33}H_{34}N_4O_3$].

iv. **Zinc-pyrochlorophyllide *a* (Zn-pyChl *a*).** PyPh *a* (71 mg, 0.138 mmol) was dissolved in CH_2Cl_2 (35 mL) and saturated zinc acetate monohydrate in MeOH (4 mL) was added to this. The solution was then refluxed at 35 °C under argon for 40 minutes, after which the solution was observed to changed colour form dark brown to dark green. The organic layer was then extracted with Et_2O (40 mL) followed by washing with water (3 x 50 mL). Drying with $MgSO_4$, filtration and solvent removal were then carried out as before to give a blue-green solid (66 mg, 0.110 mmol, 80%): ^1H NMR (400 MHz, acetone-d^6) δ (ppm) = 1.71 (q, J = 7.33, 3H), 1.85 (d, J = 7.24 Hz, 3H), 2.25 (m, 2H), 2.37 (m, 2H), 3.29 (s, 3H), 3.39 (s, 3H), 3.61 (s, 3H), 3.81(q, J = 7.33 Hz, 2H), 4.40 (d, J = 8.91 Hz, 1H), 4.63 (q, J = 7.24 Hz, 1H), 5.02 (d, J = 19.67 Hz, 1H), 5.16 (d, J = 19.67 Hz, 1H), 6.05 (d, J = 11.69 Hz, 1H), 6.23 (d, J = 18.06 Hz, 1H), 8.16 (dd, J = 11.69, 18.06 Hz, 1H), 8.66 (s, 1H), 9.42 (s, 1H), 9.70 (s, 1H), 10.57 (broad s, 1H); TOF-MS ES+, obsd = 597.2, calcd = 598.024 [(M − H)$^+$, M = $C_{33}H_{32}N_4O_3Zn$]; IR (CH_2Cl_2 solvent, cm^{-1}) = 3500 − 2400 (broad band, O-H stretch), 3010 (sp^2 C-H stretch), 2926, 2858 (sp^3 C-H stretch), 1711 (C=O stretch), 1460 (aromatic C=C stretch), 1375 (C-O stretch); UV/Vis (nm) = 433 (Soret), 578 (Q_x), 659 (Q_y); HPLC (21 min, 75% Acetonitrile in H_2O (0.1% trifluoracetic acid), detection = 254 nm) = 12.4 min, 96.8%.

v. **Succinimidyl zinc-pyrochlorophyllide *a* (SC-Zn-pyChl *a*).** Zn-pyChl *a* (10 mg, 1.67 x 10^{-5} mol) was mixed with dimethylaminopyridinium tosylate (DPTS, 5 mg, 1.7 x 10^{-5} mol), N-hydroxysuccinimide (NHS, 20 mg, 0.174 mmol) and crystalline n-(3-dimethylaminopropyl)-*N'*-ethylcarbodiimide hydrochloride (EDC, 22 mg, 0.115 mmol),

followed by evacuation and backfilling with argon. The mixture was then dissolved in dry

CH_2Cl_2 (36 mL) under an argon atmosphere, and the resulting solution was then stirred

for 16 hours at room temperature under argon. Once complete, the solution was diluted

with CH_2Cl_2 (50 mL) and washed with water (2 x 50 mL) and once more with saturated

brine solution (50 mL). The organic layer was then dried with $MgSO_4$, filtered and

evaporated as before to give a green solid (11 mg, 1.58 x 10^{-5} mol, 95%). TOF MS LD+:

expected = 695.097 g.mol^{-1}, observed = 693.5 [(M − 2H)$^+$, M = $C_{37}H_{35}N_5O_5Zn$].

b) *Synthesis, brush growth and chlorophyll attachment to poly(CysMA)*

vi. **Synthesis of cysteine methacrylate (CysMA).** L-Cysteine (7.54 g, 62.23 mmol) was

dissolved in 100 mL of deionised water, and to which 3-(acryloyloxy)-2-hydroxypropyl

methacrylate (13 mL, 14.86 g, 69.36 mmol) and dimethylphenyl phosphine (20 μL, 1.94

μg, 1.41 x 10^{-8} mol) were added. The cloudy solution was then stirred at room

temperature for 2 hours, after which time the solution became colourless. Once complete,

the water layer was washed with EtOAc (2 x 100 mL) followed by CH_2Cl_2 (3 x 100 mL).

The water was then removed by rotary evaporation at 55 – 60 °C to produce a white solid.

After collection, the solid was then dried under reduced pressure for 48 hours, with

analysis confirming the CysMA monomer (16.175 g, 48.12 mmol, 77%). ^{1}H NMR (400

MHz, D_2O) δ (ppm) = 1.86 (s, 3H), 2.60 – 3.15 (m, 6H), 3.74 (m, 1H), 3.84 (m, 1H), 4.08

– 4.43 (m, 4H), 5.67 (s, 1H), 6.09 (1H); ^{13}C NMR (400 MHz, D_2O) δ (ppm) = 17.37,

26.41, 32.18, 33.95, 53.61, 65.27, 65.34, 66.90, 127.18, 135.66, 168.72, 172.75, 174.14;

TOF MS LD+: expected = 335.37 g.mol^{-1}, observed = 336.0 [(M + H)$^+$, M =

$C_{13}H_{21}NO_7S$]; HPLC (30 min, 10% Acetonitrile in H_2O (0.1% trifluoroacetic acid),

detection = 225 nm) = 22.8 min, 90.0 %.

vii. **Grafting of poly(CysMA) brushes by ARGET-ATRP to gold substrates.** Chromium-

gold coated substrates were prepared as described in chapter 2. Samples for polymer

brush growth were cut from the slides (~ 22 x 5 mm) and immersed in a solution of bis[2-

(2-bromoisobutyryloxy)undecyl] disulfide (DTBU) in argon-degassed EtOH (2 mM) for

48 hours to form a bromine-terminated initiator monolayer. Once complete, solutions of

CysMA (750 mg, 2.231 mmol, 4 mL H_2O, 0.56 M), $CuCl_2$ (14.6 mg, 0.109 mmol, 5 mL

H_2O), 2,2'-bipy (38.8 mg, 0.248 mmol, 5 mL EtOH) and l-ascorbic acid (100 mg, 0.568

mmol, 10 mL H_2O, 56.8 mM). The $CuCl_2$ and 2,2'-bipy solution were mixed together to

form the vivid blue $Cu(bipy)_2Cl_2$ complex solution (10 mL, [$CuCl_2$] = 10.9 mM, [2,2'-

bipy] = 24.8 mM). To the CysMA solution, the ascorbic acid solution (0.18 mL, 1.02 x

10^{-5} mol) was added first, followed by the Cu/bipy solution (0.35 mL, n(Cu) = 3.82 x 10^{-6}

mol). The solution was then shaken to ensure complete mixing and left for 5 minutes, by

which time a brown colour had formed in solution, indicating the generation of active

Cu(I) complexes. A sample of gold/initiator substrate was then introduced to the solution

for polymer grafting. Polymer layer thickness was controlled by the length of time of

immersion. Once a desired time period of polymerization was reached, the sample was

withdrawn from the solution and washed well with deionised water. For storage, polymer

samples were washed again with EtOH and stored in degassed EtOH until required. This

same procedure was used for both unpatterned gold substrates and patterned gold

nanoarrays.

For samples studying the effect of decreasing brush density on chlorophyll attachment

efficiency, DTBU was mixed with 1-undecanethiol (UDT) in varying molar amounts, 1:1,

1:5 and 1:10, and dissolved in degassed EtOH to give a total concentration of 2 mM. Each subsequent step was then carried out in an identical fashion.

viii. **Attachment of succinimydyl zinc-pyrochlorophyllide *a* to solvated poly(CysMA) brushes.** Succinimydyl chlorophylls were either used straight after synthesis or stored under dry argon at − 20 °C to prevent hydrolysis before use. When needed, a 1 mM solution of SC-Zn-pyChl *a* was made by dissolving it in THF, DMF, 1:3 DMF: H_2O, 1:1 DMF: H_2O and 3:1 DMF: H_2O. Once dissolved, the chlorophyll solution was applied to cut poly(CysMA) samples of a volume of 0.5 mL (~ 5 x 5 mm samples) – 1.0 mL (~ 10 x 10 mm samples), and functionalisation allowed to occur for 16 hours. Once complete, samples were washed with DMF followed by deionised water and dried with an N_2 stream.

ix. **Ellipsometry characterisation under liquids.** Additional liquid measurements were carried out on the Alph-SE instrument using a liquid cell. DMF, PBS, Water and 1:3 DMF: H_2O were used as the solvent mixtures and fitted using an effective medium approximation (EMA) model (**Appendix 2 i)**). For pH measurements, 0.1 M HCl and 0.1 M NaOH were used with a measured pH of 1.35 and 12.71 respectively. These measurements were carried out on samples before and after functionalisation with SC-Zn-Chl *a*.

3. Results and discussion

a) Synthesis of succinimidyl-zinc-chlorophyllide a

Literature reports of the extraction of chlorophyll *a* from spinach rely upon solvent extraction using acetone. Here, two modifications were made. First, a blender was used to macerate the spinach in acetone, greatly enhancing the removal of pigments from the natural material after vacuum filtration and enabling larger amounts of organic material to be processed quickly. Second, instead of extracting chlorophyll directly we extracted the metal-free variant, pheophytin *a*. Pheophytins can be extracted in larger yields than metallated chlorophylls, and the reaction scheme required demetallated chlorophylls anyway. By treating the extracted and washed extract with glacial acetic acid, demetallation of the chlorophylls could be carried out before column separation, thus simplifying matters given the similar retention of the chlorophylls and pheophytins. Using this method, the desired product was obtained in higher yield than reported elsewhere, with 235 mg isolated from 500 g of spinach leaves. The increase makes the extraction somewhat more synthetically viable, and subsequent analysis by liquid chromatography mass spectrometry showed the purified pheophytin *a* had negligible traces of side products.

The modification of naturally derived chlorophyll *a* has been known in the literature, having been used to produce new functional chlorins, dimers and aggregates using a variety of approaches (27, 239 - 244). In the present work, the goal was to convert the phytyl group of chlorophyll *a* into a carboxylic acid that could subsequently be converted to an active ester (figure 4.9). This synthesis scheme is described in the literature (240). The five-membered ring is protected to prevent a ring-opening side reaction (231, 245) and transesterified in an acid-catalysed reaction with methanol to yield the methyl ester. The product was separated

with by flash column chromatography to remove unreacted pheophytin *a* from the mixture,

resulting in a 52% yield. At these stages, the identification of the desired products could only

be determined by mass spectrometry analysis, as attempts to use NMR analysis with CDCl$_3$

and acetone-d$_6$ solvents gave poorly-resolved spectra. As it appeared that large amounts of

these compounds were needed for well-defined spectra, NMR characterisation was saved for

the final target zinc-metallized chlorin.
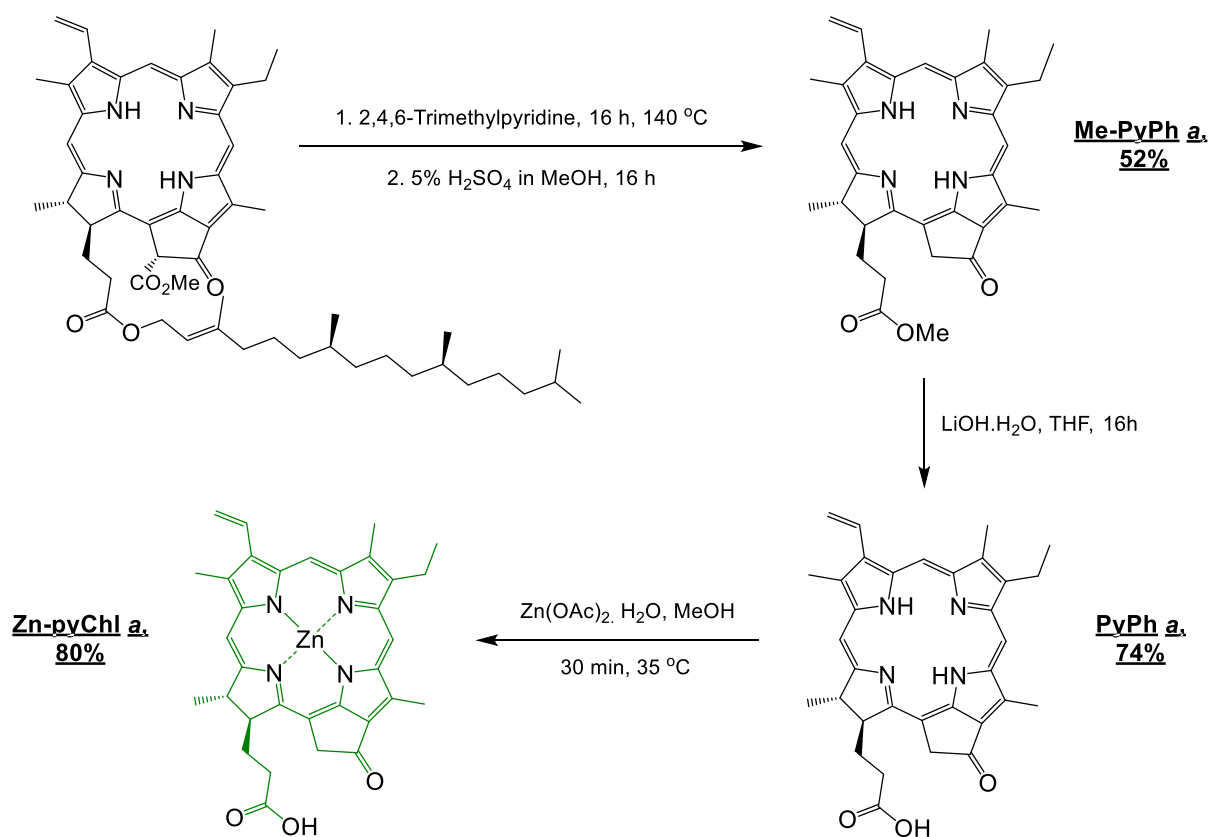
Figure 4.9: The modification scheme for extracted pheophytin a *to give a carboxylic acid group, allowing further reaction with NHS/EDC.*

The resulting methyl-pyropheophorbide *a* was hydrolysed by base in a 2.5:1

THF/water mixture to yield the carboxylic acid group. In order to reinstate a chlorophyll-type

absorption profile, zinc acetate was used to insert zinc ions into the centre of the macrocycle

resulting in a very noticeable colour change of the compound to a vivid green-blue. Using

MALDI mass spectrometry the major fraction was detected at m/z = 598, indicating the insertion without fragmentation of the ion from the centre of the chlorin. ^{1}H NMR characterisation was possible with this compound in acetone-d_6. The resulting peaks confirmed the structure of Zn-pyChl a upon comparison with NMR characterisation data for other chlorophyll derivatives in the literature (247). Issues with solubility however prevented a clear ^{13}C NMR characterisation – instead, IR spectroscopy was used to confirm the functional groups present in Zn-pyChl a, where the characteristic O-H and C=O stretch frequencies of the carboxylic acid were observed.
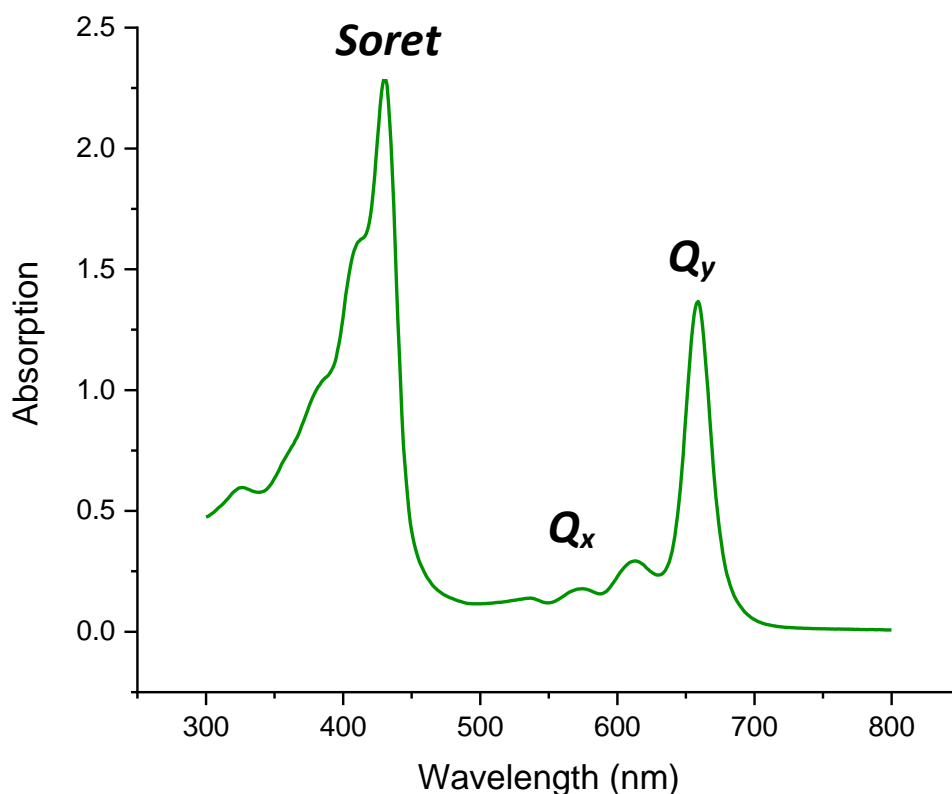
Figure 4.10: The UV/Vis absorption spectrum for Zn-pyChl a *at a 50 μM concentration in DMF.*

UV/Vis spectroscopy was used for additional characterisation and estimation of the dipole moments of the absorption bands. The resulting spectrum (figure 4.10) showed that the modified chlorophyll in fact had a similar absorption profile to the parent chlorophyll a

molecule (1), with the Soret (λ = 433 nm), Q_x (578 nm), and Q_y (659 nm) correlated strongly to the original. The Q_y transition dipole moment was estimated for Zn-pyChl a using the approach described in chapter 3. With ε_{max} = 27344.4 dm^3.mol^{-1}.cm^{-1} and δ = 22.7 nm, the dipole strength is found to be 26.4 D^2, giving a dipole moment of 5.14 D. This value correlates well with the values reported for this dipole in the literature (201) and is very similar to the value obtained for AcS-12C-BC. The Q_x dipole moment was much harder to estimate. These dipoles are much weaker and not strongly polarized due to the electronic structure of chlorins, so it was difficult to obtain a measure of the FWHM due to a strong overlap with the vibronic sub-band of Q_y.

The last synthetic step uses the carbodiimide-mediated coupling of the carboxylic acid to NHS under dry conditions, with an excess of EDC and NHS. The two-step process can be carried out in a single reaction where the reactive EDC-ester formed reacts in-situ with NHS, which simplifies the extraction of the more stable succinimidyl ester which can tolerate aqueous conditions for a longer period before possible hydrolysis. Again, after separation and drying, the process was found to be highly efficient with a maximum yield of 95% and a single new mass at m/z = 693 being detected by MALDI-MS, suggesting the displacement of the hydrogen from the carboxylic acid residue and the addition of the large succinimide ring to the chlorophyll. With the successful activation of the carboxylic acid, this presents a new chlorophyll molecule which can be coupled to a variety of nucleophiles and could be especially useful for bioconjugation purposes in future studies. Due to the sensitivity of the active ester to potential attack by water or other nucleophiles, it was determined that NMR characterisation of pure SC-Zn-pyChl a would not be feasible and the compound would be best used immediately after reaction.

b) *Derivatisation of poly(CysMA) brushes on gold surfaces with Zn-pyChl a*

#### i. *A conceptual model of the new chlorophyllide-poly(CysMA) hybrid material*

The anticipated structure of the polymer-chlorophyllide hybrid system was considered before the experiment. The basic conception of the system is that of a nanometre-scale amorphous layer of surface-bound poly(CysMA) chains to which SC-Zn-pyChl a molecules are appended to the amine functional groups of these chains. In terms of the engineering aspect of the system, the main utility of the poly(CysMA) as a scaffold was to allow the increase of density of chlorophyllides on the surface by using the height dimension. This would have a direct effect on the magnitude of strong coupling with plasmonic nanostructures by increasing the number of chlorophyllide dipoles in the plasmon mode volume (as per equation (1.15) in chapter 1). As the thickness of the brush layer increases with polymerization time, indicating longer surface chains, this would give more amine groups to be derivatized with chlorophyllides and thus increase their density. The orientation of the chlorophyllides relevant to each other, by contrast, may not be controllable. Due to the amorphous nature of the scaffold, it was anticipated that organisation of the chlorophyllide dipoles may be randomized in relation to the plasmonic field direction, unless a critical density of chlorophyllides could be achieved which may promote organizational π-π stacking within the brush layer. The chlorophyllide density was thus considered to be the primary factor which would determine the presence of strong coupling.

The main factors controlling the efficiency of derivatization with Zn-pyChl a are the same governing other post-functionalization reactions (see figure 4.6). Access for the chlorophyllides to the polymer brushes in this case are chiefly governed by the solvent used, which affects the degree of brush expansion, as well as the density of grafted polymer chains within the brush layer. In this section, the first factor was explored to examine the

chlorophyllide densities which could be achieved for a fully dense brush layer using various solvents. Using a poor solvent for poly(CysMA) solvation, such as THF, was expected to give low, surface-only attachment, while using more polar solvents were anticipated to increase the efficiency of attachment further into the brush layer structure.

ii. *Ellipsometry measurements for full density brushes before and after chlorophyllide attachment*

For gold surfaces, a monolayer of DBTU was adsorbed to give bromine initiators at the substrate interface. The synthesis of the cysteine methacrylate monomer was carried out as previously described (221) with a long drying time under reduced pressure. For the surface polymerization (figure 4.11), an approximate 1:2.7 molar ratio of $Cu(bipy)_2^{2+}$ to ascorbic acid was used. A reduction of the concentration of CysMA from 1.24 M used in the previous study to 0.56 M was used to compensate for the much lower amount of copper used (lower concentration leads to faster polymerization due to proportionately lower incidence of chain termination reactions), giving an approximate monomer: copper ratio of 600:1. To evaluate the polymer growth, several samples were prepared for polymerization times between 30 seconds and 2 hours.
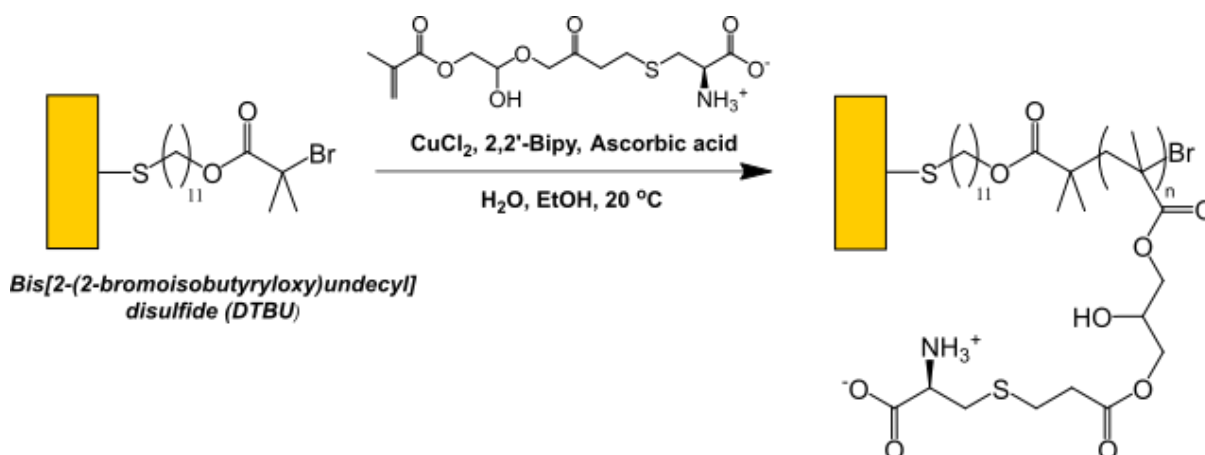
Figure 4.11: A general scheme for the ARGET-ATRP brush growth of poly(CysMA) brushes from a monolayer of initiators on a gold substrate.

The thickness of the brush layer as measured by ellipsometry as a function of polymerization time (figure 4.12). The thickness increased rapidly at short time periods, and the rate of increase slowed after ~ 10 min with a limiting thickness being after ~ 1 h. This growth drop-off is characteristic of ARGET-ATRP, due to the eventual loss of bromine terminating atoms from the growing polymer chains over time (56). A large range of dry thicknesses from 2.86 ± 0.036 nm at 30 seconds to 55.73 ± 0.204 nm at 2 h was achieved.

Height of poly(CysMA) brushes against polymerization time
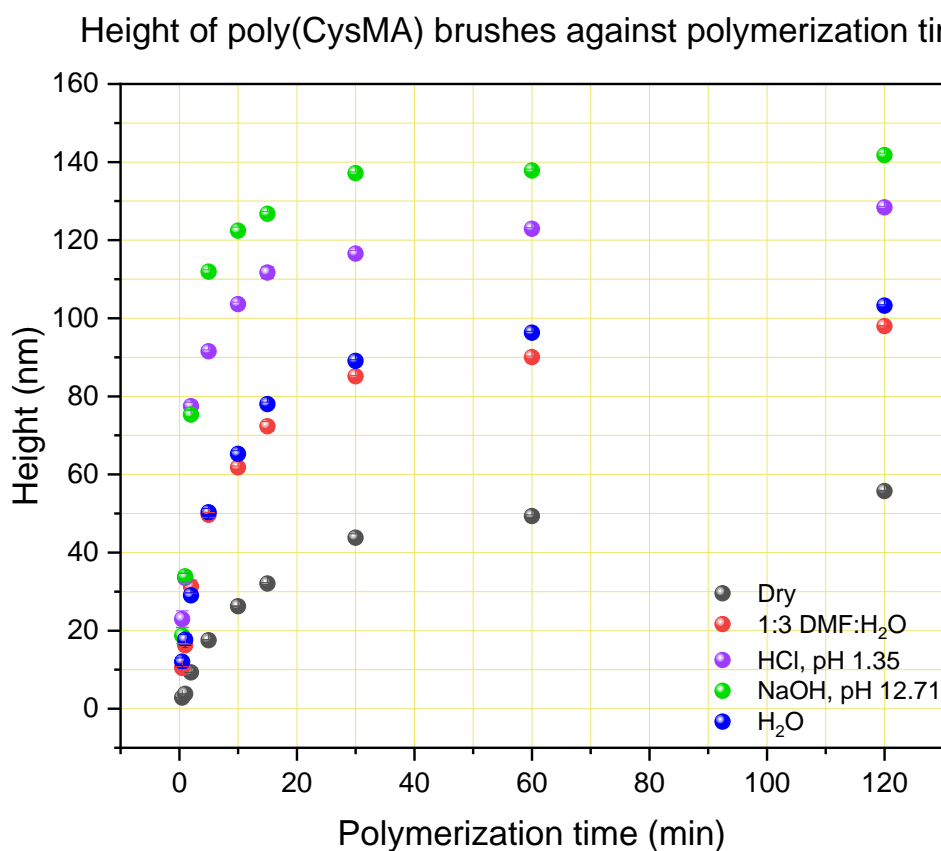
Figure 4.12: A growth curve of the thickness of poly(CysMA) brushes in various solvent conditions by polymerization time. Error bars for the thickness values are largely within the diameter of the data points.

In addition to dry measurements, the brush height was measured in several solvents (also illustrated in figure 4.12) as a reference for comparison after chlorophyllide attachment (**Appendix 2 ii**)). In general, the behaviour is like that observed in the previous study. In deionised water, the height of the brush layer increases to over twice the dry height for the

longest brushes due to swelling in the polar solvent. When 0.1 M aqueous HCl and NaOH were used as solvents, the height increased again to almost 3 times the dry height for the longest brushes, reflecting the change in charge conditions. The height of the brushes in a mixture of DMF and water mixed to a 1:3 ratio was also measured. As Zn-pyChl *a* itself is not soluble in water, DMF was introduced as an organic component to solubilise it for attachment but still at a level that potentially allowed for brush expansion. The resulting height profile shows that the swelling follows a similar behaviour to pure water, thus suggesting that the water still fully interacts with the brush despite the presence of DMF. For the chlorophyll attachment, this would allow the brush to be extended enough to allow the chlorophyll to access many of the amine groups along the brush.

To derivatise the brushes with chlorophyllides, they were immersed in a 1 mM solution of SC-Zn-pyChl *a* in 1:3 DMF: H_2O. Ellipsometry measurements were then carried out again after immersion (**Appendix 2 iii)**, figure 4.13).
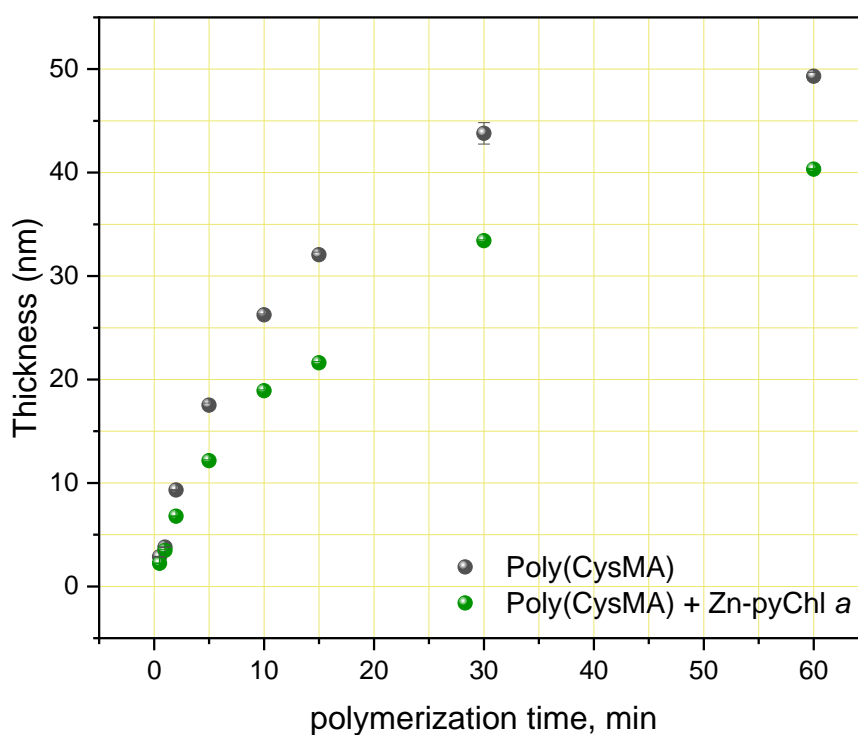
Figure 4.13: The height of poly(CysMA) polymer brushes in dry conditions before and after attachment of Zn-pyChl a.

In dry conditions, the dry brush thickness was shown to reduce for all samples on average to $76.22 \pm 7.77\%$ of their value before functionalisation. While we do not have a definitive explanation for this behaviour, we could speculate that the chlorophyllides may be engaged in π-π stacking interactions inside the brush and perhaps this has an effect of the amorphous orientation of the dry brushes, making them more compact and thus reducing the thickness. When remeasured in several solvents, the expansion behaviour was found to be relatively unchanged after derivatisation (figure 4.14). At pH 1.35, the brushes were still ~ 50% thicker than at pH 7. This indicates that after introduction of chlorophyllides there was still significant swelling due to cationic net charge, meaning that not all the amines were derivatised. At pH 12.71, the brushes are anionic as before and display the expected swelling behaviour.
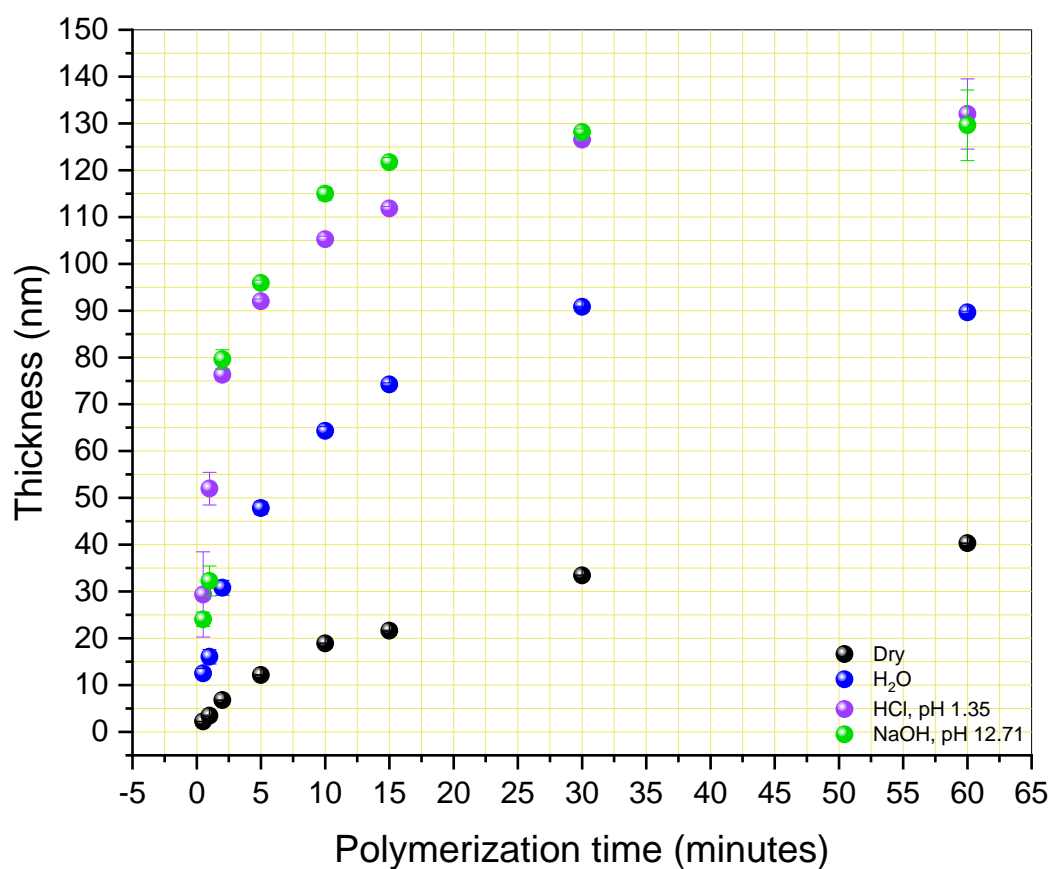

Figure 4.14: The heights of poly(CysMA) brushes in several solvent conditions after immersion in solutions of SC-Zn-pyChl a.

Other properties of the films were studied to determine if there were any changes in the properties of the brushes which indicated chlorophyll attachment. First, the percentage of polymer brush described in the effective medium approximation (EMA) model, (**Appendix 2 i)**) with water as the solvent, was studied before and after immersion in the Zn-pyChl *a* solution (figure 4.15). Before derivatisation, the percentage of poly(CysMA) increases linearly with brush height – this is consistent with a solvated brush increasing in density with height. After attachment of chlorophyllides, the percentage increases significantly in relation to height. This indicates that there may be less water solvation between the brushes. This could be attributed to the incorporation of Zn-pyChl *a*, which is hydrophobic. The chlorophyllides may therefore aggregate and bring the brushes together, expelling some water between them in the process.
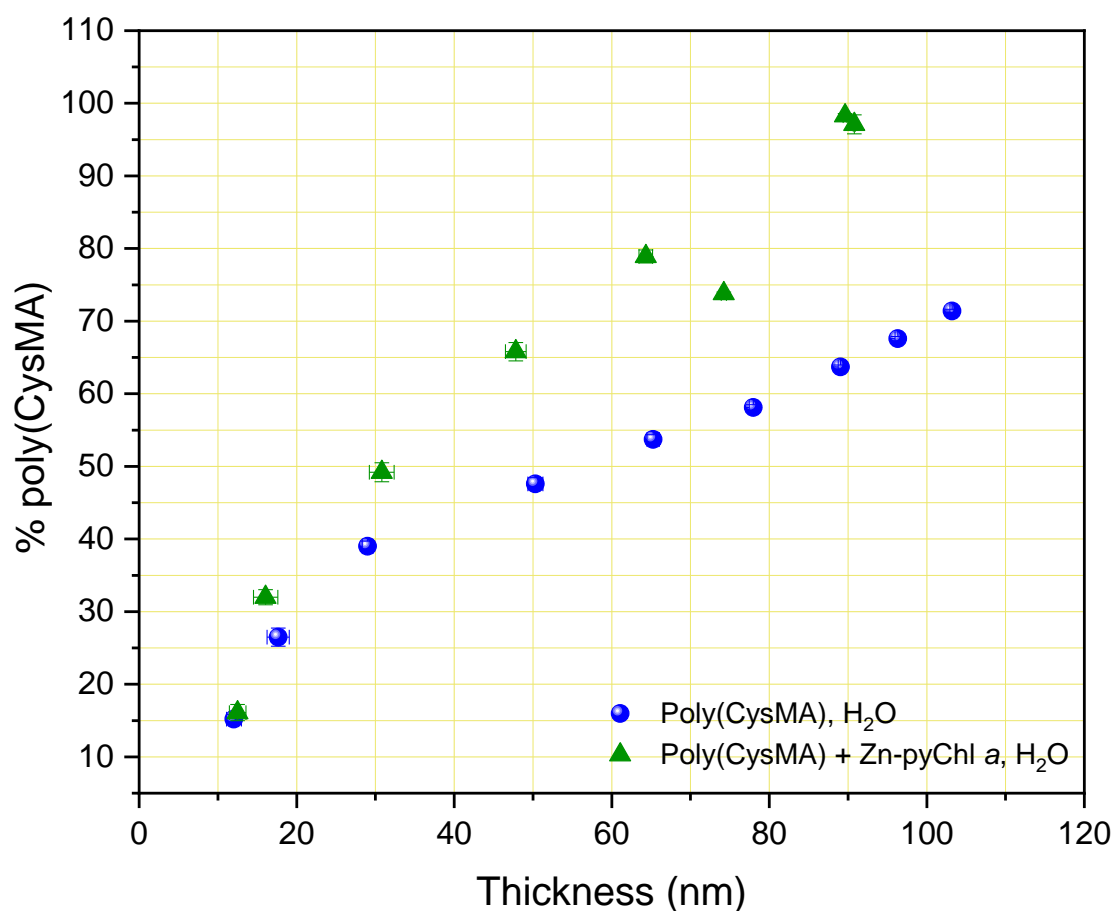
Figure 4.15: The percentage of poly(CysMA) measured in H₂O, as defined by an EMA model, for brushes before and after immersion in a SC-Zn-pyChl a solution.

In addition, the optical constant *A,* related to the refractive index *n* by the Cauchy equation, of the brush layer was measured in several solvents (figure 4.16). *A* for unfunctionalized poly(CysMA) had been previously determined to be 1.504 in dry conditions and was independent of brush height. After immersion in chlorophyllide solution, *A* was found to be much lower in short brushes under dry conditions, followed by an increase in an apparent linear fashion with height, with a minimum of 1.353 ± 0.03 at the lowest thickness (2.24 nm) up to a maximum of 1.495 ± 0.001 to the largest thickness measured (40.33 nm). In the HCl and NaOH solutions a similar behaviour is observed across their respective height ranges.
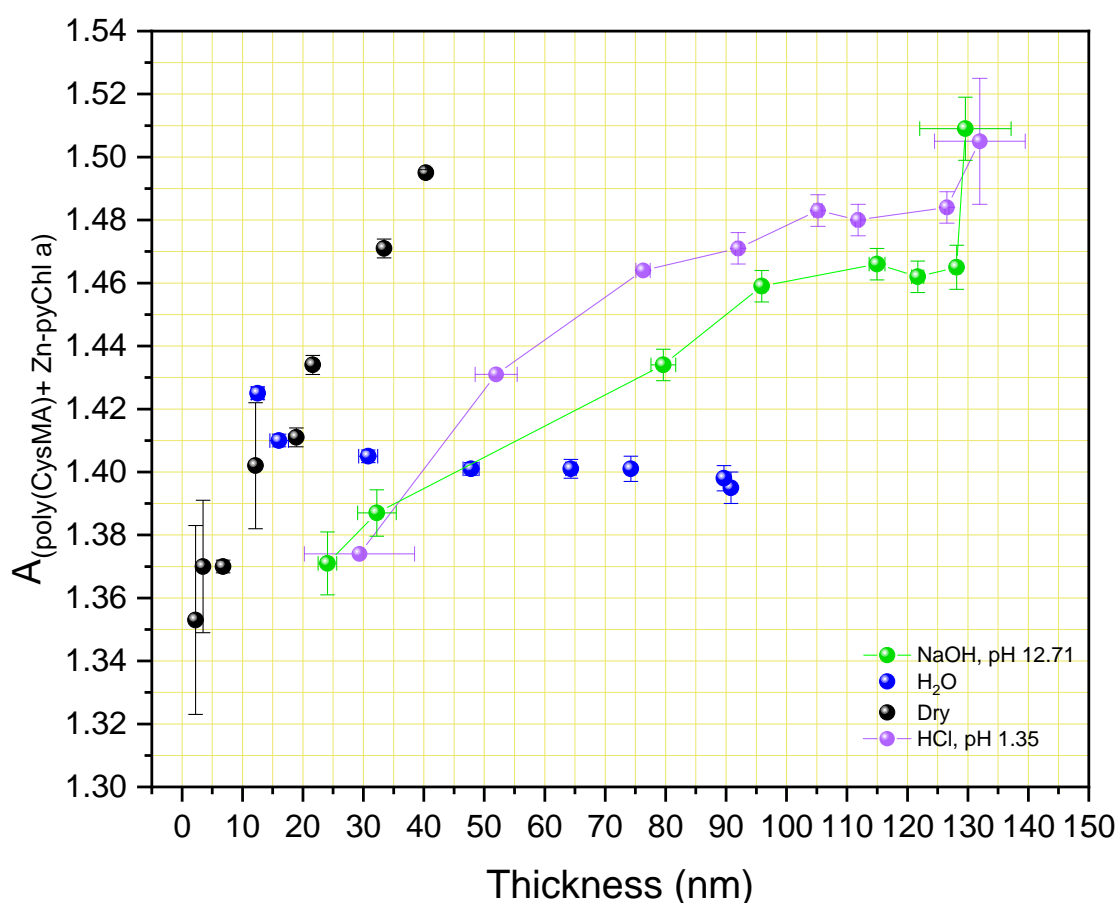
Figure 4.16: The variation of the optical constant A *for poly(CysMA) brushes with attached Zn-pyChl* a *as a function of thickness in various solvent environments.*

This evidence may point to the successful attachment of chlorophyllides, but only to a certain portion of the brush layer. For short brushes, greater incorporation as a proportion of the brush reduces *A* of the brush by a large amount. As the brush height increases, there is a lower proportion of attachment which means the optical properties are more defined by the "bulk" unfunctionalized brush. This indicates that there is a limit of Zn-pyChl *a* penetration into the brush layer as thickness increases. However, in water *A* has a smaller range which remains constant at around 1.40 for longer brushes. It is possible that *A* is sensitive to the hydrophobicity of the chlorophyllides, and the possible aggregation of them keeps the refractive index lower than expected.

iii. *XPS quantification of Zn-pyChl **a** attachment*

The composition of the brush layer was examined using X-ray photoelectron spectroscopy with high resolution scans of the C 1s, O 1s, N 1s, S 2p and Au 4f spectral regions. Before functionalisation, the positions and component fitting of the peaks conformed to the assignments given in the previous poly(CysMA) study, confirming that poly(CysMA) was grown from these surfaces. In the C 1s spectra, the atomic ratios of the C-<u>C</u>-C, C-<u>C</u>-O/C-<u>C</u>-N and O=<u>C</u>-O components were altered from the previously obtained values for poly(CysMA) grafted to APTES-BIBB monolayers. For a brush measured by ellipsometry beforehand with a height of 17 nm, the new ratio was now approximately 2.7:1.6:1, with a 32 nm brush showing a ratio of 2.4:1.6:1. It is likely that the extra C 1s electrons were emitted from the DTBU initiator monolayer, which contains 10 times the amount of carbon atoms per molecule compared to an APTES monolayer. The reduction of the ratio of the C-C peak suggests a thicker polymer layer attenuated more of the monolayer photoelectrons. This extra carbon however was observed despite the large thicknesses of the brush layers, which is unexpected given the limited depth penetration of XPS. This may be attributed to the

amorphous nature of the collapsed polymer brush layer - gaps between the polymer chains may have allowed some X-rays to penetrate to the monolayer and then photoelectrons from the base to reach the detector without collisions. This was also indicated by the Au 4f spectrum which still displays the characteristic spin-orbit coupled peaks at these lengths even with substantial attenuation of the signal with the longer brush. A significant deviation from the expected N:S ratio was also observed. For a monomer of CysMA the ratio is 1:1, and a polymer layer analysed to a 10 nm depth should reflect this. For these brushes the ratio measured approximately 0.6, but a range of 0.5 – 0.7 has been observed for subsequent samples. It is possible that the large amount of sulfur present in the disulfide monolayer was contributing to the sulphur signal in this case.

The attachment of Zn-pyChl a proceeded as for the set of ellipsometry samples, but here a variety of solvents were used for attachment - THF, DMF and 1:3 DMF: H_2O. This was done to observe the difference in degree of attachment between configurations of the brush layer – in non-polar THF the charged poly(CysMA) brush is collapsed as in air, leading to only functionalisation at the polymer-medium interface, while DMF was used as a control for comparison with the 1:3 DMF: H_2O mixture.

There was little difference in the C 1s and N 1s spectra acquired for samples derivatised in THF and DMF, which indicates that there is little or no addition of chlorophyllide contributions to the signal in these regions. However, when 1:3 DMF: H_2O was used, the ratio of the N 1s peaks for -NH_3^+ and -NH_2 did change (**Appendix 2 iv)**). This suggests added nitrogen from the chlorophyllide macrocycle may increase the -NH_2 peak area at 399.8 eV. As for the C 1s region, it was found that a new component at 287.86 eV was needed to fit the spectrum accurately. This can be attributed to the formation of amide bonds in the polymer structure, indicating that the attachment of Zn-pyChl a occurs via the amines

in the structure. The main hydrocarbon peak also increases relative to the ester peak at 288.8 eV, from 2.65:1 to 5:1, indicating addition of carbon from the chlorophyllides into the brush layer. The N 1s and C 1s XPS spectra for this system are shown in figure 4.17.
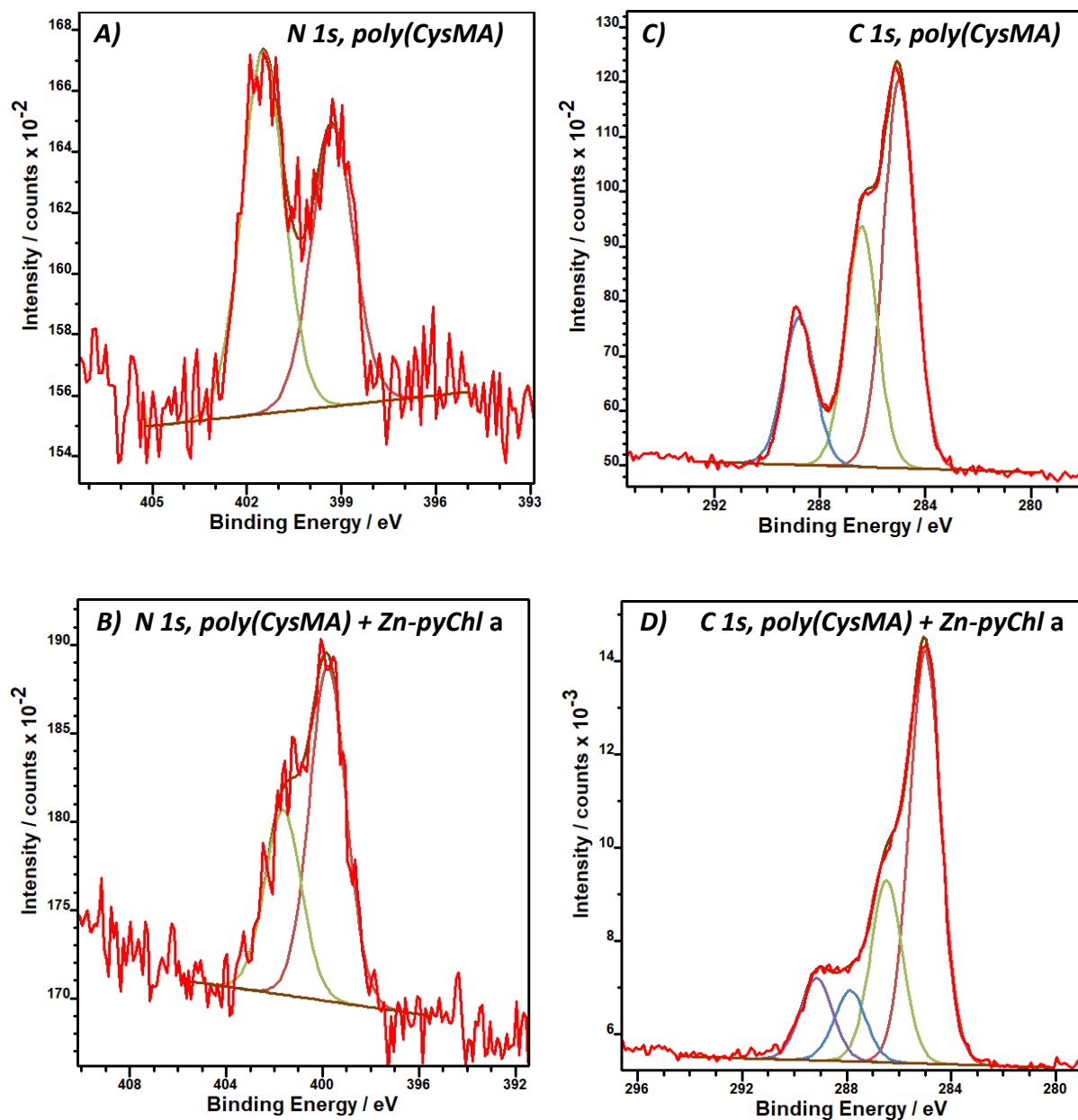
Figure 4.17: N 1s [A), B)] and C 1s [C), D)] XPS spectra for poly(CysMA) brushes (17.8 nm surface thickness) on a gold substrate, before and after derivatisation with Zn-pyChl a respectively.

The ratio of nitrogen (N 1s) to sulfur (S 2p) was used to approximate the amount of attachment. As the sulphur atomic concentration should be the same before and after attachment, the N/S ratio should increase from 1:1 to 5:1 for each monomer of the chain derivatised with a chlorophyllide. The results are summarised in table 4.

Table 4: Results for the percentage of attachment of Zn-pyChl a to poly(CysMA) brushes of various lengths in different solvents, calculated from N 1s / S 2p ratios obtained by XPS before and after attachment.

Sample	Brush Thickness (nm)	Solvent	N/S ratio (blank)	N/S ratio (after attachment)	% Free monomer	% Attached Zn-pyChl *a*
1	6.6	THF	0.776	0.730 ± 0.056	*100*	*N/A*
2	22.6	THF	0.767	0.718 ± 0.087	*100*	*N/A*
3	6.6	DMF	0.776	0.813 ± 0.168	*98.8 ± 5.4*	*1.18 ± 5.4*
4	22.6	DMF	0.767	0.660 ± 0.033	*100*	*N/A*
5	3	1:3 DMF: H_2O	0.656	1.487 ± 0.061	*68.3 ± 2.3*	*31.7 ± 2.3*
6	17.8	1:3 DMF: H_2O	0.590	1.365 ± 0.346	*67.2 ± 1.5*	*32.8 ± 1.5*
7	34.3	1:3 DMF: H_2O	0.582	1.320 ± 0.028	*68.3 ± 1.2*	*31.7 ± 1.2*

When using THF to attach chlorophyllides, the N/S ratio did not change noticeably, no matter the thickness of the brush layer. This conforms to the conceptual model - as the brush is collapsed in the unfavourable solvent, only the charged groups at the top surface of the brush layer interfacing with the solvent are present for reaction. It is possible that the charged groups are mostly withdrawn into the polymer matrix away from the hydrophobic environment. As a result, there is likely an extremely low number of sites available for

attachment, which gives either an attachment rate lower than the sensitivity of the XPS analysis or no attachment at all. Where DMF is used as the solvent, the outcome was a very small amount of attachment on the shorter brush with no discernible difference with the longer brush. As DMF is a more polar solvent than THF, there may have been a small degree of brush expansion, which allows the chlorophyllides some access for attachment within the shorter brush. However, its relative polarity to water is still low, thus it is likely that the charged groups are not stabilized enough to allow higher expansion. For sample 4 with the longer brush, the lack of swelling gives the same result as THF, indicating very low or no derivatisation, or just that the increased polymer material made the nitrogen contributions from the chlorophyllides indiscernible.

When mixed solutions of DMF with water was used, the amount of Zn-pyChl *a* attachment increased significantly. According to the analysis, almost a third of the brush structure was functionalized. This is undoubtedly due to the greater expansion allowed by the water component, which was measured by ellipsometry previously. This solvent system therefore appears to be a good compromise between chlorophyll solubility and brush access. The attachment also appeared to be independent of the brush height between 3 and 18 nm. Between samples 6 and 7, similar attachment was detected also. However, it is important to consider that the depth penetration for XPS is often limited to the top 10 nm of a material. The attachment values are therefore applicable to only to the top 10 nm of the brush layer. This could suggest that there is a highly derivatised chlorophyllide sub layer in the brush, which becomes less of a proportion of the overall brush material as height increases. In that case, the attachment would be diffusion limited through the top of the brush.

To determine whether the attachment is diffusion limited through the brush layer, angle-resolved XPS measurements were made on sample 6, where the angle of the x-ray

source was changed to give varying degrees of x-ray penetration through the brush layer
(figure 4.18).
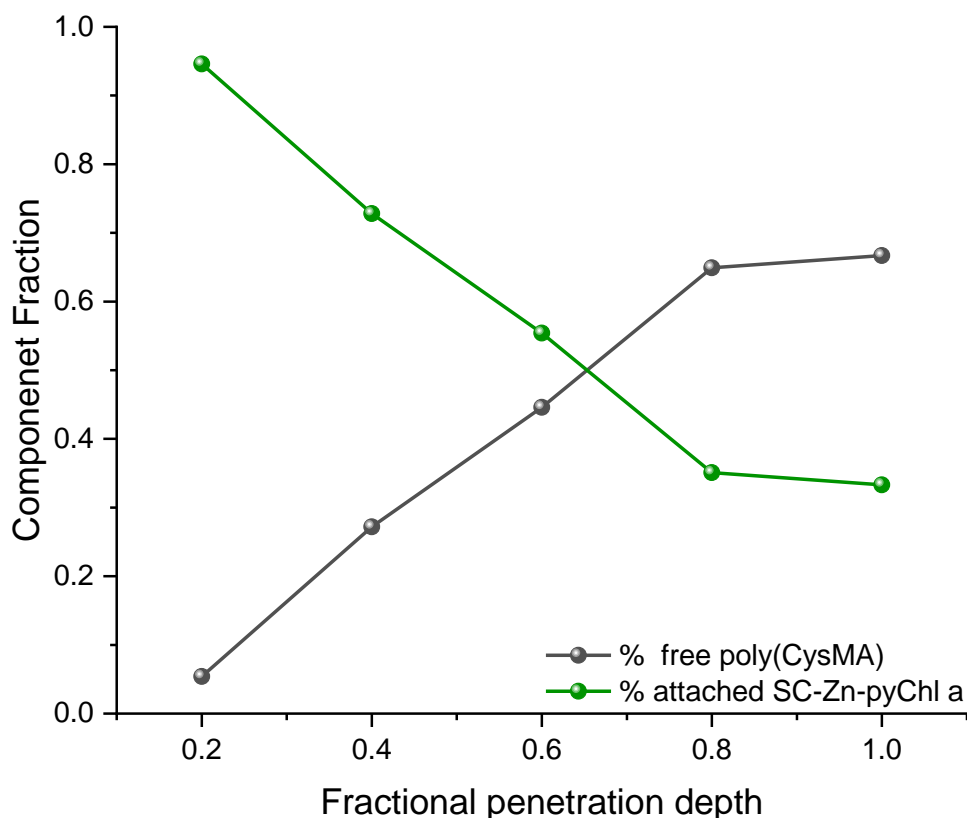
Figure 4.18: The angle-resolved values obtained for the percentage of unfunctionalized poly(CysMA)
and attached Zn-pyChl a for a 17.8 nm brush. The much higher percentage of functionalised polymer
at lower penetration depth suggests that functionalisation is by the diffusion of molecules through
the top of the polymer brush.

The original analysis was carried out with the x-ray beam source directly
perpendicular to the plane of the sample, here denoted as 0°, which gives the maximum ~10
nm penetration depth. By increasing the source angle from the perpendicular to 37°, 53°, 66°
and 78° with new measurements taken at each angle, attachment ratios were obtained for
modified penetration depths of 8, 6, 4 and 2 nm respectively. For chlorophyllides attached to
the brush in 1:3 DMF: H_2O, the attachment percentage increased at each angle from 0° until a
maximum of 94.6% at 78°. This indicates that attachment efficiency was very high in the top-

most region of the brush where there is maximum chain flexibility and access with the solvent, but as the depth increases the overall efficiency of attachment decreased due to the increasing density of the polymer chains. The attachment efficiency is thus limited by the diffusion of the chlorophyllides through the dense brush layer. This diffusion limitation appeared to be the same also when sample 7 at 34.3 nm was measured.

iv.   *Summary*

The evidence collected by surface analysis conforms to the initial conceptual model for a post-functionalized poly(CysMA) brush with Zn-pyChl *a*, with different degrees of incorporation depending on the solvent used. The analysis suggests that incorporation of Zn-pyChl *a* into a polymer brush scaffold grown from gold substrates occurs, and that a maximum of ~ 32% of the polymer chains are functionalized in a favourable polar solvent mixture. The attachment is diffusion limited at brush thicknesses greater than 10 nm, so that the top few nm of the brush is highly derivatised while the inner bulk of the brush layer still has free zwitterionic groups (figure 4.19). This is reflected in the optical properties of the brush, as *A* becomes closer to that of the unfunctionalized brush when chlorophyllides form a smaller proportion of the layer composition with increasing thickness. While poly(CysMA) has been shown to swell to twice its dry thickness in aqueous solvent as well as in a DMF-water mixture, the conformation of the brushes is likely to be part-extended coils with flexible ends at the top interface, but still form a dense layer deeper within the brush which prevents full derivatization. This suggests that for greater incorporation, the density of the polymer brushes on the surface would need to be reduced. As a result of the limited derivatization of the brush, the system retains its solvent and acid/base response for the most part after attachment. The chlorophyllides may impart some small hydrophobic character to the brush, perhaps because of chlorophyllide aggregation in aqueous solvent, but this does

not translate to a change in brush response in water. If aggregation does occur, this may point to some organisation between the pigments incorporated into the brush.
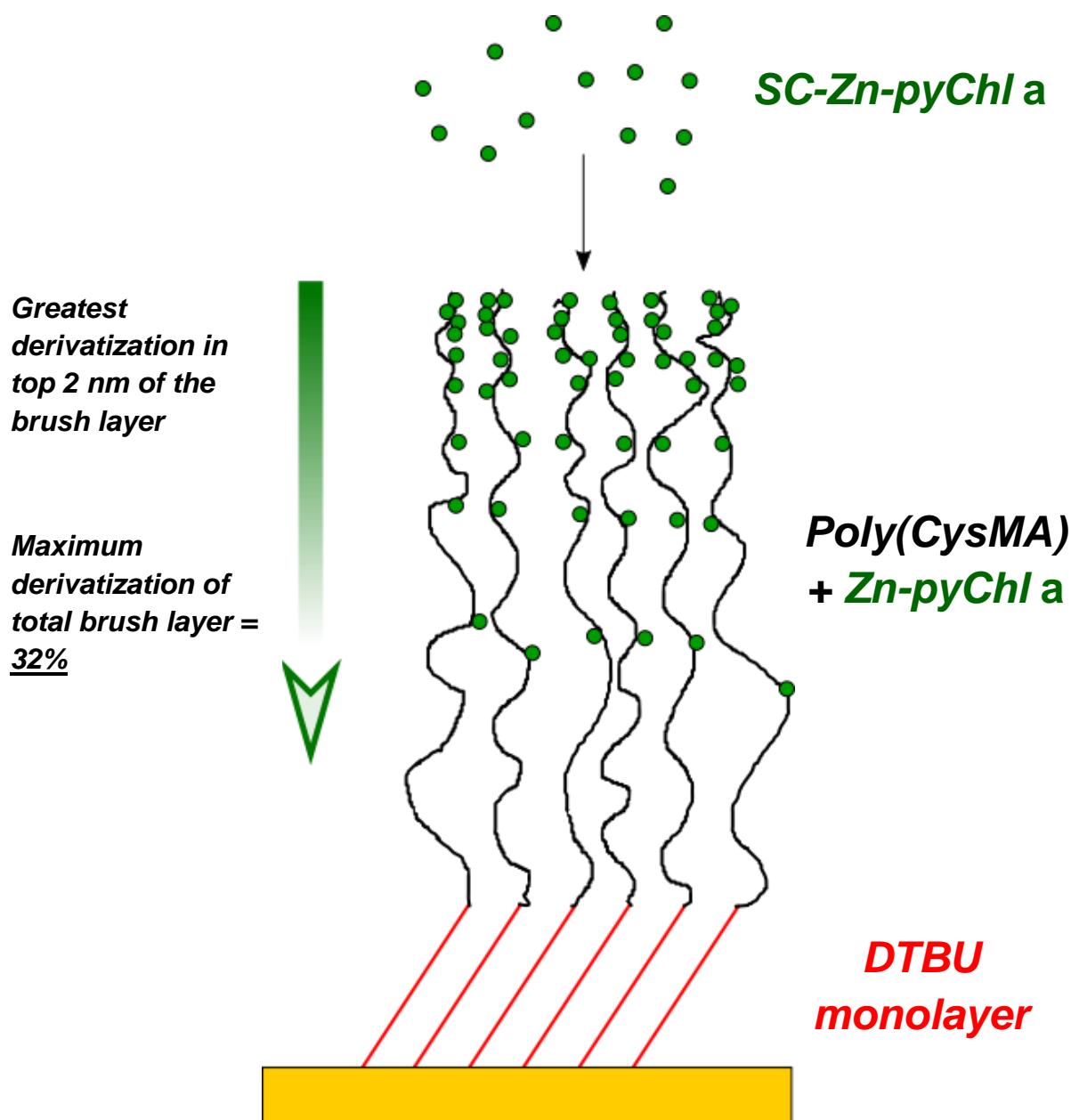

Figure 4.19: The derivatization of a poly(CysMA) brush (with the maximum surface density of polymer chains) with SC-Zn-pyChl a. The attachment of chlorophyllides is diffusion limited, leading the surface 2 nm region to be the most derivatized compared to the deeper regions.

c) *Extinction spectra of Zn-pyChl a functionalised poly(CysMA) brushes coupled to gold nanostructures*

The same conditions were used to attach chlorophyllides to polymer brushes grown on arrays of gold nanostructures. The brush growth procedure was the same as performed previously, to produce full-density polymer brush layers on top of the nanostructures of various thicknesses. 8 arrays of gold nanostructures were selected for use in this plasmonics study, which had been used successfully in previous strong coupling studies (116, 129). A summary of the samples may be found in **Appendix 3 i)**. The samples were cleaned prior to use by exposure to cooled piranha solution and characterised by AFM and UV/Vis spectroscopy (117). Surface-initiated polymerization was carried out by ARGET-ATRP, and the thicknesses of the resulting brush films were determined by ellipsometry (figure 4.20).
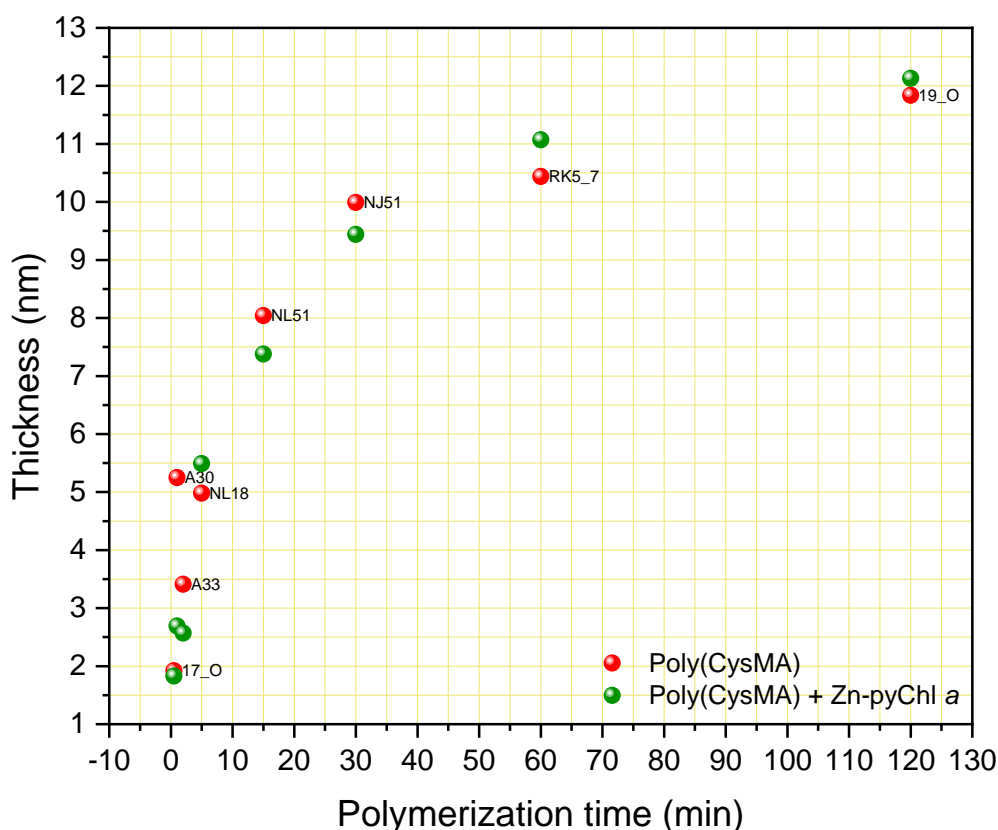
Figure 4.20: The thickness plot with polymerization time of poly(CysMA) growth on several plasmonic arrays of gold nanostructures, before and after Zn-pyChl a attachment in DMF.

The thicknesses were found to be reduced compared to those obtained on continuous gold films – for example, a brush on the gold nanostructures after 2 hours of polymerization time gave a maximum height of under 12 nm compared to approximately 50 nm on the unpatterned substrate. While ARGET is not easily controlled between polymerization experiments, it is also possible that the free volume of the brushes grown from gold nanoparticles was different from that of the equivalent polymers grown on continuous gold. This may lead to a reduction in steric repulsion between polymer chains and thus a reduction in brush thickness. Nevertheless, a series of thicknesses was produced with polymerization time, up to 11.8 nm after 2 h. With this, the possible change in coupling energy could be studied with brush height. UV/Vis absorption measurements were also taken before and after surface polymerization. After brush growth, a red shift was observed in the plasmon peak, typical of non-coupling adsorbed organic material to the surface of the nanostructures.

Two different methods for the attachment of Zn-pyChl *a* were compared: first using DMF as the solvent and then using 1:3 DMF: H_2O. Extinction spectra and coupling energy were acquired for both sets of samples. After attachment with DMF to brushes on the arrays, the thickness was found to vary slightly in each case, but not significantly. In the extinction spectra, the plasmon peak was modified significantly in linewidth, and the energy was shifted depending on its position relative to the Q_y exciton band of Zn-pyChl *a* (figure 4.21). New shoulder features also appeared, removed from the main peak but not fully resolved in linewidth. This suggested that plasmon-exciton coupling was occurring, but not strong enough to give two fully-resolved bands.
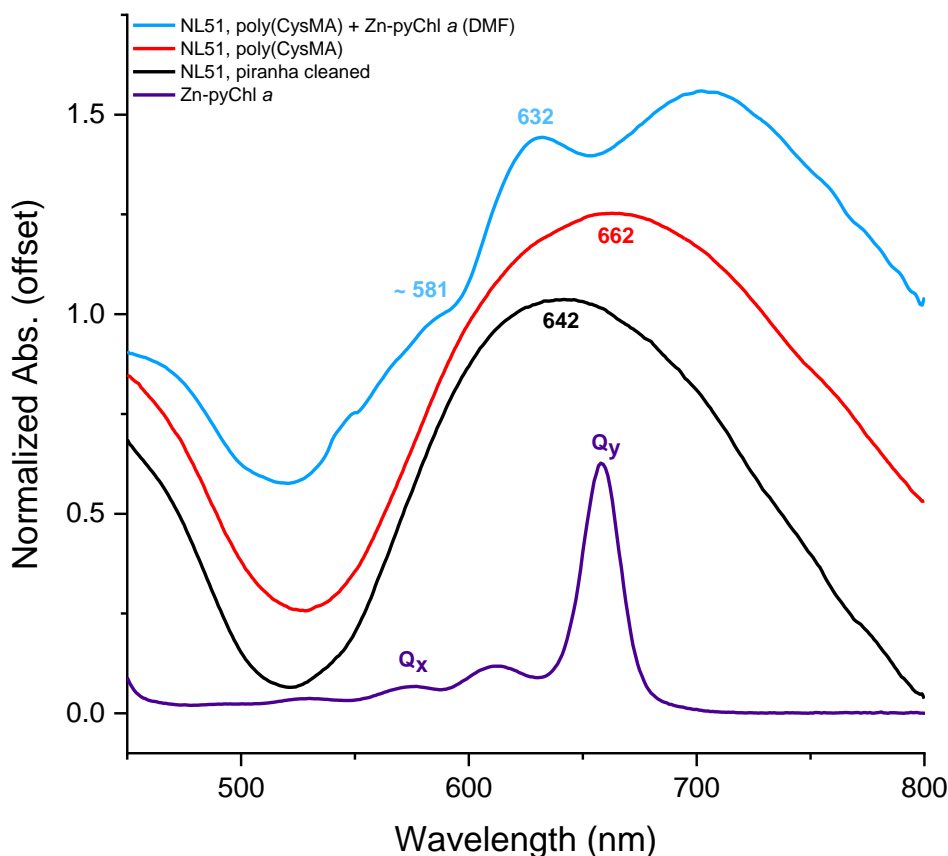
Figure 4.21: The extinction spectrum for a plasmonic array (NL51) (in black), after grafting of poly(CysMA) (red) and derivatisation with Zn-pyChl a in DMF (blue). The solution spectrum of Zn-pyChl a is included for comparison. The plasmon peak is red shifted after growth of polymer brushes on the sample, but then blue-shifted and split into a major peak with a poorly resolved shoulder feature. An additional peak feature (above 700 nm in the blue spectrum) was found to be unrelated to the plasmon-exciton coupling phenomenon.

From modelling the spectra using the harmonic oscillator model, the average coupling energy E_C was determined as 0.13 ± 0.07 eV. A criterion based on the average linewidths of plasmon and exciton modes used in these systems suggests that E_C should exceed ~ 0.24 eV for strong coupling (62). These arrays therefore approached, but did not exceed, the strong coupling limit. As for the exciton energy E_{mol}, the model gave the average as 1.97 ± 0.10 eV, between the energies of the Q_x and Q_y transitions. It is possible that as the chlorophyllides are arranged in an amorphous brush scaffold, a variety of orientations leads the plasmon mode to couple to both transitions simultaneously in many different combinations at once. This result would conform to the original conceptual model of the surface structure. Alternatively, the

plasmon mode may be coupled to one of the dipoles, but that this transition also is coupled to other transitions of adjacent chlorophyllides, perhaps by formation of *H*- or *J*-dimers (129). Lishchuk *et al* showed that because of entanglement of the excitons in chlorins via their strong coupling to a plasmon mode, the plasmon could therefore couple to a transition arising from the coupling of dipole transitions to each other, such as those found in *H*- or *J*-aggregates found in supramolecular aggregates of chlorophylls (207, 208).

The brushes were re-derivatised with a fresh SC-Zn-pyChl *a* solution using 1:3 DMF:H_2O as the solvent. This was done to observe if there was an increase in E_C with increasing number of dipoles – as DMF alone was shown to result in very low overall derivatization, there were still many free amines in the brush which could be reacted with upon application of more chlorophyllides in a better solvent environment. In the extinction spectra of the newly derivatised brushes, the plasmon-exciton splitting became more pronounced (figure 4.22). However, this did not result in an increase in E_C, with a new average of 0.09 ± 0.04 eV being obtained while E_{mol} did not change significantly. It may be the case that despite the increase in chlorophyllide derivatisation, the density of dipoles was still not sufficient to breach the strong coupling threshold. The average coupling energy was lower after the re-derivatisation, and it is not clear why. It is possible that swelling in the better solvent caused random reorientations of the chlorophyllides relative to the plasmon mode, resulting in changes in the coupling on each sample after derivatisation. This would reflect the amorphous and flexible nature of the polymer brush structure, which may not be arranged in the same way between immersions in solvent.
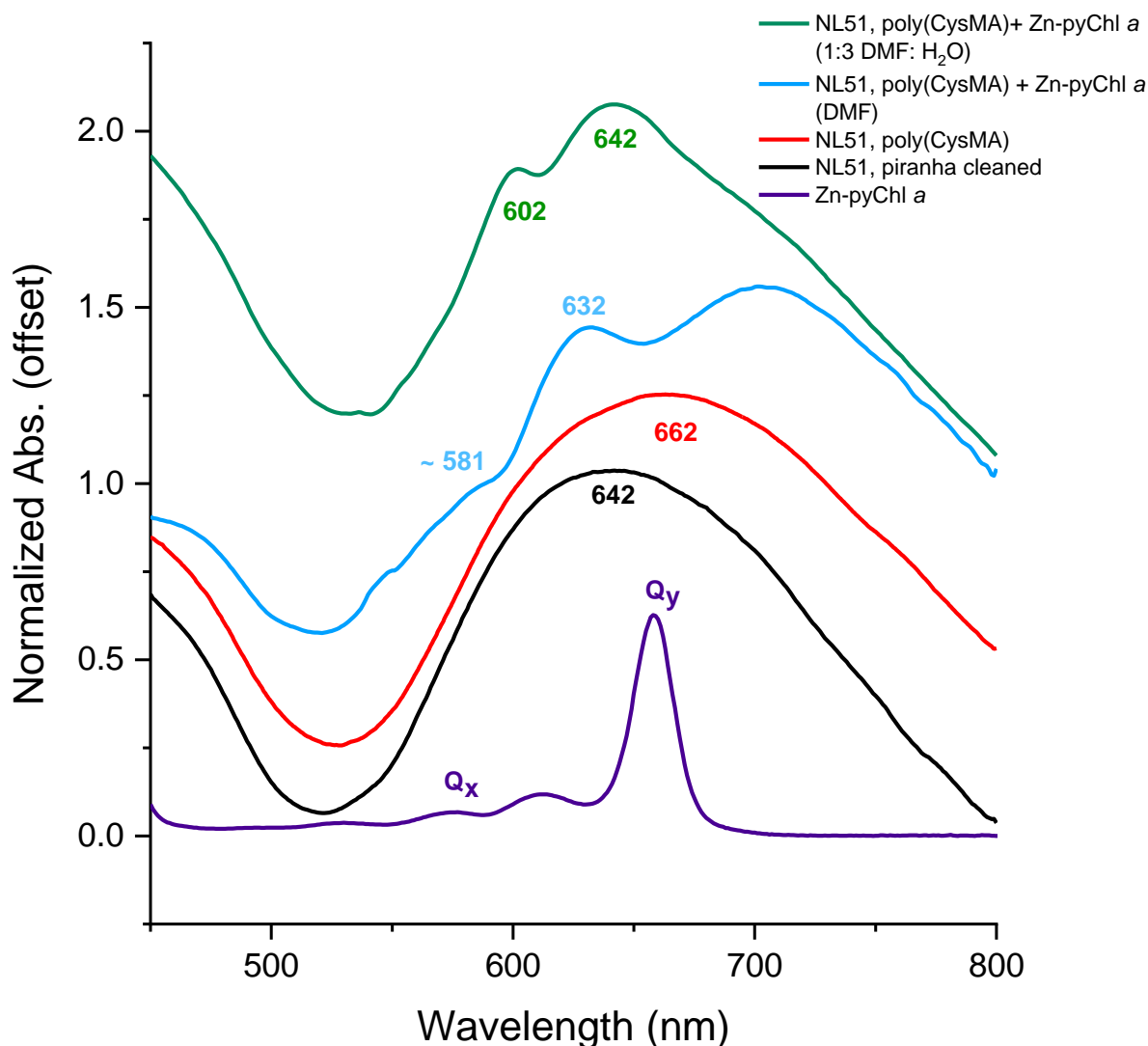
Figure 4.22: Comparison of the extinction spectrum for NL51 re-derivatised with 1:3 DMF: H₂O with the previously acquired spectra from Fig. 4.21.

The range of coupling energies was found to be large compared to the AcS-12C-BC monolayer. For a series of arrays of arrays exhibiting a range of E_{LSPR}, there was found to be no systematic relationship between E_{LSPR} and E_C (figure 4.23). For E_{mol}, there was also no obvious correlation with a larger range of energies than expected. The differences in E_{mol} were likely due to the amorphous nature of the polymer brush structure, meaning the chlorophyllides' dipoles were probably oriented in many different directions relative to the plasmonic field direction, giving a range of average exciton energies for this set of samples.
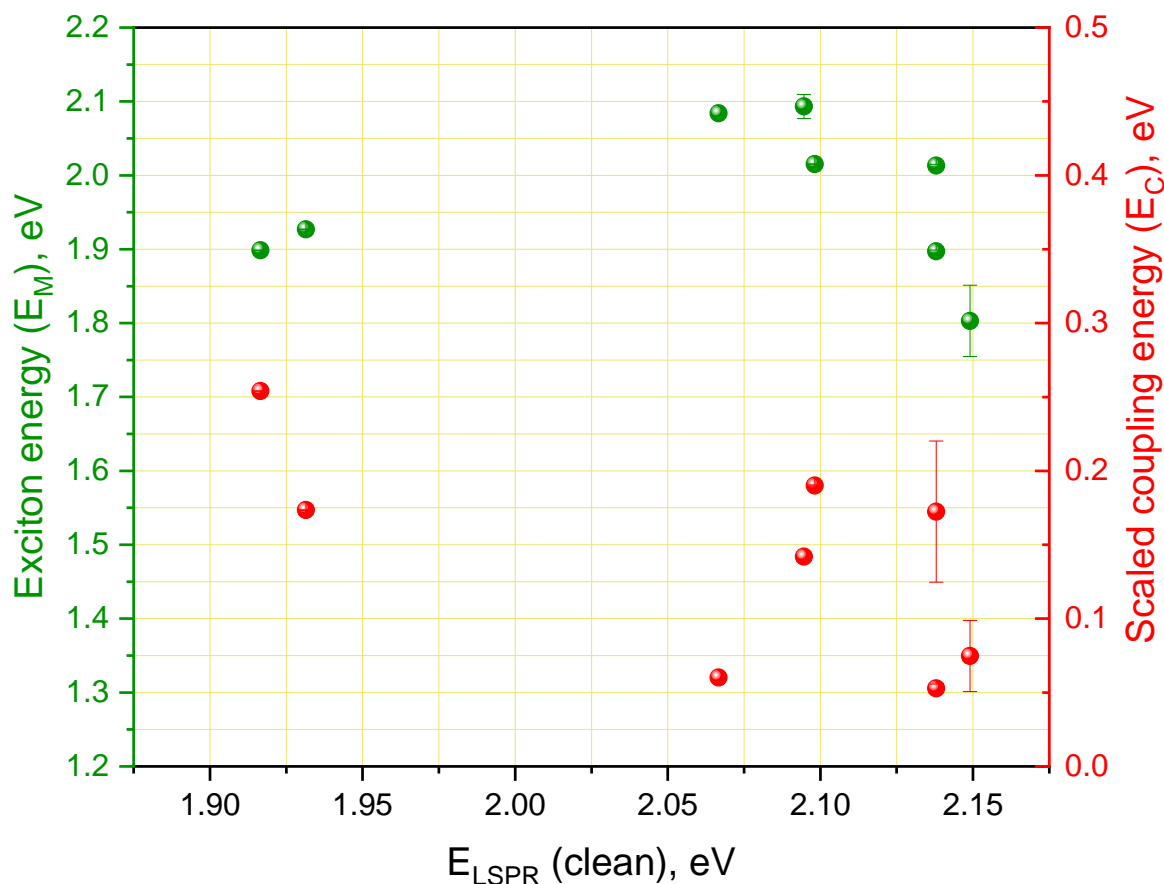
E_C was measured for several brushes of different thickness (figure 4.24). There was no clear correlation between the thickness of the brush and E_C, although the coupling energy did appear to increase to a maximum achieved at a ~ 5 nm brush thickness before decreasing again. In this sample set, NL18 (which was also used previously in the AcS-12C-BC study as discussed in chapter 3), a coupling energy above 0.25 eV was observed, just breaching the barrier for strong coupling. This observation may indicate that better control of the dipole density in the brushes would result in strong coupling. Once again, NL18 displayed a larger coupling energy than the other samples used, but in this case the explanation may be in the combination of polymer brush thickness with the response sensitivity of the plasmonic field.
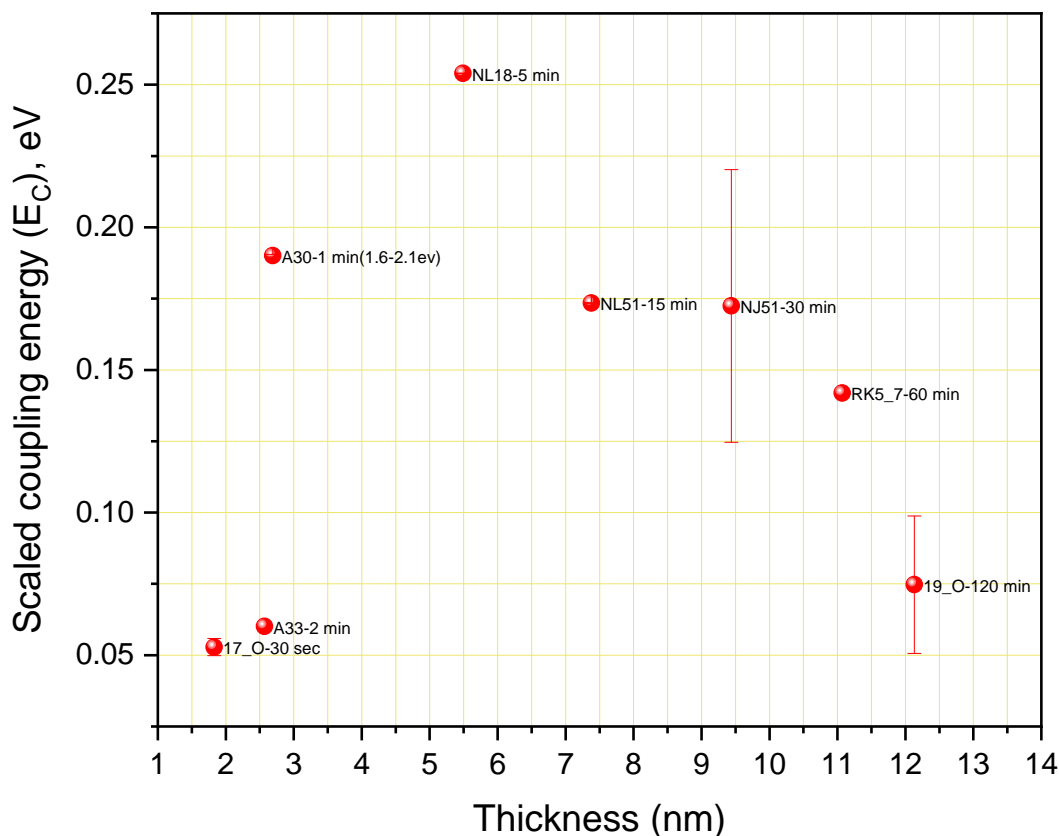
Figure 4.24: Scaled coupling energy for plasmonic nanoarrays coupled to Zn-pyChl a attached to poly(CysMA) brushes in DMF as a function of polymer brush thickness.

In the literature, it has been known that the sensitivity of the response of the LSPR energy can change with resonance wavelength and analyte thickness but is independent of nanostructure morphology (248). In general, sensitivity increases with resonance wavelength (at least within a range of 500 – 1100 nm), although given the comparatively small range of E_{LSPR} utilised in this sample set this factor is expected to be small. Of more significance in this case, sensitivity also increases with the analyte thickness but can reach a plateau after a short thickness of ~ 10 nm is reached. A similar variation in response may have occurred in the plasmonic sample set studied here – as the poly(CysMA) brush thickness increased, E_C increased due to the rise in response sensitivity until a 5 nm thickness was achieved in the NL18 sample. After this, the decrease in E_C was likely due to the variability of dipole

orientations between samples (as sensitivity as well as chlorophyllide density were expected to have reached their maximum), and samples with longer brushes may have approached the decay length of the plasmonic field (which also decreases sensitivity has been estimated to be in the 10 nm range in previous strong coupling studies (116).

It was hypothesised in the initial conceptual model of the system that the high density of polymer chains in a dense poly(CysMA) brush layer may make penetration of the chlorophyllides to the lower parts of the brush sterically hindered. This hypothesis was supported by angle-resolved XPS, which suggests the chlorophyllides were concentrated in the top 2 nm layer of the brush. Upon formation of these brush structures on plasmonic nanostructures, both E_C and E_{mol} vary widely between nominally similar arrays of structures, which suggests variable orientations of chlorophyllide dipoles within the plasmon field. This observation again conforms to the amorphous nature of the scaffold predicted in the conceptual model. As the average E_C across the sample set did not breach the strong coupling threshold, the plasmon-exciton coupling will likely not be in the strong regime while the diffusion limit prevents a higher derivatisation of the poly(CysMA) brush than ~ 33%. To maximise attachment, it would be therefore be beneficial to reduce the density of chains in the polymer scaffold, thus allowing greater depth penetration for SC-Zn-pyChl *a* and increasing the dipole density in the plasmon mode volume.

d) *Maximization of Zn-pyChl a incorporation by reducing polymer brush density*

To increase the density of chlorophyllides incorporated in the plasmon mode volume, a strategy of reducing the density of polymer chains in the brush layer was used, thus allowing greater access for diffusion further down the length of the brush. Previous work by Christau *et al* demonstrated enhanced binding of large gold nanoparticles (of diameters ~13 nm) to brushes as the density of the brush layer decreased (227). This was controlled by decreasing the number of initiator groups on the surface by co-adsorption of the initiators with an inactive spacer molecule to form the initial monolayer. As a consequence, in that specific example, the dry thickness and the grafting density of the resulting polymer brush were both found to decrease by approximately 50% when a 1:10 ratio of initiator to spacer was used to form the monolayer compared to initiator only. As a result, the particle density in the polymer brushes increased, indicating greater uptake capacity of the brushes due to the lower density of polymer chains. In this current study, it was hypothesised that a similar reduction in the poly(CysMA) grafting density might also enable better access of the chlorophyllides to pedant amine groups in the lower parts of the poly(CysMA) brushes. As chlorophyllides also have a much smaller molecular dimension (~8.5 Å in planar width using a simple optimized molecular model), it was anticipated that the derivatization of the brushes would greatly increase with the decrease in polymer chain density (figure 4.25). In keeping with the aim of the experiment however, where the density of dipoles was to be increased in the plasmon mode volume, the interplay between the increase of access as well as the reduction of scaffold material overall needed to be considered.
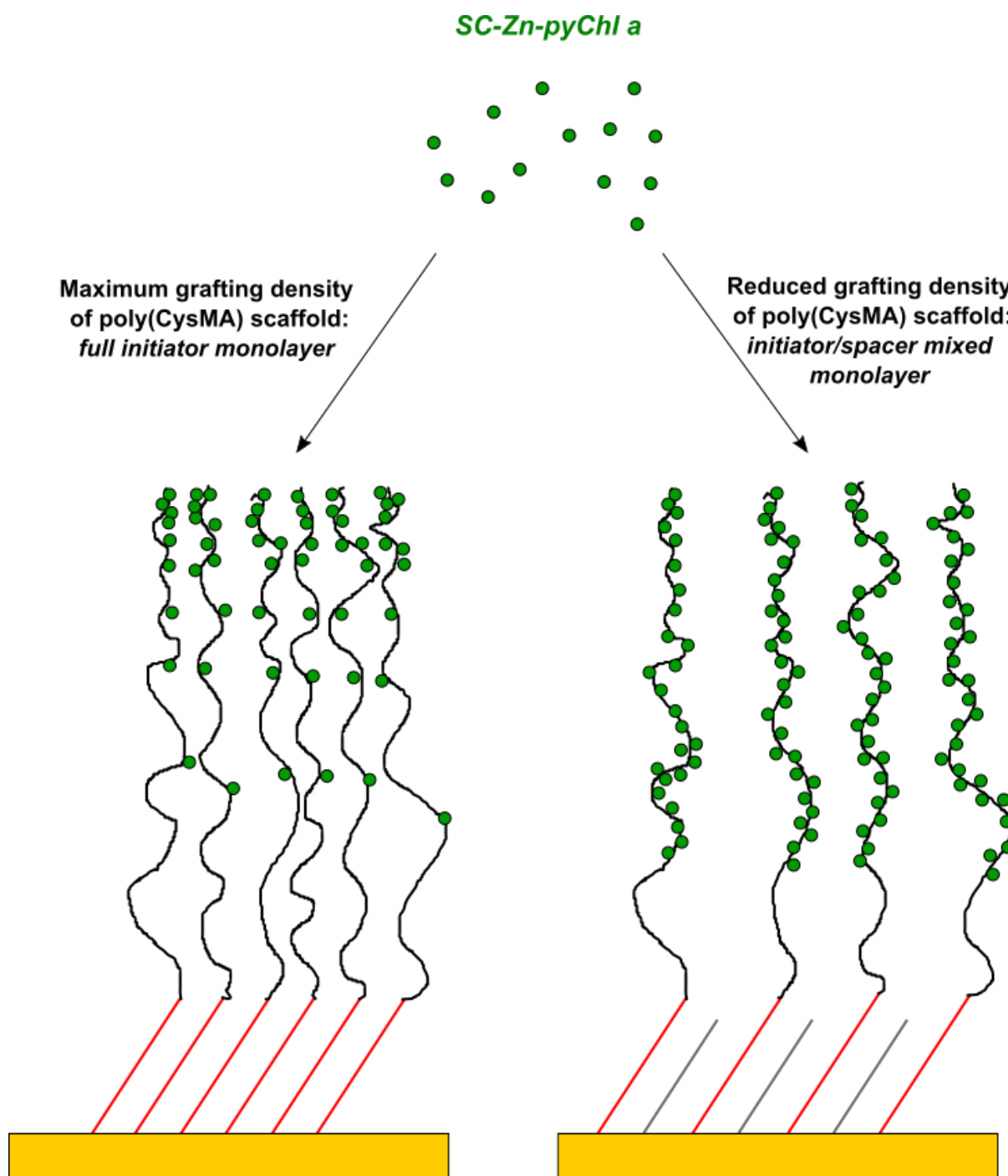
Figure 4.25: The density of Zn-pyChl a molecules appended to poly(CysMA) brushes was predicted to increase when the density of polymer chains is reduced on the surface. While full-density brush layers gave diffusion-limited attachment concentrated on the surface sites, reducing the density by reducing the number of active initiators (red) by co-adsorptions of spacers (grey) in the initial monolayer would allow greater derivatization further into the brush layer. While the total amount of scaffold material would be reduced, this would allow a larger number of dipoles within the plasmon mode volume of an array of gold nanostructures.

Co-adsorption of thiols is an effective means to achieve mixed monolayers on gold substrates. Undecanethiol was selected as the spacer thiol, as it is a few atoms shorter than the anchored DTBU molecule. This still leaves the terminal bromines available for initiation without steric hindrances from the spacer molecules. 1:1, 1:5 and 1:10 DTBU: UDT ratios were used. After adsorption, ellipsometry measurements of the monolayers showed increasing height with increasing UDT composition, reflecting the increase of close-packing from the less sterically-hindered spacer molecules (**Appendix 2 v)**).
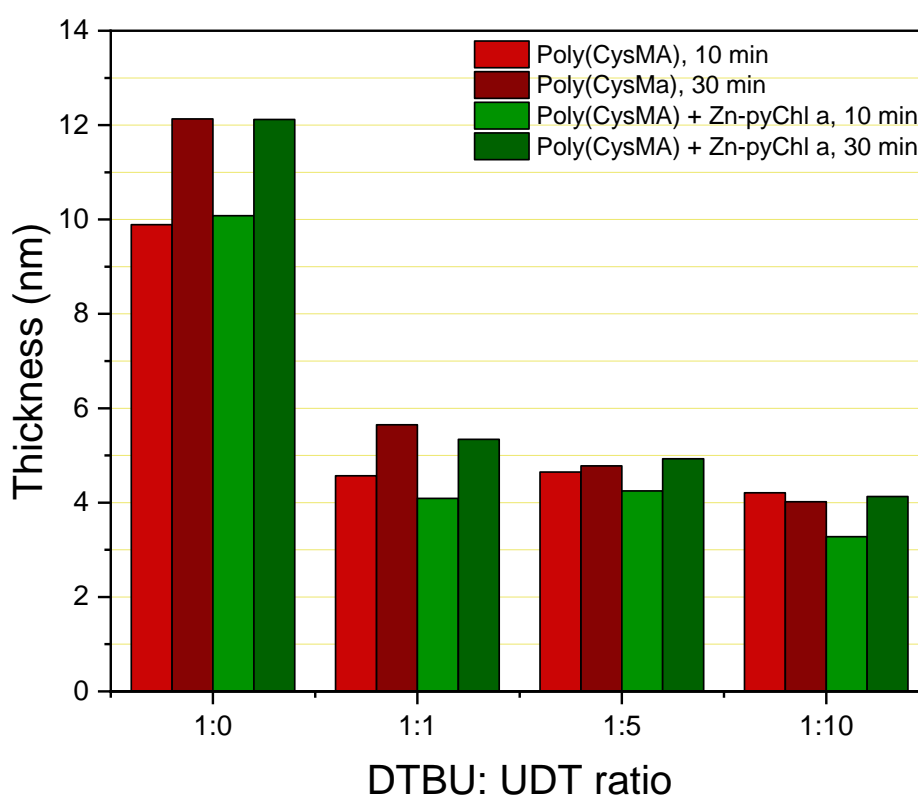
Figure 4.26: Thickness of poly(CysMA) brushes after 10 and 30 min polymerization time for various monolayer ratios of DTBU: UDT.

Poly(CysMA) was then grafted on continuous gold substrates for 10 and 30 min for each monolayer ratio studied (figure 4.26). Here, the dry thickness for the brush grown from the DTBU-only monolayers again deviated from the previous experiments, giving 9.89 and 12.18 nm for the respective polymerization times. For the mixed monolayer ratios, the

measured thickness decreased on average by a factor of 2. This reflects the reduced distance between the brushes, allowing them to collapse closer to the substrate surface than the fully dense brush layers. After attachment of Zn-pyChl *a* with 1:3 DMF: H_2O, the height difference was not significant, indicating that their incorporation did not significantly change the brush packing.

XPS measurements were also carried out on these new samples to estimate the level of attachment, using the N 1s/S 2p ratios (table 5). The full density brushes displayed attachment levels approaching a third of the brush, as expected from previous data. As the ratio of UDT to DTBU was increased, corresponding increases in the attachment were observed. For 1:1, the percentage of Zn-pyChl *a* was approximately 36%, as slight increase but comparable to the fully dense brush. With 1:5, a significant increase resulted in ~ 50% attachment, indicating a higher uptake of Zn-pyChl *a* into the brush layer. The same result was obtained for the 1:10 brush, with an average of ~ 52%.

*Table 5: Calculated values for attachment of Zn-pyChl a poly(CysMA) grafted to mixed-ratio monolayers on gold, derived from the N 1s: S 2p ratios.*

DTBU: UDT Ratio	Poly. Time (min)	N 1s: S 2p Ratio	N 1s: S 2p Ratio after Zn-pyChl *a*	% Unreacted monomer	% Attached Zn-pyChl *a*
1:0	10	0.548	1.168	**0.717**	*0.283*
	30	0.588	1.290	**0.701**	*0.299*
1:1	10	0.483	1.173	**0.643**	*0.357*
	30	0.501	1.227	**0.637**	*0.363*
1:5	10	0.460	1.372	**0.504**	*0.496*
	30	0.533	1.606	**0.497**	*0.503*
1:10	10	0.406	1.275	**0.465**	*0.535*
	30	0.468	1.425	**0.488**	*0.512*

The large increase in attachment observed between the 1:1 and 1:5 ratios of initiator to spacer indicates that there may be a critical grafting density of the brush which allows significantly more penetration of the chlorophyllides into the brush layer. This increase in derivatisation also indicates a large increase in dipole density in the brush layer relative to the number of polymer chains.

Several arrays of gold nanostructures were then functionalized with 1:0, 1:1 and 1:5 ratios of DTBU: UDT. Polymerization was then carried out for the same time periods, giving collections of samples of each monolayer ratio with 10 and 30 mins of polymerization time. These were derivatised with SC-Zn-pyChl *a* in 1:3 DMF: H$_2$O and then measured with UV/Vis spectroscopy. An example utilising the 1:5 monolayer ratio is shown in figure 4.27.
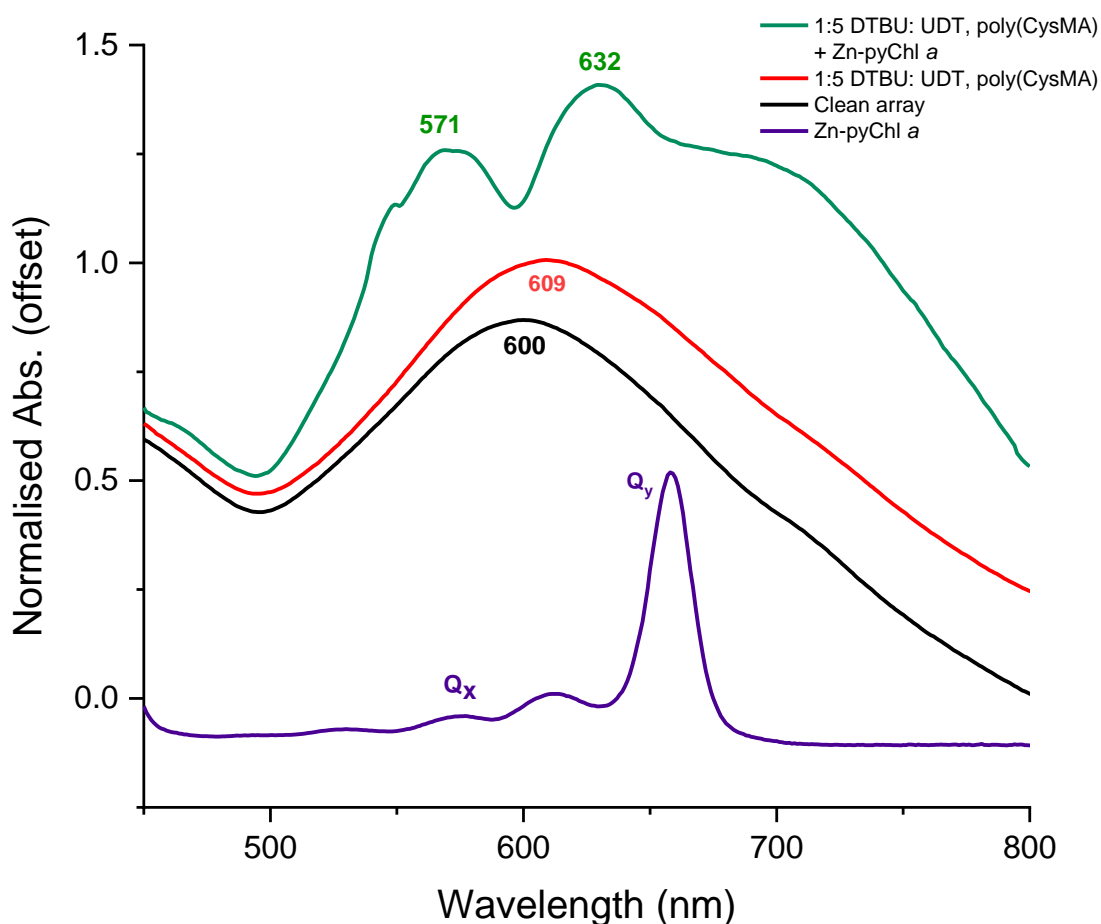
Figure 4.27: *The extinction spectrum of a clean array of gold nanoparticles, then functionalised with a monolayer of 1:5 DTBU: UDT and grafted with poly(CysMA), followed by derivatisation with Zn-pyChl* a. *The extinction spectrum for Zn-pyChl* a *in solution is included for comparison.*

For samples where 1:0 and 1:1 DTBU: UDT monolayers were used, the extinction spectra appeared similar to those observed in the previous plasmonic sample set (see figure 4.22), with a split plasmon peak exhibiting a shoulder feature. While visibly identifiable in the spectra, the lack of resolution of individual linewidths for these split peaks suggested that for 1:1 DTBU: UDT samples that a lack of strong coupling was likely. When 1:5 DTBU: UDT samples were analysed, it was found for many of them that the splitting was greater in magnitude, and the linewidths of each peak were more clearly defined, resulting in two distinct maxima in the spectrum (as shown in figure 4.27). This indicated that the plasmon-exciton coupling may have entered the strong regime and suggested that the lower density of scaffold material resulted in an increase in overall density of dipoles for coupling.

Fitting the extinction spectra with the harmonic oscillator model to obtain E_C revealed that the samples used fell into two distinct groups. With samples with polymer brushes grafted with 1:0 and 1:1 DTBU: UDT, E_C was below 0.2 eV for each sample. This was the expected result for fully dense brushes and reflects the XPS data obtained for the 1:1 ratio samples, which did not show a significant increase in chlorophyllide derivatisation. Several 1:5 ratio samples also belonged to this category, possibly indicating that the maximum derivatisation was not achieved for those particular samples or that the dipole orientations were too random in relation to the plasmonic field direction to give strong coupling. The average E_C for samples in this category was 0.11 ± 0.04 eV. However, several 1:5 ratio samples showed a much stronger response, with many samples giving E_C values approaching 0.5 eV. The average E_C of these samples was 0.43 ± 0.09 eV. These samples clearly met the criteria for strong coupling. This can be attributed to the large increase in derivatisation of the poly(CysMA) brushes for this monolayer ratio as measured by XPS. This indicates that the number of dipoles immobilised in the polymer brush scaffold within the plasmon mode volume was greatly increased compared to fully dense polymer brush layers.
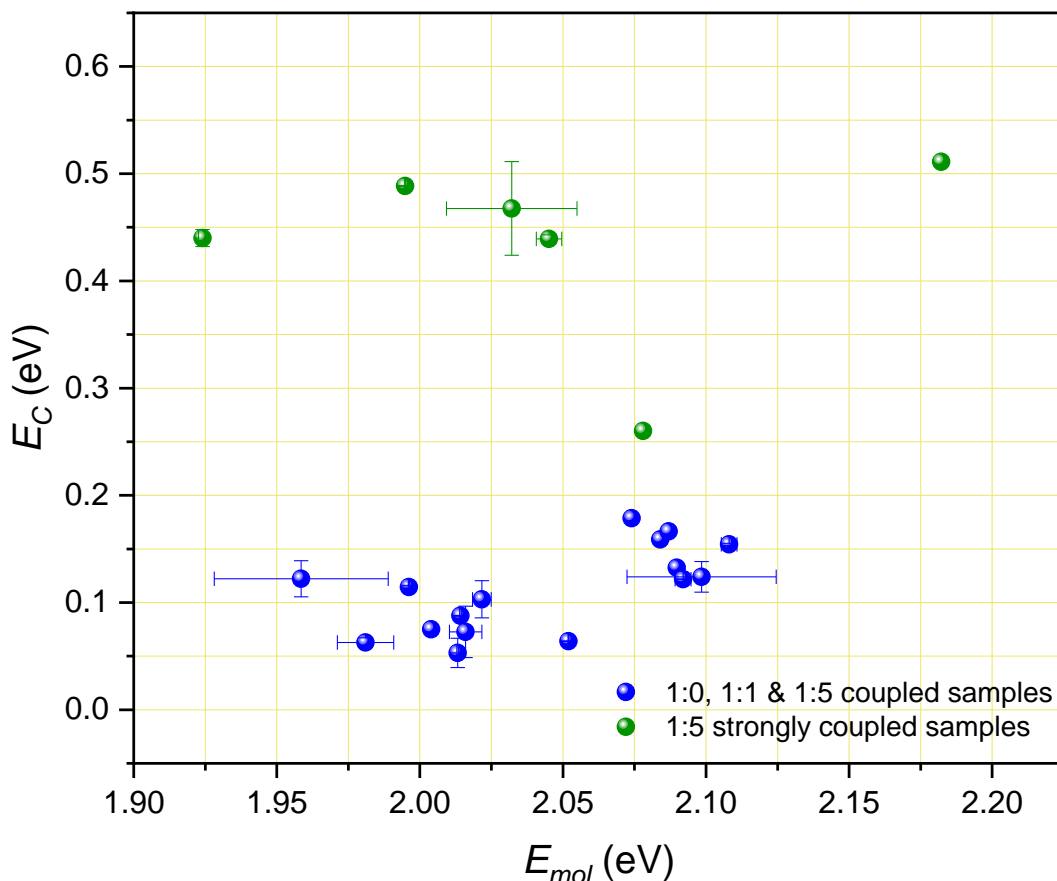
Figure 4.28: E_C *vs.* E_{mol} *for plasmonic nanostructures derivatised with poly(CysMA) and Zn-pyChl* a *using 1:0, 1:1 and 1:5 DTBU: UDT base monolayers. Samples below the strong coupling threshold* ($E_C \approx 0.24$ eV) *are shown in blue, whereas samples within the strong coupling regime are displayed in green.*

One more characteristic which may contribute to the strong coupling of the chlorophyllides was observed in the extinction spectrum of the strongly-coupled 1:5 monolayer ratio samples. Some of these samples displayed an addition shoulder feature at lower energy from the plasmon peak (as illustrated for the sample observed in figure 4.27 at ~ 694 nm). This feature appears in similar positions between the samples and is red-shifted to the Q_y transition for Zn-pyChl a in solution. It is possible that the feature could be the result of coupled Q_y dipoles between the chlorophyllides in the brush layer. The formation of *J*- and *H*-aggregates has been observed in the literature to modify the Q_y transition energy when chlorophylls are aggregated (207, 208). This feature is not observed in the spectra of samples

which are calculated to have coupling below the strong regime boundary. This suggests that the control of scaffold density may be important in enabling the large-scale formation of chlorin dimers, which have been implicated in fast coherent energy exchange in the strongly coupled plasmon-exciton regime (129). The range of exciton energies observed for the strongly coupled systems may also suggest that the energy transfer is enhanced by these aggregates despite variable orientations of the dipoles in the brush layer. Chlorosome-like assemblies of chlorophylls incorporated in polymer brushes may therefore be attractive systems to utilise exciton-polaritonic mechanisms for ultra-fast energy transfer.

4. Conclusion

Polymer brushes have been explored as a synthetic scaffold for organising chlorophyll pigments in space. Here, poly(cysteine methacrylate), a zwitterionic brush with pedant amine groups, has been grafted to gold substrates and nanoparticle arrays using a modified surface-initiated ARGET-ATRP mechanism. While the control of brush thickness is difficult between polymerizations, brushes can be grown in quick time frames using this method. A derivative of naturally-sourced chlorophyll *a* was then coupled to the brush scaffold using common cross-linking chemistry via a succinimidyl active ester coupling to the amine groups of the brush. In a conceptual model, this method of organising the chlorophyllides was anticipated to increase their density within the plasmon mode volume and give stronger coupling than observed for the AcS-12C-BC molecular monolayers. The amorphous nature of the solvent and charge-responsive poly(CysMA) brush scaffold was also predicted to give different densities of Zn-pyChl *a* dipoles, depending on how well the brush was solvated as well as the grafting density of the brushes.

As determined by XPS quantification, using various solvents affects the level of derivatisation of the brush, with a 1:3 DMF:H_2O solution giving the greatest amount of incorporation. For brush layers of full surface density, approximately a third of the brush can be derivatised with chlorophyllides. This incorporation is diffusion limited, with the top 2 nm of the brush holding the greatest density of chlorophyllides. This does not affect the general pH-responsiveness of the poly(CysMA) brush. When these brushes were grafted to arrays of plasmonic nanoparticles and derivatised with chlorophyllides, the coupling of the excitons to the plasmon mode was not in the strong regime. This was suggested to be due to the number of dipoles organised in the plasmonic field, which was initially controlled using DMF or 1:3 DMF: H_2O as the mediating solvent for the chlorophyllide attachment. Despite a 33% derivatisation efficiency in the latter solvent, the system did not increase the average coupling energy over 0.13 eV, below the threshold into the strong-coupling regime. This would suggest that the density of chlorophyllides achieved in the plasmonic field was not significantly higher in these scaffolds than in the AcS-12C-BC monolayer system. Better access of the chlorophyllides to the deeper sections of the brush was therefore required.

To increase the level of diffusion into the brush layer, thereby increasing the degree of derivatisation, poly(CysMA) brushes were grafted to monolayers with reduced initiator density, where DTBU was co-adsorbed with UDT. Where the ratio was increased to 1:1, a similar degree of derivatisation was observed compared to the fully dense brushes. However, when the ratio was increased to 1:5, a significant increase in chlorophyllide attachment led to approximately 50% of the brush layer to be derivatised. When assembled in a plasmonic field, these reduced-density scaffolds appear to increase the chlorophyllide density enough to allow strong plasmon-exciton coupling to occur, achieving coupling energies up to ~ 0.5 eV. This result suggests that while the overall scaffold material was reduced, the overall density of dipoles was increased, conforming to what was predicted in the conceptual model. The

calculations for the exciton energies in these brushes suggest that the coupling behaviour is complex due to the various orientations the chlorophyllides can adopt in relation to the plasmonic field polarization, leading to simultaneous coupling to Q_x and Q_y by varying degrees. However, formation of aggregates of chlorophyllides may be possible within the reduced-density scaffolds, allowing the system to engage in ultra-fast coherent energy transfer via an exciton-polaritonic mechanism despite the orientation of the chlorophyllide dipoles.

Polymer scaffolds for chlorophyll may therefore be an attractive material for future use as a biologically inspired energy transport system, achieving energy transfer comparable to light-harvesting complexes coupled to plasmonic systems. There is space for further development in this area by fine-tuning the scaffold density for optimum response, studying the possible relationship of brush thickness and density on the dipole density, and exploiting the pH-responsiveness of the poly(CysMA) brush to investigate the possibility of switchable coupling response in liquid media.

Conclusions and Outlook

In the present work, two molecular approaches were used to organise chlorophyll-type emitters in the plasmon mode volume of gold nanostructures. In doing this, a device may be constructed that captures and transfers energy from light with high efficiency through a strongly coupled plasmon-exciton hybrid state. As biological structures use protein scaffolds to organise emitters for optimum performance, synthetic scaffolds bound to plasmonic substrates can be used to provide a means to organise emitters within plasmonic fields.

In the first approach, a synthetic emitter inspired by natural bacteriochlorophylls was synthesised from simple starting reagents and self-assembled on gold surfaces using thiolate chemistry, as a potential surface model for chlorosome assemblies. These bacteriochlorins were likely to be assembled in upright conformations with the macrocycle plane perpendicular to the sample plane, with a surface density of $\sim 3.7 \times 10^{-17}$ m^{-2}. This was lower than expected for a self-assembled system compared to the densities found in LH2 (116), due to the large physical dimensions of the bacteriochlorins, although adsorption isotherms of the system suggest the monolayers achieved their maximum possible density. Both transition dipoles were also suggested to be part-aligned with the plasmonic field polarization. These bacteriochlorin films displayed plasmon-exciton coupling when adsorbed to gold nanostructures. For these systems, an average coupling energy of 0.12 ± 0.04 eV was achieved, indicating coupling below the strong coupling boundary. The average exciton energy was found to be between the Q_x and Q_y transitions, indicating a possible complex coupling phenomenon involving both transitions simultaneously. Other observed features in the ellipsometry and extinction spectra may also indicate formation of H- or J-aggregates in these films, like those found in chlorosomes.

Secondly, poly(CysMA) brushes were utilised as scaffolds for naturally derived chlorophyllides, where pedant amine groups of the brushes were reacted with active esters appended to the chlorophyllides. The degree of derivatisation was found to depend on the solvent-controlled swelling of the brush structures and the density of grafted polymer chains on the surface. For fully dense polymer brush layers, the maximum derivatisation was limited by diffusion to ~ 33% of the brush groups. The coupling energy of the chlorophyllides in these brushes to the plasmon mode was low, indicating the density of dipoles was too low for strong coupling. However, tailoring the scaffold density by co-adsorbing the surface initiators with inert spacer molecules increased the dipole incorporation per chain by ~ 50%. In these structures, strong coupling was observed, achieving coupling energies up to ~ 0.5 eV and suggesting that the lowering of the brush density gave a subsequent increase in incorporated dipole density in the plasmon mode volume. Even in the strongly-coupled systems a wide range of exciton energies was measured, indicating that the amorphous polymer brush matrix could allow the chlorophyllide dipoles to organise in many different orientations. This may suggest a very complex coupling relationship between the plasmons and excitons in these systems.

Chlorophyll-type excitonic emitters have been successfully arranged in plasmon modes using two molecular engineering approaches: either by "self-scaffolding" assembly or using a robust, responsive synthetic polymer scaffold with customisable surface dimensions and density. The excitons and plasmonic modes are then coupled to make hybrid plexciton states which have been implicated in fast coherent energy transfer. The coupling dynamics may be the result of simultaneous coupling of the plasmon mode to the Q_y and Q_x dipoles which are imperfectly aligned with the field polarization. This may expose a weakness in the original harmonic oscillator model used to describe these systems, which assumes that the plasmon mode is coupled to excitons directly aligned in the field direction. An update may be

required of this model for coupling to dipoles of various orientations, which is likely to increase the complexity of the hybrid plexciton state formation. However, the strong coupling observed with chlorophyllides arranged in polymer brushes indicates that these structures are attractive candidates for developing improved synthetic light-harvesting systems inspired by nature.

In future work, the monolayer system can be developed further by exploiting synthetic chemistry to produce hierarchical three-dimensional multilayers, hopefully with an increase in dipole density in the plasmon mode volume and their transition dipole moments aligned optimally for fast coherent transfer in the plasmon mode. Alternatively, the polymer chemistry could be developed further to afford new scaffold functionality. First, a greater range of grating densities may be evaluated for assembling denser pigment assemblies, as well as the relation to brush height. As poly(CysMA) is a stimulus-responsive polymer, it's use may allow pH-responsive coupling dynamics when liquid media are used, especially in conditions of high and low pH. Other kinds of pigment molecules may also be introduced into these scaffolds, including natural carotenoids with much higher transition dipole moments or synthetic pigments tailor-made for incorporation into these systems. The design of these systems may then be optimised to be included in a new generation of photovoltaic devices operating on biologically-inspired principles, perhaps as "optical circuitry" which transfers energy fast and coherently for charge separation.

Appendix 1

i. Spectroscopic Ellipsometry - Model description for AcS-12C-BC adsorbed to unpatterned gold substrates[‡]

Layer	Description	Comments	Fitted parameters	
			d	Optical constants n & k
Substrate	BK7 glass	Si_JAW		
Cr_2	Chromium	**d = 4.24 ± 0.2111 nm**	√	**X**
B-spline	Gold	starting material: Au_nk3 **d = 16.52 ± 0.4859 nm**	√	*
B-spline	AcS-12C-BC	Starting material: AcS-12C-BC *Optical constants fitted by wavelength-by-wavelength method, compared to absorption spectrum* **d = 4.31 ± 0.515 nm**	√	*
Angle offset		Only applied when "Fit Opt. Const." = OFF to avoid 100% correlation		

‡) Fitting was performed using CompleteEASE (J.A. Woollam Co., Inc), version 5.14. Material files for known materials used for the modelling were supplied in the software package.

*) Optical constants *n* & *k* of the gold layer and for AcS-12C-BC were determined separately and fixed during the fitting.

ii. *Adsorption isotherm study for AcS-12C-BC*

Set 1 – Spectroscopic ellipsometry, thickness vs. concentration, 2 hours and 65 hours adsorption time

Concentration (mM)	d (mean) + SD (nm) – 2 hours	d (mean) + SD (nm) – 65 hours
2	3.18 ± 0.113	4.145 ± 0.035
1.75	N/A	4.033 ± 0.032
1.5	N/A	3.673 ± 0.208*
1.25	N/A	4.113 ± 0.085
1	2.45 ± 0.245*	4.177 ± 0.051
0.75	N/A	4.39 ± 0.046*
0.5	2.9 ± 0.29	3.22 ± 0.193*
0.25	2.09 ± 0.209	3.81 ± 0.026
0.125	1.95 ± 0.028	2.817 ± 0.252
0.0625	1.495 ± 0.007	2.16 ± 0.052
0.032	1.655 ± 0.035	1.38 ± 0.138
0.015	1.22 ± 0.122	1.117 ± 0.756
0	0	0

*Certain data points were considered as outliers due to the deviation from the general trend of thickness with concentration. These were excluded for the purposes of fitting.

Set 2 – X-ray photoelectron spectroscopy, C 1s / Au 4f (Atomic%) vs. concentration, 65 hours

Concentration (mM)	C/S Ratio + SD (nm) – Group 1	C/S ratio (mean) + SD (nm) – Group 2
2	1.115 ± 0.111	1.114 ± 0.188
1	0.670 ± 0.058	1.487 ± 0.311
0.5	0.955 ± 0.032	0.847 ± 0.019
0.25	0.733 ± 0.068	0.744 ± 0.037
0.125	0.632 ± 0.030	0.597 ± 0.002
0.0625	0.591 ± 0.054	0.545 ± 0.050
0.032	0.650 ± 0.083	0.516 ± 0.003
0.015	0.520 ± 0.030	0.446 ± 0.020
0	0.395 ± 0.023[*]	0.395 ± 0.023[*]

[*]An unfunctionalized blank gold reference was used. Clean gold substrates show carbon composition due to adventitious adsorption of carbon-containing molecules from the atmosphere such as CO_2.

Set 2 - AcS-12C-BC, C 1s / Au 4f %[A] ratio vs. concentration immobilized on BK7 glass/Cr/Au
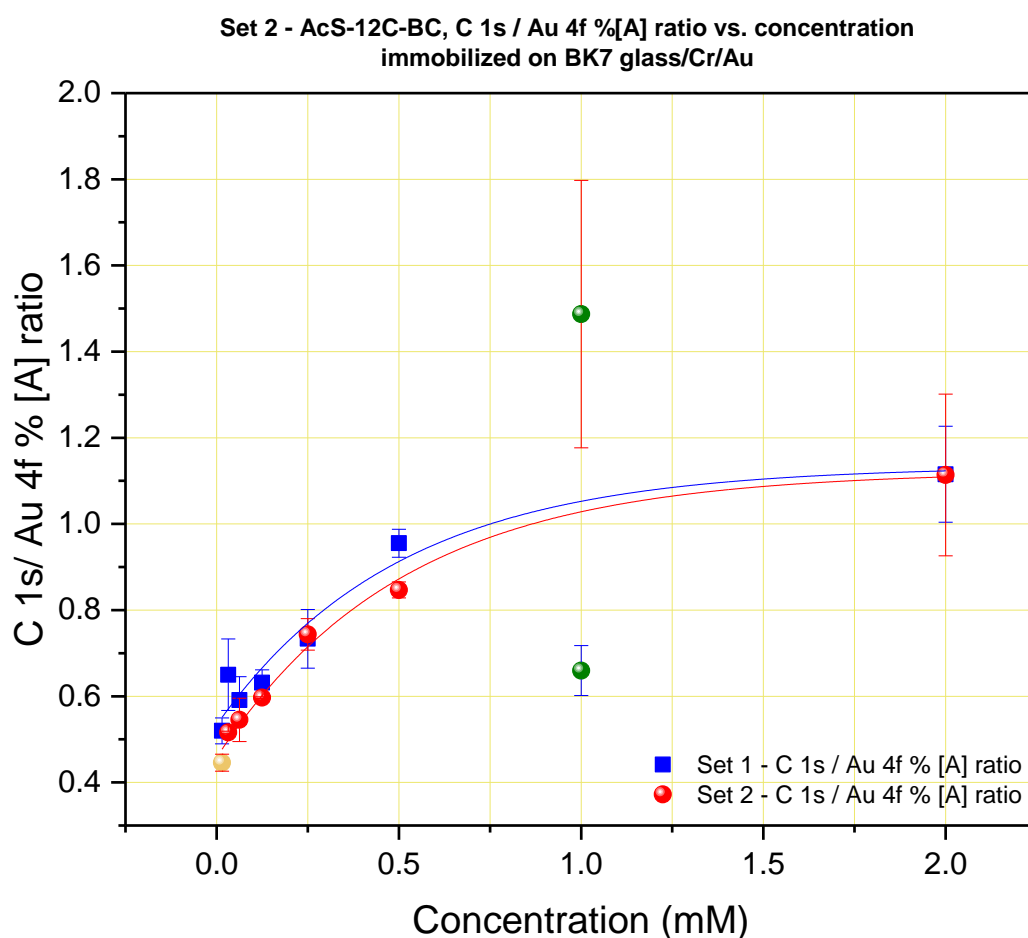
Increase of thickness of AcS-12C-BC with time, 55 minute time period

AcS-12C-BC (c=2 mM)
TIRE Fitting Results (dymanic scan)
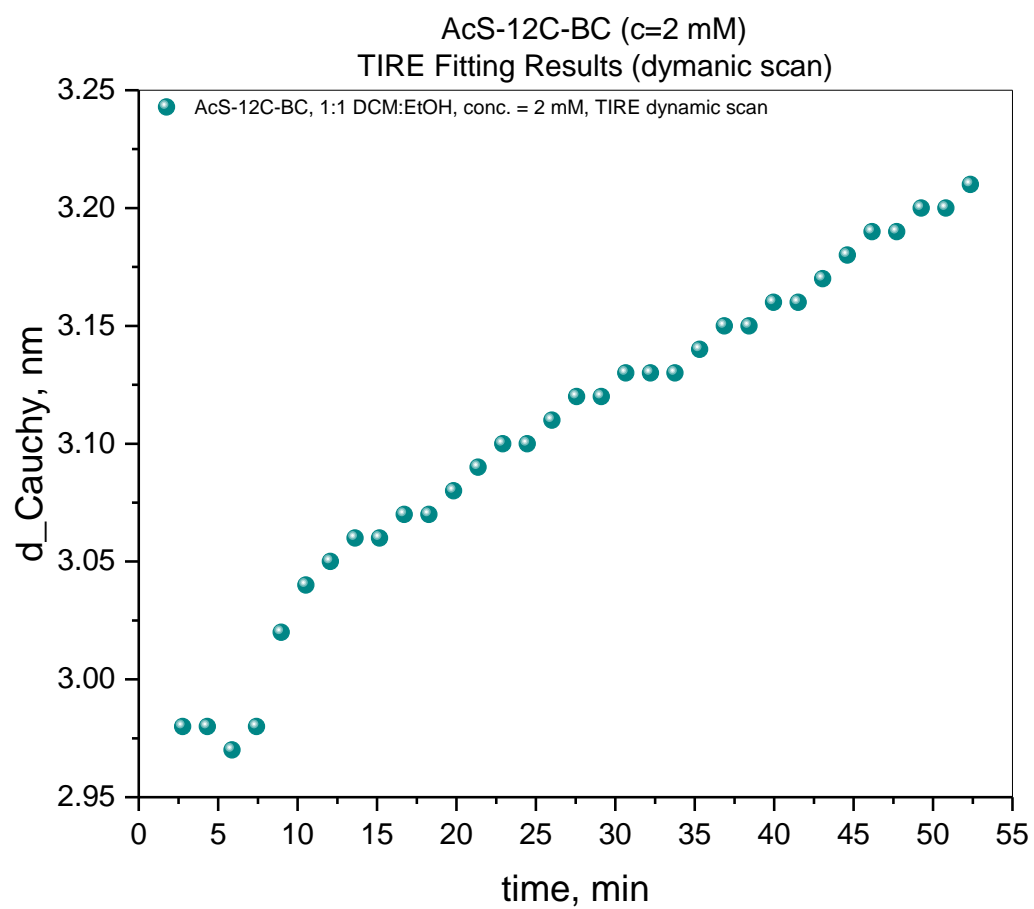
Appendix 2

i. *Model description for ellipsometry measurements of poly(CysMA) brushes in air and liquids*

Layer	Description	Environment				d	Optical constants n & k	% EMA Material #2	A/n
		H₂O	DMF:H₂O (1:3)	HCl pH = 1.31	NaOH pH = 12.68				
		n=1.33	n=1.366	A=1.334	A=1.364				
		comments							
Substrate	BK7 glass	n = 1.515							
Cr_2	Chromium					√	X		
B-spline	Gold	starting material Au_nk3				√	*		
Cauchy	initiator	A=1.399 DTBU, DTBU:UDT (1:1), (1:5), (1:10)				√	X		**
EMA Case 1: pCysMA	Material #1	"Host" material i.e. environment				√	X		
	Material #2	"Guest" material i.e. p(CysMA) (n=1.53 or A=1.504)						√	X
EMA Case 2: pCysMA +Chl a	Material #1	"Host" material i.e. environment				√	X		
	Material #2	"Guest" material i.e. p(CysMA) + Chl						√	√
Angle offset		Only applied when "Fit Opt. Const."= OFF to avoid 100% correlation							

*) Optical constants *n* & *k* of the gold layer were determined separately and fixed during the fitting.
**) Parameters B = 0.01 and C = 0 were fixed during the fitting. Thickness of the initiator layer was determined separately and fixed during the fitting.

The refractive index of the liquid mixture was calculated according to the Lorentz-Lorenz equation[1]:

$$\frac{n^2{}_{123} - 1}{n^2{}_{123} + 2} = \frac{n^2{}_1 - 1}{n^2{}_1 + 2}\varphi_1 + \frac{n^2{}_2 - 1}{n^2{}_2 + 2}\varphi_2 + \frac{n^2{}_3 - 1}{n^2{}_3 + 2}\varphi_3$$

[1] Chen, H.; Kou, X.; Yang, Z.; Ni, W.; Wang, J. Shape- and Size-Dependent Refractive Index Sensitivity of Gold Nanoparticles. *Langmuir* **2008**, *24*, 5233-5237

where n_{123} is the refractive index of the liquid mixture, n_1, n_2 and n_3 are the indices of the environment, poly(CysMA) (1.53) and poly(CysMA) + Zn-pyChl a respectively, and φ_1, φ_2 and φ_3 are the volume fractions of the three components.

ii. Ellipsometry data for poly(CysMA) brushes grown by ARGET-ATRP

Immersion time (minutes)	Thickness, nm (dry)	Thickness (H₂O)	Thickness (HCl, pH 1.35)	Thickness (NaOH, pH 12.71)
0.5	2.86 ± 0.04	12.04 ± 0.95	22.98 ± 2.09	18.71 ± 2.05
1	3.79 ± 0.03	17.65 ± 1.40	33.52 ± 1.07	33.9 ± 1.04
2	9.31 ± 0.04	29.02 ± 0.7	77.5 ± 1.0	75.3 ± 1.13
5	17.52 ± 0.2	50.31 ± 0.96	91.53 ± 0.40	111.93 ± 0.48
10	26.24 ± 0.09	65.27 ± 0.8	103.61 ± 0.55	122.42 ± 0.91
15	32.06 ± 0.26	77.99 ± 0.53	111.695 ± 1.5	126.76 ± 0.57
30	43.79 ± 1.04	89.06 ± 0.32	116.56 ± 0.75	137.13 ± 0.36
60	49.31 ± 0.38	96.31 ± 0.35	122.91 ± 0.29	137.83 ± 0.40
120	55.73 ± 0.20	103.21 ± 0.26	128.38 ± 0.27	141.77 ± 0.52

Height of p(CysMA) brushes in solvent against dry height
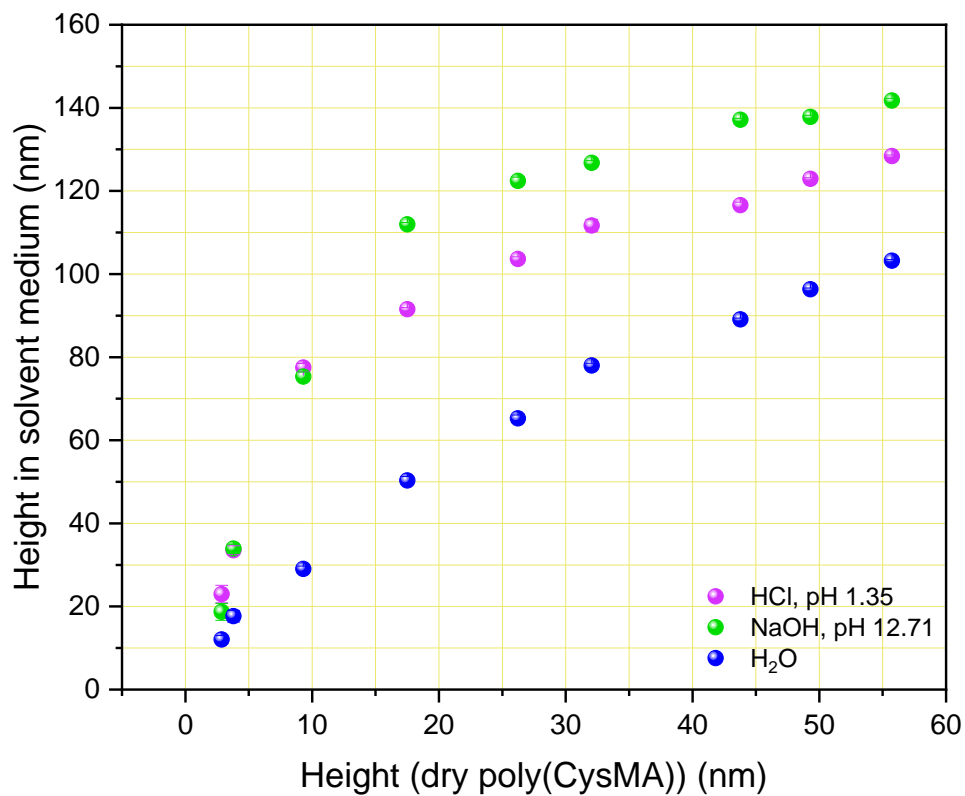
Height ratio of poly(CysMA) brushes in solvent against dry height
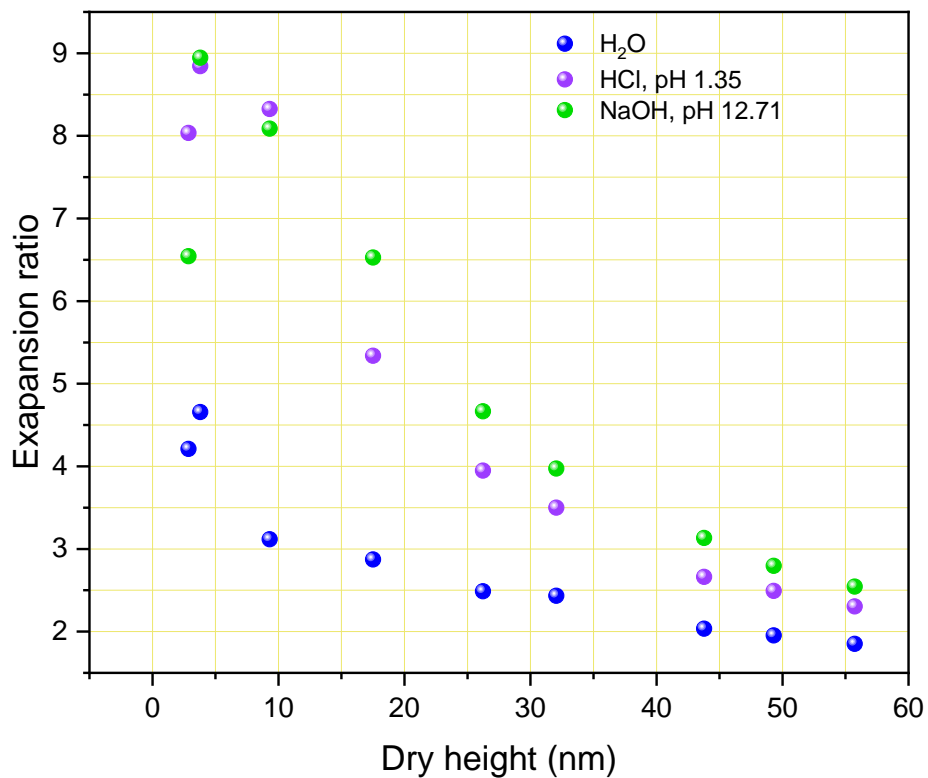
iii.   *Ellipsometry data – Zn-pyChl* **a** *attachment to poly(CysMA) brushes*

Polymerization time (minutes)	Thickness, nm (dry)	Thickness (H₂O)	Thickness (HCl, pH 1.35)	Thickness (NaOH, pH 12.71)
0.5	2.24 ± 0.01	12.5 ± 1.05	29.37 ± 9.11	24.05 ± 1.55
1	3.47 ± 0.12	16.06 ± 1.54	51.98 ± 3.49	32.23 ± 3.2
2	6.78 ± 0.04	30.8 ± 1.56	76.29 ± 1.18	79.61 ± 2.04
5	12.16 ± 0.07	47.82 ± 1.32	92.01 ± 0.45	95.9 ± 0.64
10	18.91 ± 0.09	64.33 ± 0.86	105.23 ± 0.67	114.97 ± 1.32
15	21.62 ± 0.11	74.24 ± 0.328	111.85 ± 0.44	121.7 ± 1.01
30	33.42 ± 0.08	90.8 ± 0.15	126.54 ± 0.32	128.14 ± 0.68
60	40.33 ± 0.04	89.63 ± 0.247	132 ± 7.5	129.59 ± 7.55

Height in solvent media against dry height

Height ratio of poly(CysMA) + Zn-pyChl *a* against dry height
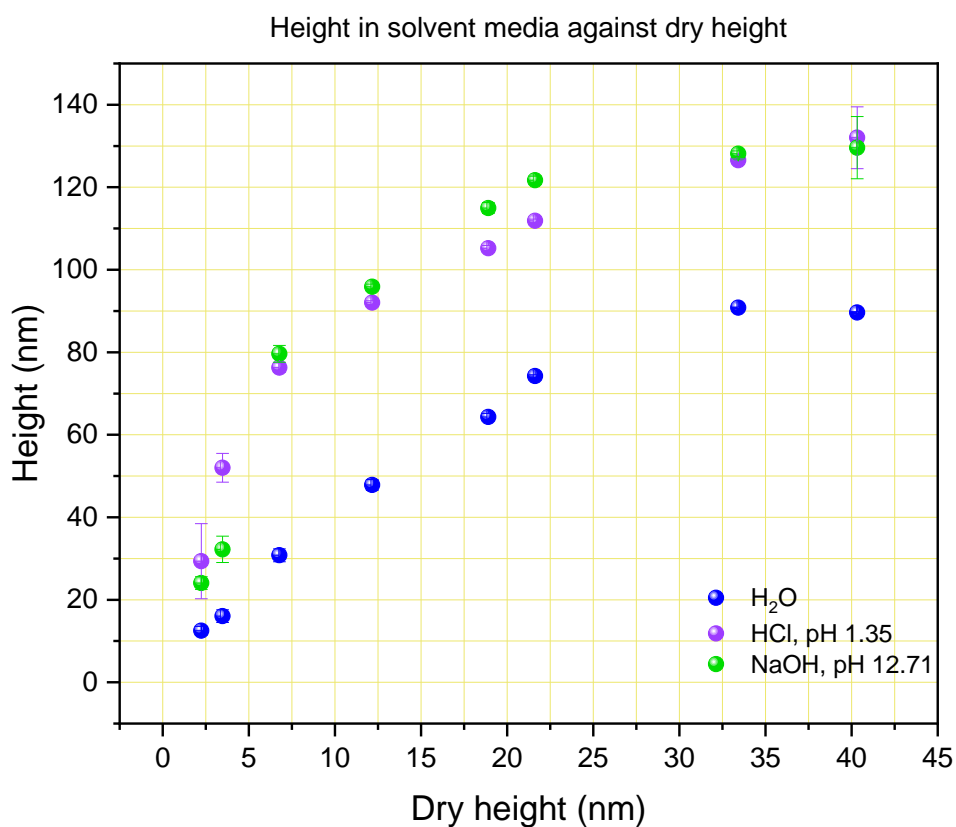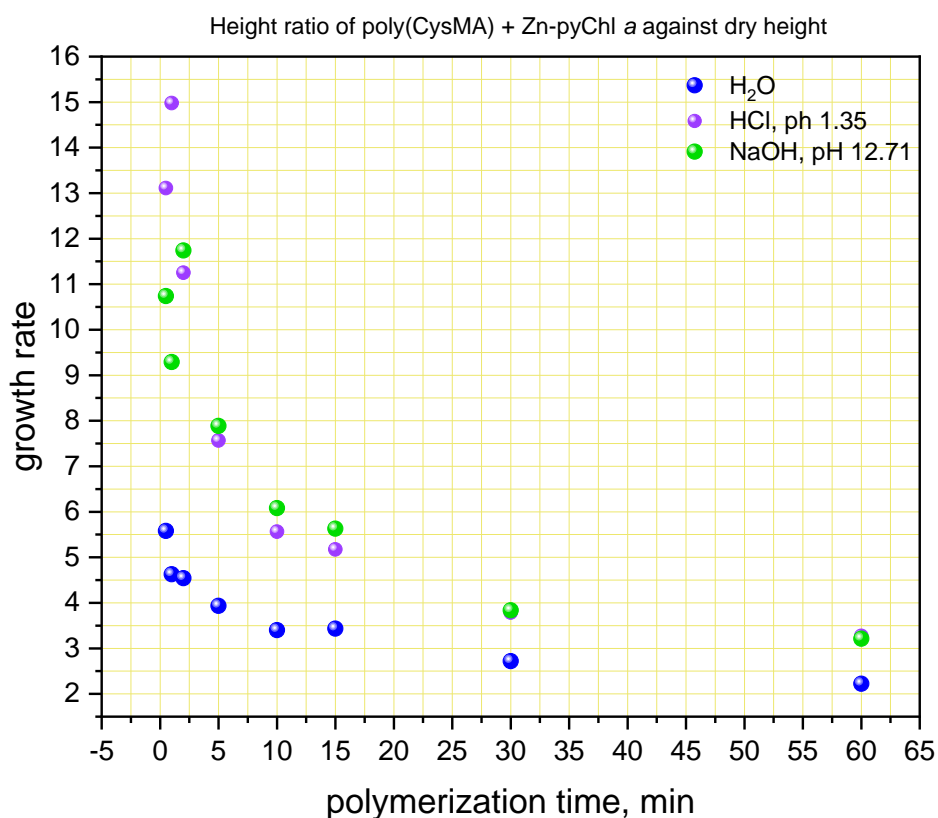
iv. *XPS: analysis of a 17.8 nm poly(CysMA) brush on gold after Zn-pyChl **a** attachment*

Binding Energy (eV)	Binding energy after Zn-pyChl a	Assignment	% Atomic Concentration before Zn-pyChl a	% Atomic Concentration after Zn-pyChl a
N 1s				
399.3	399.78	-NH₂	43.6	65.52
401.5	401.63	-NH₃⁺	56.4	34.48
C 1s				
285	285	C-C	50.12	55.23
286.42	286.47	C-C-O / C-C-N	30.99	24.35
N/A	287.86	N-C=O	N/A	9.43
288.79	289.15	O-C=O	18.89	10.99

v. ***Ellipsometry measurement of monolayers with mixed ratios of DTBU: UDT on continuous gold substrates***

Measured thickness of DTBU:UDT mixed monolayers
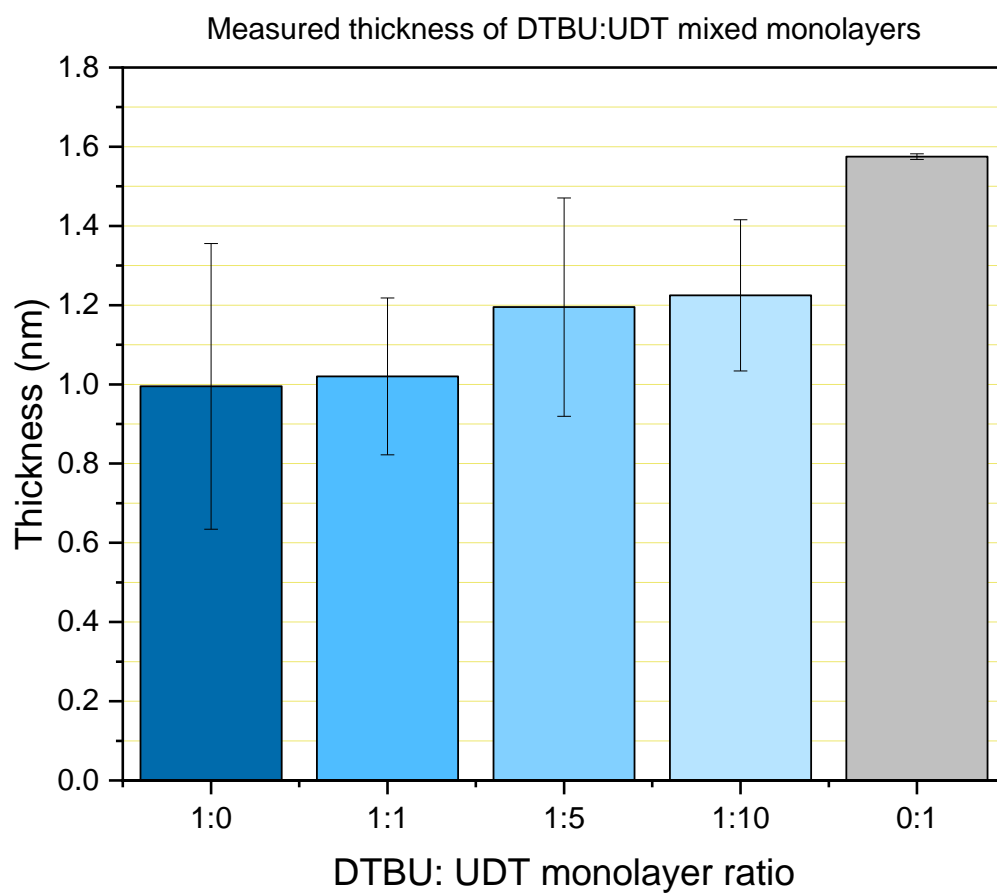
Appendix 3

i.   *Gold nanostructure arrays – physical properties and AFM images*

Sample Identifier	Rotation Angle (degrees)	λ_{LSPR} after annealing and piranha cleaning (nm)	Height (nm)	Density (μm^{-2})	Period (nm)	Image
NJ51	20	572	40	3.55	300	*A)*
A30	15	588	61	2.41	310	*B)*
NL18	10	643	98	1.67	290	*C)*
NL51	17	657	32	6.47	280	*D)*
A33	70	600	53.78	5.69	278	*E)*
RK5	60	592	39.13	1.51	263	*F)*
19_O	90	577	47.38	2.00	260	*G)*
17_O	45	580	58.70	8.68	283	*H)*

E)

Height   4.0 µm

77.1 nm

-41.9 nm

F)

Height   4.0 µm

45.4 nm

-26.5 nm

Height   74.7 nm

                         -49.3 nm

                          4.0 μm

Height   84.4 nm

                         -50.7 nm

                          2.0 μm
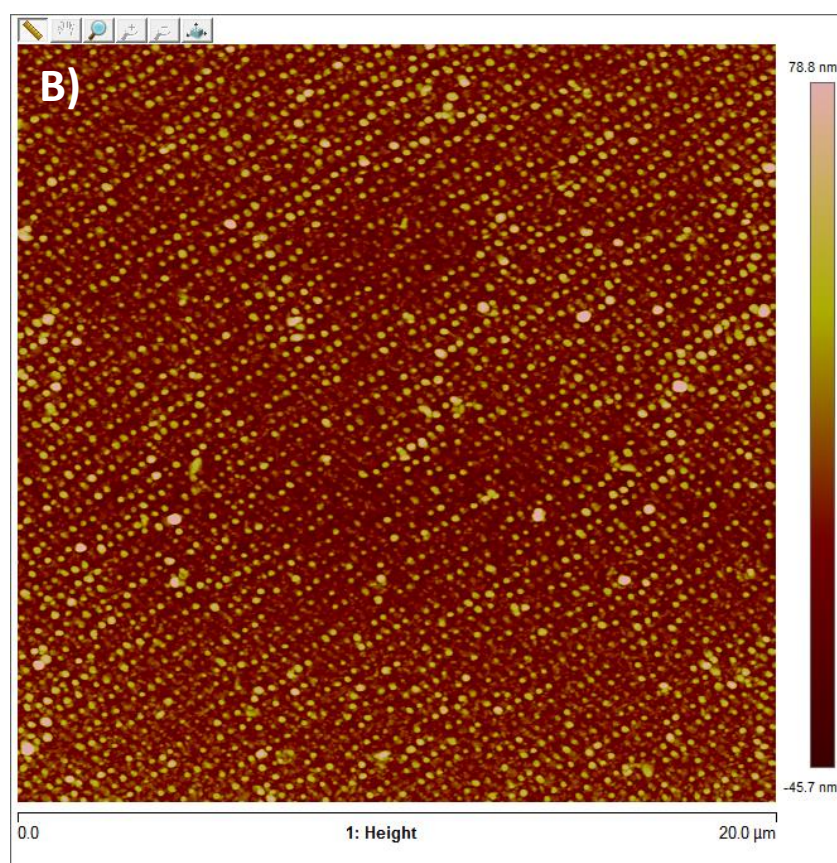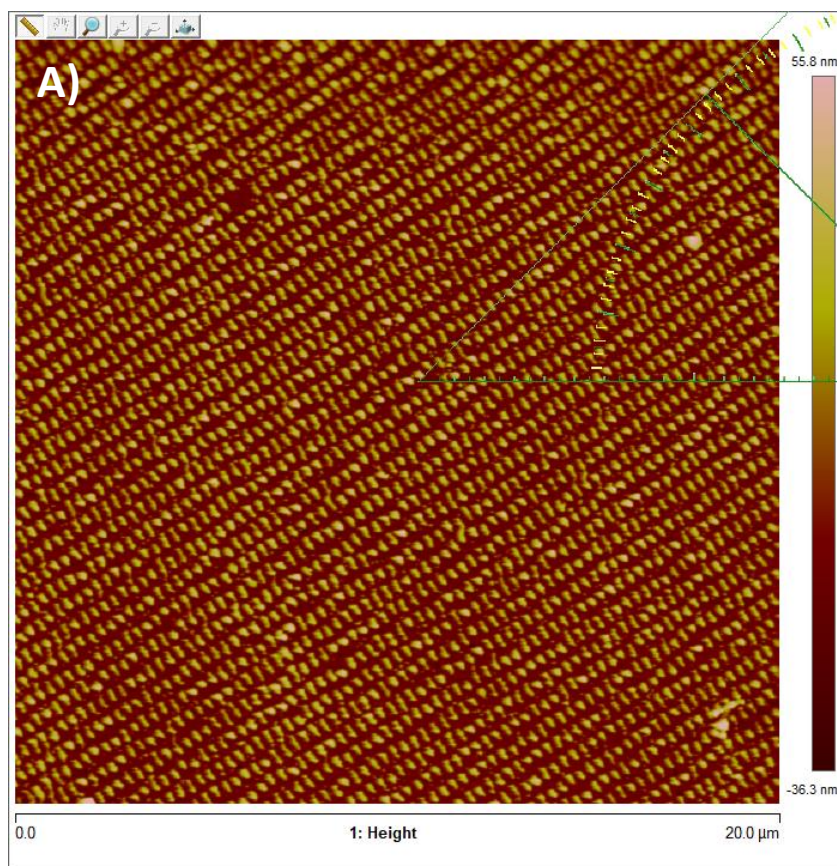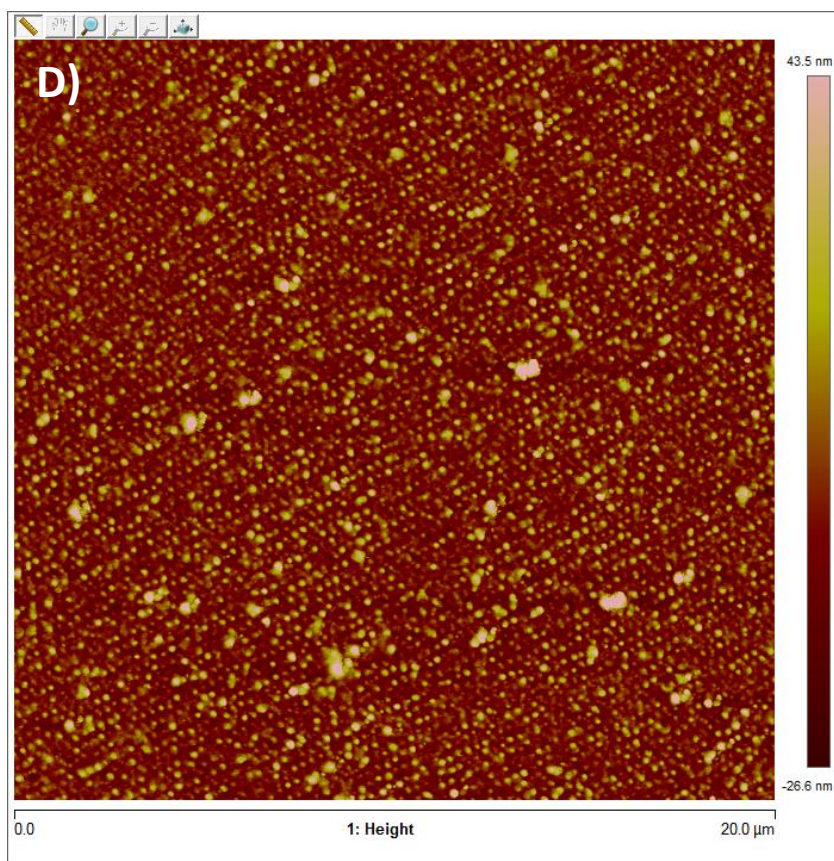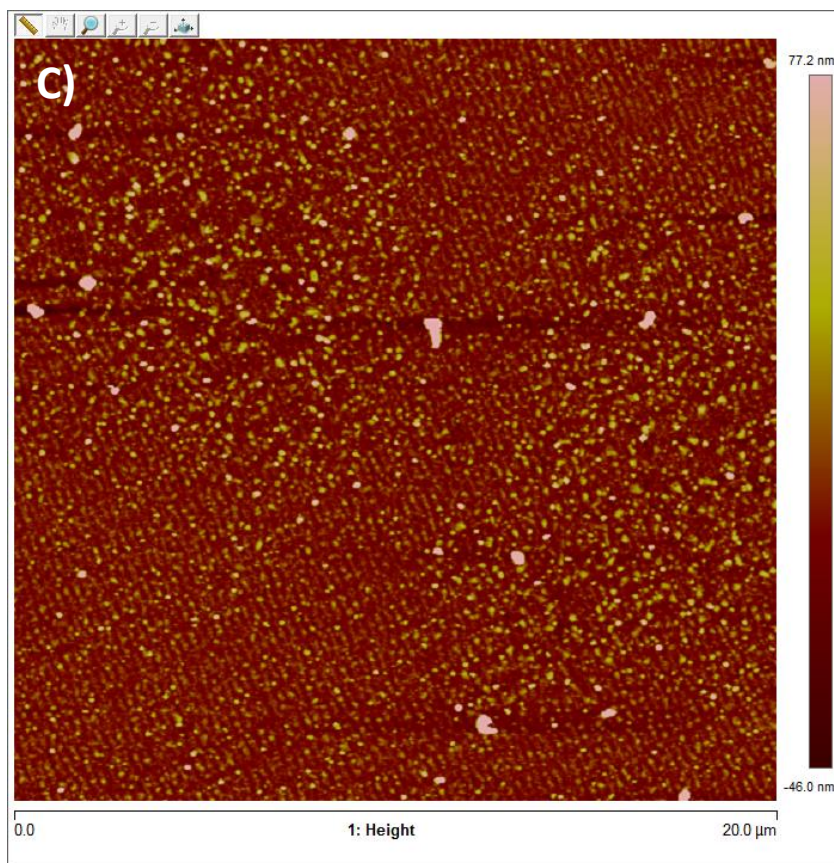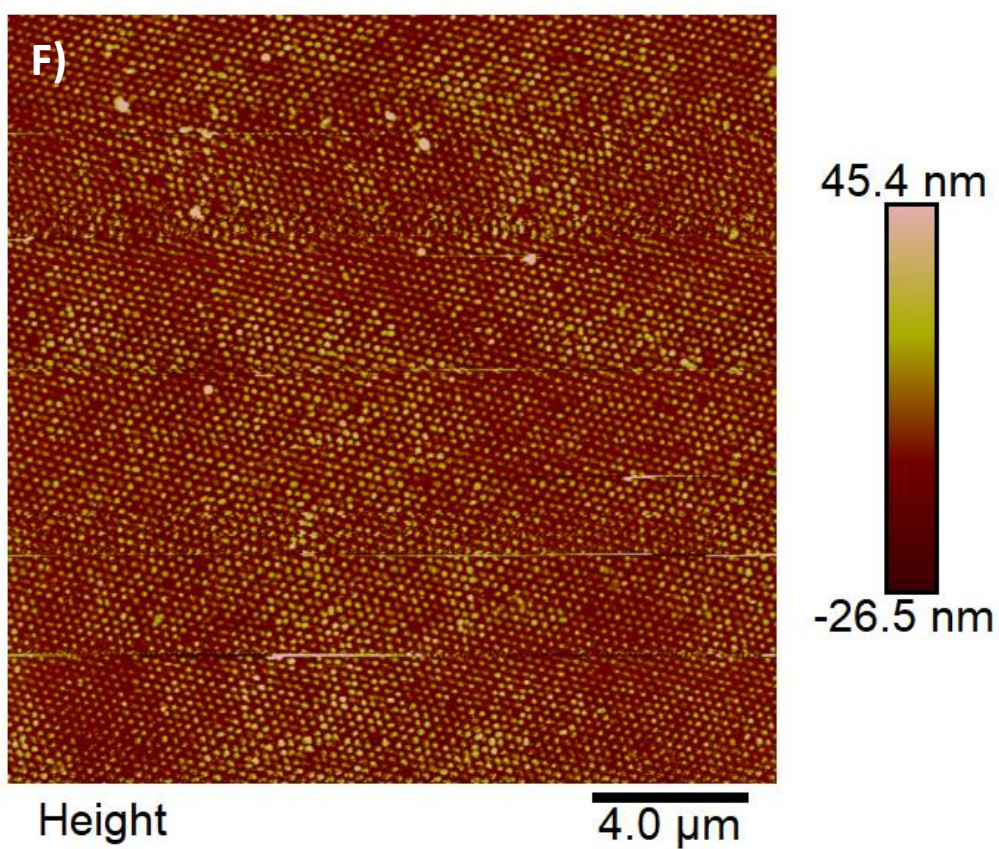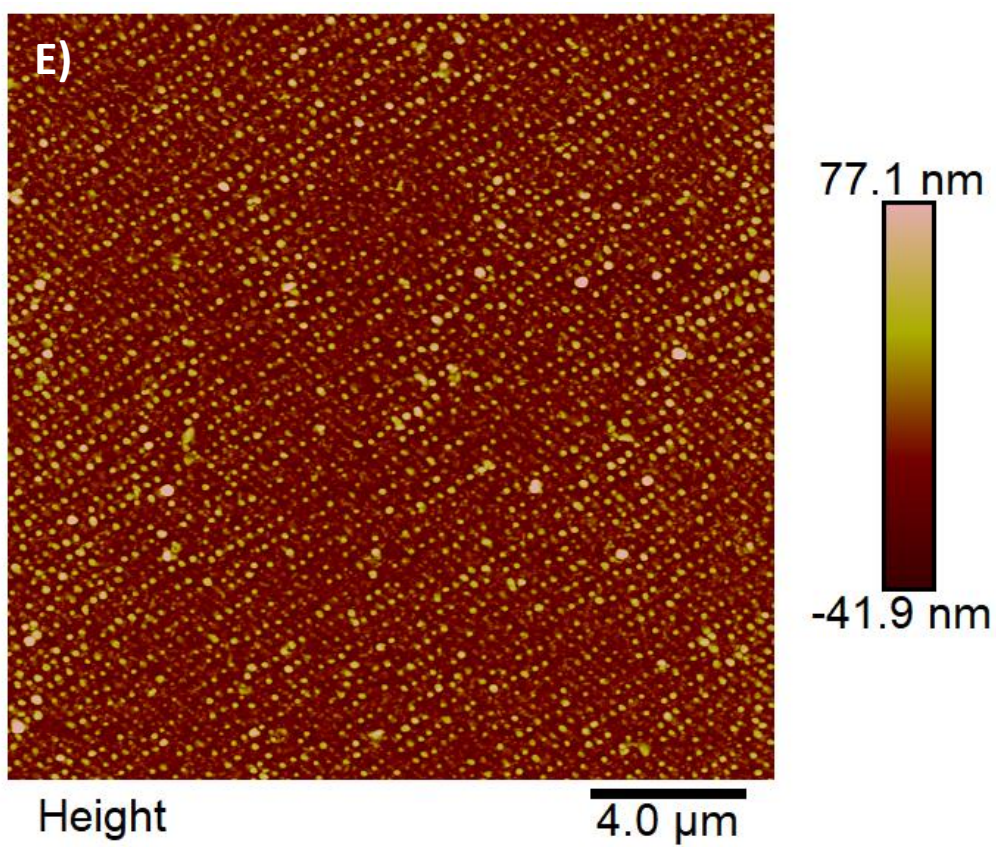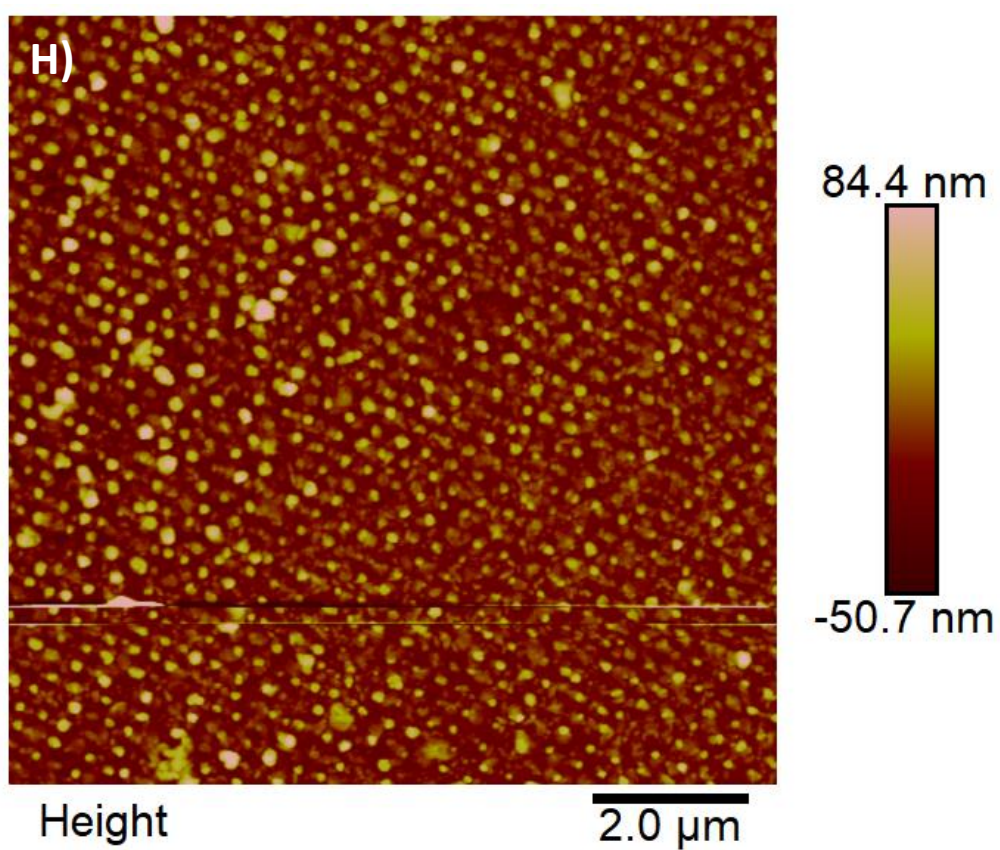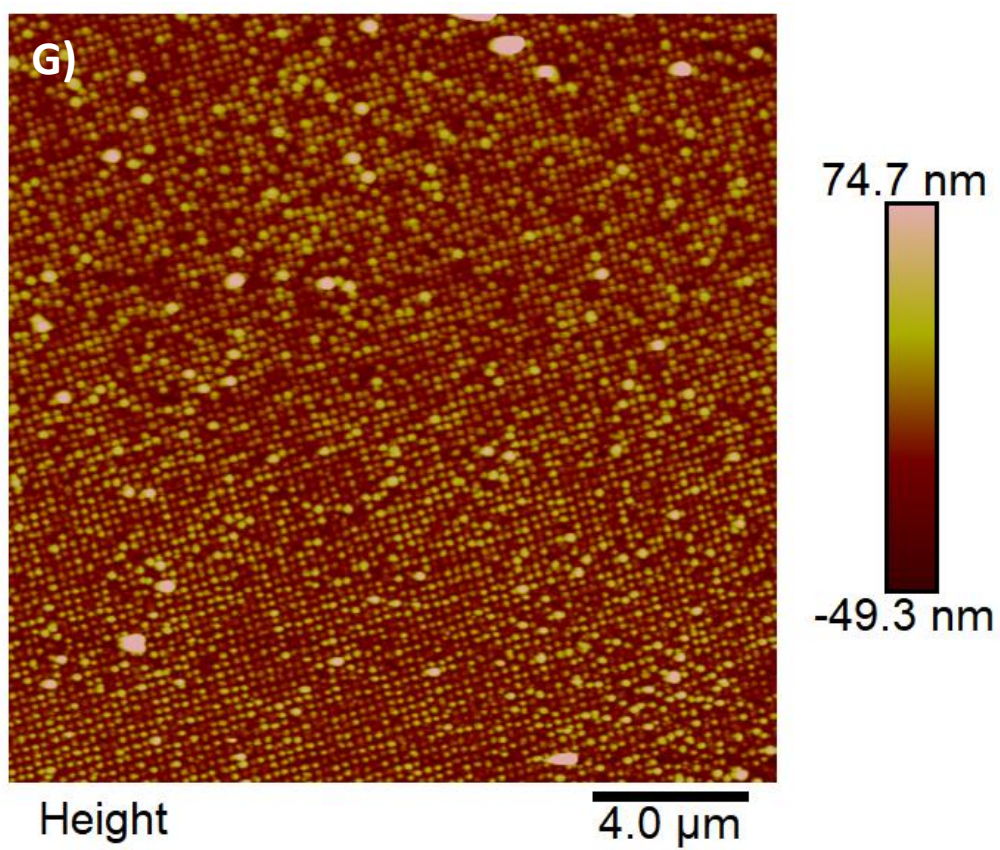
ii. *Calculated energies for AcS-12C-BC monolayers coupled to gold plasmonic nanostructures*

Sample Identifier	E_{LSPR} (eV)	E_{mol} (eV)	E_c (eV)
NJ51	2.168	1.996	0.107
A30	2.109	1.969	0.110
NL18	1.928	1.771	0.176
NL51	1.8871	1.981	0.091

iii. *Calculated energies and polymer brush thicknesses for full density poly(CysMA) + Zn-pyChl **a** layers coupled to gold plasmonic nanostructures*

Sample code	E_{LSPR} (eV)	Polym. Time (min)	Thickness (nm)	Thickness after Zn-pyChl a (nm)	E_{mol} (eV)	E_c (eV)
17_O	2.138	0.5	1.92	1.83	2.013 ± 0.002	0.053 ± 0.003
A30	2.098	1	5.25	2.69	2.015 ± 0.0003	0.190 ± 0.0004
A33	2.067	2	3.41	2.57	2.084 ± 0	0.060 ± 0
NL18	1.917	5	4.98	5.49	1.898 ± 0	0.254 ± 0
NL51	1.931	15	8.04	7.38	1.927 ± 0.0002	0.173 ± 0
NJ51	2.138	30	9.99	9.44	1.897 ± 0.002	0.172 ± 0.048
RK5	2.095	60	10.44	11.07	2.093 ± 0.016	0.142 ± 0
19_O	2.149	120	11.84	12.13	1.803 ± 0.048	0.0747 ± 0.024

(PCysMA+Chl) on nanoarrays
scaled coupling energy vs polymerization time
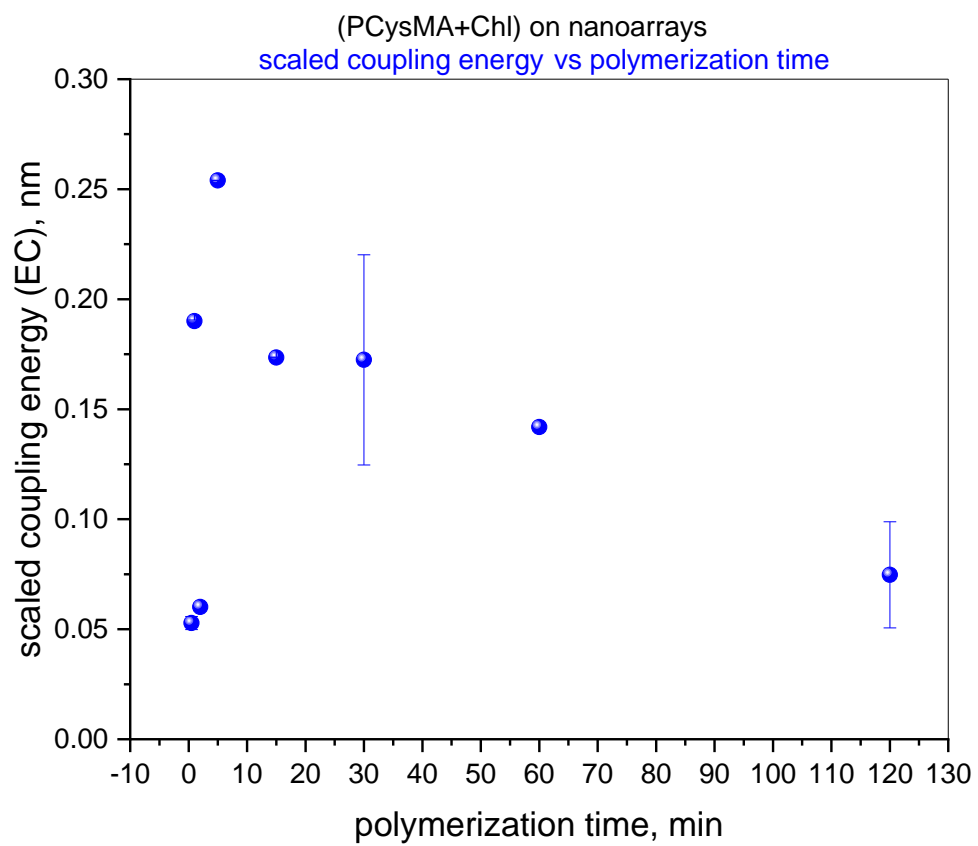
iv.   *Calculated E_{mol} and E_C for plasmonic nanostructures coupled to reduced-density poly(CysMA) + Zn-pyChl **a** brushes****

Sample	DTBU:UDT Monolayer ratio	Polymerisation time (min)	E_{mol} (eV)	E_c (eV)
1	1:0	10	2.084 ± 0	0.159 ± 0
2	1:0	10	2.014 ± 0.0003	0.088 ± 0.0001
3	1:0	10	1.981 ± 0.010	0.063 ± 0.004
4	1:0	30	2.004 ± 0	0.075 ± 0
5	1:0	30	2.022 ± 0.004	0.103 ± 0.017
6	1:0	30	2.098 ± 0.026	0.124 ± 0.014
7	1:1	10	1.959 ± 0.030	0.122 ± 0.017
8	1:1	10	2.016 ± 0.006	0.073 ± 0.024
9	1:1	30	1.996 ± 0.0002	0.114 ± 0.002
10	1:1	30	2.090 ± 0	0.133 ± 0
11	1:1	30	2.013 ± 0.0002	0.053 ± 0.014
12	1:5	10	2.078 ± 0	0.260 ± 0
13	1:5	30	2.087 ± 0	0.166 ± 0
14	1:5	30	2.182 ± 0	0.511 ± 0
15	1:5	30	2.032 ± 0.022	0.468 ± 0.044
16	1:5	30	2.045 ± 0.004	0.439 ± 0.004
17	1:5	30	1.924 ± 0.001	0.440 ± 0.008
18	1:5	30	1.995 ± 0.0002	0.489 ± 0.0002
19	1:5	30	2.052 ± 0.0001	0.064 ± 0.0001

20	1:5	30	2.074 ± 0	0.179 ± 0
21	1:5	30	2.092 ± 0.003	0.122 ± 0
22	1:5	30	2.108 ± 0.003	0.154 ± 0.0009

* The full number of samples studied could not be completely catalogued for their physical properties before submission of this thesis – full documentation will be included upon publication of this work.

References

1. Blankenship R. E., *Molecular Mechanisms of Photosynthesis.* 1ˢᵗ ed. Oxford, Blackwell Science Ltd, 2002.

2. A) Senen, M. K., Olsen, J. D., Hunter, C. N., Schulten K. Atomic-level structural and functional model of a bacterial photosynthetic membrane vesicle. *Proc. Natl. Acad. Sci. U. S. A.*, 2007, **104** (40), 15723 – 8; B) Cartron, M. L., Olsen, J. D., Sener, M., Jackson, P. J., Brindley, A. A., Qian, P., Dickman, M. J., Leggett, G. J., Schulten, K., Hunter, C. N., Integration of energy and electron transfer processes in the photosynthetic membrane of *Rhodobacter Sphaeroides*. *Biochim. Biophys. Acta*, 2014, **10**, 1769 – 1780.

3. Horton, R. H., Moran, L. A., Scringeour, K. G., Perry, M. D., Rawn, J. D. Chapter 15: Photosynthesis. *Principles of Biochemistry.* 4ᵗʰ ed. New Jersey, Pearson Prentice Hall, 1993, 449 – 452.F

4. Gouterman, M. Spectra of porphyrins. *J. Molec. Spectroscopy,* 1961, **6**, 138-163.

5. Houssier, C., Sauer, K. Circular dichromism and magnetic circular dichromism of the chlorophyll and protochlorophyll pigments. *J. Am. Chem. Soc.*, 1970, **92** (4), 779 – 791.

6. Reimers, J. R., Cai, Z. –L., Kobayashi, R., Rätsep, M., Freiburg, A., Krausz, E. Assignment of the Q-bands of the chlorophylls: coherence loss via $Q_x – Q_y$ mixing. *Sci. Rep-UK.,* 2013, **3**, article 2761.

7. A) Cogdell, R. J., Isaacs, N. W., Howard, T. D., McLuskey, K., Fraser, N. J., Prince, S. M. How photosynthetic bacteria harvest solar energy. *J. Bacteriol.,* 1999, **181** (13), 3869 – 3879; B) Cogdell, R. J., Southall, J., Gardiner, A. T., Law, C. J., Gall, A., Roszak, A. W., Isaacs, N. W. How purple photosynthetic bacteria harvest solar energy. *C. R. Chimie*, 2006, **9**, 201 – 206.

8. Sundstro, V., Grondelle, R. V. Photosynthetic light-harvesting: reconciling dynamics and structure of purple bacterial LH2 reveals function of photosynthetic unit. *J. Phys. Chem. B.,* 1999, **103**, 2327 – 2346.

9. Fleming G. R., Grondelle, R. V. Femtosecond spectroscopy of photosynthetic light-harvesting systems. *Curr. Opin. Struc. Biol.*, 1997, **7**, 738 – 748.

10. Grondelle, R. V., Dekker, J. P., Gillbro, T., Sundstrom, V. Energy transfer and trapping in photosynthesis. *Biochim. Biophys. Acta,* 1994, **1187**, 1 – 65.

11. Davydov, A. S. The theory of molecular excitons. *Sov. Phys. Usp.*, 1964, **7**, 145 – 178.

12. Liang, W. Y., Excitons. *Phys. Educ.,* 1970, **5**, 226 - 228.

13. Pishchalnikov, R. Y., Razjivin, A. P., From localized excited states to excitons: changing of conceptions of primary photosynthetic processes in the twentieth century. *Biochemistry (Moscow),* 2014, **79** (3), 242 – 250.

14. Van Grondelle, R., Excitation energy transfer, trapping and annihilation in photosynthetic systems. *Biochim. Biophys. Acta,* 1985, **811**, 147 – 195.

15. Chachisvilis, M., Pullerits, T., Jones, M. R., Hunter, C. N., Sundström, V., Vibrational dynamics in the light-harvesting complexes of the photosynthetic bacterium *Rhodobacter sphaeroides. Chem. Phys. Lett.*, 1994, **224**, 345 – 354.

16. Nagarajan, V., Alden, R. G., Williams, J. C., Parson, W. W., Ultrafast exciton relaxation in the B850 antenna complex of *Rhodobacter sphaeroides. Proc. Natl. Acad. Sci. USA*, 1996, **93**, 13774 – 13779.

17. Monshouwer, R., Baltuška, A., van Mourik, F., van Grondelle, R., Time-resolved absorption difference spectroscopy of the LH-1 antenna of *Rhodopseudomonas viridis*. *J. Phys. Chem. A*, 1998, **102**, 4360 – 4371.

18. Scholes, G. D., Rumbles, G., Excitons in nanoscale systems. *Nat. Mater.*, 2006, **5**, 683 – 696.

19. Clarke, T. M., Durrant, J. R. Charge photogeneration in organic solar cells. *Chem. Rev.*, 2010, **110**, 6736 – 6767.

20. Thompson, B. C., Fréchet, J. M. J., Polymer – fullerene composite solar cells. *Angew. Chem. Int. Ed.*, 2008, **47**, 58 – 77.

21. Brebels, J., Manca, J. V., Lutsen, L., Vanderzande, D., Maes, W., High dielectric constant materials for organic photovoltaics. *J. Mater. Chem. A*, 2017, **5**, 24037 – 24050.

22. Goodwin, H., Jellicoe, T. C., Davis, N. J. L. K., Böhm, M. L., Multiple exciton generation in quantum dot-based solar cells. *Nanophotonics – Berlin*, 2018, **7** (1), 111 – 126.

23. Zang, L., Che, Y., Moore, J. S., One-dimensional self-assembly of planar π-conjugated molecules: adaptable building blocks for organic nanodevices. *Accounts. Chem. Res.*, 2008, **41** (12), 1596 – 1608.

24. Fassioli, F., Dinshaw, R., Arpin, P. C., Scholes, G. D. Photosynthetic light-harvesting: excitons and coherence. *J. R. Soc. Interface,* 2014, **11**, 20130901.

25. Scholes, G. D., Ghiggino, K. P., Oliver, A. M., Padden-Row, M. N. Through-space and through-bond effects on exciton interactions in rigidly linked dinaphthyl molecules. *J. Am. Chem. Soc.,* 1993, **115**, 4345 – 4349.

26. Tamiaki, H., Miyatake, T., Tanikaga, R., Holzwarth, A. R., Schaffner, K., Self-assembly of an artificial light-harvesting antenna: energy transfer from a zinc chlorin to a bacteriochlorin in a supramolecular aggregate. *Angew. Chem. Int. Ed. Engl.*, 1996, **35** (7), 772 – 774.

27. Tamiaki, H., Amakawa, M., Shimono, Y., Tanikaga, R., Holzwarth, A. R., Schaffner, K., Synthetic zinc and magnesium chlorin aggregates as models for supramolecular antenna complexes in chlorosomes of green photosynthetic bacteria. *Photochem. Photobiol.*, 1995, **63** (1), 92 – 99.

28. Tamiaki, H., Takeuchi, S., Tsudzuki, S., Miyatake, T., Tanikaga, R., Self-aggregation of synthetic zinc chlorins with a chiral 1-hydroxyethyl group as a model for in vivo epimeric bacteriochlorophyll-*c* and *d* aggregates. *Tetrahedron*, 1998, **54**, 6699 – 6718.

29. Kunieda, M., Tamiaki, H., Self-aggregation of synthetic zinc oxo-bacteriochlorins bearing substituents characteristic of chlorosomal chlorophylls. *J. Org. Chem.*, 2005, **70**, 820 – 828.

30. Kelley, R. F., Goldsmith, R. H., Wasielewski, M. R., Ultrafast energy transfer within cyclic self-assembled chlorophyll tetramers. *J. Am. Chem. Soc.*, 2007, **129**, 6384 – 6385.

31. Huber, V., Sengupta, S., Würthner, F., Structure-property relationships for self-assembled zinc chlorin light-harvesting dye aggregates. *Chem. Eur. J.*, 2008, **14**, 7791 – 7807.

32. Kunieda, M., Tamiaki, H., Self-aggregation of synthetic bacteriochlorophyll-*d* analogues possessing a B-ring reduced chlorin π-system. *J. Org. Chem.*, 2009, **74**, 8437 – 8440.

33. Li, Y., Sasaki, S. –I., Tamiaki, H., Liu, C. –L., Song, J., Tian, W., Zheng, E., Wei, Y., Chen, G., Fu, X., Wang, X. –F., Zinc chlorophyll aggregates as hole transporters for biocompatible, natural-photosynthesis-inspired solar cells. *J. Power Sources*, 2015, **297**, 519 – 524.

34. Muthiah, C., Kee, H. L., Diers, J. R., Fan, D., Ptaszek, M., Bocian, D. F., Holten, D., Lindsey, J. S., Synthesis and excited-state photodynamics of a chlorin-bacteriochlorin dyad – through-space versus through-bond energy transfer in tetrapyrrole arrays. *Photochem. Photobiol.*, 2008, **84**, 786 – 801.

35. Kim, Y., Shin, S. A., Lee, J., Yang, K. D., Nam, K. T., Hybrid system of semiconductor and photosynthetic protein. *Nanotechnology*, 2014, **25**, 342001.

36. Saboe, P. O., Lubner, C. E., McCool, N. S., Vargas-Barbosa, N. M., Yan, H., Chan, S., Ferlez, B., Bazan, G. C., Golbeck, J. H., Kumar, M., Two-dimensional protein crystals for solar energy conversion. *Adv. Mater.*, 2012, **26**, 7064 – 7069.

37. Yao, K., Liu, C., Chen, Y., Chen, L., Li, F., Liu, K., Sun, R., Wang, P., Yang, C., Integration of light-harvesting complexes into the polymer bulk heterojunction P3HT/PCBM device for efficient photovoltaic cells. *J. Mater. Chem.*, 2012, **22**, 7342 – 49.

38. Amao, Y., Kato, K., Chlorophyll assembled electrode for photovoltaic conversion device. *Electrochim. Acta.*, 2007, **53** (1), 42 – 45.

39. Hassan, H. C., Abidin, H. Z., Chowdhury, F. I., Arof, A. K., A high efficiency chlorophyll sensitized solar cell with quasi solid PVA based electrolyte. *Int. J. Photoenergy*, 2016, 3685210.

40. Li, Y., Zhao, W., Li, M., Chen, G., Wang, X. -F., Fu, X., Kitao, O., Tamiaki, H., Sakai, K., Ikeuchi, T., Sasaki, S. -i., Chlorophyll-based organic-inorganic heterojunction solar cells. *Chem. Eur. J.,* 2017, **23**, 10886 – 10892.

41. Ulma, A., Formation and structure of self-assembled monolayers. *Chem. Rev.*, 1996, **96**, 1533 – 1554.

42. Love, J. C., Estroff, L. A., Kriebel, J. K., Nuzzo, R. G., Whitesides, G. M., Self-assembled monolayers of thiolates on metals as a form of nanotechnology. *Chem. Rev.*, 2005, **105**, 1103 – 1169.

43. Wasserman, S. R., Tao, Y. –T., Whitesides, G. M., Structure and reactivity of alkylsiloxane monolayers formed by reaction of alkyltrichlorosilanes on silicon substrates. *Langmiur*, 1989, **5**, 1074 – 1087.

44. Aswal, D. K., Lenfant, S., Guerin, D., Yakhami, J. V., Vuillaume, D., Self assembled monolayers on silicon for molecular electronics. *Anal. Chim. Acta.*, 2006, **568**, 84 – 108.

45. Yee, C., Kataby, G., Ulman, A., Prozorov, T., White, H., King, A., Rafailovich, M., Sokolov, J., Gedanken, A., Self-assembled monolayers of alkanesulfonic and – phosphonic acids on amorphous iron oxide nanoparticles. *Langmuir*, 1999, **15**, 7111-7115.

46. Queffélec, C., Petit, M., Janvier, P., Kight, D. A. Bujoli, B., Surface modification using phosphonic acids and esters. *Chem. Rev.*, 2012, **112**, 3777 – 3807.

47. Drain, C. M., Varotto, A., Radivojevic, I., Self-organized porphyrinic materials. *Chem. Rev.* 2009, **109**, 1630 – 1658.

48. Haensch, C., Hoeppener, S., Schubert, U. S., Chemical modification of self-assembled silane-based monolayers by surface reactions. *Chem. Soc. Rev.*, 2010, **39**, 2323 – 2334.

49. Smith, R. K., Lewis, P. A., Weiss, P., Patterning self-assembled monolayers. *Prog. Surf. Sci.*, 2004, **75**, 1 – 68.

50. Leggett, G. J., Light-directed nanosynthesis: near-field optical approaches to integration of the top-down and bottom-up fabrication paradigms. *Nanoscale*, 2012, **4**, 1840 – 1855.

51. Springer, J. W., Parkes-Loach, P. S., Reddy, K. R., Krayer, M., Jiao, J., Lee, G. M., Niedziedzki, D. M., Harris, M. A., Kirmaier, C., Bocian, D. F., Lindsey, J. S., Holten, D., Loach, P. A., Biohybrid photosynthetic antenna complexes for enhanced light-harvesting. *J. Am. Chem. Soc.*, 2012, **134**, 4589 – 4599.

52. Reddy, K. R., Jiang, J., Krayer, M., Harris, M. A., Springer, J. W., Yang, E., Jiao, J., Niedziedzki, D. M., Pandithavidana, D., Parkes-Loach, P. S., Kirmaier, C., Loach, P. A., Bocian, D. F., Holten, D., Lindsey, J. S., Palette of lipophilic bioconjugatable bacteriochlorins for construction of biohybrid light-harvesting architectures. *Chem Sci.*, 2013, **4**, 2036 – 2053.

53. Sakai, S., Noji, T., Kondo, M., Mizuno, T., Dewa, T., Ochiai, T., Yamakawa, H., Itoh, S., Hashimoto, H., Nango, M., Molecular assembly of zinc chlorophyll derivatives by using recombinant light-harvesting polypeptides with His-tag and immobilization on a gold electrode.

54. Mancini, J. A., Kodali, G., Jiang, J., Reddy, K. R., Lindsey, J. S., Bryant, D. A., Dutton, P. L., Moser, C. C., Multi-step excitation energy transfer engineered in genetic fusions of natural and synthetic light-harvesting proteins. *J. R. Soc. Interface,* 2017, **14**, 20160896.

55. Sahin, T., Harris, M. A., Vairaprakash, P., Niedzwiedzki, D. M., Subramanian, V., Shreve, A. P., Bocian, D. F., Holten, D., Lindsey, J. S., Self-assembled light-harvesting system from chromophores in lipid vesicles. *J. Phys. Chem. B*, 2015, **119**, 10231 – 10243.

56. Barbey, R., Lavanant, L., Paripovic, D., Schüwer, N., Sugnaux, C., Tugulu, S., Klok, H. – A., Polymer brushes via surface-initiated controlled radical polymerization: synthesis, characterization, properties, and applications. *Chem. Rev.*, 2009, **109,** 5437 – 5527.

57. Patel, N., Davies, M. C., Hartshorne, M., Heaton, R. J., Roberts, C. J., Tendler, S. J. B., Williams, P. M., Immobilization of protein molecules onto homogenous and mixed carboxylate-terminated self-assembled monolayers. *Langmuir*, 1997, **13**, 6485 – 6490.

58. Christau, S., Möller, T., Yenice, Z., Genzer, J., von Klitzing, R., Brush/gold nanoparticle hybrids: effect of grafting density on the particle uptake and distribution within weak polyelectrolyte brushes. *Langmuir*, 2014, **30**, 13033 – 13041.

59. Jonas, D. M. Two-dimensional femtosecond spectroscopy. *Annu. Rev. Phys. Chem.* 2003, **54**, 425 – 463.

60. Brixner, T., Mančal, T., Stiopkin, I. V., Fleming, G. R. Phase-stabilized two-dimensional electronic spectroscopy. *J. Chem. Phys.* 2004, **121**, 4221 – 4236.

61. Cho, M., Vaswani, H. M., Brixner, T., Stenger, J., Fleming, G. R. Exciton analysis in 2D electronic spectroscopy. *J. Phys. Chem. B*, 2005, **109**, 10542 – 10556.

62. Brixner, T., Stenger, J., Vaswani, H. M., Cho, M., Blankenship, R. E., Fleming, G. R. Two-dimensional spectroscopy of electronic couplings in photosynthesis. *Nature*, 2005, **434**, 625 – 628.

63. Engel, G. S., Calhoun, T. R., Read, E. L., Ahn, T. –K., Mančal, T., Cheng, Y. –C., Blankenship, R. E., Fleming, G. R. Evidence for wavelike energy transfer through quantum coherence in photosynthetic systems. *Nature*, 2007, **446**, 782 – 786.

64. Zigmantas, D., Read, E. L., Mančal, T., Brixner, T., Gardiner, A. T., Cogdell, R. J., Fleming, G. R. Two-dimensional electronic spectroscopy of the B800-B820 light-harvesting complex. *P. Natl. Acad. Sci. USA,* 2006, **103** (34), 12672 – 12677.

65. Collini, E., Wong, C. Y., Wilk, K. E, Curmi, P. M. G., Brumer, P., Scholes, G. D. Coherently wired light-harvesting in photosynthetic marine algae at ambient temperature. *Nature*, 2010, **463**, 644 – 647.

66. Wong, C. Y., Alvey, R. M., Turner, D. B., Wilk, K. E., Bryant, D. A., Curmi, P. M. G., Silbey, R. J., Scholes, G. D. Electronic coherence lineshapes reveal hidden excitonic correlations in photosynthetic light harvesting. *Nat. Chem.,* 2012, **4**, 396 – 404.

67. Richards, G. H., Wilk, K. E., Curmi, P. M. G., Davis, J. A., Disentangling electronic and vibrational coherence in Phycocyanin-645 light-harvesting complex. *J. Phys. Chem. Lett.,* 2014, **5**, 43 – 49.

68. Panitchayangkoon, G., Hayes, D., Fransted, K. A., Caram, J. R., Harel, E., Wen, J., Blankenship, R. E., Engel, G. S., Long-lived quantum coherence in photosynthetic complexes at physiological temperature. *Proc. Natl. Acad. Sci. USA,* 2010, **107** (29), 12766 – 12770.

69. Pullerits, T., Chachisvilis, M., Sundström, V., Exciton delocalization length in the B850 antenna of *Rhodobacter sphaeroides*. *J. Phys. Chem.*, 1996, **100**, 10787 – 10792.

70. Christensson, N., Milota, F., Hauer, J., Sperling, J., Bixner, O., Nemeth, A., Kauffmann, H. F., High frequency vibrational modulations in two-dimensional electronic spectra and their resemblance to electronic coherence signatures. *J. Phys. Chem. B.*, 2011, **115**, 5383 – 5391.

71. Turner, D. B., Wilk, K. E., Curmi, P. M. G., Scholes, G. D., Comparison of electronic and vibrational coherence measured by two-dimensional electronic spectroscopy. *J. Phys. Chem. Lett.,* 2011, **2**, 1904 – 1911.

72. Butkus, V., Zigmantas, D., Valkunas, L., Abramavicius, D., Vibrational vs. electronic coherences in 2D spectrum of molecular systems. *Chem. Phys. Lett.,* 2012, **545**, 40 – 43.

73. Brumer, P., Shapiro, M., Molecular response in one-photon absorption via natural thermal light vs. pulsed laser excitation. *Proc. Natl. Acad. Sci. USA,* 2012, **109** (48), 19575 – 19578.

74. Kassal, I., Joel, Yuen-Zhou, J., Rahimi-Keshari, S., Does coherence enhance transport in photosynthesis? *J. Phys. Chem. Lett.,* 2013, **4**, 362 – 367.

75. Han, A. C., Shapiro, M., Brumer, P., Nature of quantum states created by one photon absorption: pulsed coherent vs pulsed incoherent light. *J. Phys. Chem. A,* 2013, **117**, 8199 – 8204.

76. Fassioli, F., Olaya-Castro, A., Scholes, G. D., Coherent energy transfer under incoherent light conditions. *J. Phys. Chem. Lett.* 2012, **3**, 3136 – 3142.

77. Pelzer, K. M., Can, T., Gray, S. K., Morr, D. K., Engel, G. S., Coherent transport and energy flow patterns in photosynthesis under incoherent excitation. *J. Phys. Chem. B*, 2014, **118**, 2693 – 2702.

78. León-Montiel, R. de J., Kassal, I., Torres, J. P., Importance of excitation and trapping conditions in photosynthetic environment-assisted energy transport. *J. Phys. Chem. B*, 2014, **118**, 10588 – 10594.

79. Baghbanzadeh, S., Kassal, I., Distinguishing the roles of energy funnelling and delocalization in photosynthetic light-harvesting. *Phys. Chem. Chem. Phys.,* 2016, **18**, 7459 – 7467.

80. Baghbanzadeh, S., Kassal, I., Geometry, supertransfer, and optimality in the light-harvesting of purple bacteria. *J. Phys. Chem. Lett.*, 2016, **7,** 3804 – 3811.

81. Chenu, A., Brańczyk, A. M., Scholes, G. D., Sipe, J. E., Thermal light cannot be represented as a statistical mixture of single pulses. *Phys. Rev. Lett.,* 2015, **114** (21), 213601.

82. Grinev, T., Brumer, P., Realistic vs sudden turn-on of natural incoherent light: coherences and dynamics in molecular excitation and internal conversion. *J. Chem. Phys.,* 2015, **143** (24), 244313.

83. Pachón, L. A., Botero, J. D., Brumer, P., Open system perspective on incoherent excitation of light-harvesting systems. *J. Phys. B: At. Mol. Opt. Phys.*, 2017, **50**, 184003.

84. Duan, H. -G., Prokhorenko, V. I., Cogdell, R. J., Ashraf, K., Stevens, A. L., Thorwart, M., Miller, R. J. D., Nature does not rely on long-lived electronic quantum coherence for photosynthetic energy transfer. *Proc. Natl. Acad. Sci. USA*, 2017, **114** (32), 8493 – 8498.

85. Thyrhaug, E., Tempelaar, R., Alcocer, M. J. P., Židek, K., Bína, D., Knoester, J., Jansen, T. L. C., Zigmantas, D., Identification and characterization of diverse coherences in the Fenna-Matthews-Olson complex. *Nat. Chem.*, 2018, **10**, 780 – 786.

86. Ball, P., The dawn of quantum biology. *Nature*, 2011, **474**, 272 – 274.

87. Willets, K. A, Van Duyne, R. P., Localized surface plasmon resonance spectroscopy and sensing. *Annu. Rev. Phys. Chem.*, 2007, **58,** 267 – 297.

88. Maier, S., Brongersma, M. L., Kik, P. G., Meltzer, S., Requicha, A. A. G., Atwater, H. A., Plasmonics – a route to nanoscale optical devices. *Adv. Mater.*, 2001, **13** (19), 1501 – 1505.

89. Barnes, W. L., Dereux, A., Ebbesen, T. W., Surface plasmon subwavelength optics. *Nature*, 2003, **424**, 824 – 840.

90. Nagao, T., Han, G., Hoang, C., Wi, J. –S., Pucci, A., Weber, D., Neubrech, F., Silkin, V. M., Enders, D., Saito, O., Rana, M., Plasmons in nanoscale and atomic-scale systems. *Sci. Technol. Adv. Mater.*, 2010, **11**, 054506.

91. Miller, M. M., Lazarides, A. A., Sensitivity of metal nanoparticle surface plasmon resonance to the dielectric environment. *J. Phys. Chem. B*, 2005, **109**, 21556 – 21565.

92. Kelly, K. L., Coronado, E., Zhao, L. L., Schatz, G. C., The optical properties of metal nanoparticles: the influence of size, shape, and dielectric environment. *J. Phys. Chem. B*, 2003, **107**, 668 – 677.

93. Haes, A. J., Haynes, C. L., McFarland, A. D., Schatz, G. C., Van Duyne, R. P., Zou, S., Plasmonic materials for surface enhanced sensing and spectroscopy. *MRS Bull.*, 2005, **30**, 368 – 375.

94. Jensen, T. R., Malinsky, M. D., Haynes, C. L., Van Duyne, R. P., Nanosphere lithography: tuneable localized surface plasmon resonance spectra of silver nanoparticles. *J. Phys. Chem. B*, 2000, **104**, 10549 – 10556.

95. Nie, S., Emory, S., Probing single molecules and single nanoparticles by surface-enhanced Raman scattering. *Science*, 1997, **275**, 1102 – 1106.

96. Otto, A., Mrozek, I., Grabhorn, H., Akemann, W., Surface-enhance Raman scattering. *J. Phys.: Condens. Matter*, 1992, **4**, 1143 – 1212.

97. Kukushkin, V. I., Van'kov, A. B., Kukushkin, I. V., Long-range manifestation of surface-enhance Raman scattering. *JETP Lett+.*, 2013, **98** (2), 64 – 69.

98. McFarland, A. D., Van Duyne, R. P. Single silver nanoparticles as real-time optical sensors with zeptomole sensitivity. *Nano Lett.*, 2003, **3** (8), 1057 – 1062.

99. Malinsky, M. D., Kelly, K. L., Schatz, G. C., Van Duyne, R. P., Chain length dependence and sensing capabilities of the localized surface plasmon resonance of silver nanoparticles chemically modified with alkanethiol self-assembled monolayers. *J. Am. Chem. Soc.*, 2001, **123**, 1471 – 1482.

100. Anker, J. N., Hall, W. P., Lyandres, O., Shah, N. C., Zhao, J., Van Duyne, R. P., Biosensing with plasmonic nanosensors. *Nat. Mater.,* 2008, **7**, 442 – 453.

101. Haes, A. J., Van Duyne, R. P., A nanoscale optical biosensor: sensitivity and selectivity of an approach based on the localized surface plasmon resonance spectroscopy of triangular silver nanoparticles. *J. Am. Chem. Soc.*, 2002, **124**, 10596 – 10604.

102. Riboh, J. C., Haes, A. J., McFarland, A. D., Yonzon, C. R., Van Duyne, R. P., A nanoscale optical biosensor: real-time immunoassay in physiological buffer enabled by improved nanoparticle adhesion. *J. Phys. Chem. B*, 2003, **107**, 1772 – 1780.

103. Haes, A. J., Zou, S., Zhao, J., Schatz, G. C., Van Duyne, R. P., Localized surface plasmon resonance spectroscopy near molecular resonances. *J. Am. Chem. Soc.*, 2006, **128**, 10905 – 10914.

104. Zhao, J., Das, A., Zhang, X., Schatz, G. C., Sligar, S. G., Van Duyne, R. P., Resonance surface plasmon spectroscopy: low molecular weight substrate binding to cytochrome P450. *J. Am. Chem. Soc.,* 2006, **128**, 11004 – 11005.

105. Fort, E., Grésillon, S., Surface enhanced fluorescence. *J. Phys. D: Appl. Phys.*, 2008, **41**, 013001.

106. Anger, P., Bharadwaj, Novotny, L., Enhancement and quenching of single-molecule fluorescence. *Phys. Rev. Lett.*, 2006, **96**, 113002.

107. Czechowski, B. N., Piatkowski, D., Litvin, R., Mackowski, S., Brotosudarmo, T. H. P., Cogdell, R. J., Pichler, S., Heiss W., Fluorescence enhancement of light-harvesting complex 2 from purple bacteria coupled to spherical gold nanoparticles. *Appl. Phys. Lett.*, 2011, **99**, 173701.

108. Ulma, A., Formation and structure of self-assembled monolayers. *Chem. Rev.*, 1996, **96**, 1533 – 1554.

109. Love, J. C., Estroff, L. A., Kriebel, J. K., Nuzzo, R. G., Whitesides, G. M., Self-assembled monolayers of thiolates on metals as a form of nanotechnology. *Chem. Rev.*, 2005, **105**, 1103 – 1169.

110. Li, L., Chen, S., Zheng, J., Ratner, B. D., Jiang, S., Protein adsorption on oligo(ethylene glycol)-terminated alkanethiolate self-assembled monolayers: the molecular basis for nonfouling behaviour. *J. Phys. Chem. B*., 2005, **109**, 2934 – 2941.

111. Reynolds, N. P., Janusz, S., Escalante-Marun, M., Timney, J., Ducker, R. E., Olsen, J. D., Otto, C., Subramaniam, V., Legget, G. J., Hunter, C. N., Directed formation of micro- and nanoscale patterns of functional light-harvesting LH2 complexes. *J. Am. Chem. Soc.*, 2007, **129**, 14625 – 14631.

112. Leggett, G. J., Light-directed nanosynthesis: near-field optical approaches to integration of the top-down and bottom-up fabrication paradigms. *Nanoscale*, 2012, **4**, 1840 – 1855.

113. Brewer, N. J., Janusz, S., Critchley, K., Evans, S. D., Leggett, G. J., Photooxidation of self-assembled monolayers by exposure to light of wavelength 254 nm: a static SIMS study. *J. Phys. Chem. B*, **2005**, 109, 11247 – 11256.

114. Kondo, M., Nakamura, Y., Fuji, K., Nagata, M., Suemori, Y., Dewa, T., Iida, K., Gardiner, A. T., Cogdell, R. J., Nango, M., Self-assembled monolayer of light-harvesting core complexes from photosynthetic bacteria on a gold electrode modified with alkanethiols.

115. Liu, J., Lauterbach, R., Paulsen, H., Knoll, W., Immobilization of light-harvesting chlorophyll *a/b* complex (LHCIIb) studied by surface plasmon field-enhanced fluorescence spectroscopy. *Langmuir*, 2008, **24**, 9661 – 9667.

116. Tsargorodska, A., Cartron, M. L., Vasilev, C., Kodali, G., Mass, O. A., Baumberg, J. J., Dutton, P. L., Hunter, C. N., Törmä, P., Leggett, G. J., Strong coupling of localised surface plasmons to excitons in light-harvesting complexes. *Nano Lett.*, 2016, **16**, 6850 – 6856.

117. Tsargorodska, A., Zubir, O. L., Darroch, B., Carton, M. L., Basova, T., Hunter, C. N., Nabok, A. V., Leggett, G. J., Fast, simple, combinatorial routes to the fabrication of reusable, plasmonically active gold nanostructures by interferometric lithography of self-assembled monolayers. *ACS Nano*, 2014, **8** (8), 7858 – 7869.

118. Novotny, L., Strong coupling, energy splitting, and level crossings: a classical perspective. *Am. J. Phys.*, 2010, **78**, (11), 1199 – 1202.

119. Törmä, P., Barnes, W. L., Strong coupling between surface plasmon polaritons and emitters: a review. *Rep. Prog. Phys.*, 2015, **78** (1), 013901.

120. Cao, E., Lin, W., Sun, M., Liang, W., Song, Y., Exciton-plasmon coupling interactions: from principle to applications. *Nanophotonics-Berlin*, 2018, **7** (1), 145 – 167.

121. Joe, Y. S., Satanin, A. M., Kim, C. S., Classical analogy of Fano resonances. *Phys. Scr.*, 2006, **74**, 259 – 266.

122. Gallinet, B., Martin, O. J. F., *Ab initio* theory of Fano resonances in plasmonic nanostructures and metamaterials. *Phys. Rev. B*, 2011, **83**, 235427.

123. Väkeväinen, A. I., Moerland, R. J., Rekola, H. T., Eskelinen, A. –P., Martikainen, J. –P., Kim, D. –H., Törmä, P., Plasmonic surface lattice resonances at the strong coupling regime. *Nano Lett.*, 2014, **14**, 1721 – 1727.

124. Agranovich V. M., Litinskaia, M., Lidzey, D. G., Cavity polaritons in microcavities containing disordered organic semi-conductors. *Phys. Rev. B*, 2003, **67**, 085311.

125. Shi, L., Hakala, T. K., Rekola, H. T., Martikainen, J. –P., Moerland, R. J., Törmä, P., Spatial coherence properties of organic molecules coupled to plasmonic surface lattice resonances in the weak and strong coupling regimes. *Phys. Rev. Lett.*, 2014, **112**, 153002.

126. Damjanović, A., Ritz, T., Schulten, K., Energy transfer between carotenoids and bacteriochlorophylls in light-harvesting complex II of purple bacteria. *Phys. Rev. E*, 1999, **59** (3), 3293 – 3311.

127. Cogdell, R. J., Isaacs, N. W., Freer, A. A., Howard, T. D., Gardiner, A. T., Prince, S. M., Papiz, M. Z., The structural basis of light-harvesting in purple bacteria. *FEBS Lett.*, 2003, **555**, 35 – 39.

128. Olsen, J. D., Tucker, J. D., Timney, J. A., Qlan, P., Vassilev, C., Hunter, C. N., The organization of LH2 complexes in membranes from *rhodobacter sphaeroides*. *J. Biol. Chem.*, 2008, **283** (45), 30772 – 30779.

129. Lishchuk, A., Kodali, G., Mancini, J. A., Broadbent, M., Darroch, B., Mass, O. A., Nabok, A., Dutton, P. L., Hunter, C. N., Törmä, P., Leggett, G. J., A synthetic biological quantum optical system. *Nanoscale*, 2018, **10**, 13064.

130. Xia, Y., Rogers, J. A., Paul, K. E., Whitesides, G. M., Unconventional methods for fabricating and patterning nanostructures. *Chem. Rev.*, 1999, **99**, 1823 – 1848.

131. Leggett, G. J., Scanning near-field lithography – surface photochemistry with nanoscale spatial resolution. *Chem. Soc. Rev.*, 2006, **35**, 1150 – 1161.

132. Gates, B. D., Xu, Q., Stewart, M., Ryan, D., Willson, C. G., Whitesides, G. M., New approaches to nanofabrication: molding, printing, and other techniques. *Chem. Rev.*, 2005, **105**, 1171 – 1196.

133. Leggett, G. J., Light-directed nanosynthesis: near-field optical approaches to integration of the top-down and bottom-up fabrication paradigms. *Nanoscale*, 2012, **4**, 1840 – 1855.

134. Ducker, R. E., Leggett, G. J., A mild etch for the fabrication of three-dimensional nanostructures in gold. *J. Am. Chem. Soc.*, 2006, **128**, 392 – 393.

135. Brueck, S. R. J., Optical and interferometric lithography – nanotechnology enablers. *Proc. IEEE*, 2005, **93**, 1704 – 1721.

136. Lu, C., Lipson, R. H., Interference lithography: a powerful tool for fabrication periodic structures. *Laser Photonics Rev.*, 2010, **4** (4), 568 – 580.

137. Tarlov, M. J., Burgess Jr., D. R. F., Gillen, G., UV photopatterning of alkanethiolate monolayers self-assembled on gold and silver. *J. Am. Chem. Soc.*, 1993, **115**, 5305.

138. Hutt, D. A., Leggett, G. J., Influence of adsorbate ordering on rates of UV photooxidation of self-assembled monolayers. *J. Phys. Chem.*, 1996, **100**, 6657 – 6662.

139. Brewer, N. J., Janusz, S., Critchley, K., Evans, S. D., Leggett, G. J., Photooxidation of self-assembled monolayers by exposure to light of wavelength 254 nm: a static SIMS study. *J. Phys. Chem. B.*, 2005, **109**, 11247 – 11256.

140. Lampman, G. M., Pavia, D. L., Kriz, G. S., Vyvyan, J. R., Spectrocopy – International edition. 4th Ed., Belmont, Brooks/Cole, 2010.

141. Watts, J. F., Wolstenholme, J., An Introduction to Surface Analysis by XPS and AES. 1st ed. Chichester, John Wiley & Sons Ltd, 2003.

142. Vickerman, J. C., Surface Analysis – The Principal Techniques. 1st Ed., Chichester, John Wiley & Sons Ltd, 1997.

143. Pettersson, L. A. A., Optical modelling and characterization of layers and multilayer structures – organic optoelectronic devices and spectroscopic ellipsometry. *Linköping Studies in Science and Technology Dissertations*, No. 600, Linköping, 1999.

144. Carpick, R. W., Salmeron, M., Scratching the surface: fundamental investigations of tribology with atomic force microscopy. *Chem. Rev.*, 1997, **97**, 1163 – 1194

145. Takano, H., Kenseth, J. R., Wong, S. –S., O'Brien, J. C., Porter, M. D., Chemical and biochemical analysis using scanning force microscopy. *Chem. Rev.*, 1999, **99**, 2845 – 2890.

146. Olsen, J. M., Chlorophyll organization and function in green photosynthetic bacteria. *Photochem. Photobiol.*, 1998, **67** (1), 61 – 75.

147. Grimm, B., Porra, R. J., Rüdiger, W., Scheer, H., *Chlorophylls and Bacteriochlorophylls: Biochemistry, Biophysics, Functions and Applications.* 1st Ed., Dordrecht, Springer, 2006, 16 – 19.

148. Blankenship R. E., *Molecular Mechanisms of Photosynthesis.* 1st ed. Oxford, Blackwell Science Ltd, 2002, 55 - 59.

149. Law, C. J., Cagdell, R. J., The effect of chemical oxidation on the fluorescence of the LH1 (B880) complex from the purple bacterium *Rhodobium marinum. FEBS Lett.*, 1998, **432**, 27 – 30.

150. Smith, J. R. L., Calvin, M., Studies on the chemical and photochemical oxidation of bacteriochlorophyll. *J. Am. Chem. Soc.*, 1966, **88** (19), 4500 – 4506.

151. Grimm, B., Porra, R. J., Rüdiger, W., Scheer, H., *Chlorophylls and Bacteriochlorophylls: Biochemistry, Biophysics, Functions and Applications.* 1st Ed., Dordrecht, Springer, 2006, 80 – 85.

152. Dorough, G. D., Miller, J. R., An attempted preparation of a simple tetrahydroporphine. *J. Am. Chem. Soc.*, 1952, **74**, 6106 – 6108.

153. Whitlock, Jr., H. W., Hanauer, R., Oester, M. Y., Bower, B. K., Diimide reduction of porphyrins. *J. Am. Chem. Soc.*, 1969, **91** (26), 7485 – 7489.

154. Kim, H. –J., Lindsey, J. S., De novo synthesis of stable tetrahydroporphyrinic macrocycles: bacteriochlorins and a tetradehydrocorrin. *J. Org. Chem.*, 2005, **70**, 5475 – 5486.

155. Krayer, M., Ptaszek, M., Kim, H. –J., Meneely, K. R., Fan, D., Secor, K., Lindsey, J. S., Expanded scope of synthetic bacteriochlorins via improved acid catalysis conditions and diverse dihydrodipyrrin-acetals. *J. Org. Chem.*, 2010, **75**, 1016 – 1039.

156. Lindsey, J. S., Mass, O., Chen, C. –Y., Tapping the near-infrared spectral region with bacteriochlorin arrays. *New J. Chem.*, 2011, **35**, 511 – 516.

157. Van Leusen, A. M., Siderius, H., Hoogenboom, B. E., van Leusen, D., A new and simple synthesis of the pyrrole ring system from Michael acceptors and tosylmethylisocyanides. *Tetrahedron Lett.*, 1972, **52**, 5337 – 5340.

158. Lindsey, J. S., Schreiman, I. C., Hsu, H. C., Kearney, P. C., Marguerettaz, A. M., Rothemund and Adler-Longo reactions revisited: synthesis of tetraphenylporphyrins under equilibrium conditions. *J. Org. Chem.*, 1987, **52**, 827 – 837.

159. Geier III, G. R., Ciringh, Y., Li, F., Haynes, D. M., Lindsey, J. S., A survey of acid catalysts for use in two-step, one-flask syntheses of meso-substituted porphyrinic macrocycles. *Org. Lett.*, 2000, **2** (12), 1745 – 1748.

160. Sistrom, W. R., The spectrum of bacteriochlorophyll *in vivo*: observations on mutants of *rhodopseudomonas spheroides* unable to grow photosynthetically. *Photochem. Photobiol.*, 1966, **5**, 845 – 856.

161. Stromberg, J. R., Marton, A., Kee, H. L., Kirmaier, C., Diers, J. R., Muthiah, C., Taniguchi, M., Lindsey, J. S., Bocian, D. F., Meyer, G. J., Holten, D., Examination of tethered porphyrin, chlorin, and bacteriochlorin molecules in mesoporous metal-oxide solar cells. *J. Phys. Chem. C*, 2007, **111**, 15464 – 15478.

162. Mutiah, C., Taniguchi, M., Kim, H. –J., Schmidt, I., Kee, H. L., Holten, D., Bocian, D. F., Lindsey, J. S., Synthesis and photophysical characterization of porphyrin, chlorin and bacteriochlorin molecules bearing tethers for surface attachment. *Photochem. Photobiol.* 2007, **83**, 1513 – 1528.

163. Taniguchi, M., Cramer, D. L., Bhise, A. D., Kee, H. L., Bocian, D. F., Holten, D., Lindsey, J. S., Accessing the near-infrared spectral region with stable, synthetic, wavelength-tuneable bacteriochlorins. *New J. Chem.*, **32**, 947 – 958.

164. Krayer, M., Yang, E., Diers, J. R., Bocian, D. F., Holten, D., Lindsey, J. S., *De novo* synthesis and photophysical characterization of annulated bacteriochlorins. Mimicking and extending the properties of bacteriochlorophylls. *New J. Chem.*, 2011, **35**, 587 – 601.

165. Chen, C. –Y., Sun, E., Fan, D., Taniguchi, M., McDowell, B. E., Yang, E., Diers, J. R., Bocian, D. F., Holten, D., Lindsey, J. S., Synthesis and physiochemical properties of metallobacteriochlorins. *Inorg. Chem.*, 2012, **51**, 9443 – 9464.

166. Hu, G., Liu, R., Alexy, E. J., Mandal, A. K., Bocian, D. F., Holten, D., Lindsey, J. S., Panchromatic chromophore-tetrapyrrole light-harvesting arrays constructed from Bodipy, perylene, terrylene, porphyrin, chlorin and bacteriochlorin building blocks. *New J. Chem.*, 2016, **40**, 8032 - 8052.

167. Zhang, S., Kim, H. –J., Tang, Q., Yang, E., Bocian, D. F., Holten, D., Lindsey, J. S., Synthesis and photophysical characteristics of 2,3,12,13-tetraalkylbacteriochlorins. *New. J. Chem.*, 2016, **40**, 5942 – 5956.

168. Reddy, M. N., Zhang, S., Kim, H. –J., Mass, O., Taniguchi, M., Lindsey, J. S., Synthesis and spectral properties of *meso*-arylbacteriochlorins, including insights into essential motifs of the hydrodipyrrin precursors. *Molecules*, 2017, **22**, 634 – 665.

169. Liu, M., Chen, C. –Y., Hood, D., Taniguchi, M., Diers, J. R., Bocian, D. F., Holten, D., Lindsey, J. S., Synthesis, photophysics and electronic structure of oxobacteriochlorins. *New J. Chem,* 2017, **41**, 3732 – 3744.

170. Zhang, S., Reddy, M. N., Mass, O., Kim, H. – J., Hu, G., Lindsey, J. S., Synthesis of tailored hydrodipyrrins and their examination in directed routes to bacteriochlorins and tetrahydrocorrins. *New J. Chem,* 2017, **41**, 11170 – 11189.

171. Jiang, J., Chen, C. –Y., Zhang, N., Vairaprakash, P., Lindsey, J. S., Polarity-tunable and wavelength-tunable bacteriochlorins bearing a single carboxylic acid or NHS ester. Use in a protein bioconjugation model system. *New. J. Chem.*, 2015, **39**, 403 – 419.

172. Kiang, J., Yang, E., Reddy, K. R., Niedzweidzki, D. M., Kirmaier, C., Bocian, D. F., Holten, D., Lindsey, J. S., Synthetic bacteriochlorins bearing polar motifs (carboxylate, phosphonate, ammonium and a short PEG). Water-solubilization, bioconjugation, and photophysical properties. *New J. Chem.*, 2015, **39**, 5694 – 5714.

173. Zhang, N., Jiang, J., Liu, M., Taniguchi, M., Mandal, A. K., Evans-Storms, R. B., Pitner, J. B., Bocian, D. F., Holten, D., Lindsey, J. S., Bioconjugatable, PEGylated hydroporphyrins for photochemistry and photomedicine. Narrow-band, near-infrared-emitting bacteriochlorins. *New J. Chem.,* 2016, **40**, 7750 – 7767.

174. Harris, M. A., Sahin, T., Jiang, J., Vairaprakash, P., Parkes-Loach, P. S., Niedzweidzki, D. M., Kirmaier, C., Loach, P. A., Bocian, D. F., Holten, D., Lindsey, J. S., Enhanced light-harvesting capacity by micellar assembly of free accessory chromophores and LH1-like antennas. *Photochem. Photobiol.*, 2014, **90**, 1264 – 1276.

175. Sahin, T., Harris, M. A., Vairaprakash, P., Niedzwiedzki, D. M., Subramanian, V., Shreve, A. P., Bocian, D. F., Holten, D., Lindsey, J. S., Self-assembled light-harvesting system from chromophores in lipid vesicles. *J. Phys. Chem. B*, 2015, **119**, 10231 – 10243.

176. Mancini, J. A., Kodali, G., Jiang, J., Reddy, K. R., Lindsey, J. S., Bryant, D. A., Dutton, P. L., Moser, C. C., Multi-step excitation energy transfer engineered in genetic fusions of natural and synthetic light-harvesting proteins. *J. R. Soc. Interface*, 2017, **14**, 20160896.

177. Bain, C. D., Throughton, E. B., Tao, Y. –T., Evall, J., Whitesides, G. M., Nuzzo, R. G., Formation of monolayer films by the spontaneous assembly of organic thiols from solution onto gold. *J. Am. Chem. Soc.,* 1989, **111**, 321 – 335.

178. Love, J. C., Estroff, L. A., Kriebel, J. K., Nuzzo, R. G., Whitesides, G. M., Self-assembled monolayers of thiolates on metals as a form of nanotechnology. *Chem. Rev.,* 2005, **105**, 1103 – 1169.

179. Graham, D. J., Price, D. D., Ratner, B. D., Solution assembled and microcontact printed monolayers of dodecanethiol on gold: a multivariate exploration of chemistry and contamination. *Langmuir*, 2002, **18**, 1518 – 1527.

180. Vericat, C., Vela, M. E., Benitez, G., Carro, P., Salvarezza, R. C., Self-assembled monolayers of thiols and dithiols on gold: new challenges for a well-known system. *Chem. Soc. Rev.*, 2010, **39**, 1805 – 1834.

181. Alves, C. A., Smith, E. L., Porter, M. D., Atomic scale imaging of alkanethiolate monolayers at gold surfaces with atomic force microscopy. *J. Am. Chem. Soc.*, 1992, **114**, 1222 – 1227.

182. Malinsky, M. D., Kelly, K. L., Schatz, G. C., Van Duyne, R. P., Chain length dependence and sensing capabilities of the localized surface plasmon resonance of silver nanoparticles chemically modified with alkanethiol self-assembled monolayers. *J. Am. Chem. Soc.*, 2001, **123**, 1471 – 1482.

183. Haes, A. J., Van Duyne, R. P., A nanoscale optical biosensor: sensitivity and selectivity of an approach based on the localized surface plasmon resonance spectroscopy of triangular silver nanoparticles. *J. Am. Chem. Soc.*, 2002, **124**, 10596 – 10604.

184. Riboh, J. C., Haes, A. J., McFarland, A. D., Yonzon, C. R., Van Duyne, R. P., A nanoscale optical biosensor: real-time immunoassay in physiological buffer enabled by improved nanoparticle adhesion. *J. Phys. Chem. B*, 2003, **107**, 1772 – 1780.

185. Porter, M. D., Bright, T. B., Allara, D. L., Chidsey, C. E. D., Spontaneously organized molecular assemblies. 4. Structural characterization of *n*-alkyl thiol monolayers on gold by optical ellipsometry, infrared spectroscopy, and electrochemistry. *J. Am. Chem. Soc.*, 1987, **109**, 3559 – 3568

186. Zheng, T. –C., Burkat, M., Ricahrdson, D. E., A general and mild synthesis of thioesters and thiols from halides. *Tetrahedron Lett.*, 1999, **40**, 603 – 606.

187. Hu, J., Fox, M. A., A convenient trimethoxysilylthioxy-dehalogenation reaction for the preparation of functionalized thiols. *J. Org. Chem.*, 1991, **64**, 4959 – 4961.

188. Wuts, P. G. M., Greene, T. W., *Greene's Protective Groups in Organic Chemistry*. 4th ed. New Jersey, John Wiley & Sons, Inc., 2007.

189. Tour, J. M., Jones II, L., Pearson, D. L., Lamba, J. J. S., Burgin, T. P., Whitesides, G. M., Allara, D. L., Parikh, A. N., Atre, S. V., Self-assembled monolayers and multilayers of conjugated thiols, a,ω-dithiols, and thioacetyl-containing adsorbates. Understanding attachments between potential molecular wires and gold surfaces. *J. Am. Chem. Soc.*, 1995, **117**, 9529 – 9534.

190. Hacker, C. A., Batteas, J. D., Garno, J. C., Marquez, M., Richter, C. A., Richter, L. J., van Zee, R. D., Zangmeister, C. D., Structural and chemical characterization of monofluoro-substituted oligo(phenylene-ethynylene) thiolate self-assembled monolayers on gold. *Langmuir*, 2004, **20**, 6195 – 6205.

191. Lau, K. H. A., Huang, C., Yakovlev, N., Chen, Z. K., O'Shea, S. J., Direct adsorption and monolayer self-assembly of acetyl-protected dithiols. *Langmuir*, 2006, **22**, 2968 – 2971.

192. Krapchetov, D. A., Ma, H., Jen, A. K. Y., Fischer, D. A., Loo, Y. –L., Deprotecting thioacetyl-terminated terphenyldithiol for assembly on gallium arsenide. *Langmuir*, 2008, **24**, 851 – 856.

193. Singh, A., Dahanayaka, D. H., Biswas, A., Bumm, L. A., Halterman, R. L., Molecularly ordered decanthiolate self-assembled monolayers on Au(111) from in situ cleaved decanethioacetate: an NMR and STM study of the efficacy of reagents for thioacetate cleavage. *Langmuir*, 2010, **26** (16), 13221 – 13226.

194. Gregory M. J., Bruice, T. C., Nucleophilic displacement reactions at the thiol ester bond. V. Reactions of 2,2,2-trifluoroethyl thiolacetate. *J. Am. Chem. Soc.*, 1967, **89** (9), 2121 – 2127.

195. McMurry, J. E., Melton, J., A new method for the conversion of nitro groups into carbonyls. *J. Org. Chem.*, 1973, **38** (26), 4367 – 4373.

196. Chen, C. –Y., Bocian, D. F., Lindsey, J. S., Synthesis of 24 bacteriochlorin isotopologues, each containing a symmetrical pair of ^{13}C or ^{15}N atoms in the inner core of the macrocycle. *J. Org. Chem.*, 2014, **79**, 1001 – 1016.

197. Morimoto, H., Fujiwara, R., Shimizu, Y., Morisaki, K., Ohshima, T., Lanthanum(III) triflate catalysed direct amidation of esters. *Org. Lett.*, 2014, **16**, 2018 – 2021.

198. Lovrić, M., Cepanec, I., Litvić, M., Bartolinčić, A., Vinković, V., Scope and limitation of sodium and potassium trimethylsilanolate as reagents for conversion of esters to carboxylic acids. *Croat. Chem. Acta*, **80** (1), 109 – 115.

199. Soai, K., Ookawa, A., Mixed solvents containing methanol as useful reaction media for unique chemoselective reductions with lithium borohydride. *J. Org. Chem.*, 1986, **51**, 4000 – 4005.

200. Knox, R. S., Spring, B. Q., Dipole strengths in the chlorophylls. *Photochem. Photobiol.*, 2003, **77** (5), 497 – 501.

201. Oviedo, M. B., Sánchez, C. G., Transition dipole moments of the Q_y band in photosynthetic pigments. *J. Phys. Chem. A*, 2011, **115**, 12280 – 12285.

202. Hsu, C. -P., Walla, P. J., Gordon, M. H., Fleming, G. R., The role of the S_1 state of carotenoids in photosynthetic energy transfer: the light-harvesting complex II of purple bacteria. *J. Phys. Chem. B*, 2001, **105**, 11016 – 11025.

203. Smykalla, L., Shukrynau, P., Mende, C., Lang, H., Knupfer, M., Hietschold, M., Photoelectron spectroscopy investigation of the temperature-induced deprotonation and substrate-mediated hydrogen transfer in a hydroxyphenyl-substituted porphyrin. *Chem. Phys.*, 2015, **450 – 451**, 39 – 45.

204. Wasserman, S. R., Biebuyck, H., Whitesides, G. M., Monolayers of 11-trichlorosilylundecyl thioacetate: a system that promotes adhesion between silicon dioxide and evaporated gold. *J. Mater. Res.*, 1989, **4** (4), 886 – 892.

205. Diller, K., Klappenberger, F., Marschall, M., Hermann, K., Nefedov, A., Wöll, Ch., Barth, J. V., Self-metalation of 2H-tetraphenylporphyrin on Cu(111): An x-ray spectroscopy study. *J. Chem. Phys.*, 2012, **136**, 014705.

206. Killian, M. S., Gnichwitz, J. –F., Hirsch, A., Schmuki, P., Kunze, J., ToF-SIMS and XPS studies of the adsorption characteristics of a Zn-porphyrin on TiO_2. *Langmuir*, 2010, **26** (5), 3531 – 3538.

207. Sengputa, S., Würther, F., Chlorophyll J-aggregates: From bioinspired dye stacks to nanotubes, liquid crystal and biosupramolecular electronics. *Acc. Chem. Res.*, 2013, **46** (11), 2498 – 2512.

208. Shoji, S., Ogawa, T., Hashishin, T., Ogaswara, S., Watanabe, H., Usami, H., Tamiaki, H., Nanotubes of biomimetic supramolecules constructed by synthetic metal chlorophyll derivatives. *Nano Lett.*, 2016, **16** (6), 3650 – 3654.

209. Smith, E. A., Wanat, M. J., Cheng, Y., Barreira, S. V. P., Frutos, A. G., Corn, R. M., Formation, spectroscopic characterization, and application of sulfhydryl-terminated alkanethiol monolayers for the chemical attachment of DNA onto gold surfaces. *Langmuir*, 2001, **17**, 2502 – 2507.

210. Zhao, B., Brittain, W. J., Polymer brushes: surface-immobilized macromolecules. *Prog. Polym. Sci.*, 2000, **25**, 677 – 710.

211. Barbey, R., Lavanant, L., Paripovic, D., Schüwer, N., Sugnaux, C., Tugulu, S., Klok, H. –A., Polymer brushes via surface-initiated controlled radical polymerization: synthesis, characterization, properties, and applications. *Chem. Rev.*, 2009, **109,** 5437 – 5527.

212. Stuart, M. A. C., Huck, W. T. S., Genzer, J., Müller, M., Ober, C., Stamm, M., Sukhorukov, G. B., Szleifer, I., Tsukruk, V. V., Urban, M., Winnik, F., Zaushcer, S., Luzinov, I., Minko, S., Emerging application of stimuli-responsive polymer materials. *Nat. Mater.*, 2010, **9**, 101 – 113.

213. Matyjaszewski, K., Xia, J., Atom transfer radical polymerization. *Chem. Rev.*, 2001, **101**, 2921 – 2990.

214. Maillard, B., Ingold, K. U., Scaiano, J. C., Rate constants for the reactions of free radicals with oxygen in solution. *J. Am. Chem. Soc.*, 1983, **105**, 5095 – 5099.

215. Min, K., Jakubowski, W., Matyjaszewski, K., AGET ATRP in the presence of air in miniemulsion and in bulk. *Macromol. Rapid Commun.*, 2006, **27**, 594 – 598.

216. Matyjaszewski, K., Dong, H., Jakubowski, W., Pietrasik, J., Kusumo, A., Grafting from surface for "everyone": ARGET ATRP in the presence of air. *Langmuir,* 2007, **23**, 4528 – 4531.

217. Min, K., Gao, H., Matyjaszewski, K., Use of ascorbic acid as reducing agent for synthesis of well-defined polymers by ARGET ATRP. *Macromolecules*, 2007, **40**, 1789 – 1791.

218. Chen, J. –K., Hseih, C. –Y., Huangm C. –F., Li, P. –M., Kuo, S. –W., Chang, F. –C., Using solvent immersion to fabricate variably patterned poly(methyl methacrylate) brushes on silicon surfaces. *Macromolecules*, 2008, **41**, 8729 – 8736.

219. Minko, S., Responsive polymer brushes. *J. Macromol. Sci. C*, 2006, **46**, 397 – 420.

220. Ballauff, M., Borisov, O., Polyelectrolyte brushes. *Curr. Opin. Colloid In.*, 2006, **11**, 316 – 323.

221. Alswieleh, A. M., Cheng, N., Canton, I., Ustbas, B., Xue, X., Ladmiral, V., Xia, S., Ducker, R. E., Zubir, O. E., Cartron, M. L., Hunter, C. N., Leggett, G. J., Armes, S. P., Zwitterionic poly(amino acid methacrylate) brushes. *J. Am. Chem. Soc.*, 2014, **136**, 9404 – 9413.

222. Madsen, J., Ducker, R. E., Al Jaf, O., Cartron, M. L., Alswieleh, A. M., Smith, C. H., Hunter, C. N., Armes, S. P., Leggett, G. J., Fabrication of microstructure binary polymer brush "corrals" with integral pH sensing for studies of proton transport in model membrane systems. *Chem. Sci.*, 2018, **9**, 2238 – 2251.

223. Brantley, E. L., Holmes, T. C., Jennings, G. K., Modification of ATRP surface-initiated poly(hydroxyethyl methacrylate) films with hydrocarbon side chains. *J. Phys Chem. B*, 2004, **108**, 16077 – 16084.

224. Dai, J., Bao, Z., Sun, L., Hong, S. U. H., Baker, G. L., Bruening, M. L., High-capacity binding of proteins by poly(acrylic acid) brushes and their derivatives. *Langmuir*, 2006, **22**, 4274 – 4281.

225. Cullen, S. P., Liu, X., Mandel, I. C., Himpsel, F. J., Gopalan, P., Polymeric brushes as functional templates for immobilizing ribonuclease A: study of binding kinetics and activity. *Langmuir*, 2008, **24**, 913 – 920.

226. Barbey, R., Laporte, V., Albnabulsi, S., Klol, H. -A., Postpolymerization modification of poly(glycidyl methacrylate) brushes: an XPS depth-profiling study. *Macromolecules*, 2013, **46**, 6151-6158.

227. Christau, S., Möller, T., Yenice, Z., Genzer, J., von Klitzing, R., Brush/gold nanoparticle hybrids: effect of grafting density on the particle uptake and distribution within weak polyelectrolyte brushes. *Langmuir*, 2014, **30**, 13033 – 13041.

228. Zhang, Z. J., Edmondson, S., Mears, M., Madsen, J., Armes, S. P., Leggett, G. J., Geoghegan, M., Blob size controls diffusion of free polymer in a chemically identical brush in semidilute solution. *Macromolecules*, 2018, **51**, 6312 – 6317.

229. Andruzzi, L., Hexemer, A., Li, X., Ober, C. K., Kramer, E. J., Galli, G., Chiellini, E., Fischer, D. A., Control of surface properties using fluorinated polymer brushes produced by surface-initiated controlled radical polymerization. *Langmuir*, 2004, **20**, 10498 – 10506.

230. Sterner, O., Serrano, Â., Mieszkin, S., Zürcher, S., Tosatti, S., Callow, M. E., Callow, J. A., Spencer, N. D., Photochemically prepared, two-component polymer-concentration gradients. *Langmuir*, 2013, **29**, 13031 – 13041.

231. Ryan, A. A., Senge, M. O., How green is green chemistry? Chlorophylls as a bioresource from biorefineries and their commercial potential in medicine and photovoltaics. *Photochem. Photobiol. Sci.*, 2015, **14**, 638 – 660.

232. Tamiaki, H., Takeuchi, S., Tsudzuki, S., Miyatake, T., Tanikaga, R., Self-aggregation of synthetic zinc chlorins with a chiral 1-hydroxyethyl group as a model for *in vivo* epimeric bacteriochlorophyll-*c* and *d* aggregates. *Tetrahedron*, 1998, **54**, 6699 – 6718.

233. Furukawa, H., Watanabe, T., Kuroda, K., Immobilization of chlorophyll derivatives into mesoporous silica and energy transfer between the chromophores in mesopores. *Chem. Commun.*, 2001, 2002 – 2003.

234. Furukawa, H., Inoue, N., Watanabe, T., Kuroda, K., Energy transfer between chlorophyll derivatives in silica mesostructured films and photocurrent generation. *Langmuir*, 2005, **21**, 3992 – 3997.

235. Grabarek, Z., Gergely, J., Zero-length crosslinking procedure with the use of active esters. *Anal. Biochem.*, 1990, **185**, 131 – 135.

236. Sehgal, D., Vijay, I. K., A method for the high efficiency of water-soluble carbodiimide-mediated amidation. *Anal. Biochem.*, 1994, **218**, 87 – 91.

237. Olde Damink, L. H. H., Dijkstra, P. J., van Luyn, M. J. A., van Wachem, P. B., Nieuwenhuis, P., Feijen, J., Cross-linking of dermal sheep collagen using a water-soluble carbodiimide. *Biomaterials,* 1996, **17**, 765 – 773.

238. Patel, N., Davies, M. C., Hartshorne, M., Heaton, R. J., Roberts, C. J., Tendler, S. J. B., Williams, P. M., Immobilization of protein molecules onto homogenous and mixed carboxylate-terminated self-assembled monolayers. *Langmuir*, 1997, **13**, 6485 – 6490.

239. Wasielewski, M. R., Svec, W. A., Synthesis of covalently linked dimeric derivatives of chlorophyll *a*, pyrochlorophyll *a*, chlorophyll *b*, and bacteriochlorophyll *a*. *J. Org. Chem.*, 1980, **45**, 1969 – 1974.

240. Smith, K. M., Goff, D. A., Simpson, D. J., *Meso* substitution of chlorophyll derivatives: direct route for transformation of bacteriopheophorbides *d* into bacteriopheophorbides *c*. *J. Am. Chem. Soc.*, 1985, **107**, 4946 – 4954.

241. Brandis, A. S., Kozyrev, A. N., Mironov, A. F., Synthesis and study of chlorin and porphyrin dimers with ether linkage. *Tetrahedron*, 1992, **48** (31), 6485 – 6494.

242. Ma, L., Dolphin, D., Stereoselective synthesis of new chlorophyll *a* related antioxidants isolated from marine organisms. *J. Org. Chem.*, 1996, **61**, 2501 – 2510.

243. Saga, Y., Tamiaki, H., Facile synthesis of chlorophyll analog possessing a disulphide bond and formation of self-assembled monolayer on gold surface. *J. Photoch. Photobio. B*, 2004, **73**, 29 – 34.

244. Li, Y., Sasaki, S. –i., Tamiaki, H., Liu, C. –L, Song, J., Tian, W., Zheng, E., Wei, Y., Chen, G., Fu, X., Wang, X. –F., Zinc chlorophyll aggregates as hole transporters for biocompatible, natural-photosynthesis-inspired solar cells. *J. Power Sources*, 2015, **297**, 519 – 524.

245. Kenner, G. W., McCombie, S. W., Smith, K. M., Pyrroles and related compounds. Part XXIV. Separation and oxidative degradation of chlorophyll derivatives. *J. Chem. Soc., Perkin Trans.*, 1973, **1**, 2517 – 2523.

246. Jiménez, A., Sarsa, A., Blázquez, M., Pineda, T., A molecular dynamics study of the surfactant surface density of alkanethiol self-assembled monolayers on gold nanoparticles as a function of the radius. *J. Phys. Chem. C*, 2010, **114**, 21309 – 21314.

247. Scheer, H., *Chlorophylls*. 1st ed. CRC Press, 1991.

248. Zalyubovskiy, S. J., Bogdanova, M., Deinega, A., Lozovik, Y., Pris, A. D., An, K. H., Hall, W. P., Potyrailo, R. A., Theoretical limit of localized surface plasmon resonance sensitivity to local refractive index change and its comparison to conventional surface plasmon resonance sensor. *J. Opt. Soc. Am. A*, 2012, **29** (6), 994 – 1002.

List of Abbreviations

- **AGET / ARGET** - Activators (Re)Generated by Electron Transfer
- **AFM –** Atomic Force Microscopy
- **APTES** - 3-Aminopropyltriethoxysilane
- **ATRP –** Atom Transfer Radical Polymerization
- **BChl *a*** – Bacteriochlorophyll *a*
- **12-BDDA** – 12-Bromododecanoic acid
- **12-BDDC** – 12-Bromodedecanoyl chloride
- **2,2'-Bipy** – 2,2'-Bipyridyl
- **Chl *a* –** Chlorophyll *a*
- **CysMA** – Cysteine methacrylate
- **DBU** - 1,8-diazabicyclo[5.4.0]undec-7-ene
- **DMAP** - 4-dimethylaminopyridine
- **DMF** – Dimethylformamide
- **DMSO** – Dimethyl sulfoxide
- **DPTS -** Dimethylaminopyridinium tosylate
- **2,6-DTBP –** 2,6-Di-*tert*-butyl pyridine
- **DTBU** - Bis[2-(2-bromoisobutyryloxy)undecyl] disulfide
- **EDC -** 1-(3-Dimethylaminopropyl)-3-ethylcarbodiimide hydrochloride
- **LSPR** - Localised Surface Plasmon Resonance
- **NHS** - N-Hydroxysuccinimide
- **NMR** – Nuclear Magnetic Resonance spectroscopy
- **MS –** Mass Spectrometry
- **MALDI-MS** – Matrix Assisted Laser Desorption/Ionization Mass Spectrometry
- **MUA –** Mercapto-1-undecanoic acid
- **SIMS** – Secondary Ion Mass Spectrometry
- **ToF** – Time-of-Flight
- **TMSOTf** - Trimethylsilyl trifluoromethanesulfonate
- **TosMIC** - p-Toluenesulfonylmethyl isocyanide
- **UDT** – 1-Undecanethiol
- **XPS** – X-ray Photoelectron Spectroscopy

List of Figures

Chapter 2

Chapter 3

Chapter 4

Figure 4.19: The derivatization of a poly(CysMA) brush (with the maximum surface density of polymer chains) with SC-Zn-pyChl a. The attachment of chlorophyllides is diffusion limited, leading the surface 2 nm region to be the most derivatized compared to the deeper regions. 185

Figure 4.20: The thickness plot with polymerization time of poly(CysMA) growth on several plasmonic arrays of gold nanostructures, before and after Zn-pyChl a attachment in DMF. 186

Figure 4.21: The extinction spectrum for a plasmonic array (NL51) (in black), after grafting of poly(CysMA) (red) and derivatisation with Zn-pyChl a in DMF (blue). The solution spectrum of Zn-pyChl a is included for comparison. The plasmon peak is red shifted after growth of polymer brushes on the sample, but then blue-shifted and split into a major peak with a poorly resolved shoulder feature. An additional peak feature (above 700 nm in the blue spectrum) was found to be unrelated to the plasmon-exciton coupling phenomenon. 188

Figure 4.22: Comparison of the extinction spectrum for NL51 re-derivatised with 1:3 DMF: H_2O with the previously acquired spectra from Fig. 4.21. 190

Figure 4.23: The exciton energy and scaled coupling energy for plasmonic samples coupled to Zn-pyChl a in DMF against the original E_{LSPR} before polymerization and attachment.............................191

Figure 4.24: Scaled coupling energy for plasmonic nanoarrays coupled to Zn-pyChl a attached to poly(CysMA) brushes in DMF as a function of polymer brush thickness. 192

Figure 4.25: The density of Zn-pyChl a molecules appended to poly(CysMA) brushes was predicted to increase when the density of polymer chains is reduced on the surface. While full-density brush layers gave diffusion-limited attachment concentrated on the surface sites, reducing the density by reducing the number of active initiators (red) by co-adsorptions of spacers (grey) in the initial monolayer would allow greater derivatization further into the brush layer. While the total amount of scaffold material would be reduced, this would allow a larger number of dipoles within the plasmon mode volume of an array of gold nanostructures. 195

Figure 4.26: Thickness of poly(CysMA) brushes after 10 and 30 min polymerization time for various monolayer ratios of DTBU: UDT...196

Figure 4.27: The extinction spectrum of a clean array of gold nanoparticles, then functionalised with a monolayer of 1:5 DTBU: UDT and grafted with poly(CysMA), followed by derivatisation with Zn-pyChl a. The extinction spectrum for Zn-pyChl a in solution is included for comparison. 198

List of Tables